THE UNIVERSITY *of* EDINBURGH

This thesis has been submitted in fulfilment of the requirements for a postgraduate degree (e.g. PhD, MPhil, DClinPsychol) at the University of Edinburgh. Please note the following terms and conditions of use:

This work is protected by copyright and other intellectual property rights, which are retained by the thesis author, unless otherwise stated.
A copy can be downloaded for personal non-commercial research or study, without prior permission or charge.
This thesis cannot be reproduced or quoted extensively from without first obtaining permission in writing from the author.
The content must not be changed in any way or sold commercially in any format or medium without the formal permission of the author.
When referring to this work, full bibliographic details including the author, title, awarding institution and date of the thesis must be given.

MESOSCOPIC ANALYSIS OF DAMAGE MECHANISMS IN CONCRETE MATERIAL

Thesis submitted for the degree of

Doctor of Philosophy

Rongxin Zhou

Institute for Infrastructure and Environment

School of Engineering

The University of Edinburgh

August, 2016

This thesis is dedicated to

My wife Hanmei and My son Leyang

Table of Contents

Figures and Tables

Declaration

I hereby declare that,

This thesis was composed by me and the work contained therein was solely the work of the author except otherwise acknowledged in the text.

No part of this thesis has been submitted for any other degree or professional qualification.

Signed:

Rongxin Zhou

The University of Edinburgh

Date submitted: 29/08/2016

Lay Summary

Concrete is the most widely used construction material in the world. It has a great variety of applications in the field of structural engineering. A realistic description of the failure mechanisms is very important to ensure the safety of concrete structures. However due to the highly non-homogenous composition with large heterogeneities, the failure mechanisms of concrete structures are not well understood, especially under complex stress conditions. Computational modelling of concrete-like materials at mesoscale, which considers the concrete compositions as coarse aggregates, mortar matrix and the interface transitional zone (ITZ), is deemed to be a powerful means to better understand the failure mechanisms of concrete structures. Therefore developing the mesoscale modelling framework to an effective and efficient level for a realistic description of concrete materials and a sound representation of the mesoscopic damage mechanisms has been the main target of this research project.

To cater the needs for better representing the fracture process in concrete, a coupled cohesive-contact interface approach in a mesoscale model is developed. The scheme is implemented in the 2D mesoscale framework, and at first for the interface transition zone (ITZ) between the aggregates and the mortar matrix; subsequently the scheme is extended for all the three components at the mesoscale throughout the mesh grids. Such a mesoscale interface model allows the explicit representation of the crack initiation, propagation and friction mechanism during the whole fracture process in the concrete.

In order to overcome the inherent limitation of the 2D mesoscale concrete model, a full 3-D mesoscale finite element model for concrete-like materials with the realistic random structure is developed in which the actual shape and size of the aggregate particles are well captured and the possibility of high packing density of the aggregate is also enabled.

After verifying against typical experimental evidence, specific numerical models are subsequently set up to explore the intrinsic failure mechanisms underlying important phenomena in concrete structures such as fracture propagation in tension and compression, the well-known size effect, and the strain rate effect subjected to high rate loading.

Acknowledgements

The research project presented in this thesis is funded by the China Scholarship Council and the University of Edinburgh through a joint scholarship. I take this opportunity to sincerely acknowledge the China Scholarship Council and the University of Edinburgh for providing me the financial assistance during these years.

I am heartily grateful to my supervisor Professor Yong Lu for his unreserved guidance, advice and discussion during my PhD study. He has spent countless time on discussing my research and going through in great detail of my work at every stage. His broad range knowledge, in-depth insight to the research field have been a great value for me. Specifically, his rigorous scientific approach really impresses me and would benefit me a lot during all my academic career.

I also want to thank my colleagues and friends at IIE for enjoyable conversation and discussion, as well as playing sports like badminton and football – all of these will be precious memories in my life. Dr. Jiaming Xu, Dr. Chuanchuan Hou, Dr. Fengchen An, Mr. Lige Wang and Mr. Xiaobo Cheng deserve special mention for their company and help in most aspects of life in Edinburgh.

I am deeply indebted to my wife Hanmei and my son Leyang for their unconditional support and endless love. They have sacrificed a lot due to my research abroad, and to them this thesis is dedicated.

To my friends and family, particularly my two elder sisters, I wish to thank you all for the understanding and encouragement, which mean so much to me in my way of studying.

Finally, special thanks are given to my parents and parents-in-law for their loving support and tolerance. I highly appreciate their willingness and kindness in helping me to take care of my son so that I can focus on this research project. Without their love and support, it would not be possible for me to complete this thesis.

Abstract

Concrete is a highly non-homogeneous composite with large heterogeneities of quasi-brittle character. Failure of concrete structures is usually accompanied by cracking of concrete, which is strongly affected by the mesoscale structure and the behaviour of the interface between the aggregates and the mortar matrix, especially under complex stress conditions. Analysis of the failure mechanisms of concrete at the mesoscale is therefore crucial for a better understanding of the macroscopic behaviour of the material, which can in turn contribute to improved design of concrete structures and finding new ways to enhance the material properties.

This research aims to investigate the intrinsic failure mechanisms of concrete-like materials from a mesoscale point of view. To do this, continued developments from existing work on mesoscale modelling are carried out to cater the needs of realistically simulating the damage process in concrete under complex loading conditions. The new developments focus on two key aspects. Firstly, techniques to realistically simulate the fracture process of concrete are developed and these involve the incorporation of a combined cohesive and contact mechanisms for the interface between aggregates and mortar matrix. Such interface modelling allows the crack initiation and propagation at the mesoscale to be explicitly represented. Secondly, a full 3D mesoscale finite element model for concrete-like materials with random aggregates and the possibility of high packing density is developed. Use is then made of these enhanced mesoscale models to explore the intrinsic mechanism governing the fundamental behaviour of concrete such as fracture propagation in tension and compression, the well-known size effect and the dynamic strain rate effect.

The research investigation begins with an analysis of the size effect in plain concrete beams under three-point bending using a generic 2D mesoscale model. The analysis aims to provide preliminary insight into the use of a mesoscopic computational tool for examining the concrete damage mechanisms with the well-known size effect phenomenon as a benchmark scenario. The shapes and the sizes of the fracture process zone (FPZ) during the whole fracture process are captured. The role of detailed FPZ features is discussed accordingly. On the other hand, the results also

point out the deficiencies of the continuum-based mesoscale framework at capturing the evolution of the local fracture process, and to resolve this problem requires explicit simulation of the initiation and propagation of the micro-cracks and thus a realistic reproduction of the fracture process zone, and this becomes the subject of research in much of the later chapters of the thesis.

To cater to the needs of better representing the fracture process in concrete, a coupled cohesive-contact interface approach is proposed to model the crack initiation, crack propagation and the friction mechanism within the transition zone between the coarse aggregates and the mortar matrix. The cohesive-contact combined model is verified to perform well under simple as well as complex loading conditions. The interface approach in a mesoscale model framework provides a new platform for investigating the failure mechanisms in terms of the cohesive fracture process and the contact friction process.

A more comprehensive and robust mesoscale interface modelling approach, in which the cohesive plus contact interface is inserted along all mesh grids, is developed to study the complex dynamic behaviour of concrete with the consideration that fractures can spread in a fine distributed manner within larger damage areas including the strong aggregate, particularly under high loading rate. By allowing local fractures to develop explicitly, the issues with fracture damage description with a continuum material model can be largely resolved. The effectiveness of such an approach is demonstrated and employed in an investigation into the intrinsic mechanisms governing the sensitivity of the dynamic tension resistance with the loading rate.

Subsequently, a re-visit of the size effect in terms of the evolution of the fracture process zones using the mesoscale model with cohesive plus contact interface model is conducted and the results are presented. The preliminary observations from using the continuum-based mesoscale model are examined and verified. Additional insight into the fracture processes in the concrete beams with various sizes is obtained and the intrinsic mechanisms of the size effect are further discussed.

On the real 3D mesoscale modelling methodology, the new development focuses on achieving a realistic representation of the actual shapes and sizes of aggregate particles and at the same time allowing for high volumetric ratios of aggregates (packing density) to be attained. In addition to specific techniques to enhance the conventional take-and-place procedure, an algorithm to generate supplementary aggregates to allow increased packing density is proposed and implemented. Example 3D mesoscale specimens so created are then verified against standard experimental tests such as uniaxial compression, uniaxial tension and compression with lateral confinements, and applied to examine the dynamic behaviour of concrete under high strain rate compression.

Chapter 1 : Introduction

1.1 Background

Concrete is the most used construction material. The mechanical behaviour of concrete is well known to be complex and the complexity varies dramatically under different stress conditions, and under quasi-static and dynamic loadings. A couple of interesting, yet hard to fully explain, examples follow. Under quasi-static loading conditions, the nominal strength of concrete is observed to be strongly dependent on the specimen size, and the smaller the specimen size the stronger it is. This phenomenon is also well known as size effect. When concrete is subjected to high strain rate (or loading rate), whether in compression or tension, the apparent strength tends to be sensitive to the strain rate; with increasing of the loading rate, the apparent strength increases, which is known as strain rate effect. Although almost all the experimental investigations arrive at the conclusion that these phenomena are linked to the fracture processes, such as crack initiation and propagation within the concrete, experimental techniques themselves cannot fully demonstrate the intrinsic mechanisms underlying such behaviours. Therefore numerical modelling in which the failure mechanisms and the influence of individual parameters can be studied in detail is highly desirable. Such modelling analysis will ultimately enable a better understanding of the macroscopic behaviour of the material, which can in turn contribute to improved design of concrete structures and finding new ways to enhance the material properties.

Modelling of concrete at the mesoscale which considers the concrete compositions as coarse aggregates, mortar matrix and the interface transitional zone (ITZ) is deemed to be a powerful means for understanding of the physical processes underlying the macroscopic strength and failure behaviour of the composite materials under various loading conditions. To this end, the development of a comprehensive and robust mesoscale framework is required, but there are several challenges that require continued research. Among them, an effective way to generate randomly shaped and

distributed aggregates at desired packing density remains to be a key issue that needs to be tackled. Appropriate modelling of the interface between the aggregates and the mortar matrix is next. Furthermore, as concrete behaves like a continuum solid in the intact state, but when damage cumulates it gradually becomes discontinuous, realistic modelling of the fracture and the behaviour of fractured material from a mesoscale perspective is yet another critical issue.

1.1.1 Challenges on generating 3D meso-structure

Generally speaking, generation of the meso-structure should be no trouble in a 2D modelling framework and a number of studies on the 2D mesoscale modelling of concrete can be found in the existing literature (Wang et al. 1999; Zhou & Hao 2008a; Tu & Lu 2011; Grassl et al. 2012; Pedersen et al. 2013). However, mesoscale modelling of concrete-like material in 2D has inherent limitation in representing a realistic stress and strain condition in concrete, particularly when pressure and confining stress becomes important such as in dynamic compression where lateral inertial confining effect is deemed a critical factor.

The primary difficulty arises from the representation of a random aggregate structure in 3D. To circumvent this difficulty, simple shapes of aggregate particles like spheres (Mishnaevsky Jr 2006; Wriggers & Moftah 2006) or mixed spheres and ellipsoids (Leite et al. 2004) are mostly used in previous research. Further proposal of a modified version of the ellipsoid function (Häfner et al. 2006) made it possible to better approximate real aggregates. Also a more accurate approximation of particle shapes represented by polyhedrons, which were generated from Voronoi tessellation point set, has been adopted by some researchers (Caballero et al. 2006; Benkemoun et al. 2010; Galindo-Torres et al. 2012). This method can approximate the real aggregate shape better than simple spheres and ellipsoids but it is difficult to satisfy the pre-defined aggregate size grading curve as it is rather dependent upon the pattern of the random points. Some more recent studies have focused on developing approaches which can generate and randomly pack polyhedron aggregates following a predefined grading curve (Song & Lu 2011; Yin et al. 2015; Wang et al. 2016). However a common challenge to most existing meso-structure models of concrete is

a relatively low aggregate packing density and it is generally difficult to reach an aggregate volume ratio as in the real concrete specimens. It is worth noting that in some studies where higher volume fractions of aggregates have been reported (e.g. Du et al. 2011; Liu et al. 2014), those were not the real packing densities for the polyhedron aggregates but the equivalent spherical particles. These equivalent spherical particles were defined by introducing an equivalent diameter of which the value is an average size of the aggregates.

In a different approach, direct mapping of the aggregate particle from physical samples has been explored using computer image analysis and computed tomography (CT-scan) (Man & Van Mier 2011; Huang et al. 2015; Roubin et al. 2015; Skarżyński & Tejchman 2016). However, the major limitation of this technique is that it would be very time-consuming and expensive to obtain meaningful analyses by preparing, fabricating, cutting specimens and then dealing with the scanned images.

1.1.2 Challenges on modelling ITZ

At a mesoscopic level, aggregates are usually much stronger than mortar, and therefore the mortar matrix constitutes the primary source of damage and nonlinear behaviour. Particularly at the boundary of mortar with the aggregates, a weaker transition layer which is known as the interface transition zone or ITZ forms. Compounded by stress concentration due to the incompatibility of the mechanical properties between mortar and aggregates, crack tends to initiate and grow from the ITZ. Consequently, the macroscopic failure in concrete is much dependent on the interface between aggregate and mortar, and as such a sound representation of the ITZ mechanical properties and the fracture at the ITZ is crucial for a realistic modelling of the mesoscopic damage mechanisms for concrete-like materials.

It is generally understood that the real ITZ has a thickness in the range of 20-50 μm (Scrivener et al. 2004), and its mechanical properties are different from the cement paste. An exact incorporation of such a thin layer of material in the mesoscale FE model is impractical; instead, using zero initial thickness cohesive elements is deemed to be a rational representation. The mechanical properties of the interface are

generally described using a cohesive law, which represents a gradual loss of the strength with increasing separation and can also be related to the work of separation, or fracture energy that is required for the complete formation of a free surface.

An equivalent layer of solid elements approach is also used by many researchers, but that is effectively an equivalent treatment due to an inevitable exaggerated thickness and the properties of the equivalent layer can only be determined in an empirical manner (Tu & Lu 2011). Moreover, as crack damage grows the solid ITZ layer is subject to distortion and consequently numerical instability may occur in advanced damage state.

Understandingly, the option to use cohesive elements for the modelling of ITZ in a mesoscale model depends upon the capacity of the cohesive elements in catering to complex stress conditions. A classical cohesive model, as available in LS-DYNA, is suited for modelling the interface failure involving interaction of model I and mode II fractures. Applying this cohesive element model proves to work well under tension-dominated loading, but it performs poorly in other loading conditions including axial compression (Tu & Lu 2011). The reason is deemed to relate to the inability of the cohesive element in representing the shear failure of the ITZ under a complex stress condition, and more specifically under compressive stress in the normal direction. As generally known, the shear strength of the ITZ in concrete-like materials is strongly dependent on the normal stress at the interface. With the presence of a compressive stress, the shear strength is expected to increase significantly, but this important mechanism is not adequately represented in the classical cohesive model.

Nagai et al (2004) proposed a Rigid Body Spring Model (RBSM) in which normal and shear springs are placed at the boundary of elements for the simulation of concrete. The constitutive model of the normal spring is quite similar to a cohesive model. It allows damage evolution after the normal spring reaches a specified tensile strength, and in compression it behaves only elastically and does not fail nor exhibit softening behaviour. For the shear spring, an elastoplastic model is adopted, and the plastic shear strength is dependent upon the current condition of the normal spring. It should be noted that a simple 2D mesoscale model with only circularly shaped

aggregates is used in their work, and moreover the framework of their model is based on beam lattice network. A major drawback is the difficulty in defining the material properties input in connection with the lattice geometry.

Some other techniques have also been developed in attempt to address the coupled effect of normal and shear stresses at a cohesive interface. An interface element which incorporates the interaction of cohesion, tensile strength and the friction angle in a constitutive model has been proposed (López et al. 2008a) to investigate the concrete fracture mechanism under complex loading conditions. The main feature of this interface element is that it introduces the friction dissipative mechanism between two potential crack surfaces into the cohesive law internally. By defining several loading fracture surfaces at different loading stages with shape parameters, their model can generally simulate the whole process from fracture to pure friction. However some of the parameters used in their model cannot be obtained straightforwardly and some are also case dependent. Moreover, as Ruiz et al. (2001) suggested, the contact and friction process should be regarded as independent from the cohesive law because physically fracture and friction are two independent phenomena, and in particular the presence of friction may result in a steady frictional resistance while the normal cohesive strength simultaneously weakens. Thus a contact-friction algorithm should be used to treat the interaction resistance at the cracking and cracked surfaces.

1.1.3 Challenges on modelling fracture process in concrete

In numerical models, a key factor that determines the extent to which the mesoscopic failure mechanisms may be realistically represented is the modelling of fractures. In lattice models, fracture is generally represented by continuingly breaking (removing) the lattice members (beam or truss elements) when a failure criterion is met. This approach is suitable for crack opening, but it cannot accommodate possible crack closure which could happen during the complex evaluation of damage within the bulk of concrete, not to mention reversed loading. The discrete element or particle models possess inherent advantages in accommodating crack-induced discontinuity; however its ability in modelling the continuum and partially damaged phases of concrete is very much subject to the equivalent description of the continuum

properties through point contacts, and such equivalent description is difficult to generalize for different stress conditions.

Mesoscale models in a finite element framework is clearly superior in the representing the nature of concrete as non-homogenous continuum to start with. As in the general FE model of concrete as homogeneous medium, cracks may be described using either a smeared or a discrete approach. Previous research has shown some well-known problems, such as mesh size dependency, and limited deformation modes of the standard continuum elements in the smeared crack approach when the softening behaviour is involved (López et al. 2008b). And it performs more poorly in dynamic loading condition where stress wave effect is involved. To tackle these problems, a variety of techniques have been developed for regularization and tracking of cracks. But no universal method is in sight yet for solving a general fracture problem for concrete-like materials.

In contrast to the above continuum damage-based technique to model fracture within a finite element framework, the discrete approach can explicitly follow the initiation and propagation of multiple cracks. The potential cracks are introduced via zero-thickness interface elements equipped with a fracture based constitutive law, which may be inserted along all the grid lines of the mesh. These interface lines can branch, coalesce, and eventually form new free surfaces. Therefore by extending the cohesive plus contact approaches used in ITZ into all the grid mesh lines, the local fracture mechanisms including cohesion and friction developed during the failure process in concrete can be explicitly simulated. In this way the issues with fracture damage description with a continuum material model can be largely resolved.

1.2 Objectives and scope

This research endeavours to investigate the intrinsic failure mechanisms of concrete-like materials from a mesoscale point of view. To do this, continued developments from existing framework on mesoscale modelling are carried out to cater the needs of realistically simulating the damage process in concrete under complex loading conditions.

There are two key aspects on the new developments for the mesoscale numerical framework. Firstly, techniques to realistically simulate the fracture process of concrete are developed and these involve the incorporation of a combination of the cohesive and contact mechanisms for the interface between aggregates and mortar matrix. Such interface modelling approach allows the crack initiation and propagation at the mesoscale to be explicitly represented. These enhanced mesoscale models are verified against standard experimental observations under quasi-static compression and tension. Secondly, in order to overcome the inherent limitation of the 2D mesoscale concrete model, a full 3D mesoscale finite element model for concrete-like materials with a realistic representation of the actual shape and sizes of aggregate particles and at the same time allowing the high packing density of aggregates is developed Use is then made of these enhanced modes to investigate the intrinsic micro-mechanisms governing the failure behaviour of concrete such as the well-known size effect, and the dynamic strain rate effect both in tension and compression.

1.3 Methodology

The generation of the mesoscale geometric structures is carried out using the Take-and-Place approach in conjunction with the creation of the individual aggregate particles based on computational geometry, and the whole procedure is implemented by in-house programming with MATLAB.

The geometric data is subsequently brought into meshing processors. For 2D mesoscale framework, ANSYS pre-processor is used to perform the FE meshing while for 3D highly unstructured space, a more robust meshing tool named TETGEN is adopted to do the meshing. For 3D mesoscale models, an algorithm is developed to then generate supplementary aggregates to increase the packing density to a desired level.

An in-house procedure is developed for the insertion and identification of the cohesive element within the initial meso-structure of the concrete specimen and the procedure is also coded with MATLAB.

The developed mesoscale models are applied to investigate the behaviours of concrete from various aspects including quasi-static and dynamic loadings. The transient analysis hydrocode LS-DYNA is employed to perform the simulations.

1.4 Organization of the thesis

Following the introduction of this research in Chapter 1, Chapter 2 presents a literature review on a few major topics which define the scope of this thesis. The review of more specific techniques concerning each topical area is incorporated in the individual chapters.

In Chapter 3, a generic 2D mesoscale framework developed earlier in this research group is applied to investigate the size effect phenomenon in plain concrete beams under three-point bending, with an enhanced treatment of fracture by a nonlocal description within the mesoscale continuum damage-based framework. In the model, concrete is modelled as a random heterogeneous three-phase material (coarse aggregates, mortar matrix and the interface transitional zone, also known as ITZ). The macro response of stress-strain curves as well as the shapes and sizes of fracture process zones (FPZ) calculated from numerical simulations are firstly verified against representative experimental evidences. The role of detailed FPZ features in the size effect problem is discussed accordingly. The necessity of representing the mesoscopic structure of the material in the calculation of the shape and size of the fracture process zone is highlighted. Finally, the deficiencies of the continuum damage-based mesoscale framework at capturing the evolution of the local fracture process are pointed out. Resolving this problem becomes part of the motivation for the subsequent work on developing a holistic interface model, which are the topics of Chapter 4 onwards.

Chapter 4 presents the development of a mesoscale model in which the interface between the aggregates and mortar matrix (i.e. the ITZ) is explicitly modelled with a combined cohesive and contact interface algorithm, thus allowing explicit modelling of fracture and the fracture effects at the interfaces. In this approach, the contact-friction process is regarded as an independent phenomenon outside the cohesive law. Parametrisation is conducted to examine and set benchmark on the effects of the

individual parameters in the proposed combined model. The mesoscale cohesive-contact combining contact model is then verified against representative experimental evidences. The model is also applied in an analysis of the dynamic properties of concrete under dynamic compression. The developed interface approach in a mesoscale model framework provides a new platform for investigating the failure mechanism in term of the cohesive fracture process and the contact friction process.

In Chapter 5, the mesoscale model with an explicit representation of the ITZ is further developed such that the cohesive plus contact interface is realised along all mesh grids. In this way, simulation of complete fracture initiation and propagation through the entire concrete composite domain become possible, as this situation occurs in many applications and fracture could even split the stronger aggregates under high dynamic loading. Much effort has been devoted to developing an algorithm to insert cohesive elements throughout the mesh grids in a concrete specimen, and to identifying the cohesive element properties based on the original mesoscale structure. After parameter studies in terms of the cohesive element properties, the model is used to investigate the mesoscopic mechanisms underlying the sensitivity of the dynamic resistance of the concrete material to the strain rates. The contribution of dynamic strength enhancement due to micro crack inertial effect, material heterogeneity and the interaction among multiple cracks is evaluated.

In Chapter 6, with the availability of the more robust mesoscale cohesive plus contact interface model, the size effect problem which was preliminarily discussed in Chapter 3 is re-visited with particular attention paid on tracking the local fracture process. The unique advantages of the new model in simulating the local fracture process from an explicit mesoscopic viewpoint as well as directly achieving mesh independent results for both global and local response without any special treatment are highlighted. The analysis provides new insight into the mechanisms of the evolution of the fracture process zone, in addition to the general observations from using the continuum damage-based mesoscale model.

Chapter 7 is dedicated to the development of a realistic 3D mesoscopic model with a special focus on increasing the volumetric ratio (packing density) of the aggregates. The standard take-and-place procedure is used for generating the main 3D meso-

structure. Enhanced procedures are incorporated to improve the efficiency in the generation of the basic 3D mesoscale geometry. In particular, an algorithm is developed to overcome the barrier on the packing density, such that supplementary aggregates are created to meet a targeted volume ratio of aggregates in a typical range of around 45% as in normal concrete. The 3D mesoscale model generated from the enhanced procedure is verified against standard experimental observations under quasi-static compression and tension. With the expectation that the crucial lateral confinement effect during the transient dynamic response can be realistically represented, the model is then further applied to simulate the dynamic behaviour of concrete under high strain rate compression. In the last part of this chapter, the contribution to the dynamic strength enhancement from the stronger aggregates is evaluated.

Chapter 8 summarizes the main conclusions and recommendations for further research.

Chapter 2 : Literature review

2.1 Introduction

The failure process of concrete structures is accompanied by many interesting behaviours. For instance, in the quasi-static loading regime, the nominal strength of concrete is observed to be dependent on the specimen sizes. The smaller the specimen the stronger it is, and this is known as the size effect. On the other hand, when concrete specimens are subjected to dynamic loading especially at high strain rates, the mechanic response is reported to be very sensitive to the loading rate. With increasing of the loading rate, the apparent strength tends to show an increasing trend; this is called the strain rate effect. As such behaviours as the size effect and strain rate effect relate to the fundamental characteristics of concrete, they have attracted wide and continued interest in the research community concerning the mechanics of concrete and its appropriate analysis and modelling.

This chapter provides a review of general literature on the main topics which define the scope of this thesis. More specific review of the techniques which are closely related to the developments in this thesis will be presented in the individual chapters.

This literature review commences with studies on the size effect phenomenon, under quasi-static loading. Typical theories used for interpreting such a behaviour will be summarised, with an emphasis on the investigation of fracture process zone. This is followed by a review of studies on the strain rate effect of concrete under dynamic loadings, with a focus on the possible mechanisms affecting the dynamic response in tension due to a close connection to the cohesive plus contact modelling approach developed in this thesis. The review then continues with more recent studies on the mesoscopic modelling framework concerning the analysis of concrete failure behaviour. The approaches to modelling the mesoscale geometry, extending from 2D to 3D, are compared and discussed. Finally, an overview of the developing trend in fracture modelling of concrete from continuum damage-based techniques to discrete approaches is presented.

2.2 Studies of size effects in concrete

The size effect in quasi-brittle materials such as concrete is a well-known phenomenon and it has attracted numerous experimental, theoretical and numerical studies in the last few decades. Although almost all physical properties, including compressive strength, tensile strength, elastic modulus and fracture energy have been reported to be dependent on specimen sizes, attention has been focused on the variation of failure strength with specimen size in most references (Bažant 2000). In a typical definition, the size effect is the dependence of the dimensionless nominal strength σ_N of a specimen on its characteristic structure size (dimension) D when geometrically similar specimens are compared. The smaller the specimen size, the greater is the nominal strength (Bažant 1999).

2.2.1 Theoretical studies and possible mechanisms

At the beginning, it was widely believed that any experimentally observed size effect on the nominal strength of structures was of statistical origin (Weibull 1951; Mihashi 1983), caused by randomness of local material strength and described by Weibull statistical theory based on the fact that the larger the structure the greater the probability to encounter weak points in its volume.

However since early 1980s, it became known that there should exist another type of size effect, namely deterministic size effect, even homogeneous material properties were considered (Bazant 1984; Bažant 2000). It is further firmly established that the size effect in quasi-brittle materials like concrete, mortar, and rocks is mainly the deterministic one (Morel & Dourado 2011). This is because unlike metal materials, there is a sizable fracture process zone (or FPZ in short) made of micro-cracks around and ahead of the crack tip, which may strongly influence the macro facture behaviour of concrete.

Bažant (2000) proposed that the presence of the sizeable FPZ at or around crack tip could lead to a stress redistribution within the specimen, which would result in a mismatch between the size dependence of the energy release rate and the rate of

energy consumption. And this unbalance energy rate could be the source of deterministic size effect.

However Hu & Duan (2004; 2008) insisted that the size effect phenomenon is actually due to the interaction of FPZ with the nearest structure boundary. They also concluded that the key factor in determining the size dependent fracture parameters is not the specimen size itself, but actually the ratio of FPZ versus its distance to the nearest structure boundary. And the well-known size effect for geometrically-similar specimens of different sizes is only a special case of quasi-brittle fracture determined by the FPZ-boundary interaction.

Thus the debate continues as what is the specific relation between FPZ and the size effect phenomenon, though the important role of FPZ during the fracture process has been commonly accepted.

2.2.2 Experimental studies on FPZ

Realizing the importance of the FPZ during the fracture process in concrete, it is significant to be able to measure the size of the FPZ and on this basis to investigate the role of the FPZ in the size dependence of fracture parameters. Various measurement techniques have been employed to track the fracture process in concrete experimentally.

Otsuka and Date (2000) used the X-ray and 3D acoustic emission (AE) techniques to investigate the influence of specimen size on the shape and size of FPZ in concrete. Their results showed that the shape and size of FPZ are strongly affected by the specimen size.

Muralidhara et al. (2010) applied AE technique to investigate the fracture process in notched concrete beams under three-point bending test. The formation and evolution of FPZ in concrete were discussed based on the results of the AE measurement. The FPZ size was obtained by evaluating the acoustic emission energy, instead of amplitude, associated with each of the event.

Wu et al. (2011) conducted a comprehensive experimental investigation on the properties of the FPZ in concrete using the digital image correlation (DIC) techniques. Notched concrete beams under three-point bending test with different spans and notch depths were tested in the experiment. When the results were compared in the specimens with similar geometrical properties, it was found that the FPZ length at the peak load and the maximum FPZ length increases with an increase in specimen size.

2.2.3 Numerical studies on FPZ

Using numerical simulations to describe the FPZ in concrete has also been reported by many researchers in the literature.

Veselý and Frantík (2010) outlined a technique for estimating the size and shape of an inelastic zone evolving around a crack tip during the tensile failure of concrete structures. It was found that the shape and size of the damage zone, which was referred to as an inelastic zone in their simulations, agree well with the results measured by the AE approach.

Tejchman (2010) and Skarżyński et al. (2011) performed several mesoscopic simulations to investigate the fracture process of notched concrete beams subjected to three-point bending. The FPZ was depicted as a localized damage zone with a non-local strain softening damage constitutive model. The influences of meso-structure such as aggregate distribution, aggregate size, bond thickness etc. on the shape and size of FPZ were discussed. Numerical results were also compared with experimental evidence measured by the DIC technique.

Grassl et al. (2012) investigated the size effect on fracture process zone in notched and un-notched beams under three-point bending with a mesoscopic lattice modelling framework. The FPZ is determined numerically by evaluating the average of spatial distribution energy densities from the resulting damage patterns of the lattice elements. It was found that the shape and size of FPZ are strongly dependent on the size of the specimen.

Alam et al. (2013) developed a method to depict FPZ according to the crack opening profiles inspired by the method used in DIC techniques. An isotropic non-local strain softening damage constitutive law was adopted for the numerical model. Global and local results from numerical simulations were compared with experimental data. And a shortcoming of the numerical model was found to be related with the material description.

However the specific physical relation between FPZ and the size dependent nominal strength has been generally accepted. Thus the first task in the present study has been to provide new insight into addressing this issue with the advancement in the development of the mesoscale model.

2.3 Studies of strain rate effects in concrete

Concrete is generally known to be strain-rate sensitive. When it is subjected to high strain-rate loading, the apparent strength has been observed to increase dramatically with the loading rate. A dynamic increase factor (DIF), which is defined as the ratio of dynamic strength to static strength, is generally used to represent the strength enhancement for the design and analysis of protective structures.

2.3.1 Experimental studies

Laboratory experimentations concerning the dynamic response of concrete have been extensively conducted using various test devices and procedures. For compressive response under relative low strain rate (up to 10 /s), the hydraulic testing machines (Bresler & Bertero 1975) and the drop-hammer techniques (Hughes & Gregory 1972; 1978) can be directly used to meet experimental demands. High strain rates (10 – 1000 /s) could be reached by the adaptation of the Split Hopkinson Pressure Bar (SHPB) equipment (Ross et al. 1995). For ultra-high strain rates (order of 10000 /s), the plate impact experiments may become the best choice (Grote et al. 2001a).

Comparing to the dynamic compression tests, it is more difficult to set up dynamic tension apparatus for concrete materials due to their low tensile failure strain. A direct tensile test performed on a high-speed hydraulic press may be used to investigate the dynamic tensile behaviour of concrete over strain rate from 1e-3 /s to

about 1 /s (Erzar & Forquin 2011a). Alternative devices that may be used in a relatively high loading range (0.1 /s – 10 /s) include the Split Hopkinson pressure bar (SHPB) adapted for direct tension testing (Ross et al. 1995), as well as indirect tension with the Brazilian tests via SHPB (Ross et al. 1996). To achieve higher strain rates in dynamic tensile test of concrete materials, other experimental techniques have been developed. The most commonly used one is the spalling test (Schuler et al. 2006; Weerheijm & Van Doormaal 2007; Erzar & Forquin 2010), which can achieve strain-rates in the order of 100 /s for brittle specimens that have much higher compressive strength than tensile strength to avoid the pre-damage by the compressive wave. Extremely high strain rates in the range of few thousands /s to even 1e4 /s may be obtained in plate-impact experiments (Grote et al. 2001b) in which the specimen is essentially loaded in a uniaxial strain state.

2.3.2 Numerical simulations on dynamic compression

Although all the experimental investigations described above arrive at the conclusion that the response of concrete material is very sensitive to the loading rates, the limitation of the experimental technique itself as well as the composite nature of the concrete material make it very difficult to truly understand the detailed behaviour of concrete structure under dynamic loading conditions. Thus various numerical models which aim to delve the mechanisms underlying the dynamic response have been developed.

Donze et al. (1999) simulated the dynamic compression behaviour of concrete with a 3D discrete element model (DEM) by reproducing the Split Hopkinson Pressure Bar apparatus. The results from their simulations showed that even the viscosity effect was not embedded in the material constitutive model the numerical data could still agree well with experimental evidence. This may suggest that the strength enhancement under dynamic compression from experimental test can be simply attained from the lateral inertial confinement effect which is a nature product within the sample structure during dynamic loading process.

Georgin and Reynouard (2003) simulated the same experimental set-up (SHPB), but the cylindrical concrete specimen was developed by a homogeneous finite

continuum-based element model. In the simulation, the results from hydrostatic stress dependent and independent constitutive models were scrutinised and compared. It showed that the lateral inertial force in a hydrostatic stress dependent model may develop a confinement effect in the test, which leads to an apparent strength increase in the specimen.

A more comprehensive and extensive 3D numerical simulation of SHPB tests was conducted by Li et al. (2009). Both solid and tubular cylindrical mortar specimens were performed from numerical simulations. The results showed that while a smaller lateral confinement effect was observed in the tubular specimen, the apparent DIFs obtained from the tubular specimens were also smaller than those in solid ones at the same strain-rate. This observation tends to confirm the dominant role of lateral inertial confinement effect in causing an apparent increase of DIFs under dynamic compression.

More recently a lot of effort has been spent on analysing the dynamic response of concrete on mesoscopic level, taking the mesoscopic fracture process into account. Park et al. (2001) simulated a plate impact test with a mesoscale concrete model accounting for two phases, i.e. coarse aggregates and mortar. An extended hydrostatic stress dependent material model incorporating the strain rate sensitivity was used for the two constituent phases. Besides a combination of effects of the inertial confinement and material viscosity, the simulation results showed that the random mesoscopic structure can also have strong influence of the dynamic response within a concrete specimen at an extremely high strain rate loading. In particular the effect of aggregate volume fraction on the dynamic strength increase was characterised.

Zhou and Hao (2008a) conducted a numerical simulation of SHPB tests with a very simple 2D mesoscale concrete model within which only a circular shape of aggregates was assumed. By comparing the simulation results with those from a homogeneous model, it was concluded that the lateral inertial confinement was more significant in the mesoscale concrete model, and in this way the presence of aggregate particles tends to make a contribution to the strength enhancement in dynamic compression.

However after conducting a series of numerical simulations with a more comprehensive 2D mesoscale concrete model, Lu et al. (2010) pointed out that mesoscale modelling of concrete-like material in 2D has inherent limitation in representing a realistic stress and strain condition in concrete specimen, particularly in dynamic compression where lateral inertial confining effect tends to play an important role. Thus they developed a pseudo 3D mesoscale concrete model with a sandwich layout, a layer of the plane mesoscale model and a body of the homogeneous concrete material. Besides demonstrating the advantage of pseudo 3D mesoscale concrete model in terms of withholding a realistic 3D inertial confining effect, they also found a sensible role of the mesoscale heterogeneity in the observed DIF in the apparent dynamic compressive strength of concrete.

2.3.3 Numerical simulations on dynamic tension

Regarding the numerical work on dynamic tensile response in concrete, Ruiz et al. (2000) performed a numerical simulation of Brazilian cylinder test in a SHPB setting. Cohesive elements embedded in FEM model were used to explicitly predict the micro-crack initiation and propagation. Even if the cohesive properties were set as rate-independent, the numerical simulations could still capture closely the experimental observed rate sensitivity of the dynamic strength of concrete. Thus it was concluded that the micro-crack inertial effect in dynamic micro-cracking initiation and propagation may be responsible for the rate sensitivity in the tensile behaviour of concrete.

Barpi (2004) used a visco-plasticity material model in which a viscosity parameter was defined as a function of strain rate to describe the dynamic tensile response of concrete under splitting test. The results revealed that the viscosity appeared to be the key reason for the increase of DIF in tension. Hentz et al. (2004a) stated a similar augment by simulating the dynamic loading with SHPB for both compression and tension. A 3D discrete element method was adopted for their simulations. The results showed that while the DIF in compression could be largely contributed by inertial-based hypothesis (structure effect), the DIF in tension may be more a material intrinsic effect (material property) than a structure effect.

However Cotsovos and Pavlović (2008) performed a direct dynamic tension simulation on a simple concrete prism with a non-linear rate-independent constitutive material model. Based on their results they suggested that the effect of strain rate on the specimen behaviour must be viewed as a structure effect, which was directly linked to the axial inertial effect of its mass and the boundary conditions, instead of intrinsic material property. It should be noted that the specimens simulated in their numerical analysis were of large size.

Lu and Li (2011) reproduced three representative dynamic tensile loading apparatuses, namely direct dynamic tensile test, dynamic splitting test and spalling test by numerical simulations using a homogeneous strain-rate independent concrete damage model. It was found that the numerical results from all these three types of dynamic tensile tests did not show any stain rate dependency. Hence they concluded that the strain rate enhancement of the tensile strength observed in dynamic tensile test is a genuine material effect. They further conducted a qualitative study on a micro-mechanism model and concluded that micro crack inertial effect and material property heterogeneity could be the intrinsic mechanisms responsible for the dynamic tensile response in concrete.

Most recently, Ožbolt et al. (2014) conducted a series of numerical simulations to investigate the dynamic fracture of concrete in tension using micro-plane constitutive model in which rate dependency is considered to be a combination effects of growing micro-crack and material viscosity. Based on the results they proposed that the apparent strength enhancement at relatively high loading rate should consists of two contributions, namely the true material strength which is controlled by the rate dependent constitutive law and the inertial structural effect which is automatic in a dynamic analysis using a fine FE model. They also concluded that the results of any indirect tension test such as splitting test with SHPB require careful interpretation since the apparent strength recorded from such experiments may get mixed up with the true material strength and the structural inertial effect.

Mesoscopic numerical simulations on dynamic tension response in concrete was also conducted by many researchers. Zhou and Hao (2008b) performed a mesoscopic analysis of dynamic behaviour in Brazilian cylinder under splitting tensile loading

condition using simplified mesoscale model. It was found that the mesoscopic features like ITZ properties, aggregate positions and aggregate volume fractions can have some influence on the crack pattern and the measured tensile strength.

Erzar and Forquin (2011a) developed a mesoscopic approach in which the matrix and the randomly distributed aggregates are differentiated to check and validate the accuracy of experimental measurement techniques. Two representative dynamic tensile tests, namely a spalling test and an edge-impact test were both reproduced by numerical simulations. The mesoscopic computational results show good agreement with experimental evidences. Thus they concluded that the mesoscopic approach can be very useful to validate testing techniques and to simulate the dynamic behaviour of concrete.

Pedersen et al. (2013) proposed a comprehensive mesoscopic model to analyse the dynamic tensile response of concrete specimen under a SHPB test (or Modified Hopkinson Pressure Bar test). A regularized constitutive model in which a moisture effect can be incorporated with material viscosity was adopted for each constituent phase. The influence of the mesoscopic features, the moisture content as well as the loading rates on the dynamic response within concrete specimen were studied. The results showed that the mesoscopic features, particularly the ITZ properties, have strong influence on the global tensile strength. Besides, the moisture content could also affect the dynamic tensile strength by affecting the micro-crack initiation inertial effect.

To summarise, a numerical simulation can be an important and useful tool to enhance our understanding about the failure mechanisms underlying the dynamic behaviour of concrete. While there is a general consensus that the dynamic compressive strength enhancement may largely attributable to the lateral inertial confinement effect, the mechanisms behind the strain rate dependent dynamic tension response is still not quite clear. Further exploration on this topic from micromechanical processes that combine effects of the material heterogeneity and micro crack initiation and propagation is required.

2.4 Mesoscopic numerical modelling of concrete

Mesoscopic modelling of concrete materials has attracted a continuous and widespread research interest in the past few decades due to its advantages in the description of failure process in concrete. A lot of effort has been spent on developing an elegant and robust mesoscale model satisfying the following two conditions: a). Generating a random aggregate structure in which the shape, size and distribution of the coarse aggregate closely resemble real concrete in the statistical sense. b). Accurate prediction of the fracture process within composites.

Generally three types of mesoscale concrete models, namely distinct-element model (DEM), lattice-element model (LEM) and finite-element model (FEM) can be found in the literature. Unlike the continuum-based FEM, materials in DEM are simulated as collection of rigid or deformable particles, which are assembled through contact and cohesion. The continuum medium in LEM is represented by a grid of truss or beam elements forming triangular or rectangular shape, which enable the transfer of moments, axial and shear forces.

2.4.1 Generation of mesoscopic structure

2.4.1.1 In DEM

Idealised shapes like circles/spheres or ellipses/ellipsoids are generally used to generate particle configurations in the DEM approach. When such a model is used to describe the meso-structure of concrete-like materials, the irregular shapes of aggregates may be modelled by either using superquadrics or bonding a number of spheres together.

Jensen et al. (2001) developed an algorithm to achieve representation of complicated shapes in 2D through clumping and shape addition. However most of these methods are only limited in 2D scheme, and there is still a lack of efficient algorithms to represent complicated particle shapes in 3D.

More recently the X-ray computed tomography technique has been adopted to achieve the 3D meso-geometry of concrete-like materials for the DEM approach

(Wang et al. 2007; Latham et al. 2008). Actual shapes of particles may be captured by this method, but specimens need be scanned individually; and moreover it is not easy to come up with a contacting algorithm in a DEM model to describe the interface resistance along the irregular boundaries between aggregates and mortar matrix.

2.4.1.2 In LEM

In lattice models the mesoscopic structure in concrete is generally described by superimposing the aggregate shape on top of the mesh grid. Lattice elements falling into the aggregate, matrix or interface domains are attributed with the corresponding material properties respectively. In this way the three-phasic nature of the concrete composite can be mimicked. Generally speaking circular shapes in 2D or spherical shapes in 3D for aggregate particles are mostly used in the literature (Schlangen & Van Mier 1992; Lilliu & Van Mier 2003).

Leite et al. (2007) developed a stochastic-heuristic algorithm to generate elliptical shape aggregates, which improved the generation of mesoscale structure in 3D concrete specimen, making it closer to the real concrete.

2.4.1.3 In FEM

Mesoscale modelling of concrete using finite-element framework (FEM) allows for the material heterogeneity on mesoscale level to be explicitly represented. Thus it is possible to approximate the real aggregates in a more realistic fashion. However the main challenges of this approach come from generation of meso-geometry and FE meshing for the meso-structure, particularly in three-dimensional case.

Tu and Lu (2011) developed a robust 2D mesoscale model framework based on a methodology proposed by Wang et al. (1999). The generation of the mesoscale geometry follows a commonly adopted take-and-place procedure, satisfying non-overlapping and minimum gap requirements. The aggregates are represented by random polygon particles, and the nominal size of the individual aggregates obeys a given grading curve, making the mesoscale structure very close to real concrete in statistic sense.

However it is not straightforward at all to get an extension of the mesoscale structure from 2D to 3D. The primary difficulty arise from the representation of a random aggregate structure in 3D.

Simple shapes of aggregates particles like spheres (Wriggers & Moftah 2006) or ellipsoids (Häfner et al. 2006) are most used in previous research.

Caballero et al. (2006) presented a new method to generate aggregate particles in the shape of polyhedrons using Voronoi/Delaunay tessellation approach. This method made it possible to model different shapes to lead to a better approximation of real aggregates, but it is difficult to control the size distribution with Voronoi polygons.

Difficulties in 3D mesoscale modelling concrete also arise from FE meshing for the highly unstructured meso-domain as well as the demand of a high packing density of aggregates to represent real concrete. A typical way to work around the difficulties has been to firstly perform a background meshing and then bundling groups of the meshed elements into aggregates of targeted (or mapped) shapes (Riedel et al. 2008; Du et al. 2011). However such an approach cannot preserve the actual surfaces of aggregates, making a saw-tooth shaped boundaries between aggregates and mortar matrix, which may consequently affect the representation of the mesoscopic mechanisms.

As mentioned earlier, direct mapping of the aggregate particle from physical samples has also been explored using computer image analysis (Al-Rousan et al. 2007) and computed tomography (CT-scan) (Man & Van Mier 2008). However it always requires a real specimen; therefore it is suitable for mapping and modelling specific concrete specimens, but cannot generate new samples on its own.

Thus developing a robust 3D mesoscale model with a realistic representation of the actual shapes and sizes of aggregate particles and at the same time allowing for high volumetric ratios of aggregates becomes one of the tasks in the present study.

2.4.2 Modelling fracture process

As stated above a key factor that determines the extent to which the mesoscopic failure mechanism may be realistically represented is the modelling of fracture.

2.4.2.1 In DEM

The distinct element or particle models possess inherent advantages in accommodating crack-induced discontinuity by incorporating the cohesion and bonds contact between each pair of particles (Puri & Uomoto 2002; Hentz et al. 2004b). However its ability in modelling the continuum and partially damaged phases of concrete is very much subject to the equivalent description of the continuum properties through point contacts, and such equivalent description is difficult to generalize for different stress conditions.

2.4.2.2 In LEM

In lattice simulations, fracture processes are reproduced by continuingly breaking the lattice elements from the mesh when a failure criterion is met. A linear-elastic material model is generally used for the lattice elements (Lilliu & Van Mier 2003; Prado & Van Mier 2003). But a damage-based constitutive model has also been employed in some studies (Grassl & Jirásek 2010; Grassl et al. 2012) to simulate the fracture process in concrete by numerically evaluating the average of spatial distribution of dissipated energy densities. Kim and Lim (2011) incorporated visco-plastic model in which a parameter was defined as strain rate sensitivity in LEM to simulate the dynamic fracture process in concrete.

Although the lattice element model has been proved to be suitable to model the crack opening, it may not accommodate possible crack closure which could happen during the complex evaluation of damage within the bulk of concrete, not to mention reversed loading.

2.4.2.3 In FEM

The fracture process of concrete has been conducted extensively using a finite-element framework. Two types of approaches, namely smeared crack model and discrete crack model, have been generally used to describe cracks in concrete.

In smeared crack model, the cracks in concrete are described by a continuum-based damage constitutive material model. Previous research has revealed that the smeared crack model may bring in some problems such as mesh size dependency, and limited deformation modes with the standard continuum elements when the response enters a softening stage (Carol et al. 2011). Although a variety of techniques have been developed for regularization and tracking of cracks, no universal method is in sight yet for solving a general fracture problem for concrete like materials.

In contrast to the smeared crack model, the discrete crack approach directly models the crack via a displacement-discontinuity in an interface element that is inserted between two solid elements. In this way it can explicitly follow the initiation and propagation of multiple cracks, thus avoiding some difficulties with the smeared crack approach.

Dugdale (1960) firstly proposed a cohesive zone model to simulate the gradual process of the cracking surface separation with a cohesive law. Hillerborg et al. (1976) applied the cohesive law in the finite element framework for concrete-like materials. Since then several cohesive constitutive models have been developed in the literature to reproduce the mechanical behaviour of different physical problems.

However as Tu and Lu (2011) pointed out, the classical cohesive model could work well in a tension-dominated loading condition, but it tends to perform poorly in other loading conditions, including axial compression. The reason is deemed to relate to the inability of the cohesive element in representing the shear strength in concrete, which is strongly dependent on the normal stress at the interface.

López et al. (2008a) proposed an improved interface element which could incorporate the interaction of cohesion, tensile strength and the friction angle in a constitutive model to investigate the concrete fracture mechanisms under complex

loading conditions. The main feature of this interface element is that it introduces the friction dissipative mechanism between two potential crack surfaces into the cohesive law intrinsically.

However as pointed out by Ruiz et al. (2001), the contact friction process is an independent phenomenon outside the material constitutive law physically. A contact--friction algorithm should instead be used to treat the interaction resistance between each pair of two cohesive crack surfaces.

The advantages of using cohesive elements in analysing dynamic response of concrete-like materials have also been reported in many publications (e.g. Camacho & Ortiz 1996; Ruiz et al. 2001; Pyo & El-Tawil 2013). One of the advantages of cohesive elements in a dynamic analysis is deemed to be that cohesive theories could introduce an intrinsic time scale into the material description. This intrinsic time scale permits the modelled material to discriminate between slow and fast loading rates and ultimately allows for an accurate prediction of dynamic fracture properties in materials like concrete.

Thus developing an efficient mesoscale FE model with ability to accommodate discrete cracking and further applying this model to investigate the dynamic responses in concrete-like materials has become a key objective in this research.

Chapter 3 : Mesoscopic analysis of size effect in concrete materials

3.1 Introduction

Size effect is a major issue in concrete materials and structures. Although almost all physical properties, including compressive strength, tensile strength, post-peak softening and fracture energy, are associated with size effect in concrete materials, in most reference publications in the literature, attention has been focused on the variation of peak load and failure strength with the specimen size (Bazant & Planas 1998). For plain concrete structures subjected to bending, the nominal strength is observed to strongly depend on the size of structures. Thus three-points bending test has been the most popular apparatus in the study of concrete size effect as such a setup is also easy to operate (comparing to direct tension). In a typical definition, the size effect is the dependence of the dimensionless nominal strength of a beam on its depth when geometrically similar specimens are compared. The smaller the specimen size, the greater is the nominal strength.

This interesting phenomenon has been observed and under continued investigation for many years. At the beginning, it was widely believed that any experimentally observed size effect on the nominal strength of structures was of statistical origin, caused by randomness of local material strength and described by Weibull statistical theory based on the fact that the larger the structure the greater the probability to encounter weak points in its volume. However nowadays it gradually becomes clear that there exists another type of size effect, namely deterministic size effect, which exists even if exactly the same material parameters are used for different sized structures. It has also been firmly established that the size effect in quasi-brittle materials like concrete, mortar, and rocks is mainly the deterministic one (Morel & Dourado 2011).

As it is well known that unlike metal materials, there is a localized damage zone made of micro-cracks between the grains or through the grains around and ahead of crack tip (shown in Figure 3.1). This localized damage zone which is also known as fracture process zone (FPZ) is deemed to have a direct relation with the macro fracture behaviour of concrete. Some researchers also concluded that the existence of the FPZ in front of a growing crack before the maximum load in concrete structure might be the intrinsic reason for the size dependence of the fracture parameters (Zhang & Wu 1999). Bažant (2000) proposed that the presence of sizeable FPZ at or around crack tip could lead a stress redistribution within the specimen, which would result in a mismatch between the size dependence of the energy release rate and the rate of energy consumption. And this unbalance in the energy rates might be the source of deterministic size effect. Hu and Duan (2008) disagreed, however, and they concluded that the size effect mechanism could result from the interaction of FPZ with the nearest structure boundary.

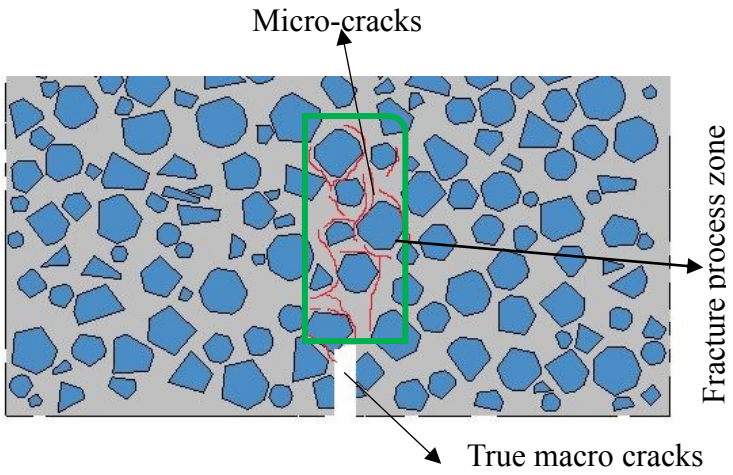

Figure 3.1 Sketch of fracture process in concrete

Due to the important role of FPZ during fracture process in concrete, it is significant to be able to measure the size of the FPZ and on this basis to investigate the role of the FPZ in the size dependence of fracture parameters. Recently various measurement techniques are already employed to track the fracture process in concrete experimentally, for example the holographic interferometry method, the dye penetration method, the scanning electron microscopy method, acoustic emission (AE) techniques, laser speckle techniques, and digital image correction (DIC)

method (Veselý & Frantík 2010). Among all the experimental methods used to detect the fracture process zone, the DIC is adopted mostly. In the DIC method, the fracture process zone is measured by a crack opening profile. Using the displacement field data, the crack opening at various locations of a crack is measured. The length of FPZ is determined as the distance from the notch tip to the location where the crack opening displacement (COD) becomes approximately equal to zero i.e. no damage.

From the perspective of the numerical simulation of fracture process zone, various methods have also been used. Inspired by the method used in DIC experiments, Alam et al. (2013) defined the fracture process zone according to the crack opening profiles which are calculated as the relative (horizontal) displacement field between the nodes of the finite element mesh situated on either side of the localized damage zone. Veselý and Frantík (2010) outlined a technique for estimation of the size and shape of an inelastic zone evolving around a crack tip during the tensile failure of structures made of concrete-like materials. They concluded that the shape and size of the damage zone, which referred to an inelastic zone in their mode, agree well with the fracture process zone measured by AE (acoustic emission) from the experiments. Grassl et al. (2012) analysed the size effect on fracture process zone in notched and un-notched beams under three points bending with a lattice model at meso-scale. The fracture process zone of concrete is determined numerically by evaluating the average of spatial distribution energy densities from the resulting damage patterns of the lattice elements. Skarżyński et al. (2011) investigated the fracture process at meso-scale in notched concrete beams subjected to quasi-static three point bending. The fracture process zone was described as a localized damage zone with a nonlocal strain softening damage constitutive model. They further discussed the influence of the meso-structure, including aggregate distribution, aggregate packing, aggregate size, aggregate roughness, aggregate stiffness, bond thickness, and characteristic length on the shape and size of the fracture process zone.

However, given the complexity of the internal structure of concrete, the debate is still ongoing as ‘How to exactly define FPZ and further measure the size of FPZ’, ‘Whether size of fracture process zone can be considered as an intrinsic material

property and what is the influencing physical mechanism between FPZ and the size dependent fracture parameters?'

The present study is aimed to provide some new insight into addressing the above issues and to contribute to the understanding of the role of FPZ in the size dependent nominal strength in three points bending test. In order to better approximate the real situation involving irregular aggregates, concrete is modelled as a random heterogeneous three-phase material consisting of coarse aggregates, mortar matrix and interfacial transition zone (ITZ). FPZ is defined as a localized plastic damage zone using a continuous plastic damage model enhanced by the nonlocal theory. The macro response of stress - strain curves as well as the shapes and sizes of plastic damage zones calculated from numerical results are first verified against experimental observations. The influences of the specimen sizes on the shape and size of FPZ and the stress states within it are discussed in detail. Finally, it is found that the stress states interaction theory, which is proposed in present study based on the strip yield model in fracture mechanics, can be used to interpret the size dependent nominal strength observed in experiments.

3.2 Overview of the 2D mesoscale model

For the present simulation, a 2D mesoscale modelling scheme is adopted following the previous development (Tu and Lu, 2011). An overview of the main procedure and considerations of such a 2D mesoscale model is provided below.

3.2.1 Generation of the 2D mesoscale model

In this model, the mesoscale structure of concrete is represented by a stochastic distribution of aggregates embedded in the mortar matrix. The aggregates are modelled by random polygon particles, and the nominal size of the individual aggregates obeys a given grading curve. The generation of the mesoscale geometry follows a commonly adopted take-and-place procedure (Wang et al. 1999), satisfying non-overlapping and minimum gap requirements. The procedure is programmed using Matlab. The density of the aggregates can be controlled by specifying a volume ratio.

After the generation of the mesoscale structure, the geometrical data can be fed into a finite element meshing processor. In the present study, ANSYS pre-processor is used, to perform the FE-meshing. Figure 3.2 shows the mesoscale structure of one concrete specimen (a) and its subsequent FE meshing results (b).

(a) Mesoscale structure (b) FE mesh results

Figure 3.2 Mesoscale structure and its corresponding FE mesh result

In the generation of the mesoscale geometry, only the coarse aggregates are considered to form the discrete aggregate phase. For normal concrete, the coarse aggregates include those with a minimum nominal size of 4.75 mm (Wriggers & Moftah 2006). Smaller aggregates are lumped into the mortar phase. The volumetric ratio (or area ratio in 2D) of the coarse aggregates in present study is in a range of 0.4-0.5 with the maximum aggregate size around 8 mm.

The interface transition zone (ITZ) between aggregates and mortar matrix is considered to play an important role affecting the damage initiation and growth in the concrete material. Therefore, in the present mesoscale model the ITZ is explicitly modelled as a separate (third) phase in the composite. Two alternative methods may be considered for the modelling of the interfacial transition zone (ITZ), one using an equivalent layer of solid elements, and another using the zero-thickness cohesive plus contact interface elements as developed in Chapter 4&5. Preliminary analyses have indicated that, as far as the analysis of the mesoscale processes on the size effect is concerned, the use of the simpler solid element representation of the ITZ is sufficient. Therefore in the study presented in this chapter, the mesoscale model employed will involve the solid element representation for the ITZ.

A verification study on the simulation of the size effect using mesoscale model incorporating an explicit cohesive interface model, developed in the present thesis as described in subsequent chapters, will be given in Chapter 6.

3.2.2 Material model and material parameters

Under a general loading condition, damage and the nonlinear behaviour in concrete occur primarily in the mortar matrix and along ITZ. Therefore appropriate nonlinear material models need to be considered for these two parts in order to represent the underlying damage process. The material model employed for these two parts in the present study is the K&C Concrete Damage Model (Malvar et al. 1997). This material model is capable of describing the material failure due to tension, shear, as well as compression under various stress conditions, and it also includes pressure and strain rate dependent features.

The K&C concrete model uses three independent strength surfaces, namely, an initial yield surface, a maximum failure surface and residual surface, with consideration of all the three stress invariants (I_1, J_2, J_3). The strength surfaces are uniformly expressed as:

$$\Delta\sigma = \sqrt{3J_2} = f(p, J_2, J_3) \tag{3.1}$$

where $\Delta\sigma$ and p denote, respectively, the principle stress difference and pressure. The detail information of this material model can be found in (Malvar et al. 1997; Tu & Lu 2009) .

For normal concrete, the coarse aggregates are usually of much higher strength than the mortar matrix and nearly no damage can be found within them under quasi-static loading cases. Thus selection of the precise properties for aggregates are not that important and it is reasonable to use a simple linear elastic material model for aggregates for low rate loading. And as a general guideline in mesoscale numerical framework, the strength properties for mortar are higher than concrete and the properties of the ITZ layer are difficult to determine precisely but it is generally known to be weaker than the mortar matrix (Tejchman 2010; Tu & Lu 2011).

3.3 Numerical model for the three-point test beam

3.3.1 Geometric dimensions of the test specimens

The experiment conducted by Wu et al. (2011) is chosen for the numerical simulation with a mesoscale model. In the experiment, a series of tests were performed on the properties of FPZ in concrete using the DIC technique. In the numerical model, the geometrical dimensions of the specimen are set the same as the experimental case, and the detail are given in Figure 3.3 and Table 3.1. Generally for all the specimens, the span to height ratio $S/D = 4$, the thickness $B = 40$ mm which is kept as constant for all the specimens and the original notch length to the height ratio $a_0/D = 0.3$.

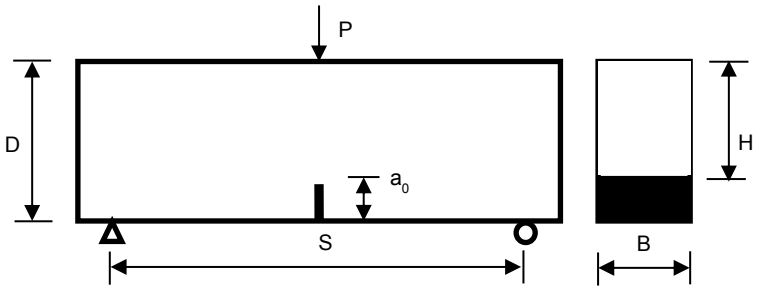

Figure 3.3 Specimen geometry

Table 3.1 Geometrical parameters of specimens

Size range	Small	Medium	Large
Span $\boldsymbol{S}$	160	240	320
Depth $\boldsymbol{D}$	40	60	80
Notch depth $\boldsymbol{a_0}$	12	18	24
Thickness $\boldsymbol{B}$	40	40	40
Ratio $\boldsymbol{a_0/D}$	0.3	0.3	0.3

Since the notch widths of the beam were not given in (Wu et al. 2011), a nominal value of 3 mm is chosen in the present numerical simulations. The widths of the notches are kept the same for all specimens, similar to the treatment as some previous studies on the size effect in the literatures (Bobiński et al. 2009; Skarżyński et al. 2011; Grégoire et al. 2013). To control the cost of computing time, in the finite element analysis, the specimen is modelled as a plane stress problem.

3.3.2 Basic material property parameters

Following the above guidelines, the material properties for the three independent components are determined firstly to match the experimental macro response of the concrete beams reported in (Wu et al. 2011). The details of these material parameters are given in Table 3.2. Figure 3.4 shows the nominal stress versus strain curves under tension and compression, respectively, from the mesoscale model with the above property parameters. The compressive strength is found to be around 43 MPa which is very close to the target strength 42.9 MPa and its corresponding Young's modulus, tension strength is around 35.5 GPa and 3.7 MPa, respectively.

Table 3.2 Material properties

Components	Compressive strength f_c (MPa)	Young's modulus E (MPa)	Poisson's ratio ν (--)	Max aggregate size d_{max} (mm)
Macro	42.9	35000	0.2	8
Aggregates	---	50000	0.2	---
Mortar	54	--	0.2	---
ITZ	40	--	0.2	---

It should be noted here that in the present analysis we focus our attention on investigating the influence of the specimen size only. For this purpose the details of the mesoscale model itself, including the aggregate volume ratio, maximum aggregate size, and the aggregate size distribution are kept the same in the three specimens of different sizes.

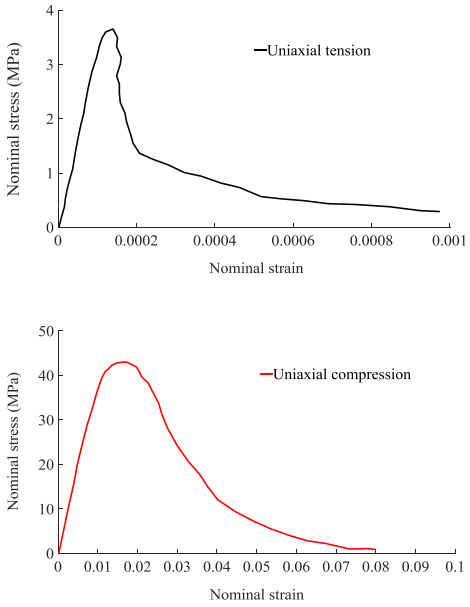

Figure 3.4 Uniaxial tension and compression response of current mesoscale model

3.3.3 Modelling fracture process zone

In some experimental studies mentioned earlier where the DIC technique was used, the fracture process zone was measured by analysing the crack opening profiles. The crack opening profiles were calculated from the digital images considering the sum of the horizontal displacement of points at a certain distance on either side of the crack. More specifically in (Wu et al. 2011) the fracture process zone was defined from the notch-tip to the location where a threshold tensile strain of 83 με was reached. This threshold tensile strain referred to the maximum tensile strain below which concrete could still withstand stress without forming a continuous crack, and it is also known as tensile strain capacity (Swaddiwudhipong et al. 2003). A similar idea is adopted in the present numerical simulation where the fracture process zone is defined as the area within which the element has already entered into softening stage. In the concrete model used in the present study, i.e. the K&C concrete model in LS-DYNA, the identification of this zone may be done easily with the help of the scaled damage factor (*SDF*) that is associated with the material model. The size of the

fracture process zone is then determined accordingly instead of measuring the displacement field or the stress field in the specimens.

The scaled damage factor *SDF* is defined as:

$$SDF = \frac{2\lambda}{\lambda + \lambda_m} \tag{3.2}$$

where λ is a function of effective plastic strain and it is a positive non-decreasing variable. λ_m refers to the value of λ at the maximum failure surface. Therefore *SDF* is in the range of 0~2 for each independent element with $0 < SDF < 1$ meaning no damage, and $1 \leq SDF < 2$ indicating a plastic softening process. Therefore the *SDF* being in the range of 1~2 can be defined as the softening zone, which is equivalent to the fracture process zone.

3.3.4 Model setup for the test beam

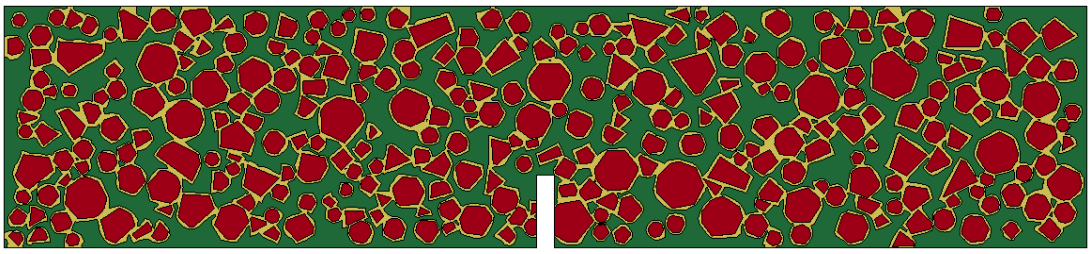

(a) Full meso-structure beam

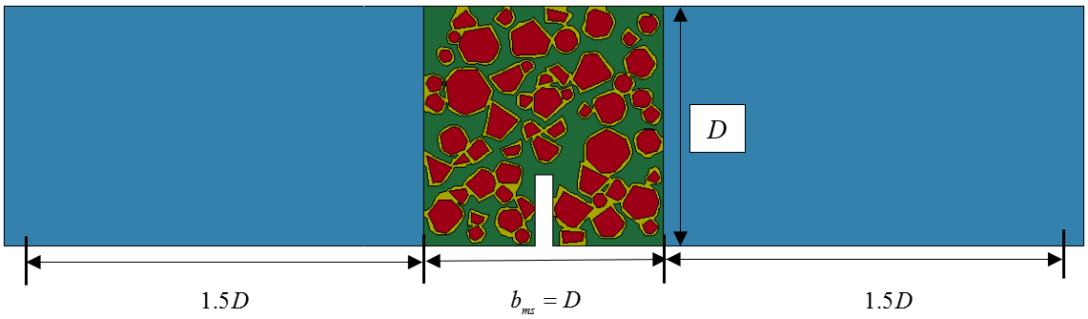

(b) Partial meso-structure beam

Figure 3.5 Two numerical models illustration

In modelling concrete structures such as the beam herein with a mesoscale model, two options may be considered: a) modelling the entire beam with the mesoscale model, as shown in Figure 3.5(a), and b) modelling only the critical region of the beam with the mesoscale model, while the remaining regions are modelled by a homogenous model, as illustrated in Figure 3.5(b). If the critical region(s) can be identified clearly beforehand, use of the second option would be effective and more efficient.

Considering that the damaged zone may only localize in a region close to the notch while the remaining parts are intact with no damage in a notched concrete beam under three-point bending test, the meso-structure is only used in the middle part of the beam to reduce the computational time. The length of the mesoscale region in the middle of the beam is selected to be equal to the depth of the beam ($b_{ms} = D$, see Figure 3.5). The remaining parts of the beams are modelled by elastic properties describing the average of the elastic response of the matrix, aggregate and interfacial transition zone of the composite in the meso-scale region. To demonstrate that such a modelling scheme is sound in preserving the fracture behaviour of the concrete beam, direct comparisons of the beam response in terms of the nominal stress vs. nominal strain relations between the full mesoscale beam model and the partial (middle region) mesoscale model in a small sample beam (D = 40 mm) are presented in Figure 3.6. The damage zones are depicted in Figure 3.7. A mesh size of 0.5 mm is chosen for both models.

Note that the nominal stress here for the notched beam is defined according to the elastic beam theory for the ligament area above the notch without considering the stress concentration factor, and by simple arrangement it can be written as:

$$\sigma_N = \frac{1.5PS}{BH^2} \tag{3.3}$$

where P is the applied load, S is the span which has $S = 4D$, B is the thickness of the beam, and H is the ligament length above the notch,

$$H = D - a_0 = 0.7D \tag{3.4}$$

Therefore Equation (3.3) can be further simplified as:

$$\sigma_N = \frac{6P}{0.49BD} \tag{3.5}$$

The nominal "strain" here is defined as the total deflection of the midpoint u above the notch divided by the beam height D, which is purely for a comparison purpose:

$$\varepsilon_N = u/D \tag{3.6}$$

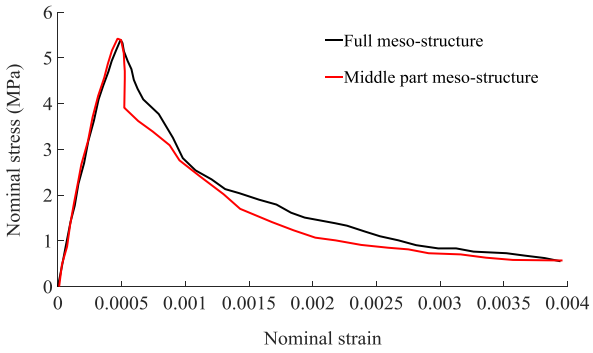

Figure 3.6 Nominal stress - strain curves for full and partial mesoscale beam models

The results show that the responses from the two beam models are essentially the same. Note that some slight difference appears in the shapes of the damage zones between these two models, and this is largely due to the differences in the detailed aggregare distributions in the critical regions as the meso-geometry for the two models was created in two separate operations.

In the subsequent analysis, the partial mesoscale modelling approach is adopted for the modelling of the beam under three-point bending, with the length of the mesoscale portion for the notched middle region being equal to the beam depth.

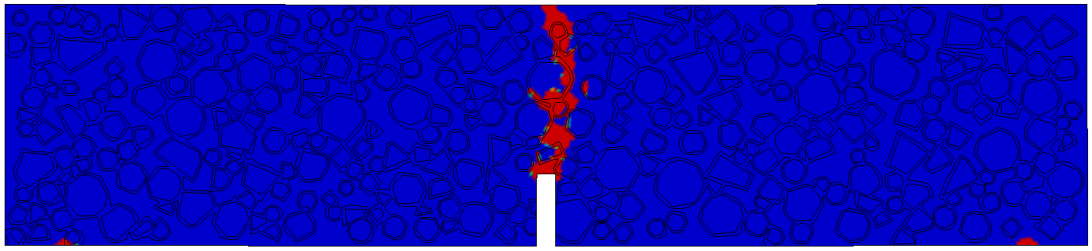

(a) Full mesoscale model

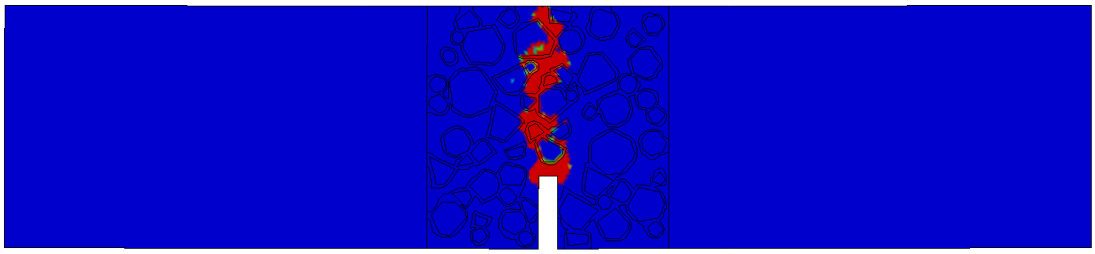

(b) Partial (middle portion) mesoscale model

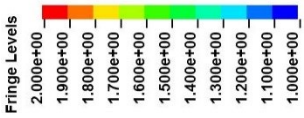

Figure 3.7 Comparison of local damage zone between the two models

3.4 Mesh-objective treatment

3.4.1 Fracture energy conservation (crack band theory)

In the constitutive modelling and numerical analysis of structures made of softening materials, the mesh sensitivity associated material damage is a key issue. A smeared crack band model was first proposed by Bažant and Oh (1983) with the assumption that cracks localize in a band whose width is usually associated with a characteristic length L_c. For a constitutive law incorporating the crack band theory to achieve a mesh independent result, three parameters, namely the model I fracture energy G_f^I, the tensile strength f_t, and the width of the smeared crack band L_c are used to control the softening behaviour of concrete.

In the case where the element size in the FE model is larger than L_c, a function of the above three parameters is suggested to obtain the strain softening modulus as (Bažant & Oh 1983):

$$E_t = \left(\frac{1}{E} - 2 \frac{G_f^I}{f_t L_c} \right)^{-1} \tag{3.7}$$

In the case where the element size is smaller than L_c, a fracture energy compensation approach as expressed in Eq. (3.8) is adopted so that the total fracture energy consumption is preserved, assuming the failure in the local region of the FE model would be restricted to only one element width.

$$G_f^I = h_c \int \sigma d\varepsilon = L_c \int \sigma^* d\varepsilon^* \tag{3.8}$$

where σ and ε are the stress and strain in the FE element, and σ^* and ε^* are the nominal stress and strain over the presumed crack band width L_c.

Eq. (3.8) indicates that the softening branch of the stress strain curve for the 'localized' element would become mesh-dependent to achieve a mesh convergent macroscopic response. This method removes the sensitivity to the mesh size in terms of the global solutions, but the strain and displacement in the local field would be mesh-dependent. This would make it difficult to evaluate the fracture process zone as it would be dependent on the chosen mesh size.

The small sample beam as specified in Table 3.1 is used for an illustrative examination. Four different mesh sizes, being 2 mm, 1 mm, 0.5 mm and 0.25 mm, respectively, are performed. As the failure in the notched concrete beam under three-point bending is tension dominated, the numerical localisation length is kept equal to the element size, i.e. $L_c = h_c$.

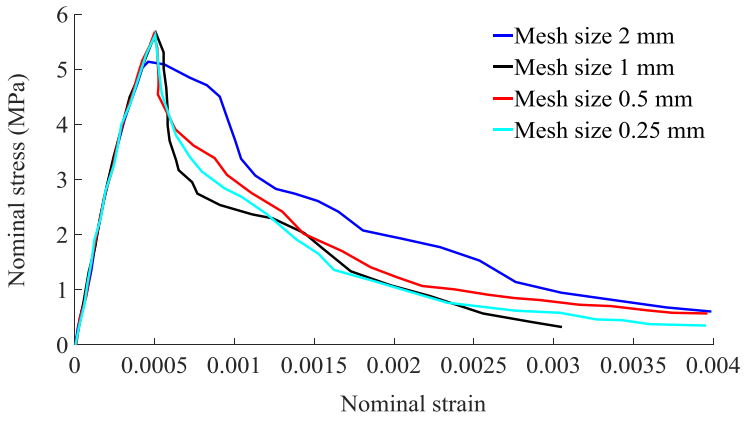

Figure 3.8 Nominal stress and strain curves for different mesh sizes

The mesh convergence results for the nominal stress and strain curves are shown in Figure 3.8. As it is shown in Figure 3.8, the global response is not sensitive to the range of mesh size except for the mesh size of 2 mm, in which the nominal strength is slightly lower and the post-peak behaviour is noticeably different from those from the other three mesh cases. This is understandable as the 2 mm mesh size is apparently too coarse for the mesoscale model where the maximum aggregate size is around 8 mm. The other stress-strain curves are almost identical and this indicates that mesh convergence is maintained as far as the global response is concerned. This also implies that for a notched three-point bending test, the damage mode of the specimen is tension-dominated and hence the mesh regularization measure employed in K&C concrete model is effective.

However in terms of the local damage, as shown in Figure 3.9, the fracture process zones (described by the *SDF*) from models of different mesh sizes exhibit noticeable mesh dependency. The width of the damage zone localizes into a narrow band whose width depends directly upon the element size.

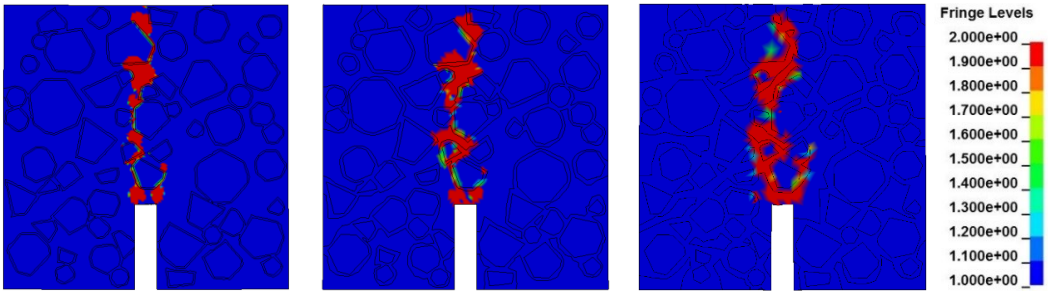

(a) mesh 0.25 mm (b) mesh 0.5 mm (c) mesh 1 mm

Figure 3.9 Local damage zone for different mesh sizes

3.4.2 Enhancement with a nonlocal approach

As mentioned earlier, a nonlocal approach is introduced here into the numerical model to better approximate the fracture process in concrete. The underlying principle of the nonlocal theory is that the failure criterion of a certain point of the material is not only dependent on the stress state at that point but also on the stress state in the surrounding region. Bazant (1994) provided supporting evidence to this argument by the observation that there exists a certain level of interaction among the multiple micro-cracks within the fracture process zone. In a nonlocal approach, a material characteristic length R_c is introduced to replace a pointed local material response with a weighted average over a given area to describe the stress (or strain) state of the material.

In the present study an average weighted function based on the work by (Buste et al. 1999) is implemented. If $f(x)$ is a local field in a domain V then the corresponding nonlocal field is $\bar{f}(x)$:

$$\bar{f}(x) = \frac{\int \alpha(x,\xi) f(\xi) d\xi}{\int \alpha(x,\xi) d\xi} \tag{3.9}$$

Eq. (3.9) integrates within the influencing domain V, where $\alpha(x,\xi)$ is the weighting function:

$$\alpha(x,\xi)=\left[1+\frac{\|x-\xi\|^{p}}{R_c}\right]^{-q} \tag{3.10}$$

The weighting function depends on the distance r between the source point ξ and the target point x. The weighting function is a monotonically decreasing function as r increases, as a source point closer to the target point has a higher influence compared to the ones farther away. The material characteristic length R_c is actually the largest interaction radius of the source point ξ that affect the nonlocal average at point x. Thus it restricts a representative area for the nonlocal treatment, which can be clearly interpreted in Figure 3.10. The parameters p and q in the weighting function (see Eq. (3.10)) can be set as 4 and 2 respectively as suggested in (Buste et al. 1999).

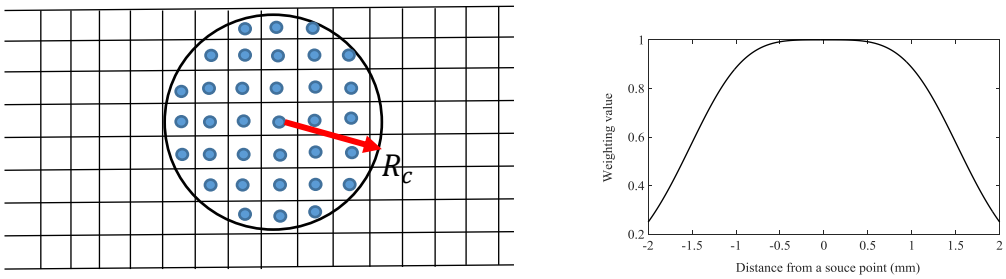

Figure 3.10 Nonlocal treatment and a weighting function

Theoretically, any local history variables, such as the energy release rate, strain and displacement, can be adopted for the nonlocal treatment during the calculation process. In the present study, the effective plastic strain is chosen for the weighted average during the whole process. Hence according to Eq. (3.9), the average effective plastic strain $\bar{\varepsilon}_{ep}$ can be written as:

$$\bar{\varepsilon}_{ep}=\frac{\int \alpha(x,\xi)\varepsilon_{ep}(\xi)d\xi}{\int \alpha(x,\xi)d\xi} \tag{3.11}$$

where $\varepsilon_{ep}(\xi)$ is the local effective plastic strain at a source point ξ. Using the effective plastic strain $\bar{\varepsilon}_{ep}$, the damage parameter *SDF* can be calculated accordingly, from there the fracture process zone can then be evaluated.

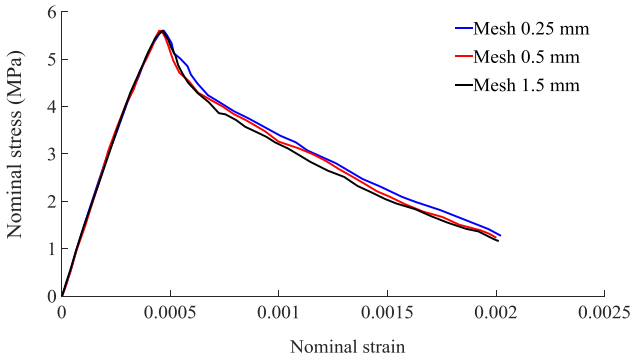

Figure 3.11 Nominal stress and strain curves for different mesh sizes by nonlocal treatment

Figure 3.11 shows the global response in terms of the nominal stress-strain curve for the three mesh sizes (0.25 mm, 0.5 mm and 1 mm) with the nonlocal treatment. The corresponding fracture process zones are depicted in Figure 3.12. As expected, with the nonlocal treatment there is negligible mesh sensitivity. The post-peak behaviour of the nominal stress-strain curves in Figure 3.11 are virtually identical for all the mesh sizes. This ensures the overall fracture energy is the same irrespective of the mesh size.

Mesh independent results become also apparent in the depiction of the shape and size of the fracture process zone (see Figure 3.12). The width of the strain localization band is almost constant for different mesh sizes. The slight variation is actually due to a different number of elements involved within the interaction domain, and this is deemed acceptable especially in a mesoscale model where the size and shape of individual elements inevitably varies to a certain extent. Hence we can state that the nonlocal treatment takes a good effect here, and it benefits not only in obtaining a mesh independent global response but also in predicting the onset and evolution of the fracture process in the concrete material.

Therefore the nonlocal averaging approach is adopted in the subsequent analysis of the size effect using the mesoscale model. It is worth noting that the computational cost increases by an order of 3-5 times as a consequence.

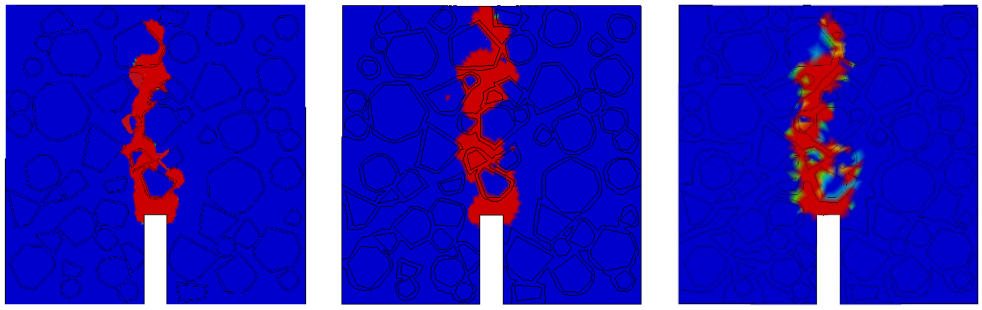

(a) mesh 0.25 mm (b) mesh 0.5 mm (c) mesh 1 mm

Figure 3.12 Fracture process zone depicted by nonlocal treatment for different mesh sizes

However it should be pointed out that the numerical results from the nonlocal approach are actually highly dependent on the value of the characteristic length R_c. Unfortunately, the determination of the value for this parameter is not straightforward in concrete material due to the complex random micro-structure and the complicated failure process within it (Bazant & Jirásek 2002). Furthermore the value may also vary with different weighting functions. Hence in order to get an objective value for the material characteristic length for a specific numerical model, a simple but effective way would be by parameter investigation towards matching representative experimental observations.

Physically the interaction radius R_c should span a few neighbourhood elements in which the nonlocal approach is implemented. However, increasing the value of the interaction radius would also increase the computing time. Furthermore, when a large interaction radius is used, the nonlocal influence domain will also increase which would bring in a well-known boundary problem in the nonlocal approach. This boundary problem would lead to unstable performance or even collapse of the calculation. Some methods have been proposed to reduce such a problem (Borino et al. 2003; Krayani et al. 2009; Bazant et al. 2010), but this is beyond our current topic.

The effect of the material characteristic length on the evolution of the fracture process zone in the present model framework is shown in Figure 3.13, again using the small concrete beam specified in Table 3.1. As it is shown, with increasing

material characteristic length, the width of the fracture process zone depicted in the numerical model apparently increases. By benchmarking against the experimental observations reported in (Wu et al. 2011), which will be presented in detail in next section, an empirical value of R_c = 1.5 mm is adopted in present numerical simulations. Note that this value is actually consistent with the suggestion on setting the material characteristic length in nonlocal approach in (Skarżyński et al. 2011).

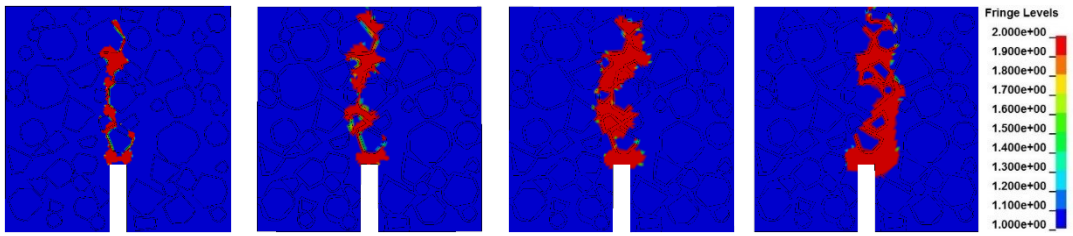

R_c = 0.5 mm R_c = 1 mm R_c = 1.5 mm R_c = 2.5 mm

Figure 3.13 Caculated fracture process zones for different R_c values

3.5 Model verification

In order to verify that the damage zone (DZ) obtained in the numerical simulation indeed represents the actual fracture process zone, the damage processes of the simulated damage zones are compared with that of FPZs observed by the DIC technique in (Wu et al. 2011).

3.5.1 Macroscopic Load-CMOD responses

The macroscopic responses in terms of the load versus crack mouth opening displacement (CMOD) curves were given in (Wu et al. 2011). In their experiments load was actually the force applied on the specimen while the CMOD was measured by a clip gauge installed at the centre of the notch. In the current numerical simulations, this information can be directly obtained from post-processing the simulation results (using LS-PREPOST herein).

Figure 3.14 shows a comparison of the experimental and simulated Load-CMOD curves for specimens of different sizes. A very good agreement can be observed

across all size groups, and this confirms that the current numerical models represent well the properties and the behaviour of the specimens used in experiment.

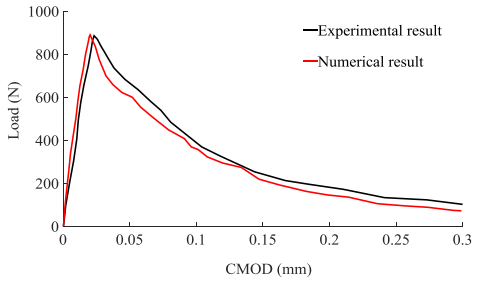

(a) Load-CMOD curves for small specimen (D = 40 mm)

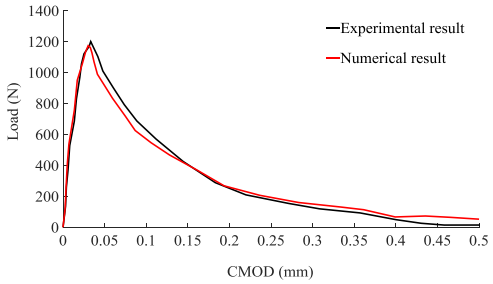

(b) Load-CMOD curves for medium specimen (D = 60 mm)

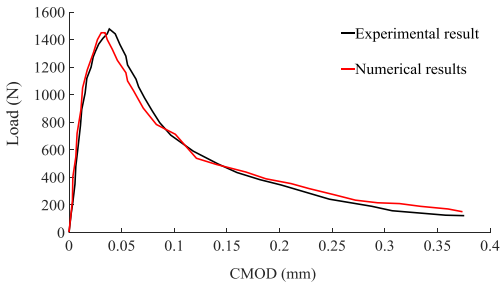

(c) Load-CMOD curves for large specimen (D = 80 mm)

Figure 3.14 Comparison of macroscopic Load-CMOD curves with experiment

3.5.2 Evolution of fracture process zones

The development processes of the damage zones defined by *SDF* are further checked with experiemental observations in this part. Note that the numerical results are obtained from the mesoscale models with the nonlocal material description.

Figure 3.15-3.17 illustrate the development of the fracture process zone from the simulation of the specimens of three different sizes. As can be seen from the above graphs, the numerical results agree favourably with those from the experimental measurements using the DIC technique. Note that there appear to be some slight differences in the shapes of the highly irregular damage zones between the numerical and experimental results. These differences may be attributed to the randomness in the locations and shapes of the aggregates in the actual specimens which cannot be reproduced exactly in the numerical models.

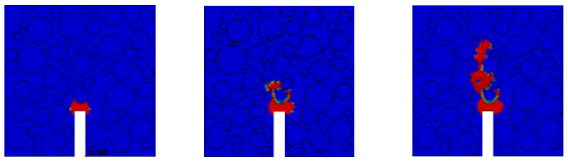

(a) Numerical results

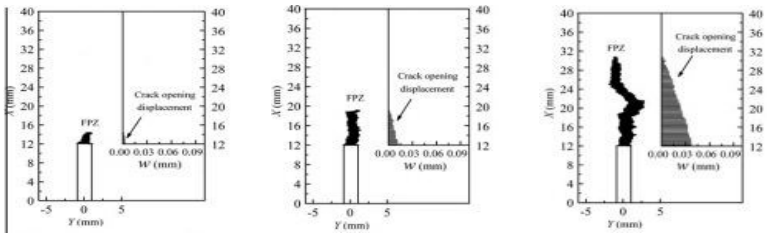

(b) Experimental results (after Wu et al. (2011))

Figure 3.15 Development of FPZ at three loading points for small specimen (D = 40 mm) (Left: pre-peak, 71.4% peak load; Middle: peak load; Right: post-peak, 60.6% peak load)

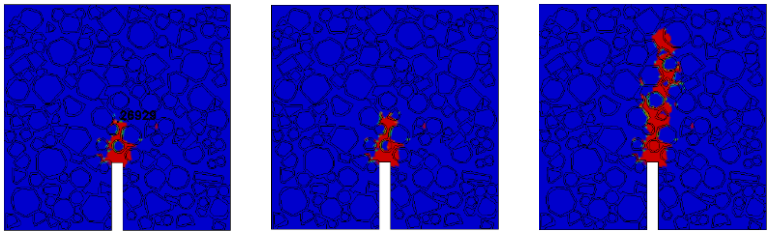

(a) Numerical nonlocal results

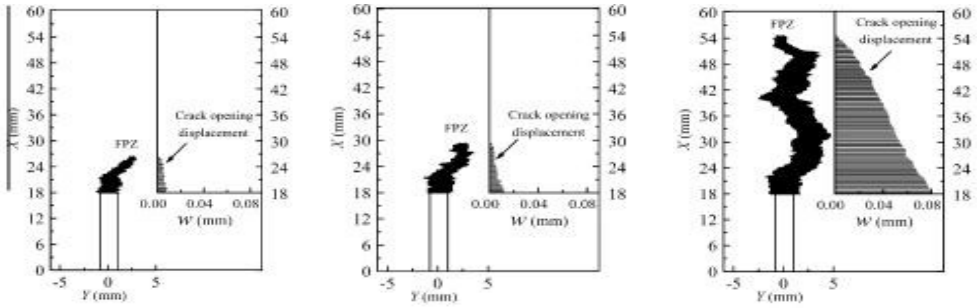

(b) Experimental results (after Wu et al. (2011))

Figure 3.16 Development of fracture process zone at three loading points for medium specimen (D = 60 mm) (Left: pre-peak, 85.1% peak load; Middle: peak load; Right: post-peak, 40% peak load)

However, in terms of the measurable quantity i.e. the width and length of the damage zones, the numerical simulation results exhibit good agreement with the experimental counterparts for all the three speciments and at different loading stages. It is therefore reasonable to conclude that the present numerical model can be employed to simulate the fracture process zone for the purpose of investigating the associated size effect.

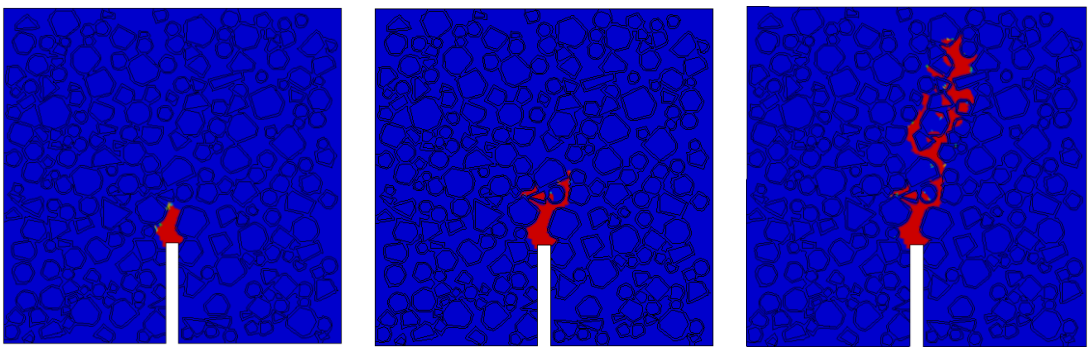

(a) Numerical nonlocal results

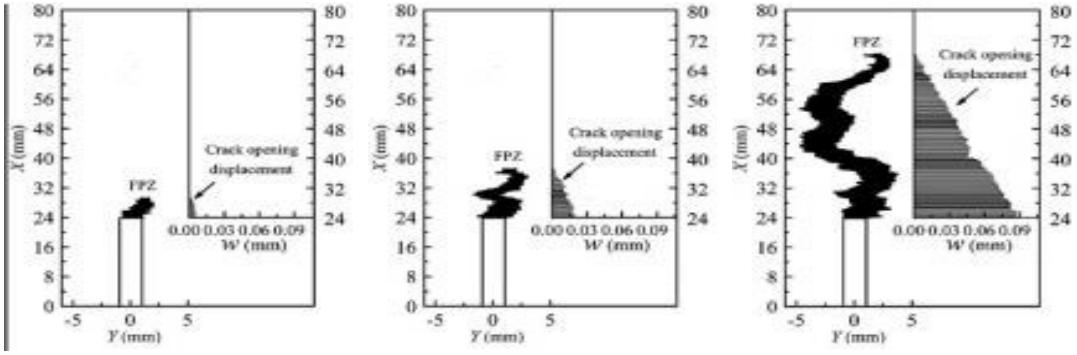

(b) Experimental results (after Wu et al. (2011))

Figure 3.17 Development of fracture process zone at three loading points for large specimen (D = 80 mm) (Left: pre-peak, 80.1% peak load; Middle: peak load; Right: post-peak, 31.4% peak load)

3.6 Results and discussion

In this section the phenomena of the deterministic size effect from the numerical simulations are examined. The reasons underlying the size-dependent nominal strength are discussed based on the detailed numerical results. To better illustrate the tendency of the size effect, two more specimens of larger sizes with $D = 120$ mm and 160 mm, respectively, are also simulated and the results are included in the discussion. All other properties except the size are maintained the same in all the numerical specimens.

3.6.1 Size effect on the size of the fracture process zone

As mentioned before, the size of the fracture process zone ahead of the notch tip before the peak loading point could be an intrinsic reason for the size effect phenomenon. Therefore it is of particular interest to examine the properties of the fracture process zone in speciemens of different sizes.

Figure 3.18 shows the shapes and sizes of the fracture process zones at peak loading point for the five specimens. As can be observed, the widths of the fracture process zones are almost the same (around 5 mm) for all the specimens. This phenomneon is consistent with the observations reported by Skarżyński et al. (2011) using the DIC technique and previous numerical work by Grassl et al. (2012). It suggests that the width of the fracture process zone may be considered as a material property. As a matter of fact, in the crack band thoery the width of the fracture process zone is already assumed to be a constant value, and (Bažant & Oh 1983) gave it three times of maximum aggregate size. However the width of the FPZ from the present numerical simulation appears to be smaller than the above assumed value.

On the other hand, the absolute length of the fracture process zone at the peak loading point appears to be strongly dependent on the specimen size. Clearly, the greater the specimen size, the longer is the localized damage zone. The length increases from around 7.8 mm for the smallest beam ($D = 40$ mm) to 26.5 mm for the largest beam (D = 160 mm). This strong depdendence of the fracture zone length on the size may be explained by the decrease of stress gradient with the increase of the beam size (see Eq. (3.13) later).

However if we further look at the relative or normalised fracture process zone length, i.e. the ratio of the length of the fracture process zone to the ligament length above the notch, l_{FPZ}/H at the peak load, we can observe an opposite trend, such that the ratio decreases as the specimen size increases. The trend is plotted in Figure 3.19. This result from the current numerical simulation actually echoes nicely the observations made from experimental studies (Wu et al. 2011; Alam et al. 2013). It suggests that the normalised length of the fracture process zone is not a material parameter but is dependent on the speciemen size. This size-dependent normalised

length of the fracture process zone provides an intrinsic explanation to the size effect which will be discussed in more detail later.

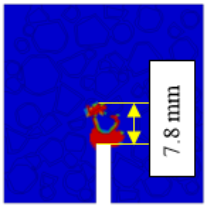

D = 40 mm

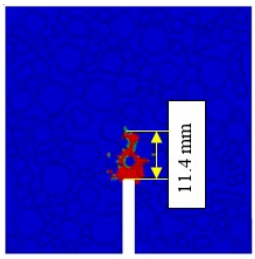

D = 60 mm

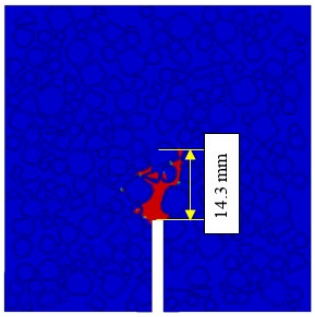

D = 80 mm

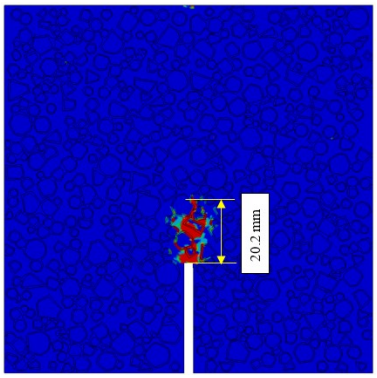

D = 120 mm

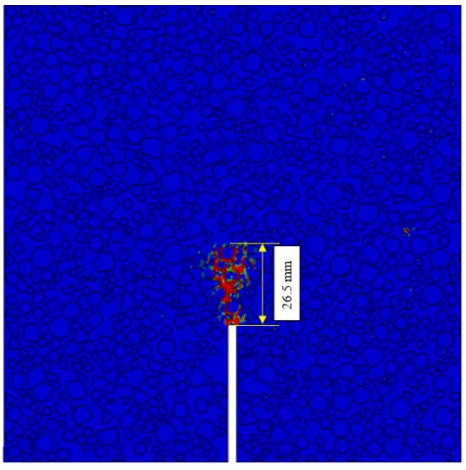

D = 160 mm

Figure 3.18 The FPZs at peak load points for different specimens in mesoscale concrete model

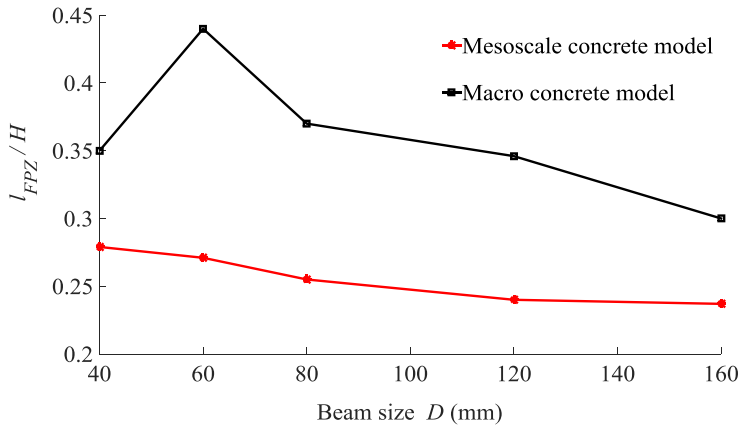

Figure 3.19 Relative fracture process zone length at peak load

From the damage patterns in Figure 3.18, we can aslo observe that the fracture process zones are strongly curved due to the presence of the aggregtes and the corresponding weak interface zone around the aggregates. This suggests that the mesostructure of concrete may also have certain effects on the formation and propagation of the fracture process zone. For this reason a set of simple comparative models in which the specimens are treated as entrirely homogeneous is also analysed, where the single-phased material are given the macro material properties as shown in Table 3.2. The material characteristic length R_c in the nonlocal weighting function is still set at 1.5 mm. In order to avoid any influences from the meshing among the models, the comparative homogeneous models use exactly the same mesh structures as their counterpart mesoscale models, except that all the elements in the homogenuous models are given the uniform material properties.

Figure 3.20 shows the caculated results in terms of the shape and size of the fracture process zone for the concrete beams of different sizes from the homogenuous concrete models. As it is shown, in contrast to the mesoscale concrete model, the evolution paths of the fracture process zones from the homogenuous models are generally straight.

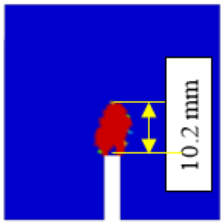

D = 40 mm

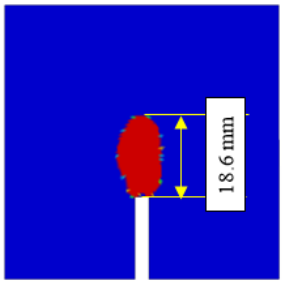

D = 60 mm

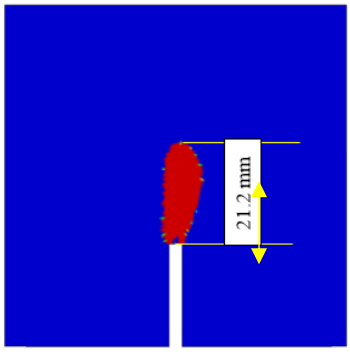

D = 80 mm

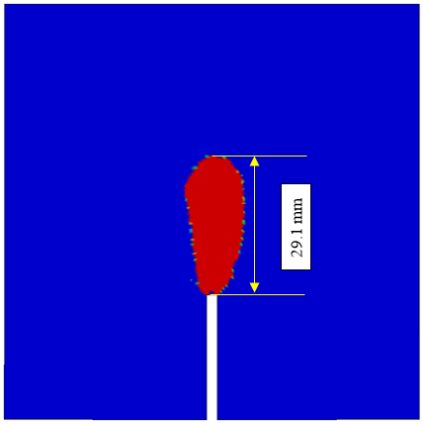

D = 120 mm

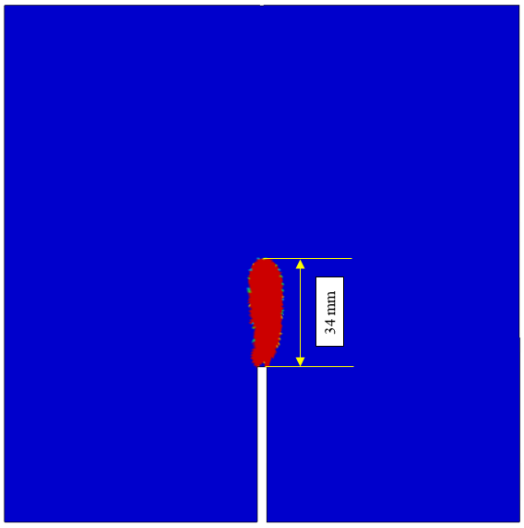

D = 160 mm

Figure 3.20 The FPZs at peak load points for different specimens with homogenuous models

On the size of the fracture process zone, the general trend is similar to the mesoscale models, such that the length of the fracture process zone is strongly dependent on the size of the beam while the width is insensitive to the change of the beam size. However, the homogenuous models appear to produce longer fracture process zone lengths than the mesoscale concrete models do. The normalised fracture process zone lengths, as also shown in Figure 3.19, show some scatter; nevertheless the overall trend is similar to that from the mesoscale models. These observations suggest that composition of the material at the meso-scale is a significant factor that needs to be taken into account so that a more reliable evaluation of the fracture process zone may be made.

3.6.2 Size effect on nominal strength

Figure 3.21 shows the nominal stress and strain curves for the five different sized specimens from the mesoscale concrete models. The nominal stress and strain are defined according to Eq. (3.5) and Eq. (3.6), respectively. The results clearly demonstrate the so-called deterministic size effect, such that the nominal strength increases persistently as the specimen size decreases, and at a significant rate.

Figure 3.22 plots the variation of the nominal strength with the size of the beams. For a comparison, the variation curve based on a deterministic size effect law by Bažant (2004), which is valid for a structure with pre-existing notches, is also enclosed wherein the nominal strength is calculated as:

$$\sigma_N = \frac{Kf_t}{\sqrt{1+(D/D_0)}} \tag{3.12}$$

where f_t is the tensile strength of the concrete, D is the beam depth and K, D_0 are size dependent parameters which are determined by fitting a set of data (with a non-linear least-square Trust-Region algorithm).

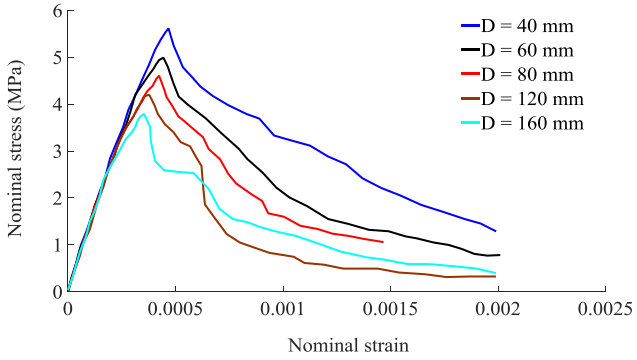

Figure 3.21 Nominal stress and strain curves

As it can be observed, the nominal strength of the beam from the mesoscale concrete model show a clear size dependence, and the variation matches well the size effect law proposed by Bazant (2004). Similar to the situation with the FPZ length, the nominal strength results from the homogeneous beam models show some scatter, but the overall variation trend with the size can still be captured.

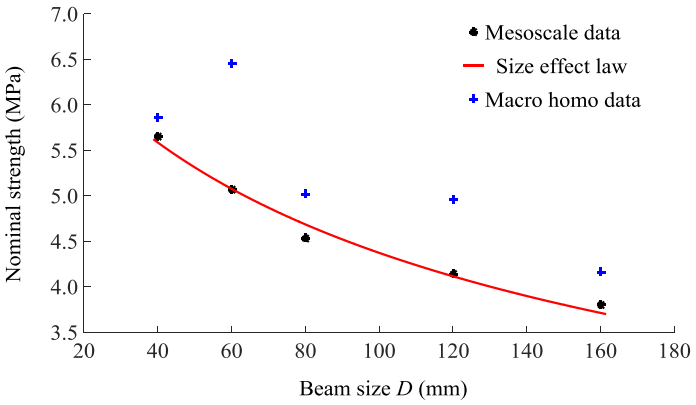

Figure 3.22 Nominal strength size effect tendency

With a comparison to Figure 3.19, it can be found that the nominal strength variation with size is generally in line with the trend of the normalised fracture process zone length, and the scatter in the homogeneous models appear in a similar fashion. The results indicate clearly that the size dependent nominal strength is directly related to the size dependent fracture process zone. The scattered points on the size effect curves from the homogeneous beam models suggests to be a result of lacking the

ability to realistically reproduce the formation and propagation of the fracture process zone in a homogeneous model, thus affecting the detailed stress and strain states of concrete in the critical damage region.

3.6.3 A theoretical model for prediction of size effect

As discussed above, the current mesoscale model enhanced by nonlocal treatment can well predict the size-dependent nominal strength as well as the size sensitive fracture process zone, which agree well with representative experimental evidences. However no direct relationship between the two size-dependent factors has been established in the literature and the exact role of the size sensitive fracture process zone in contributing to the size effect on the nominal strength has not been fully understood. Herein an attempt is made to propose a theoretical model, herein referred to as a stress interaction theory, to filling in this gap and establish a quantitative relationship for the evaluation of the size effect on the nominal strength.

The reference condition is still based on elastic beam bending, as adopted in the original definition of the nominal strength. So according to the elastic beam theory, there is a linear stress variation in a bent beam:

$$\sigma_E(y) = \sigma_L\left(1 - \frac{2y}{H}\right) \tag{3.13}$$

where $\sigma_E(y)$ is the elastic stress field along a specific cross section in the beam, σ_L is the stress at the lowest fibre (bottom free surface) of this cross section, hereafter it is called the effective elastic stress, y is measured from the lowest fibre where $y = 0$; and H is a length parameter which is related to the depth of the cross section and therefore also represents the specimen dimension.

For a notched elastic beam, if the stress concentration is not considered, H becomes:

$$H = D - a_0 \tag{3.14}$$

where D is the depth of the beam and a_0 is the length of original notch.

In a hypothetic situation without stress concentration and without nonlinearity in the fracture zone, the concrete beam would fail if σ_L reaches the tensile strength, and consequently there would also be no size effect if the material properties are the same for the beams with similar geometrical shapes.

However, in reality there exists a sizable fracture process zone, especially in concrete-like materials, within which the stress state is highly non-linear before the applied load reaching its maximum value. Herein we shall denote the non-linear stress in FPZ as $\sigma_P(y)$. Consequently the equivalent elastic stress σ_L deviates from the tensile strength. If σ_L could be evaluated from the properties of the FPZ, that would give a direct prediction of the size effect.

We postulate that the variation in the stress states within FPZ directly leads to the size dependent nominal strength, and by examining the interaction between the stress states between the elastic stress field in the absence of FPZ and the actual stress field within FPZ it could lead to an explicit correlation.

For this purpose we adopt the strip yield model concerning fracture proposed by (Barenblatt 1962). In the strip yield model, a long and slender plastic zone is assumed at the crack tip in a non-hardening material in a plane stress condition. The strip yield plastic zone is modelled by assuming a crack with a length of $(2a + 2\rho)$, where ρ is the length of the plastic zone, with a closure stress $\sigma_p(y)$ applied at each tip, as shown in Figure 3.23.

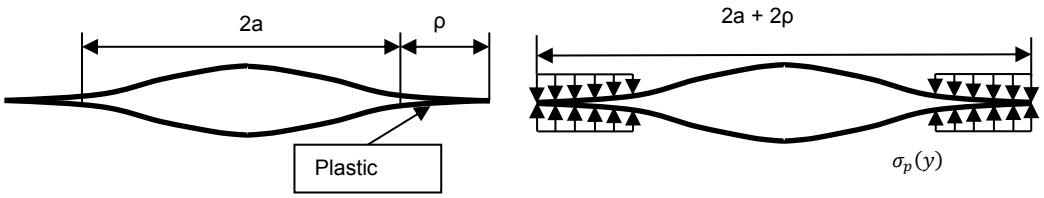

Figure 3.23 Sketch of strip yield model

Since the stresses are finite in the non-hardening materials, there cannot be a stress singularity at the new crack tip. Therefore the stress intensity factors from the applied tension and closure stress cancel one another,

$$K_{total} = K_{applied} + K_{closureflo\,w} = 0 \tag{3.15}$$

Satisfying the above equation with the detailed formulation of the stress intensity factors, the following equation can be obtained (Tada et al. 2000):

$$\int_0^l \frac{\{\sigma_E(y) - \sigma_p(y)\}}{\left(l^2 - y^2\right)^{1/2}} dy = 0 \tag{3.16}$$

where l is the length of the plastic zone and y is the coordinate of the point within the plastic zone.

In numerical simulations the present stress state $\sigma_P(y)$ within plastic zone can be directly extracted for every single element. Therefore the integral for the plastic stress in Eq. (3.16) can be calculated approximately by adding up all the elements within the plastic zone, i.e.:

$$\int_0^l \frac{\sigma_p(y)}{\left(l^2 - y^2\right)^{1/2}} dy \approx \sum_1^N \frac{\sigma_P(y)}{\left(l^2 - y^2\right)^{1/2}} \Delta y \tag{3.17}$$

where N is the total number of elements along the length of the plastic zone and Δy is the element mesh size adopted in the FE model.

Combined with Eq. (3.13) and Eq. (3.17), Eq. (3.16) can be transformed to:

$$\frac{\pi\sigma_L}{2} - \frac{2l\sigma_L}{H} = \sum_1^N \frac{\sigma_P(y)}{\left(l^2 - y^2\right)^{1/2}} \Delta y \tag{3.18}$$

The effective elastic stress can then be calculated as:

$$\sigma_L = \frac{2\sum_1^N \frac{\sigma_P(y)}{\left(l^2 - y^2\right)^{1/2}} \Delta y}{\pi - 4(l/H)} \tag{3.19}$$

As far as the nominal strength in concerned, this can be calculated using the effective elastic stress expressed in Eq. (3.19), provided the FPZ properties, including the non-linear stress field, are available at the peak loading point.

If Eq. (3.19) can be validated as being capable of depicting the size effect tendency, it would be reasonable to deduce that the above theoretical formulation based on the interaction of the stress states theory adequately describes the intrinsic mechanism of the size effect. This will be discussed in the next subsection.

3.6.4 Mechanisms behind size effect

In Section 3.6.3, an explicit relationship relating the nominal strength and the fracture process zone is established based on the concept of interaction of the stress fields. To check its validity, we can evaluate the effective stress at the peak load accordingly from the numerical simulation results.

All the required information for the calculation of the nominal stress in Eq. (3.19) can be easily obtained from the numerical simulation (through post processing), including the geometry parameters of each element involved as well as the stress state within the fracture process zone at peak load. The stress state $\sigma_P(y)$ for each y position in the equation is determined as the average stress of the elements which share almost the same y coordinate within the fracture process zone. The resulting nominal stress for each concrete beam calculated by Eq. (3.19) is presented in Figure 3.23.

For an additional point of view, if we simply assume that in Eq. (3.16) the stress $\sigma_P(y)$ within fracture process zone remains constant at the fracture strength f_t, while the fracture process develops, then combining with Eq. (3.13), Eq. (3.16) can be reduced to:

$$\frac{\pi}{2}\sigma_L - \frac{2l}{H}\sigma_L = \frac{\pi}{2} f_t \tag{3.20}$$

i.e.

$$\sigma_L = \frac{f_t}{1 - \frac{4}{\pi} \times \frac{l}{H}} \tag{3.21}$$

Using the material property f_t = 3.7 MPa and the normalized fracture process zone length in Figure 3.19, the effective stress for beams of different sizes can be calculated. The results are also included in Figure 3.24 for comparison.

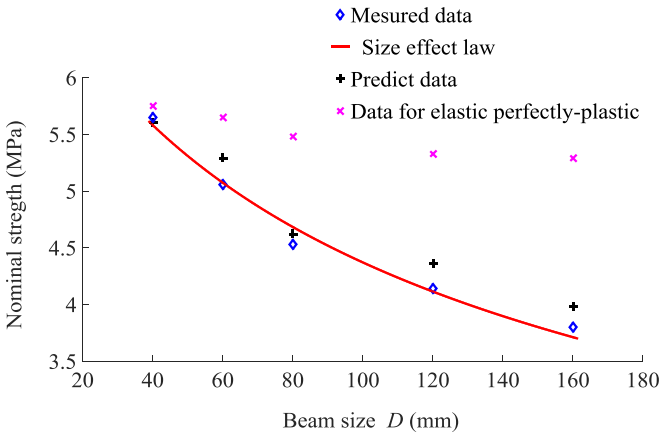

Figure 3.24 Size effect tendency comparison

It is remarkable to find that the effective stress calculated by Eq. (3.19) well captures the size effect tendency and the effective stress value at the peak load for each beam matches very closely the measured values from Eq. (3.5). The effective stress obtained from Eq. (3.21) using a hypothetic elastic-perfectly plastic stress field for the FPZ indicates a similar trend but considerably under-predict the degree of the size effect in the concrete beams.

The above results suggest that quantitatively it is possible to establish the trend of the size effect on the nominal strength in accordance with the stress state interaction theory proposed in present study. The comparison with the result from involving an elastic-perfectly plastic assumption in the fracture process zone provides additional insight as to why the size effect is a more significant phenomenon in quasi-brittle materials like concrete and rock than in ductile materials (such as steel).

3.7 Concluding Remarks

In this chapter the classical topic of size effect in concrete structures is investigated by means of numerical simulations on geometrically similar plain concrete beams of different sizes subjected to three-point bending. The concrete beam is modelled using

a mesoscale approach where three components, namely coarse aggregates, mortar and the interface transition zone are explicitly represented. A nonlocal approach is introduced to enhance the numerical model in minimising the mesh-dependent issue in the model. The numerical results are compared with relevant experimental observations using DIC technique for verification and validation purposes, and the trend of the size effect on the fracture process zone and hence the nominal strength is evaluated and discussed based on the numerical simulation results. Finally, a stress field interaction theory based on the strip yield model is proposed to establish a direct relationship between the (deterministic) size effect and the fracture process zone parameters.

Based on the results, the following main conclusions may be drawn:

1. The continuum-based mesoscale concrete model, with enhancement by a nonlocal treatment, can well describe the general shape and size of the fracture process zone. The width of fracture process zone does not depend on the beam size, but the length of the fracture process zone at peak loading point is strongly dependent on the beam size, and the length of the fracture process zone increases as the beam size increases. The normalized length of fracture process zone at peak loading point, however, show an opposite trend, and in normalised terms it actually decreases with the increase of the beam sizes.

2. The mesoscopic heterogeneity appears to have a noticeable effect on the evolution of the fracture process zone, and hence the size effect as a whole. By comparison a homogenised model lacks the ability to realistically simulate the shape and size of the fracture process zone, and this leads to an inaccurate representation of the local stress and strain states within the fracture process zone.

3. The nominal strength as produced from the mesoscale model simulation shows a good agreement with the experimental observations, and the general results confirm that the size effect is directly related to the properties of the fracture process zone at the peak load.

4. The stress field interaction theory based on the strip yield model explains very well the size effect phenomenon, and the formulation provides an explicit relationship between the size-dependent nominal strength with the length of the FPZ and the stress distribution within the FPZ.

It should also be noted that the continuum-based FE model has an inherent limitation in representing the evaluation of fracture which effectively is a nature of discontinuity. With a mesh-objective material description, and enhanced by a nonlocal treatment, the essential features of the fracture process can be represented in a rather effective manner, but a more direct and explicit description of the discontinuity and the fracture process within a fracture zone would be more desirable. For this reason and the more general aim of developing holistic mesoscale approaches for modelling concrete in general stress conditions, incorporation of the cohesive element model with associated contact mechanisms is deemed to be important and necessary. Further development of the mesoscale model incorporating cohesive interface element becomes the subject of research in much of the later chapters of the thesis. Once the new model is available, the same problem (size effect) will be re-visited and this will be presented in Chapter 6.

Chapter 4 : Modelling of mesoscopic fracture in concrete using a cohesive plus contact interface approach

4.1 Introduction

Concrete is a highly non-homogeneous composite with large heterogeneities of quasi-brittle character. The behaviour of concrete is fundamentally affected by the fracture mechanisms, particularly at interfaces between the constituent material (aggregates and the mortar matrix) because the initiation of macroscopic damage generally starts from the fracture along the interface between aggregates and the mortar matrix (the so called interface transition zone, or ITZ). Consequently, a sound representation of the ITZ mechanical properties and the fracture at the ITZ is crucial for a realistic modelling of the mesoscopic damage mechanism for concrete-like materials.

However, as highlighted in Chapter 1 (Section 1.1.2), there are remarkable challenges on modelling such a thin layer of component which is generally in the range of 20-50 μm in the mesoscale FE model. In Chapter 3, an equivalent layer of solid elements approach has been used for treating ITZ in the mesoscale concrete model. But obviously, the thickness of the ITZ is exaggerated in such an equivalent treatment and consequently the properties of the equivalent layer can only be determined in an empirical manner. Moreover, as crack damage grows the solid ITZ layer is subjected to distortion and consequently numerical instability may occur in advanced damage state.

Understandingly using zero initial thickness cohesive elements is deemed to be a rational representation for modelling the ITZ in a mesoscale model but it depends upon the capacity of the cohesive element in catering to complex stress conditions. As mentioned in the Introduction chapter (Section 1.1.2), a typical cohesive model lacks the ability in representing the shear failure of the ITZ under complex stress

conditions, and does not represent very well the strong dependence of the shear strength of the ITZ in concrete like materials in the presence of normal pressure.

In this chapter, a new approach is proposed with the aim to overcome the inherent shortcomings of the classical cohesive element by introducing a contact-friction mechanism into the cohesive fracture process. Since in a mesoscale model the complex geometric interface between the mortar and random aggregates is already well represented through the mesoscale structure, it is possible to employ relatively simple physical laws, without the need to resort to sophisticated mechanical constitutive models which has been mostly used in the existing literature, to capture the mesoscopic fracture mechanism at the ITZ of concrete under general loading conditions. In the current mesoscale cohesive plus contact model, the contact and friction process is regarded as an independent phenomenon outside the cohesive law, which makes the model simple but with clear physical meaning. As will be demonstrated by the numerical results later, the proposed model is also effective in predicting the failure mechanism and the global response of concrete.

The chapter is organized as follows. In Section 4.2, the background theories of mesoscale structure of concrete, the interface model, and the contact/friction algorithm are briefly discussed. Simple numerical models are used in shear tests with normal pressures to show the principle of the combine effects in Section 4.3. In Section 4.4, the mesoscale model is verified against representative experimental evidences and the effects of key parameters are also studied. Section 4.5 provides example applications of the current mesoscale model with cohesive-contact ITZ model in the analysis of the dynamic properties of concrete. Finally, concluding remarks and future research needs are presented in Section 4.6.

4.2 Modelling approach for ITZ in a mesoscale framework

4.2.1 Overview of the mesoscale model and meso-structure generation

At the mesoscopic level, concrete can be considered as a composite material comprising of coarse aggregate, mortar matrix and the interfacial transition zone

(ITZ). The mesoscopic structure may be modelled in 2D or 3D, as discussed in the preceding chapters. For the present development incorporating an interface model using a cohesion plus contact approach, we shall confine ourselves to a 2D mesoscale model.

In the 2D mesoscale model herein, the coarse aggregates are represented by random polygon particles which are embedded in the mortar matrix. As described in Chapter 3, the generation of the mesoscale geometry follows a commonly adopted take-and-place procedure, satisfying a set of physical constraints including non-overlapping and a certain minimum gap between the closet points of two adjacent aggregates. After the generation of the mesoscopic geometric structure, the geometric data is fed into a meshing processor. In the present study, ANSYS pre-processor is used to perform the FE meshing.

Figure 4.1 shows a typical mesoscale model geometry. In this figure, only two material components namely aggregates and the mortar matrix are present. The third component, i.e. the interface transition zone (ITZ) between aggregates and mortar matrix can be created subsequently. While the approach of using an equivalent thin layer of solid elements has shown some robust performance in various loading conditions, as have been seen in Chapter 3, its capacity in representing the mesoscopic damage process is indirect and is therefore limited.

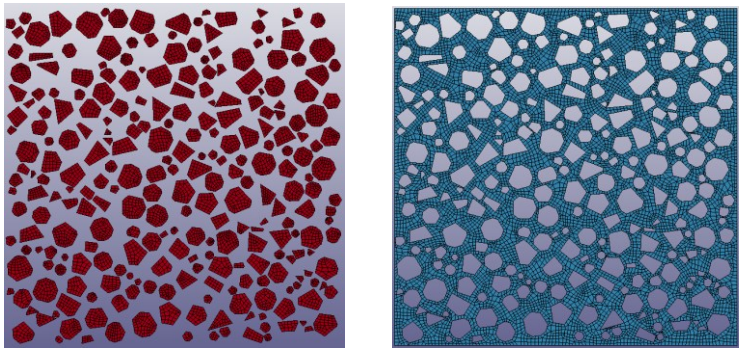

(a) Aggregates (b) Mortar matrix

Figure 4.1 Mesoscale model of concrete and FE mesh

Herein the ITZ is explicitly modelled with a combined classic zero-thickness cohesive interface element plus a contact algorithm. The creation of such a combined interface element will be discussed in the next section.

4.2.2 Modelling of ITZ with a cohesive zone model

The cohesive zone model (CZM) which can simulate the gradual process of the cracking surface separation with a cohesive law is first proposed by Dugdale (1960). Hillberg et al. (1976) applied the cohesive law in the finite element framework for concrete-like material. Since then several cohesive constitutive models have been developed in the literature to reproduce the mechanical behaviour of different physical problems. The main idea of this kind of models stems from relating the relative displacement δ of two associated points of the interface to the traction force per unit area *T* that is needed for separation. Different cohesive laws may be defined for the normal and tangential directions, respectively, but in most models the cohesive laws for the two directions are coupled, meaning both the normal and tangential tractions (T_n, T_t) depend on both the normal and tangential opening displacements (δ_n, δ_t).

4.2.2.1 Cohesive elements insertion

In the present mesoscale model only the ITZ zone will be modelled using cohesive elements. Thus the boundaries between aggregates and mortar matrix will be treated as the potential crack surfaces, where the zero-thickness elements will be inserted. During this process, a duplicate set of the nodes will be required at the interface locations. The original nodes and the duplicated nodes thus form the two potential cracking surface of cohesive elements, which can separate during crack propagation. Each pair of two nodes at the same location (see Figure 4.2) will be constrained by a separation-traction law.

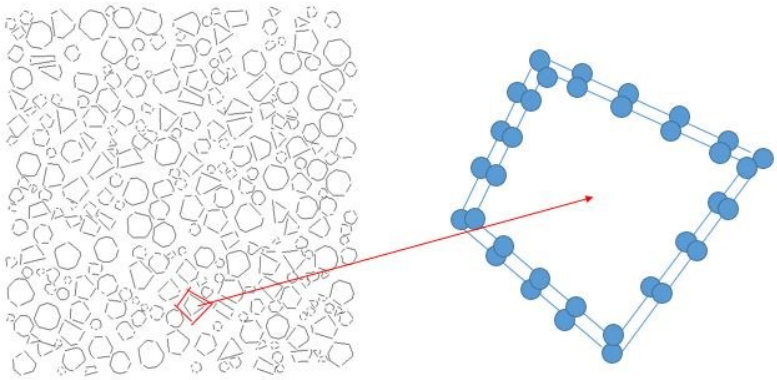

Figure 4.2 Illustration of zero-thickness interface elements insertion

Depending on the response of the cohesive surface prior to the development into the softening stage, two types of cohesive zone approaches may be considered when the cohesive elements are inserted, namely intrinsic and extrinsic cohesive zone models (Snozzi et al. 2011). Intrinsic cohesive elements are embedded in the discretized structure at the beginning of the simulation and during the whole simulation process the mesh connectivity remains unchanged. Extrinsic cohesive models, on the other hand, insert the cohesive elements adaptively into the mesh, which means the cohesive elements are inserted only when the boundary stresses reach the critical material strength. Thus the interface will exhibit an initial elastic behaviour for intrinsic approach or is assumed to be initially rigid for extrinsic approach. Generally the intrinsic cohesive model allows easier implementation than the extrinsic model as it does not require a constant mesh updating which can be complicated, although it may introduce some problem in some cases such as formation of unexpected crack paths. In the present study, we adopt the intrinsic cohesive model approach for the ITZ to avoid further complexity in handling the mesoscale mesh during the course of the analysis. It is also worth noting that in the mesoscale model the crack paths will be subject to natural regularisation due to the presence of the heterogeneity (particularly aggregates), therefore potential issues with the intrinsic approach as compared to the extrinsic approach diminish.

A further point to emphasize here is that a cohesive element is defined in essence like a solid element, but the numbering of nodes must follow a strict order. For a 8-node

cohesive element, the first 4 nodes (1-2-3-4 see Figure 5.3) must form one face of the cohesive element, and the next four nodes (5-6-7-8 in Figure 4.3) must form the opposite surface. Each pair of nodes at the same location (1-5, 2-6, 3-7, 4-8 in Figure 4.3) are thus constrained by the traction-separation laws.

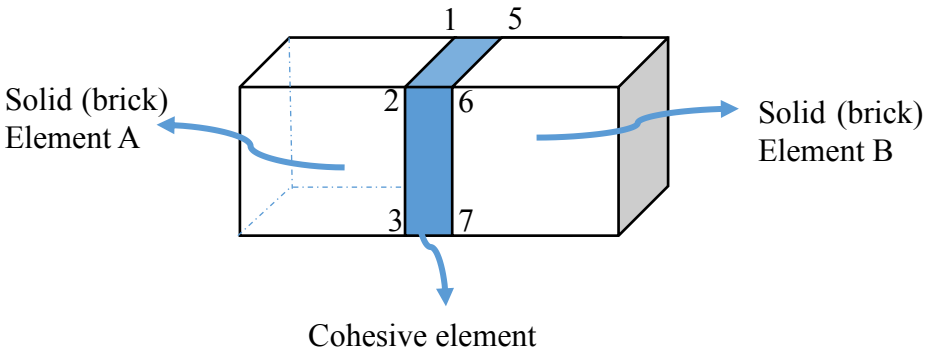

Figure 4.3 Illustration of cohesive element formation

4.2.2.2 Cohesive constitutive model

Several cohesive models with different traction laws, such as linear or bilinear, trapezoidal, exponential etc., have been proposed and applied in the analysis of the fracture behaviour in recent years (Park & Paulino 2011). The cohesive constitutive model used in the present study is a typical simple bilinear cohesive model for modelling the interface failure involving interaction between mode I and mode II fractures. It considers the irreversible damage and allows for independent definitions of the constitutive relations for different fracture modes of tension and shear (Figure 4.4).

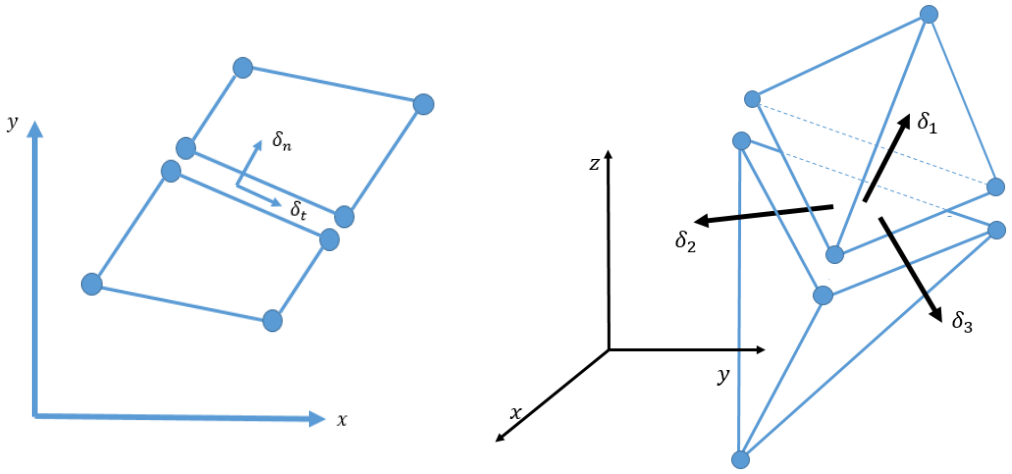

(a) 2D cohesive element (b) 3D cohesive element

Figure 4.4 Sketch of deformation of cohesive element

Figure 4.5 shows schematically the constitutive laws used in the cohesive material model. The constitutive laws used for modelling of mode I and mode II fracture are depicted by the curves in the 'traction-δ_I' and 'traction-δ_{II}' planes respectively, where δ_I and δ_{II} denote respectively the normal and tangential separation distance. Generally the interface layers will not be subject to just pure mode I or pure mode II loading. Therefore, a mixed-mode displacement δ_M is calculated from the single-mode displacement,

$$\delta_M = \sqrt{\delta_I^2 + \delta_{II}^2} \tag{4.1}$$

where δ_I is the displacement in tension (model I) $\delta_I = \delta_1$, and δ_{II} is the resultant shear displacement (mode II), $\delta_{II} = \sqrt{\delta_2^2 + \delta_3^2}$.

There are many laws for coupling the two independent fracture modes. In the present study, the representative power law is employed (Gerlach et al. 2005). The mixed-mode damage initiation displacement δ_M^P, and the ultimate mixed-mode displacement δ_M^F (total failure) can be calculated as:

$$\delta_M^P = \delta_I^P \delta_{II}^P \sqrt{\frac{1+\beta^2}{\left(\delta_{II}^P\right)^2 + \left(\beta\delta_I^P\right)^2}} \tag{4.2}$$

$$\delta_M^F = \frac{2(1+\beta)^2}{\delta_M^P}\left\{\left(\frac{K_N}{G_{IC}}\right)^n + \left(\frac{K_S \times \beta^2}{G_{IIC}}\right)^n\right\}^{-1/n} \tag{4.3}$$

where $\delta_I^P, \delta_{II}^P$ are the damage initiation displacement in the respective single modes, $\beta = \delta_{II}/\delta_I$ is the ratio of mode mixity, and K_N, K_S are the cohesive stiffness in normal and tangential directions, G_{IC} and G_{IIC} are the fracture energy release rate for pure mode-I and mode-II, and n is the power index. The damage of cohesive element initiates when the traction reaches a criterion established in term of the normal and shear tractions. The crack propagation occurs when the fracture energy release rate reaches a critical value G_c.

Thus the constitutive relations for this bilinear cohesive model are very simple and straightforward. Only some key parameters such as the stiffness, K_N and K_S, the peak tractions σ_I^P,σ_{II}^P and the fracture energies G_{IC}, G_{IIC} in the normal and shear directions respectively, need to be specified. While the peak traction and the fracture energy in Mode-I, σ_I^P, G_{IC} can be directly obtained from representative experiments for most engineering materials, the corresponding values in the shear direction often require extensive parameter studies for a particular type of material due to the difficulty in obtaining direct experimental data. Moreover, choosing suitable values for the stiffness K_N, K_S require some particular attention for intrinsic cohesive element in a finite element model, which will be discussed later.

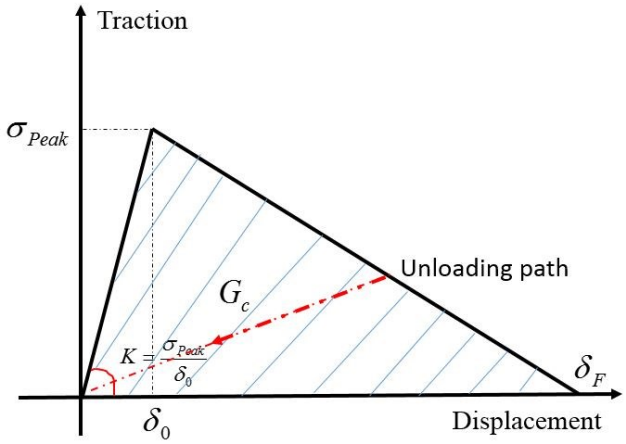

(a) Pure mode

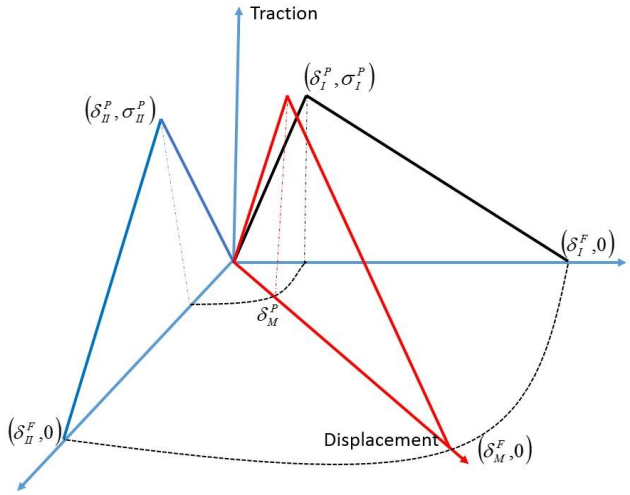

(b) Mixed mode

Figure 4.5 Illustration of mixed-mode constitutive law for cohesive elements (Gerlach et al. 2005)

4.2.2.3 Notes on using CZM in a finite element framework

The cohesive zone model implemented into a finite element model has inherent advantages in modelling the crack initiation and propagation for concrete-like materials. However, to obtain a successful simulation using this approach, two conditions must be met (Rice & Beltz 1994; Ruiz et al. 2001; Turon et al. 2006):

(a) The fictitious compliance, which refers to an exaggerated deformation in the model due to the introduction of the cohesive element, should be avoided.

(b) The element size must be less than the cohesive zone length l_{cz}, which is measured as the distance from the crack tip to the point where the maximum cohesive traction is attained.

As mentioned earlier, the intrinsic cohesive element model is adopted in the present study due to its easy implementation in FE package without updating the element node connections after each computational step. However the main problem of the intrinsic cohesive element is that it may introduce artificial compliance when a small stiffness is used (Turon et al. 2007). This aspect can be illustrated on a simple 1D case, shown in Figure 4.6, which can be considered as a small component in a whole specimen, where an intrinsic cohesive element is inserted between two bulk elements. The equilibrium condition for this simple problem yields:

$$\sigma = \frac{F}{A} = E\varepsilon = K\delta \tag{4.4}$$

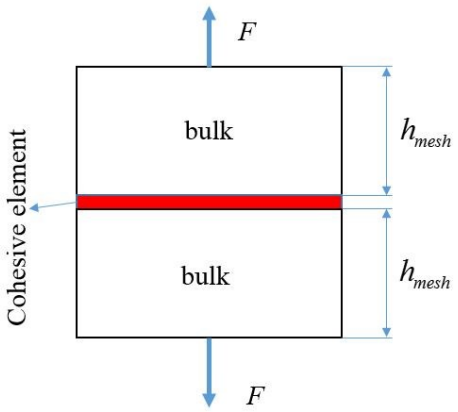

Figure 4.6 Simple illustration of CZM

where F is the applied force, ε the strain in the bulk element (mesh size h_{mesh}, cross section area A), E the Young's modulus for bulk element, K the initial stiffness of the intrinsic cohesive element and δ is the displacement jump cross the cohesive zone.

The overall strain of this component (taken one bulk element attaching one cohesive element) is:

$$\bar{\varepsilon} = \varepsilon + \frac{\delta}{h_{mesh}} = \frac{\sigma}{E} + \frac{\sigma}{Kh_{mesh}} \tag{4.5}$$

Assuming the apparent Young's modulus of the assemblage is E_{eff}, the equilibrium condition can also read:

$$\sigma = E_{eff}\,\bar{\varepsilon} \tag{4.6}$$

Thus one can deduce the normalized apparent Young's modulus:

$$\frac{E_{eff}}{E} = \frac{\sigma}{E\bar{\varepsilon}} = \frac{\alpha}{1+\alpha} \quad \text{with } \alpha = \frac{Kh_{mesh}}{E} \tag{4.7}$$

According Eq. (4.7), the ratio α appears to be the key parameter in controlling the initial stiffness of the intrinsic cohesive element, i.e.

$$K = \frac{\alpha E}{h_{mesh}} \tag{4.8}$$

More precisely, the artificial compliance due to the introduction of intrinsic cohesive element could vanish $(E_{eff} \to E)$ when $\alpha \to +\infty$. However, an excessive large stiffness for the interface element may cause other numerical problems such as spurious oscillations of the traction (Turon et al. 2006). Furthermore, large stiffness may also reduce the critical time step when an explicit dynamic algorithm is used (e.g. LS-DYNA), which would increase the calculation burden.

Many guidelines have been proposed for selecting an appropriate stiffness for the intrinsic cohesive element based on the ratio value of α in order to define 'invisible' CZM at the scale of structure. Espinosa and Zavattieri (2003) suggest $\alpha \geq 10$ based on the observation that such setting can ensure the elastic wave speeds remain unchanged across a cohesive line. Turon et al. (2007) conducted numerical simulations of delamination using CZM, taking α larger than 50 to ensure the loss of stiffness is less than 2% by the presence of the cohesive interface. But it should also

be noted that Eq. (4.8) also brings in a mesh-dependent aspect into the analysis, which introduces a further dimension into the problem. A possible way of dealing with the complexities is to perform a parameter investigation on a determined mesh size. This will be discussed in detail for the combining model in Section 4.2.5.

Another concern of the CZM implemented into FEM results from the length scale between the mesh size h and the cohesive zone length l_{cz}. As stated earlier, the damage of the cohesive element initiates when the traction reaches a criterion established in term of the tractions in pure mode-I and mode-II. But the fracture process is usually controlled by the fracture toughness, which means the crack can only propagate when the fracture energy release rate reaches a critical value G_C. Therefore it introduces a length scale, named cohesive zone length l_{cz} into the material description.

Many approaches have been proposed to predict the length of the cohesive zone, and a general form may be expressed as

$$l_{cz} = \beta E \frac{G_C}{\sigma_{Peak}^2} \tag{4.9}$$

where E is the Young's modulus of the bulk material, G_C is the critical fracture energy, σ_{Peak} is the maximum interfacial strength, and β is a parameter with a general value around 1 (Hillerborg et al. 1976).

The length of cohesive zone has an important influence around the crack tip in numerical simulations and actually imposes a constraint on the mesh size of the original bulk element. In order to obtain accurate numerical results using cohesive element the following relation has to be satisfied (Falk et al. 2001; Moës & Belytschko 2002; Turon et al. 2007):

$$h < l_{cz} \tag{4.10}$$

where h is the element size (bulk element in the FE model) in the direction of crack propagation. This means that a minimum number of elements, $N_e = l_{cz}/h$, is needed in the cohesive zone to obtain reasonable FEM results. However debates on the

minimum numbers of elements needed in the cohesive zone continues for the last decades. Falk et al. (2001) performed numerical simulations of crack growth using 2 to 5 elements in the cohesive zone while Moes and Belytschko used more than 10 element in their work (Moës & Belytschko 2002). Nevertheless it is not possible to clearly determine the minimum number of element in cohesive zone for complex stress conditions (because the choice of the traction and the fracture energy release rate is ambiguous). Furthermore, when the inner complex meso-structure of composites (e.g. concrete) is considered in numerical modelling work, it is also very difficult to determine the Young's modulus for the interface between two different component materials. Thus for specific cases, simulations with different mesh sizes may need to be conducted to assist in finding a convergence result. A suitable mesh size would be determined for the current cohesive plus contact model, which will be discussed in detail in Section 4.2.5.

4.2.3 Introducing contact-friction mechanism

When a crack is growing under compressive or shear loading, as mentioned earlier the performance of the traditional cohesive model in which no friction mechanism are introduced is poor. The incorporation of a contact-friction algorithm is expected to overcome the limitation. Generally speaking, three distinctive methods for handing this are all available in general purpose FE software such as LS-DYNA, namely the kinematic constraint method, the penalty method, and the distributed parameter method. The major advantage of the penalty algorithm is that it can show very stable results without special treatment of intersecting interfaces and it does not require solving a nonlinear system of equations in every time step (Vulovic et al. 2008). For this reason, the penalty method is adopted in the present study.

In a penalty-based contact algorithm, an elastic, compression-only spring is placed in the normal direction to resist penetration (see Figure 4.7). Each slave node is checked for penetration through the master surface. If there is no penetration nothing is done but when it does penetrate, an interface force is applied between the slave node and its contact point. The magnitude of this force depends on the amount of penetration

with a linear relationship. The coefficient can be regarded as the interface spring stiffness which gives:

$$k = \frac{\lambda K_b A^2}{V} \tag{4.11}$$

where for solid element where K_b is the material bulk modulus, λ is the penalty scale factor (normally 0.1 by default), A is the segment area and V is the volume of the elements in contact.

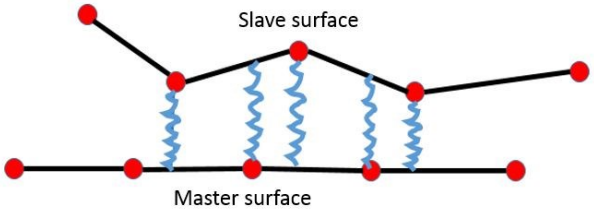

Figure 4.7 Sketch of the penalty-based contact method

In the tangential direction, nonlinear interface springs are used to model the friction effects between each two contact surfaces. As it is well known that the friction stress according to the Coulomb Friction law can be identified into two types, namely, the static friction and the kinetic friction. The static friction is the frictional force acting on between two surfaces which are attempting to move, but are not moving and the kinetic friction is the frictional force acting between two surfaces which are in motion against each other. While the kinetic friction is found to be proportional to the normal force, the static friction hardly follow this rule but only depends on the equilibrium condition. Normally the maximum static friction is higher than the kinetic one. These two friction mechanisms are both considered in the present study. While the friction stress developed in the kinetic stage can be easily defined by introducing the kinetic Coulomb Friction law, the extremity of the static friction stress before completely de--cohesion may need a special consideration, which will be discussed in detail for the combining model in Section 4.2.5

4.2.4 Cohesive plus contact model

As stated earlier, we simulate cohesive fracture and the contact/friction as two independent mechanisms. Depending on the stress condition, an interface element may develop into a full crack state without activating any contact frictional effect, or it may involve degradation of cohesion and friction sliding at the same time. To enable both mechanisms to work, it is important to define how friction should develop while the cohesion degrades, which indicates crack opening at the same interface. In the literatures the treatment of the transition stage from cohesion to pure friction varies, from the very beginning to a complete de-bonding of the cohesive zone. Tvergaad (1990) introduced the friction mechanism to a cohesive law to take effect only when de-cohesion is fully attained. This approach can successfully predict the residual stress after de-bonding but failed to model the additional load-carrying capacity due to the fracture roughness. Chaboche et al. (1997) modified the interface law by introducing a friction term from the very beginning. This model viewed the friction mechanism as a kinematic hardening effect with a decreasing hardening modulus as the damage progresses thus is capable of predicting the additional load capacity due to friction. More recent works on this topic have focused on coupling the initiation of friction to start with the onset of fracture, for instance (Alfano & Sacco 2006; Sacco & Toti 2010; Koutromanos & Shing 2012).

Preliminary explorations reveal that simply adding the cohesive and contact/friction components together cannot yield satisfactory results; the model could easily become unstable and produce inaccurate results. This is most probably because traditional contacts can only introduce the frictional resistance after the complete failure of cohesion, causing stability issue and an inability to predict the additional load capacity due to friction during the transition stage. Based on the above considerations, we propose to introduce the friction mechanism to the whole process from the very beginning with an understanding that any relative sliding between two contacting surfaces will result in friction force. However to reflect different degree of friction engagement at different states of the interface, in the present study the whole process is subdivided into three stages, which can be clearly identified from a representative numerical result from the combined model in Figure 4.8. Stage 1

refers to the process before any damage of the cohesive element. During this stage, the cohesion dominates and the friction term is negligible. Stage 2 is the process from the onset of fracture until full de-cohesion. In this stage, the friction and the remaining cohesion act on the same interface simultaneously. The friction term acting at this stage may be viewed as a hardening effect leading to increased resistance capacity of the bulk material. It should be noted that the frictional movement during this stage is not an explicit interface slide but constrained by the constitutive cohesion law that relates the friction force to the shear deformation, and therefore is effectively a static friction. The pure "sliding" friction stage is defined as stage 3. In this stage, the interface is fully separated thus the two contacting surfaces slide against each other with a frictional law. The friction at this stage is of kinetic character.

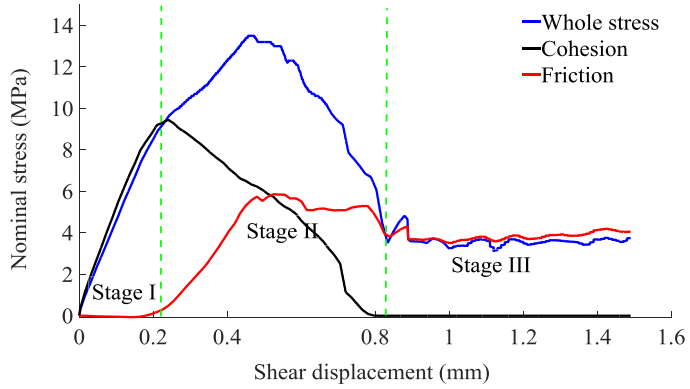

Figure 4.8 Evolution of the combining mechanism during different stages

4.2.5 Parameter settings in the combined interface model

As stated earlier suitable values of initial stiffness, mesh size should be chosen for the cohesive zone model. Furthermore as the combined interface model also involves the frictional contact mechanism, dedicated mesh convergence study needs to be performed and a suitable value for the static friction stress limit (*SFSL*) should be specified. To set up benchmark simulations with different mesh size, different cohesive stiffness are conducted and suggestion values of *SFSL* for the cohesive plus contact model are discussed in this section.

A representative shear test with a lateral confining pressure of 3 MPa is reproduced for this investigation. To create a simple but effective model for the shear test, a structural model inspired by the classical triplet experiment is adopted. The triplet experiment is commonly used in the testing of masonry materials to determine the ultimate shear strength of the mortar joints. Figure 4.9 shows a schematic of the experimental apparatus. The two side blocks (bricks) are supported rigidly at the lower edge, whereas the shear load is applied on the upper edge of the middle brick. A constant normal pressure can be introduced by applying horizontal compression force on the lateral surfaces of the outer bricks. Considering symmetry, only half of the specimen is modelled.

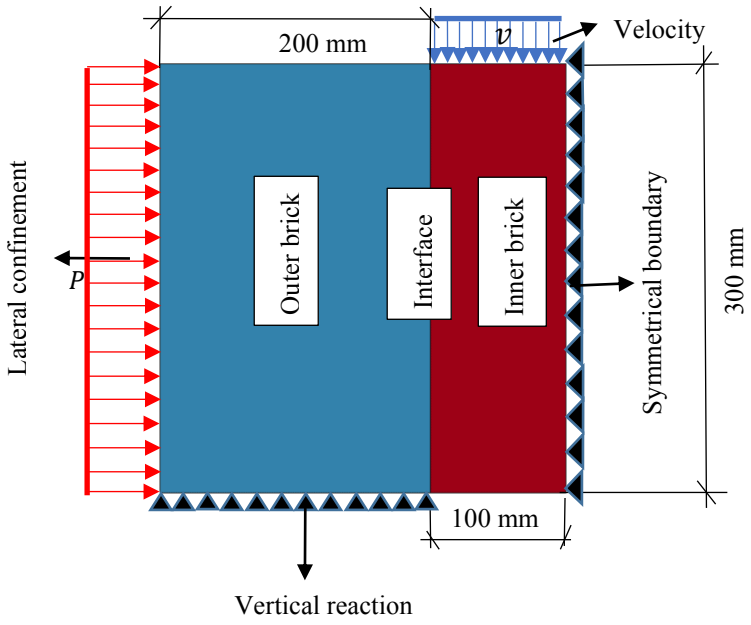

Figure 4.9 Numerical model of shear test

For the sake of simplicity, the bricks are modelled as elastic, while the interface layer is nonlinear and is modelled by the combined cohesive plus contact model. The parameters used in defining the model parameters are given in Table 4.1 and Table 4.2. It should be noted that these parameter values are in line with masonry but the simulation itself is generic for quasi-brittle solids and is not intended to tie with any physical experiment at this stage.

Table 4.1 Material properties for bulk elements

Elastic modulus $\boldsymbol{E}$ (MPa)	Poisson's ratio $\boldsymbol{\nu}$ (--)	Density $\boldsymbol{\rho}$ (g/mm^3)
3.7E4	0.2	2.3E-3

Table 4.2 Properties for interface

$\boldsymbol{\rho}$ (g/mm^3)	$\boldsymbol{\sigma_I^P}$ (MPa)	$\boldsymbol{\sigma_{II}^P}$ (MPa)	$\boldsymbol{G_{IC}}$(N/mm)	$\boldsymbol{G_{IIC}}$ (N/mm)	$\boldsymbol{\mu}$ (--)
2.3E-3	2.7	10.8	0.03	0.3	0.7

4.2.5.1 Mesh size

Simulations with five different mesh sizes, namely h = 50, 25, 10, 5, 2 mm are conducted in this study. In order to eliminate mesh dependent influence introduced by the initial stiffness of the cohesive element (see Eq. (4.8)), a sufficiently large stiffness $K_N = K_S = 10^6$ MPa / mm is used for all the cases.

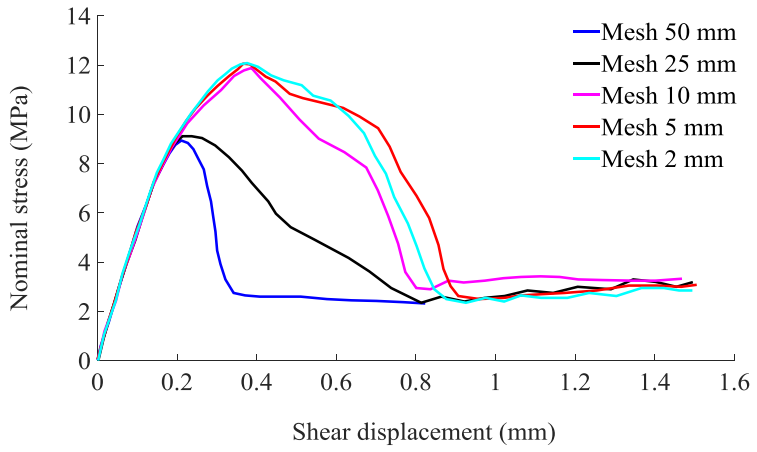

Figure 4.10 Mesh size effect on whole stress

The nominal shear stress-displacement curves obtained for several levels of mesh refinement are shown in Figure 4.10. The shear stress is defined as the applied force divided by the original cross section area of the interface between the mortar joint

and the bricks, whereas the shear displacement is recorded as the relative displacement of the two bricks measured from the loading boundary. It can be seen that the results tend to converge with a mesh size no larger than 5 mm.

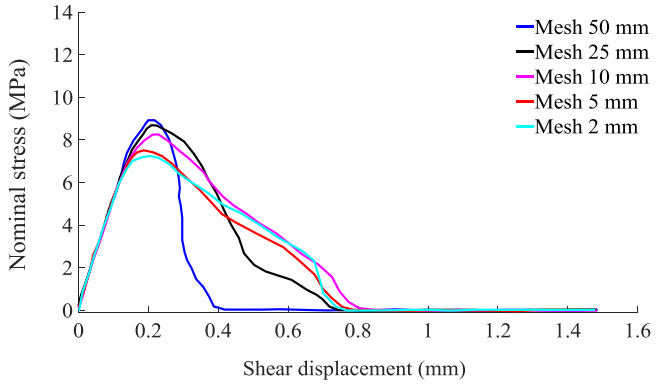

(a) Mesh size effect on cohesion

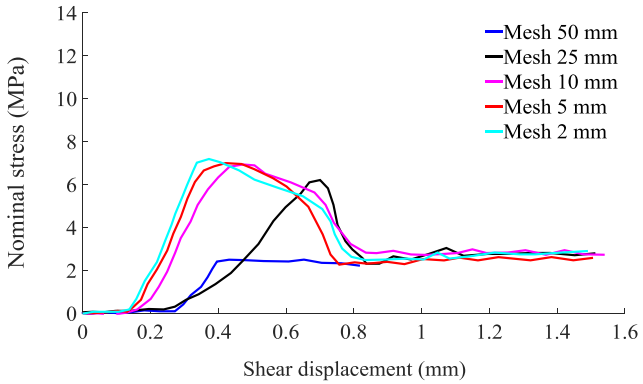

(b) Mesh size effect on friction

Figure 4.11 Mesh size effect on cohesion and friction

However a further examination of the effects of the mesh size on the two independent mechanisms (cohesion and friction) shows some more interesting results. The cohesion is derived from the average shear stress of all the cohesive elements between two brick plates in the model, while the friction stress is calculated simply from the friction force divided by the area in contact. As it is shown in Figure 4.11, the cohesion can quickly attain a generally convergent result when the mesh size is smaller than 25 mm. However the friction needs much finer mesh to approach

the convergence. Generally a convergent result can be obtained for both cohesion and friction when the mesh size is no larger than 5 mm. Hence the mesh size 5 mm at the interface layer has been chosen for the simple shear test on the cohesive plus contact model hereinafter. Recall Eq. (4.9), the cohesive zone length in the model can be calculated as around 95 mm with $\beta = 1, \mathrm{E} = 3.7 \times 10^4$ MPa, $G_c = 0.3$ and $\sigma_{peak} = 10.8$ MPa (see Table 4.1 & Table 4.2). Such a length of the cohesive zone contains nearly 20 cohesive elements which is somewhat larger than the suggested value (2 to 10) in some references (Falk et al. 2001; Moës & Belytschko 2002) for a mesh size of 5 mm. This indicates that the current cohesive plus contact model requires a much finer mesh in order to get a convergence because of the involvement of contact-friction algorithm.

4.2.5.2 Initial stiffness of cohesive element

From the basic discussion in Section 4.2.2, we have got a general idea that a suitable value for the initial stiffness of the cohesive elements is crucial for an adequate behaviour of the CZM. In this section, a more specific examination is carried out on the cohesive plus contact model with five different interface stiffness parameters, namely, α = 0.05, 1, 10, 50 and 100. All of these analyses are performed on the same mesh size of h = 5 mm (see Eq. (4.8)). The results are compared and then discussed.

Figure 4.12 shows the simulated nominal shear stress vs. shear displacement results. As it is shown, the stiffness generally has a slight influence on the global stress-displacement curves. Further examinations into the effect on the cohesion and friction, respectively, are shown in Figure 4.13. The effect of the stiffness on the cohesion response is also very limited; there is only a slight increase of the stiffness when α is increased from 0.05 to 100. In contrast, the friction response is significantly influenced by the cohesive stiffness. When the cohesive stiffness is set relatively small (α = 0.05 or 1), it can be found that the frictional mechanism is involved from the very beginning of the shear process. On the other hand, if the cohesive stiffness is set relatively large ($\alpha \geq 10$), the frictional mechanism comes into action only after a certain degree of 'separation'. It is interesting to find that when the stiffness parameter is larger than 10 the friction mechanism is not engaged

until the shear displacement reaches about 0.2 mm, which is actually a typical threshold of fracture (Vandewalle 2000; Nakamura et al. 2010).

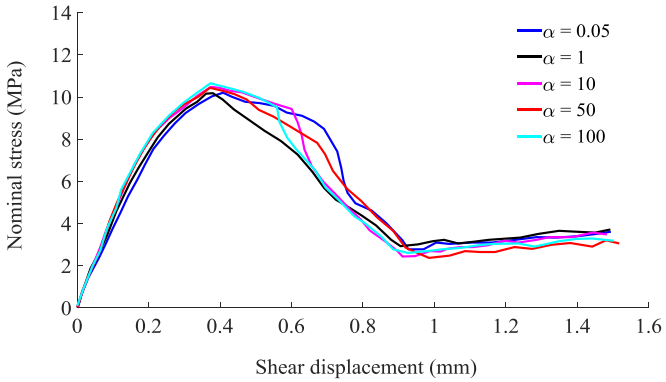

Figure 4.12 Cohesive effect on global response

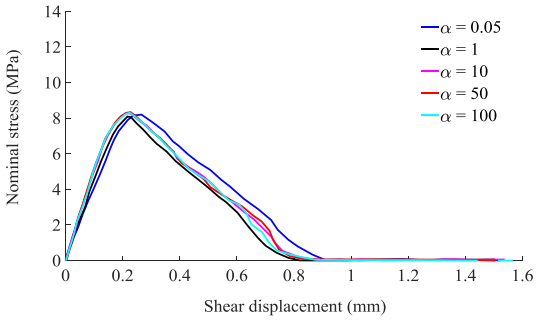

(a) Initial stiffness effect on cohesion

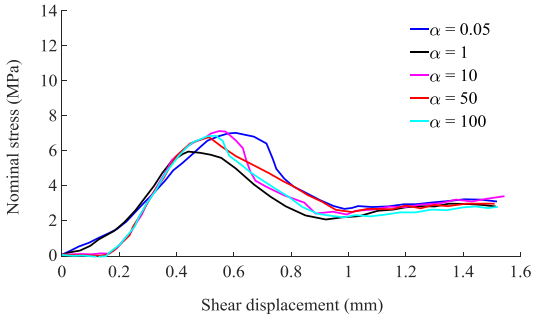

(b) Initial stiffness effect on friction

Figure 4.13 Cohesive stiffness effect on cohesion and friction

From these results, it may be concluded that a relatively large value (e.g. $\alpha \geq 10$) needs to be employed for the cohesive stiffness in order to ensure that the friction starts from the onset of fracture. With respect to also the computational cost, which increases with the increase of the cohesive stiffness as mentioned earlier in Section 4.2.2, a value of $\alpha = 50$ is deemed to be appropriate and this value is used hereafter in present study. It is worth mentioning that such a setting is consistent with the suggestions for CZM in some previous studies (Turon et al. 2007)

4.2.5.3 Friction stress limit

As stated above, before the complete loss of cohesion, the process is a combined de--cohesion (degradation in cohesion) and contact, in which the nodes that are initially at the same locations are still constrained by the cohesive constitutive law but permit tangential motion with frictional sliding. At this stage, the model has no response to the Coulomb's kinetic friction law because there is essentially no 'free' relative slip between each pair of nodes. The friction stress that develops at this stage can be very large. It is reasonable and necessary to impose a static friction stress limit parameter (*SFSL*) to set a limit value for the maximum static frictional stress.

The static friction limit value must ensure a realistic static friction and at the same time guarantee a smooth transition from the de-cohesion process to the pure friction stage. In this respect this parameter should on one hand directly relate to the shear strength of the bulk material and on the other hand relate to the kinetic frictional coefficient of the contacting surface. However, the bulk materials on the two sides of a cohesive element are generally treated as simple linear-elastic material as in the present study. Based on preliminary analyses, it is suggested that the static friction limit be set as two times of the cohesion strength (in the shear direction) for concrete-like materials, while a general kinetic frictional coefficient of around 0.7 is adopted (Mattock 2001; Mohamad et al. 2015; Figueira et al. 2016).

4.3 Model performance and experimental verifications

4.3.1 Model under different lateral pressures

When the cohesive combined with contact model is subjected to a mixed loading condition of shear with a certain level of normal pressure, the contact/friction effects will be involved and this is expected to increase the overall shear strength. The simulated shear stress vs. shear displacement curves for various levels of the normal compression pressure are shown in Figure 4.14.

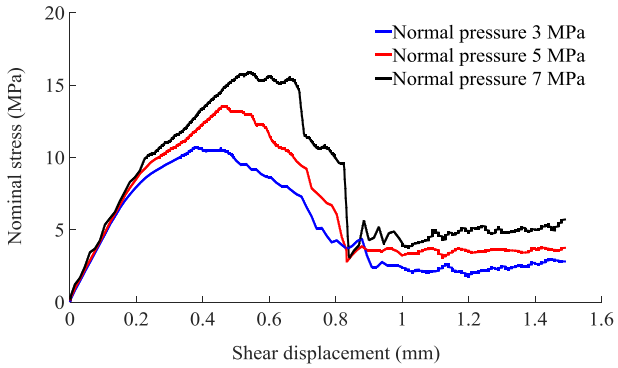

Figure 4.14 Shear stress vs. shear displacement relations under various normal compressions

It can be observed that the shear strength increase persistently as the normal compression increases. Although the cohesive component has a zero residual strength, the overall shear stress of the simulated specimen exhibits a residual strength which is dependent on the normal pressure. This is attributed to the basic friction effect which is equal to the friction coefficient ($\mu = 0.7$) times the normal stress.

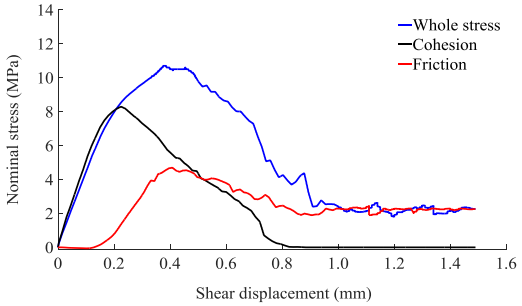

(a) Normal pressure 3 MPa

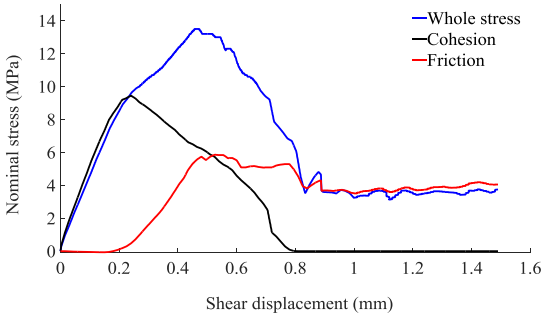

(b) Normal pressure 5 MPa

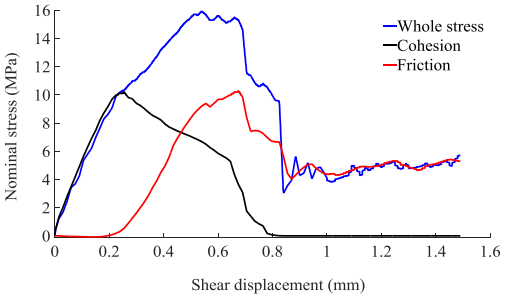

(c) Normal pressure 7 MPa

Figure 4.15 Cohesion, friction and shear stresses

A further check on the evolution of cohesion and friction for all the three cases are presented in Figure 4.15. As it is shown, the total shear stress of the model under normal compression is comprised of cohesive stress and friction stress, and both components are significant throughout the fracture process until the cohesive effect diminishes. This phenomenon is quite similar with the basic idea in discrete element

method (DEM) modelling in which two particles are linked with cohesion and friction, following Mohr-Coulomb rule.

4.3.2 Model with different friction coefficients

The current cohesive combined with contact model is then further checked by the shear test with a constant normal compression 5 MPa but with various friction coefficients in the contacting surfaces. As stated earlier, a suitable value of the static friction stress limit should be used to obtain a smooth transition from the de-cohesion process to a pure kinetic friction stage. While a value of two times of the cohesion strength for this parameter could guarantee a perfect performance for the combined model with a kinetic friction coefficient around 0.7, it may need a slight adjustment when different friction coefficients are adopted.

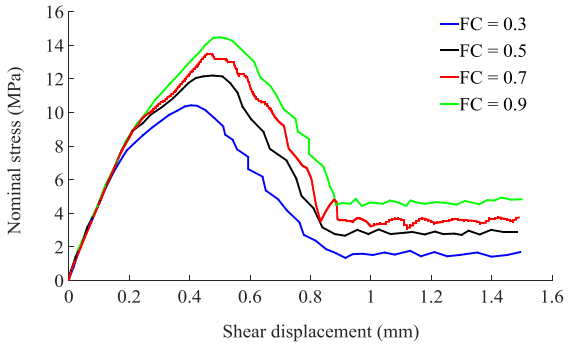

Figure 4.16 Shear stress vs. shear displacement relations for different friction coefficients (FC)

Figure 4.16 depicts the nominal shear stress against relative shear displacement with four representative frictional coefficients, namely, 0.3, 0.5, 0.7 and 0.9, with the adjustment range of the static friction stress limit parameter in 17.5~23. As shown the model can also exhibit a continuous stable and smooth performance provided the *SFSL* is set properly. Again the friction stress and the average cohesive stress against relative shear displacement for each friction coefficient are all presented in Figure 4.17 for reference. The average cohesive stress-displacement curves for different friction coefficients are almost the same. The enhancement of the shear strength of the model is mainly resulted from the static friction effect while the dynamic friction

coefficient dominates the pure friction mechanism at the final stage. A smooth transition from the de-cohesion process to the pure kinetic friction stage is also well captured.

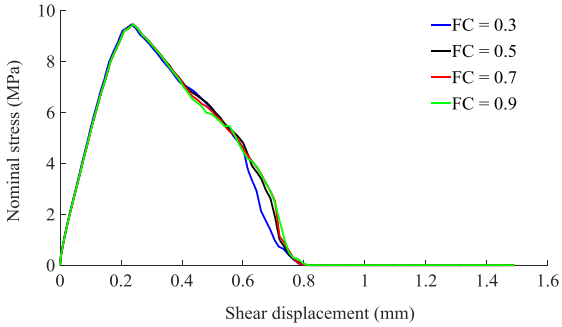

(a) Cohesive stresses with varying FCs

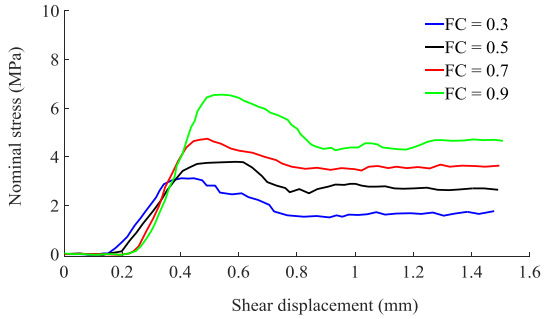

(b) Friction stresses with varying FCs

Figure 4.17 Cohesive and friction stresses vs. shear displacement for different FCs

4.3.3 Experimental verification

Having examined the working principles of the proposed combined cohesive and contact model and the general effects of the key parameters, this section presents an experimental verification against a representative test on masonry specimens (Beyer et al. 2010) to further validate the numerical model. As mentioned, the experimental setup is simple and has been commonly used in the testing of masonry materials to determine the ultimate shear strength of the mortar joints. The failure mode is well controlled to the mortar joint interfacing two masonry blocks, and hence it provides a well-defined benchmark for the present verification purpose.

Table 4.3 Material properties for brick elements

Elastic modulus $\boldsymbol{E}$ (MPa)	Poisson's ratio $\boldsymbol{\nu}$ (--)	Density $\boldsymbol{\rho}$ (g/mm^3)
1.2E4	0.15	9.32E-4

Table 4.4 Properties for mortar joints

$\boldsymbol{\rho}$ (g/mm^3)	$\boldsymbol{\sigma_I^P}$ (MPa)	$\boldsymbol{\sigma_{II}^P}$ (MPa)	$\boldsymbol{G_{IC}}$ (N/mm)	$\boldsymbol{G_{IIC}}$ (N/mm)	$\boldsymbol{\mu}$ (--)
1.65E-3	0.25	0.25	0.17	2.55	0.71

As reported in (Beyer et al. 2010), the crack can only propagate along the interface boundaries between brick and mortar, whereas bricks largely remain intact. Therefore in the numerical model the brick parts are given a simple elastic constitutive law with parameters given in Table 4.3. The Young's modulus and density of the bricks are directly taken from the experimental test. For the Poisson's ratio, since there was no direct data from the experiment, it is assumed to be 0.15 in the current numerical model, and this value coincides with the masonry material property reported in (Alfano & Sacco 2006). For the material properties of mortar joint between the bricks, the two key parameters, i.e. the critical (cohesive) stress and the friction coefficient, are directly obtained from the best-fit Mohr-coulomb relationships in experimental test, and the values are summarised in Table 4.4. The values for Mode-I and Mode-II fracture energy are taken from (Pina-Henriques & Lourenço 2006).

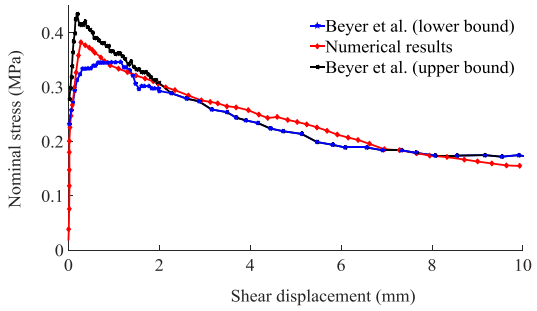

(a) Shear test for wallet with normal pressure 0.2 MPa

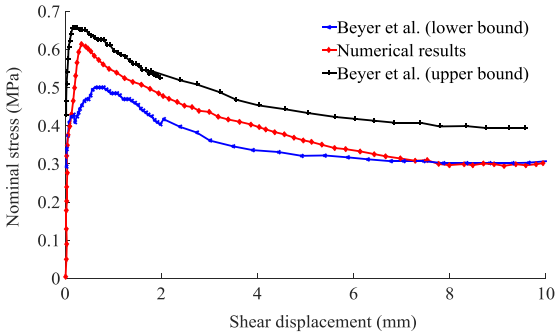

(b) Shear test for wallet with normal pressure 0.4 MPa

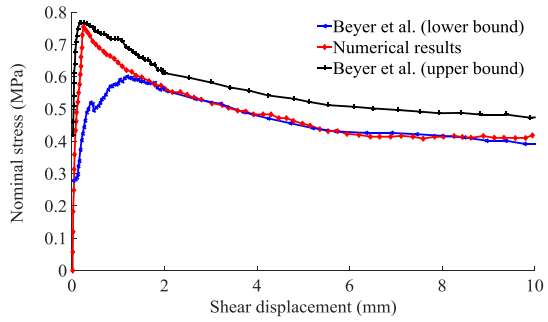

(c) Shear test for wallet with normal pressure 0.6 MPa

Figure 4.18 Triplet tests comparison with experimental evidence by Beyer et al. (2010)

The initial stiffness of the interface can be determined according to Eq. (4.8). The Young's modulus for brick element is $E = 1.2 \times 10^4$ MPa (see Table 4.3); subsequently the stiffness of interface is $K_N = K_S = 1.2 \times 10^5$ MPa / mm, taking

the parameter $\alpha = 50$ for mesh size 5 mm. The static friction stress limit parameter is taken as two times of the cohesion strength in shear (i.e. $SFSL = 0.5$ MPa) according to the guideline discussed earlier, considering $\sigma_{II}^{P} = 0.25$ MPa and $\mu = 0.71$.

The comparison of the shear stress - shear displacement relationship between the experiments and the numerical simulation is illustrated in Figure 4.18. In general, the numerical simulation results agree well with the experiments. The transition from cohesion to friction regime is very smooth, and the combined cohesive and friction model predicts correctly the pure friction stage.

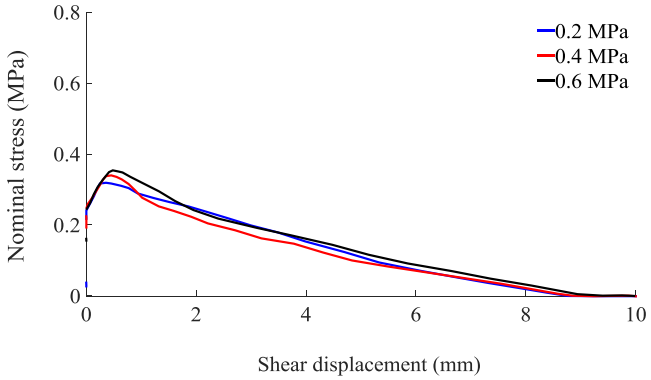

Figure 4.19 Stress strain response of the model without contact

To highlight the fact that the model would exhibit a poor performance if only the cohesive element was used without incorporating the contact function, Figure 4.19 shows the corresponding results. As it is shown, such a cohesive model fails to represent the dependency of the shear behaviour on the stress condition in the normal direction. Furthermore, from the damage pattern in Figure 4.20, a serious penetration problem occurs in the model with only cohesive elements. The most likely reason of this poor response could be that the default cohesive model cannot resist mixed loading conditions like shear with normal compression. After the cohesive elements failed, the two parts in the model penetrate with no restriction or resistance. The serious penetration problem from the cohesive-element only model is well resolved in our current cohesive combined with contact model, and the final failure model agrees very well with the representative triplet experiment in (Beyer et al. 2010). This demonstrates the robustness of the proposed new model.

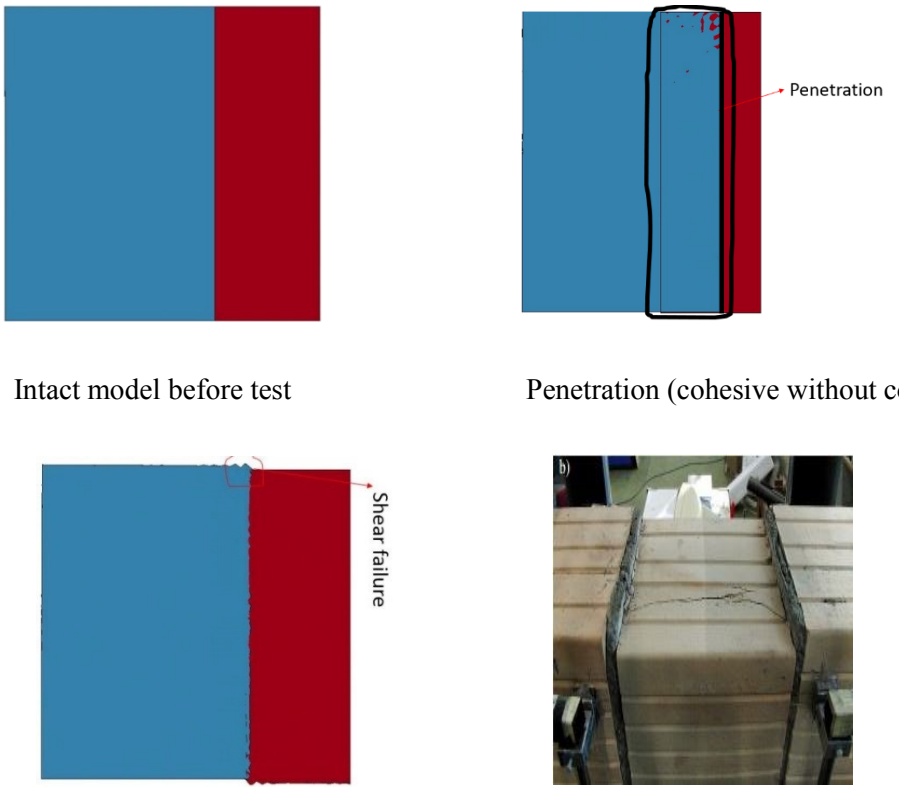

Intact model before test | Penetration (cohesive without contact)

Shear failure mode (new model) | Beyer et al. (2010)

Figure 4.20 Illustration of deformations in the two models

This model is therefore deemed ready to be further applied in the mesoscale concrete framework to simulate the fracture mechanisms along the interface between the aggregate and mortar matrix, and this will be presented in Section 4.4.

4.4 Mesoscopic analysis of concrete incorporating the interface model

In this section, the proposed new approach is applied in the mesoscale concrete model framework. A cubic concrete specimen of 100 mm is modelled for uniaxial tension and compression. Compressions with different lateral confinements on the mesoscopic cohesive plus contact model are also verified towards experimental evidences. 2D plane stress model is employed.

4.4.1 Material parameters for mesoscale concrete

In the mesoscale model, the interface model with the combined cohesive and contact/friction components is used to model the fracture process at the interface between aggregates and mortar matrix, i.e., the ITZ. The two bulk constituents, namely the aggregates and mortar matrix, are modelled as continuum solids. Since the aggregate material is usually much stronger than mortar, it is reasonable to model the aggregates with a linear elastic material model. The mortar matrix may be represented by a damage-plasticity model to account for the damage and plastic deformation that may incur within the mortar matrix. Herein we use the K&C concrete damage model (material #72R3 in LS-DYNA) which has been calibrated extensively (e.g. Tu & Lu 2009). The detailed material properties used for bulk materials (aggregate and mortar matrix) are summarized in Table 4.5 while the parameters used for the ITZ are listed in Table 4.6. All these parameters here are assigned with values to represent a class of concrete with a nominal compressive strength of 30 MPa. These material properties are determined based on data collected from relevant literature (e.g. Nagai et al. 2004; López et al. 2008a).

One may note that it is nearly impossible to clearly determine the initial stiffness for the cohesive element in the complex mesoscale concrete model because the choice of Young's modulus is ambiguous. But according to (ACI 2008), the global elastic modulus of concrete with a nominal compressive strength 30 MPa is around 30 GPa. Therefore the initial stiffness of the interface is set to $K_N = K_S = 1.5\times10^6$ MPa / mm according to Eq. (4.8) taking $\alpha = 50$ as proposed. As for the mesh size, the simple shear test model above in which similar material properties are used shows that $h = 5$ mm can already give a convergence result. Clearly for the mesoscale model the mesh size is generally much finer than this and so the mesh convergence concerning the cohesive plus contact model should not be a problem. Therefore a more refined mesh $h = 1$ mm, which is dictated by the need of discretising the mesoscale geometry, is adopted for the mesoscopic analysis of concrete behaviour with cohesive plus contact model hereafter.

It should be noted here that the mechanical properties of ITZ, including tensile strength and modulus, are set to be 50% of the mortar properties. As for the shear properties of ITZs e.g. the shear strength and the fracture energy in shear mode, they are not precisely known in the literature. Therefore it is necessary to conduct parameter studies to find proper values for them, which will be given later.

Table 4.5 Material properties for concrete

Component	Density $\boldsymbol{\rho}$ (g/mm^3)	Elastic modulus $\boldsymbol{E}$ (MPa)	Poisson's ratio $\boldsymbol{v}$ (--)	Compressive strength $\boldsymbol{\sigma_c}$ (MPa)
Aggregate	2.6E-3	6E4	0.2	--
Mortar	2.3E-3	--	0.2	45

Table 4.6 Properties for interface

Density $\boldsymbol{\rho}$ (g/mm^3)	Normal peak traction $\boldsymbol{\sigma_I^P}$ (MPa)	Energy release rate in mode-I $\boldsymbol{G_{IC}}$ (N/mm)	Friction coefficient $\boldsymbol{\mu}$ (--)
2.3E-3	2.3	0.03	0.7

4.4.2 Parametrisation of other important material properties

In order to identify the influence of key variable parameters like shear strength of cohesive material *S*, shear fracture energy G_{II} and the friction stress limit parameter in the present cohesive plus contact model, a series of simulations has been performed to examine them by comparing the macroscopic stress-strain relationship with classical concrete experiments. Since these three parameters primarily influence model II cracking, and have little influence on the tension response, the parameterisation is conducted by examining the behaviour of the mesoscale model in quasi-static uniaxial compression.

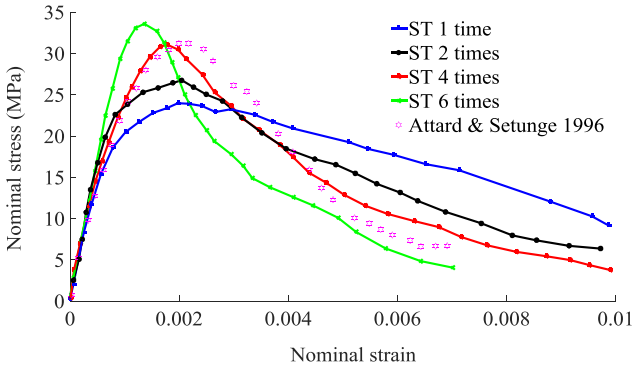

Figure 4.21 Influence of shear strength

The first parameter being examined here is the shear strength. The ratio between the shear and the normal critical traction (ST ratio) for a cohesive model is of particular importance for concrete. Experimental evidences (Swartz & Taha 1991; Jia et al. 1996; Cedolin et al. 1999) suggest that the peak strength is significantly larger in pure shear mode-II than in pure mode-I owing to the interlocking of aggregate particles in concrete. Swartz et al. (1991) estimates the ST ratio to range between 3 and 6 by analytical and numerical simulations of several mixed-mode tests.

Figure 4.21 shows the global stress-strain relationships in compression produced by the mesoscale model with different ST ratios. As can be seen, the ST ratio apparently affects the compressive peak strength of concrete, as well as the post peak softening behaviour. With an increase of the ST ratio, the compressive strength increases. For the targeted concrete of 30 MPa compressive strength, it appear that a ST ratio of 4 (shear fracture strength being 4 times of tensile strength) is appropriate for the cohesive material. This value is slightly lower than the one chosen in (Ruiz et al. 2001) in which a ST value of 5 was used for a homogeneous concrete model.

It is also interesting to observe that the cohesive shear strength also has an influence on the damage patterns, which relate to the softening behaviour. As shown in Figure 4.22, the final cracking patterns are markedly different for the lower shear strength cases (ST ratio of 1 or 2) as compared to the higher shear strength case (ST ratio of 3). The final damage pattern from the higher shear strength case agrees very well

with experimental evidence (Fatima et al. 2013) and the numerical result by other researchers (López et al. 2008a).

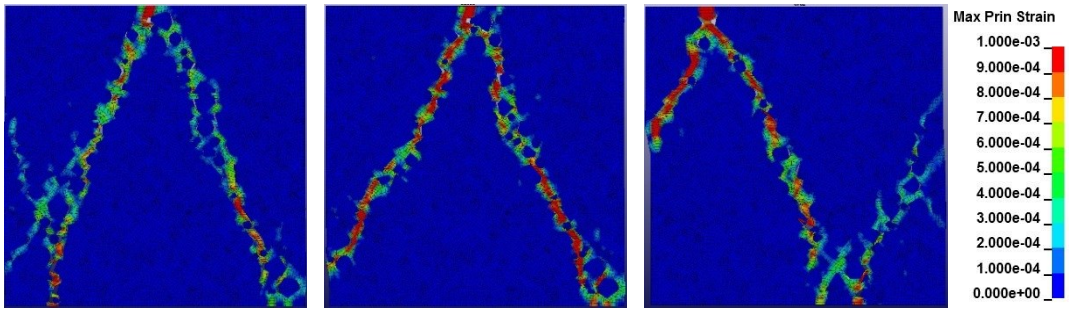

(a) 1 time (b) 2 times (c) 4 times

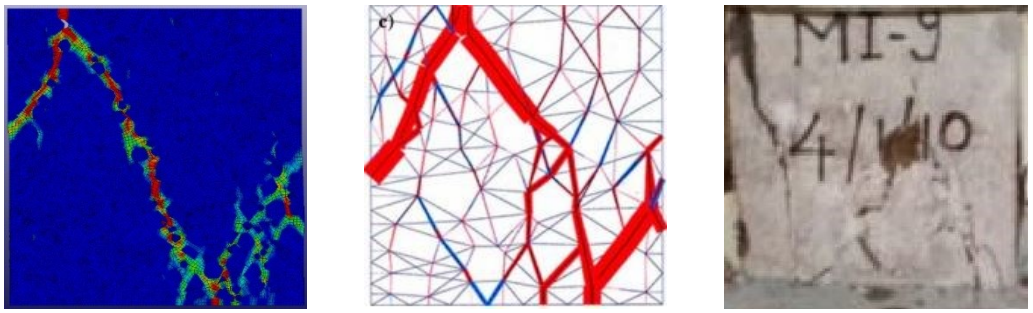

(d) 6 times (e) Lopez et al. 2008a (f) Fatima et al. 2013

Figure 4.22 Final damage (cracking) patterns with different shear strength

(Characterised by maximum principle strain hereinafter in this chapter)

Another important factor is one which defines the fracture energy ratio between the Mode-II and the Mode-I for the cohesive model, herein referred to as SE ratio. Experimental observations generally suggest that the fracture energy in pure mode-II is much larger than in tension mode-I (Achintha & Burgoyne 2013). The larger fracture energy in mode-II may be explained by the fact that the shear fracture energy includes not only the energy to create micro-cracks in fracture process zone but also the energy to break the shear resistance owing to interlock of aggregates and rough fracture surfaces behind the crack front. However there is a large scatter in the specific SE ratios used by different researchers, for examples, 8 to 10 in (Swartz et al. 1988) but around 25 in (Bažant & Pfeiffer 1986).

Figure 4.23 shows the global stress-strain relationships for the model with different SE ratios. As can be seen, with a higher value of G_{II}, the dissipated fracture energy increases and thus modifies mostly the post-peak behaviour and shifts the transition to softening towards higher strain value. Therefore a SE value of 10 (i.e. the fracture energy in cracking mode II being 10 time that in mode I) has been set in consideration of the strain at peak strength which is generally around a constant value of 0.002 for conventional unconfined concrete. This choice of SE of 10 is also consistent with the experimental evidence in (Swartz et al. 1988), but a little bit lower than the experimental observation in (Bažant & Pfeiffer 1986) where 25 was reported. Since the meso-structure of the aggregates have already been explicitly represented in the present model, it is expected that the interlock phenomenon, which contributes in part to the shear resistance at the interface, is automatically simulated in the model. Thus a SE ratio of 10 in fracture energy between mode-II and mode-I can be acceptable.

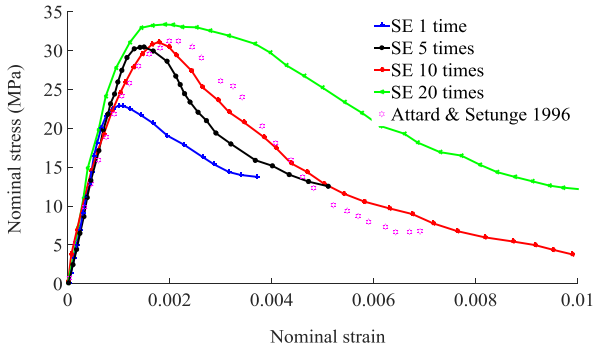

Figure 4.23 Influence of shear fracture energy

As discussed earlier, *SFSL* is a key parameter used in the cohesive plus contact model. It can control the static friction mechanism before de-cohesion and thus affects the global response of the combined model. A suggested value for this parameter based on the preliminary numerical analysis is two times of cohesion. To further check the adequacy of this suggestion and to enable modification of this value of *SFSL* for the mesoscale concrete model, a parametrisation study has also been conducted on this parameter. Figure 4.24 shows the nominal stress-strain relationships for different values of *SFSL*. It appears that the value of two times of

cohesion still can offer a stable and reasonable performance for the mesoscale concrete model.

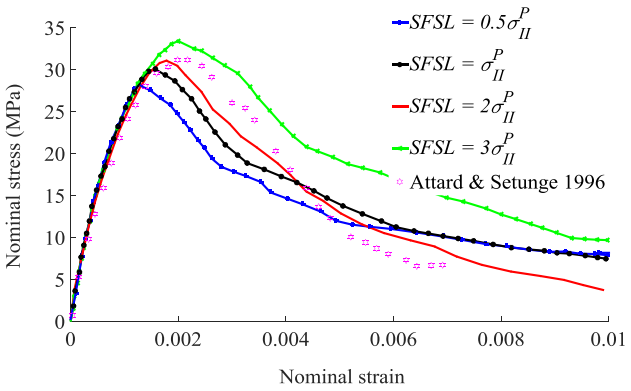

Figure 4.24 Influence of friction limit SFLS

4.4.3 Uniaxial tension test

For the uniaxial tension simulation, the cubic model is subjected to a velocity boundary condition which is directly applied on the top face. No artificial enhancement layer at the loading end is used due to the inherent advantage of the mesoscale numerical model.

Figure 4.25 illustrates the development of the major crack in the concrete specimen under uniaxial tension. The damage is characterised by maximum principle strain in vertical direction in the range of (0, 0.001) as can be seen in Figure 4.25. It can be observed that upon the peak stress many micro-cracks have developed and are located mostly at the interface between aggregates and mortar. As the strain increases, concentrated macro cracks starts to emerge, and this bring the specimen into the softening stage. Because of the stress relief, unloading and recovery of the elastic deformation takes place in the areas outside the macro crack. Many small micro-cracks stop opening further. As the applied tension deformation further increases, the concentrated macro cracks propagate transversely, cutting through the ITZ region, and finally coalesce to form virtually a single crack across the entire width of the specimen. This phenomenon is a reproduction of what has been observed in many representative experiments (e.g. Lin et al. 2013).

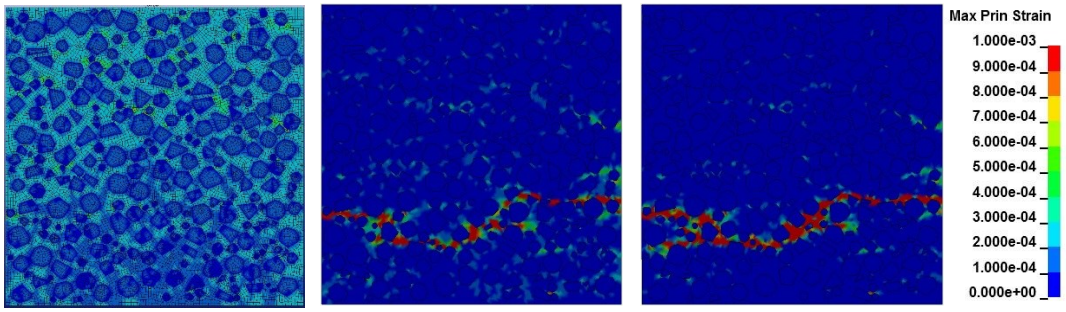

(a) Before peak load (b) Around peak (c) After peak load

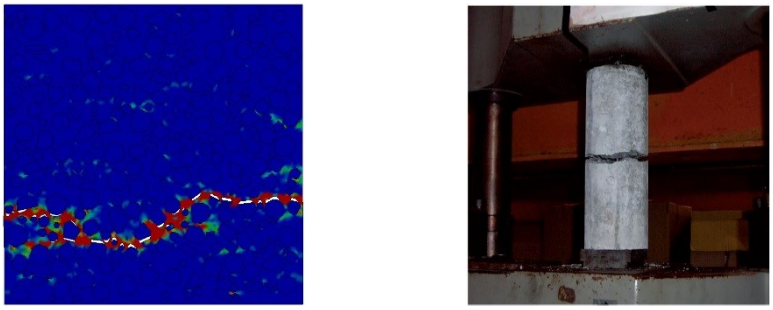

(d) Final crack pattern (scaled by 10 times) (e) Experiments (Lin et al. 2013)

Figure 4.25 Crack patterns in tension and comparison

The corresponding tensile stress-strain curve is given in Figure 4.26. For comparison the tensile stress-strain curve produced with a model without involving the contact mechanism is also presented. The experimental data obtained from (Li & Ansari 1999) is used directly for benchmark. It can be seen that the stress-strain curve from the cohesive plus contact model gives almost the same result as the pure cohesive model under an axial tension. This is because almost no contact-frictional mechanism is involved in a tension situation. The tensile strength is around 3 MPa, as expected, with a corresponding strain around 1.2e-4 (120 micro-strain) which agrees very well with experimental observations.

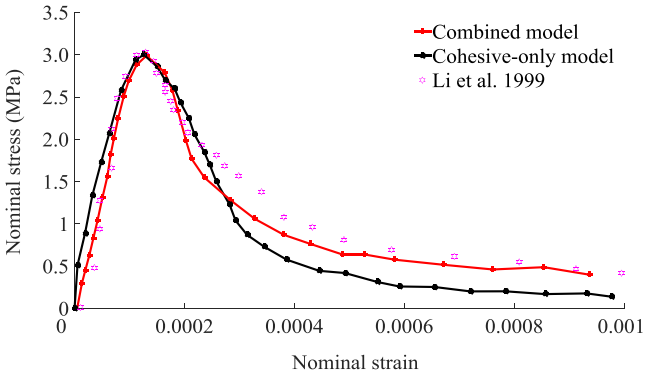

Figure 4.26 Stress strain curves in tension

4.4.4 Uniaxial compression test

Uniaxial compression simulations without any lateral constraint on the loading faces are conducted in this part. The results are compared in Figure 4.27. The inherent problem with the pure cohesive model becomes apparent; such a model fails to achieve satisfied results both in terms of the compression strength and the softening response. On the other hand, the stress strain curve from the cohesive plus contact model is consistent with the general expectation based on experimental evidences. The compressive strength is around 30 MPa with the corresponding strain around 1.95e-3.The softening response also appears to be reasonable.

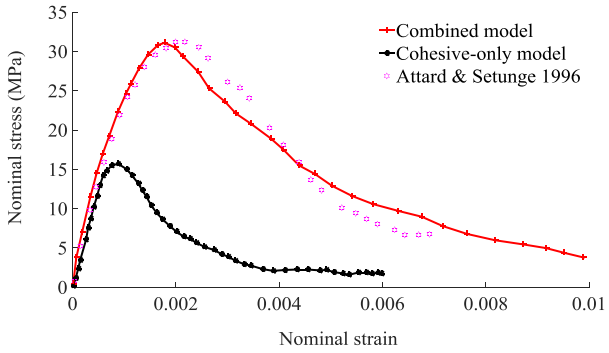

Figure 4.27 Stress-strain curves in uniaxial compression

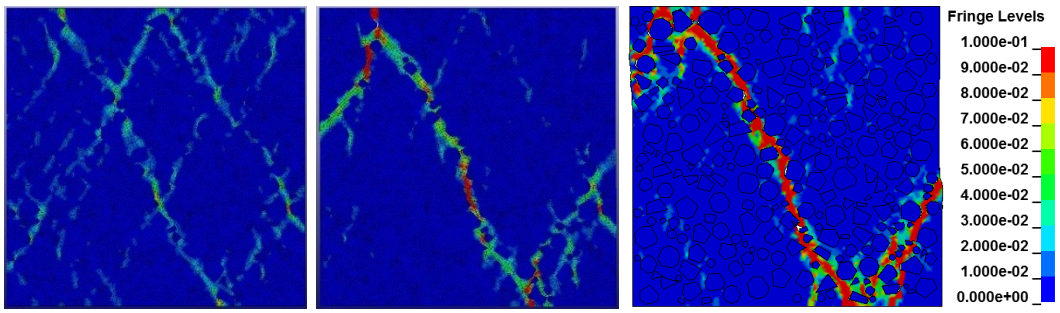

Before peak Around peak After peak load

Figure 4.28 Damage (cracking) process in compression

Figure 4.28 depicts the fracture process of the concrete model under uniaxial compression. Many micro cracks develop around the interface (ITZ) between aggregate and mortar matrix in the specimen during the loading process. But finally a distinctive crack pattern involving only a few inclined macro cracks emerges at the post-peak stage. The final crack pattern agrees very well with the experimental evidence and numerical result by other researchers (López et al. 2008a; Fatima et al. 2013).

4.4.5 Compression with lateral confinement

Experimental results have revealed that the compressive behaviour of concrete is very sensitive to the lateral confinement. Generally with the increase of the lateral confinement pressure, both the compressive strength and the ductility show significant enhancement.

To validate the present mesoscale concrete model concerning the confinement effect, simulations for several levels of confinement, at 1.5, 4.5, and 9.0 MPa, respectively, have been performed. The confinement pressure is applied as lateral force on the side edges (left and right) of the specimen, while the axial loading is still controlled by the velocity boundary condition. With the explicit analysis scheme, the lateral confinement pressure is applied gradually in order to minimize spurious oscillations. To save the computing time the lateral pressure is applied in parallel with the axial load but is completed before the axial load reaches its peak to ensure that its full effect on concrete damage is covered.

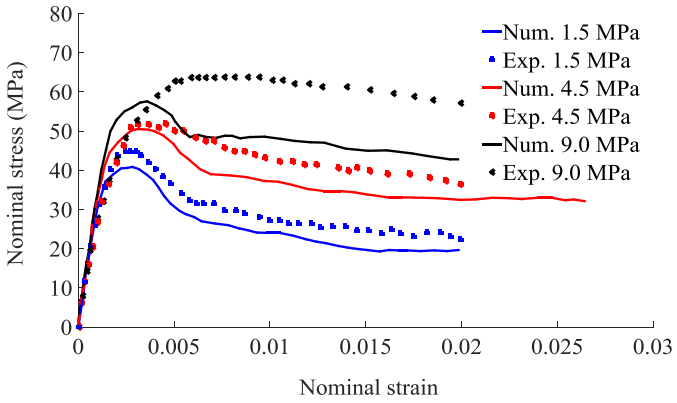

Figure 4.29 Confinement effects

Figure 4.29 illustrates the nominal axial stress-strain responses of the specimens under different confining pressures. The experimental evidences from triaxial loading tests reported in (Sfer et al. 2002) are selected for a direct comparison. Generally as expected the compressive strength of the concrete increases significantly with an increase of confining pressure. Moreover one can notice that lateral confinement also results in an increase in the ductility, or decrease in the slope of the post-peak branch, of the concrete material. Both trends are predicted well by the current mesoscale concrete model with a cohesive plus contact interface model for the ITZ. Comparing to the experimental curves, it appears that the peak strengths under lateral confinement from the simulations are relatively lower, and generally speaking with the increase of the confinement the scatter increases. This suggests that in a 2D FE framework, the mesoscale model with the cohesive plus contact interface model tends to underestimate the lateral confinement effect, especially in higher pressure cases. This issue may only be properly resolved if the proposed interface model is implemented in a 3D mesoscale model, as one can anticipate from the development of the 3D mesoscale model in Chapter 7. But such an implementation would require a drastic increase of the computational cost, which is a subject beyond the scope of the present study.

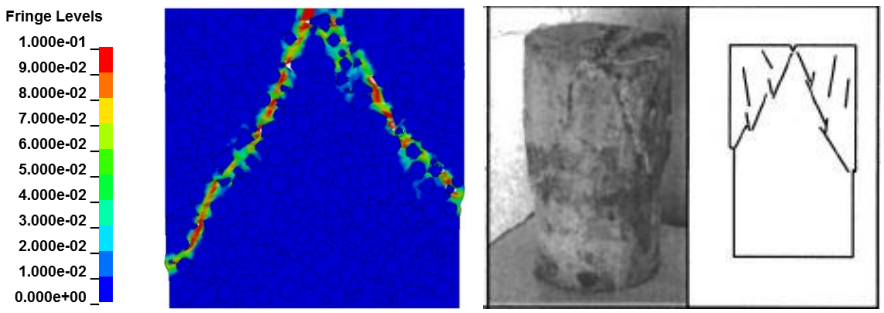

(a) Lateral confinement 1.5 MPa

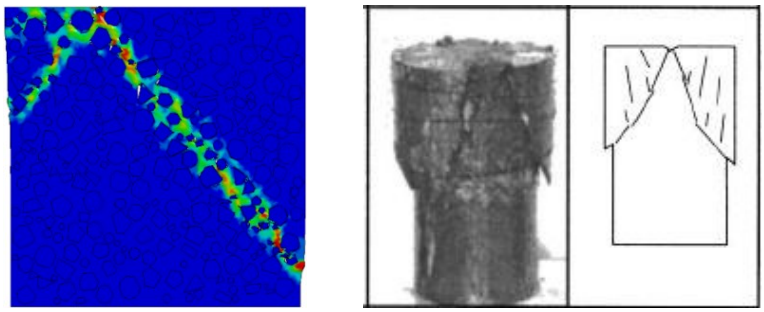

(b) Lateral confinement 4.5 MPa

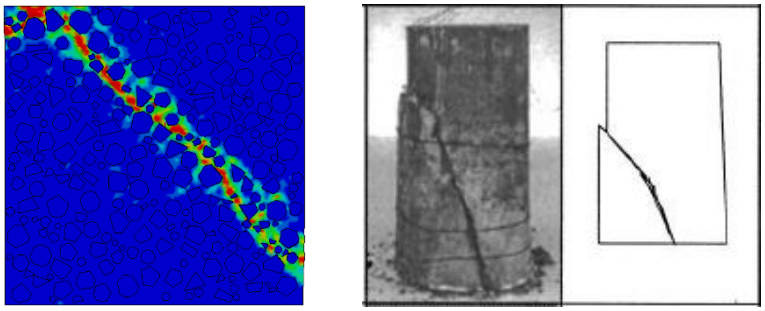

(c) Lateral confinement 9 MPa

Figure 4.30 Final damage patterns under different confinements (Left: numerical results; Right: Sfer et al. 2002)

The final cracking patterns are depicted in Figure 4.30. As one can notice, the confinement pressure also affects the damage patterns. Generally speaking, with the increase of the confining pressure, the angle of the main cracks to the axial loading direction increases while the number of the macro-cracks eventually reduces to just a single major crack. This appears to simply indicate that there is a change in the mode of failure from splitting to crushing failure as the confinement increases. Again the

failure modes from the numerical simulations agree favourably with experimental evidences.

4.5 Dynamic compression

Classical experimental results have shown that the "apparent" dynamic compressive strength increases with the increase of the strain rate, and such an increase is generally defined by a Dynamic Increase Factor. However, the true mechanism underlying the occurrence of the DIF is still a subject of continued debate. As far as dynamic compression is concerned, various analytical and numerical studies in more recent years, as well as the analysis using the 3D mesoscale model in Chapter 7, suggest that the lateral inertial confinement plays a key role in the enhancement of the dynamic compressive strength.

In this section the current 2D mesoscale model with cohesive plus contact interface for the ITZ is employed to simulate the dynamic compression. The aim of this simulation study is to verify the robustness of the combined model for in the dynamic loading conditions. Furthermore, with an explicit representation of the ITZ through the cohesive plus contact model, the model is expected to describe the dynamic fracture process and its influences more directly, and thus provides additional insight into the dynamic behaviour of the concrete material. For a comparison, a 2D homogeneous model and a 2D mesoscale model with equivalent solid ITZ layer are also analysed for the same variation range of the strain rates. To facilitate an unaltered observation of the contribution of the structural inertial effects, all the constituent materials are considered to be rate insensitive, i.e, no embedded strain rate enhancement factor is adopted in the material properties in all the models. This means any increase in the apparent compressive strength of the simulated test specimen is attributable to the structural effect, including the inertial confinement and the dynamic interface contact mechanisms, as well as the material heterogeneities.

A velocity boundary condition as adopted in the quasi-static analysis is also used in the dynamic simulation, but a higher velocity and a shorter time duration is adopted in order to achieve a desirable strain rate.

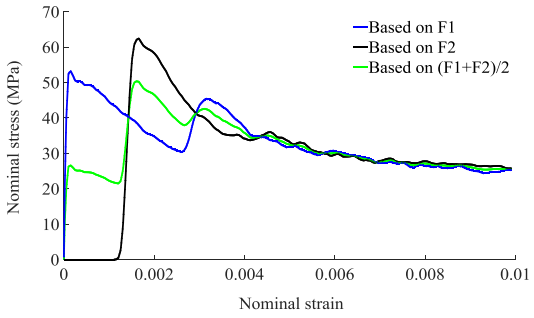

Figure 4.31 Stress-strain responses based on three different methods at rate 50 /s.

In the current numerical experiment, the dimension of concrete specimen is 100 mm for which a strain rate up to about 50 s^{-1} may be considered as acceptable according to Song and Lu (2012). The simulations in the higher strain rate range do not satisfy the stress equilibrium and strain uniformity requirements for the size of the specimen.

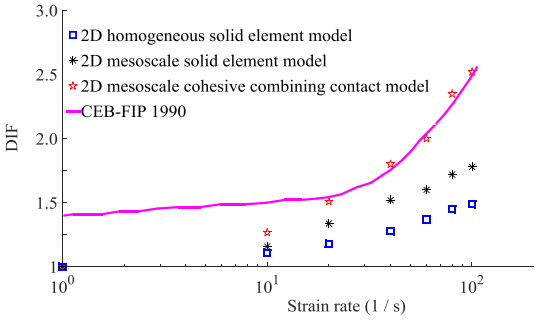

Figure 4.32 Predicted DIF with the strain rate

Thus we only provide the DIF curves up to a strain rate of 100 /s. The nominal dynamic compressive strength is evaluated from the average stress on both the loading (F1) and supporting (F2) faces, and the stress on these two faces is in turn calculated as the total nodal force in the axial direction divided by the cross-section area. As can be seen from Figure 4.31, for the size of the current specimen under a

strain rate of 50 /s, F1 and F2 forces exhibit a clear time lag until after about 0.003s. Nevertheless, the average of the two forces gives a better estimate of the peak strength of the sample specimen.

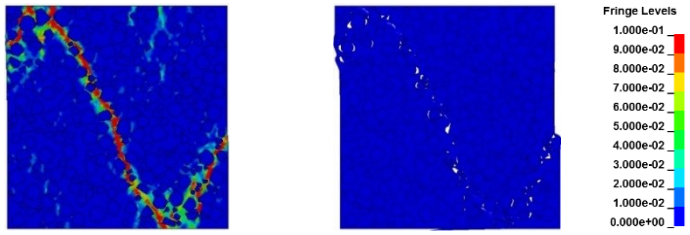

(a) Strain rate 1 /s

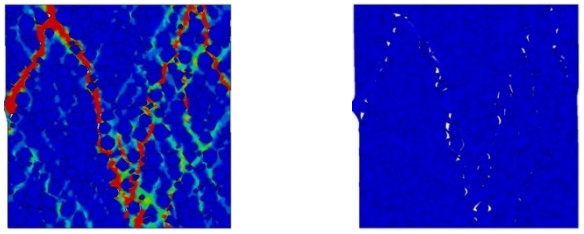

(b) Strain rate 10 /s

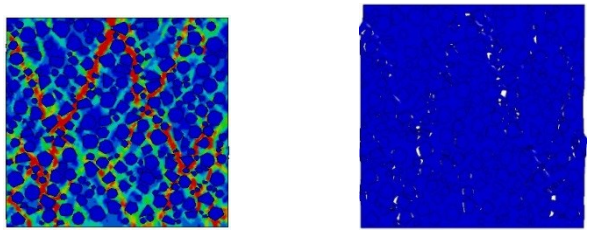

(c) Strain rate 50 /s

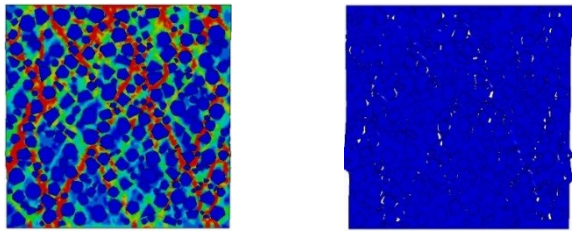

(d) Strain rate 100 /s

Figure 4.33 Damage patterns and final crack patterns under various strain rates

Figure 4.32 plots the DIF values for different levels of the strain rate from the simulation results against the strain rate. The results from using the three different modelling approaches are presented in the same figure for a comparison. One can observe that all models exhibit a significant increase in the nominal compressive strength as the strain rate increases, despite that no strain rate enhancement has been incorporated in the material constitutive model. The general trend of the DIF curves in numerical model resemble well with the curves given by the empirical formula in CEB-FIP (Code 1990). The cohesive plus contact model tends to predict the upper bound DIF among all numerical results, and this is deemed to be attributable to the enhancement of the contact mechanism from the lateral inertial confinements.

Representative damage and crack patterns under various strain rates are provided in Figure 4.33. One can notice that with the increase of the loading rate, the number of micro-cracks also increases. Cracks tend to propagate within the matrix phase bypassing the aggregate inclusions within the strain rate range under consideration.

4.6 Conclusions

In this chapter, a 2D mesoscale concrete model with cohesive plus contact-friction mechanisms for the ITZ has been presented. The contact mechanism is modelled as an independent mechanisms which work alongside the cohesive approach. The general behaviours of the combined model has been verified with relevant numerical tests involved confined shear. The numerical results have shown that the model is capable of representing the physical process of shear resistance under normal compressive pressures. A continuous and smooth transition from nucleation of cracks to the pure fictional state can also be realised with this model.

Parameter investigations have also been conducted to examine the influence of shear properties for the ITZ, for which the experimental data are generally lacking, on the macro responses in concrete experiments. The model is then validated from various aspects by simulating representative experimental scenarios under uniaxial tension, uniaxial compression, and compression with lateral confinement. All the results show consistent agreement with the corresponding experimental observations.

The cohesive plus contact ITZ model is then further applied in the dynamic compression loading cases to examine the strain rate effect. The numerical simulation with the current model predicts the increase of the DIF with the strain rate in a very consistent manner comparing to empirical results such as the CEB-FIP model for the DIF. Comparing with the results from 2D mesoscale FE model with equivalent solid ITZ elements and from the 2D homogeneous FE model, it may concluded that enhancement on the contact mechanisms occur under dynamic compression due to the lateral inertial confinement and this brings in a further contribution to the DIFs of the compressive strength of concrete.

It should be noted that in the current mesoscale model, the cohesive plus contact model has been employed only for the ITZ layer surrounding the aggregates. This approach can explicitly simulate fracture and fracture-induced discontinuity across the ITZ, which constitutes the key damage process in concrete under general loading conditions. However, ultimately the fracture and damage within concrete can extend into the mortar matrix and even into the aggregates under certain loading conditions. One such scenario is fracture of concrete under dynamic tensile loading, in which case crack can propagate through the mortar and aggregates when the loading rate becomes extremely high, and this means cracking and friction mechanisms are no longer limited at the interface between aggregates and mortar matrix. Furthermore, in such a case fractures can spread throughout the entire specimen. To facilitate a realistic simulation of fracture process in concrete in a more robust manner, a model allowing for discontinuity and friction mechanisms to develop potentially along all the mesh grid lines for all three mesoscale parts, i.e. aggregates, mortar and ITZ, will be needed. The development of such a model within the same general mesoscale framework is presented in the next chapter.

Chapter 5 : Mesoscopic analysis of dynamic fracture of concrete in tension

5.1 Introduction

The dynamic behaviour of concrete has been a subject of continuous research interest over the last few decades. In concrete structures, the behaviour under dynamic loads is complex due to significant sensitivity of concrete to loading rate. Abundant experimental test data (Hughes & Watson 1978; Ross et al. 1995; Grote et al. 2001a; Klepaczko & Brara 2001; Schuler et al. 2006; Weerheijm & Van Doormaal 2007) show that there is an apparent increase of the dynamic strength and fracture energy, i.e. the so called DIF, when concrete is subjected to high strain (loading) rates both in compression and tension. However as generally recognized, while the DIF in compression may largely be attributed to the involvement (Zheng & Li 2004; Erzar & Forquin 2011a) of inertia-induced radial confinement (Donze et al. 1999; Li & Meng 2003; Zhou & Hao 2008a; Lu et al. 2010), the mechanism behind the increase of the dynamic tensile strength and fracture energy is not clear. The limitation comes from the difficulties in the test setup and instrumentation on experimentally studying the dynamic tensile behaviour of concrete. Thus little reliable experimental data under dynamic tensile loading is available.

Generally three indirect methods employing the Hopkinson bar have been developed to investigate the dynamic tensile behaviour of brittle material like concrete at various range of strain rate, namely direct dynamic tensile test, splitting test technique and spalling test work (Forquin et al. 2013). Although all the experimental investigations arrive at the conclusion that there is a definite link between the loading rate and the exhibited response of the specimen, the limitation of the experimental technique itself as well as the composite nature of the concrete material make it very difficult to truly understand the behaviour of concrete structures under dynamic tension. Therefore numerical simulation in which the influence of individual parameters can be studied separately in more detail can be helpful.

Various numerical models which aim to reproduce the experimental setup have been developed to predict the response of concrete under dynamic tensile loading. However, the key factor of successfully predicting the dynamic response of concrete structures from numerical simulation is to select a realistic material model (constitutive relationship). Up to date many constitutive models, treating concrete as a continuum, have been employed, for example, visco-elastic-plastic model (Barpi 2004; Pedersen et al. 2008), rate-dependent (or independent) damage model (Cotsovos & Pavlović 2008; Tu & Lu 2011) , micro-crack plane model (Ožbolt et al. 2013; 2014; 2015) and cohesive crack model (Ruiz et al. 2001; Snozzi et al. 2011; Pyo & El-Tawil 2013) etc. Depending on the model used, different hypotheses have been proposed to interpret the mechanism behind the progressive increase of experimentally measured resistance under dynamic tensile loading, which will be given in more detail below. However the key questions are directed on (i) is the strength enhancement really a material property or rather due to some structure effects? (ii) is it necessary to consider the dynamic tensile strength enhancement in the material constitutive relationship and should the consideration be different for different types of analysis models?

Cotsovos and Pavlović (2008) performed a direct dynamic tension simulation on concrete prism with a non-linear rate-independent constitutive model. Based on their results they suggest that the effect of strain rate on the specimen behaviour must be viewed as a structure effect which is directly linked to the axial inertial effect of its mass and the boundary conditions instead of intrinsic material property. Most recently (Ožbolt et al. 2013; 2014; 2015) conducted a series of numerical simulations to investigate the dynamic fracture of concrete in tension using micro-plane constitutive model in which rate dependency is considered to be related to growing micro-cracks and viscocity. Based on the results they proposed that the apparent strength enhancement at relatively high loading rate should consist of two contributions, namely the true material strength which is controlled by the rate dependent constitutive law and the inertial structure effect which develops automatically from dynamic analysis. They also concluded that the results of any indirect tension test such as split Hopkinson bar test need careful interpretation since the apparent strength recorded from experiments may mix up with true material

strength and the inertial effect. While the inertial effect at micro-crack level may delay the initiation and growth of micro-cracks, the structural inertial effect at macro-cracks level could affect the crack propagation directions and velocities and then further significantly change the structural response.

On the other hand, Barpi (2004) used a viscoplasticity based model, in which a viscosity parameter is defined as a function of strain rate, to describe the dynamic mechanical properties of concrete under splitting test. Their results suggest that viscosity should be the key reason for the increase of DIF in tension. A similar argument has been made by Henz et al. (2004a) who developed a 3D discrete element method to simulate the dynamic loading under both compression and tension with Split Hopkinson Pressure Bar. They reported that while the DIF in compression can be largely explained by inertial-based hypothesis (structure effect) the DIF in tension cannot be explained by inertial alone and the rate sensitivity in dynamic tension is more a material intrinsic effect (material property).

Lu and Li (2011) simulated three indirect dynamic testing apparatus, direct dynamic tensile test, dynamic splitting test and spalling test by numerical modelling with a homogeneous rate-independent concrete damage model. It was found that the numerical results from these three types of dynamic tensile tests do not show any strain-rate dependency. Hence they concluded that the strain rate enhancement of the tensile strength observed in dynamic tensile tests is a genuine material effect. They further conducted a qualitative study on a micro-mechanism model and concluded that micro crack inertia and material property heterogeneity could be the intrinsic mechanisms responsible for DIF.

Another qualitative study which investigated the relationship between crack velocity and strain rate response of concrete was conducted in by (Pyo & El-Tawil 2013). Their results suggested that the strain rate sensitivity of concrete material was strongly associated with the characteristics of dynamic crack growth, and specially, inertial effects at the boundaries of the crack. Post-mortem analysis conducted on experimental tests revealed an important increase of cracking density with strain rate. The density of micro-cracking increases with increasing loading rate, but only beyond a certain threshold. The interaction of multiple cracking would affect the

stress field of the crack tip and then further reduce the stress intensity factor around each crack tip, which would finally increase the resistance of concrete specimens.

Despite the debates there are still some consensuses:

1. The key difference between the response to static and dynamic loading is 'time' (Weerheijm & Forquin 2013). The fracture process develops in the heterogeneous concrete material with different timescales in static and dynamic loading conditions. Thus the failure mechanisms including the structural response and the material response can be affected by 'time'.

2. Under relatively low strain rate, up to the order of 1 /s, some weak strain rate sensitivity of concrete-like material under both tension and compression occur and this may be attributed to the free water that is present inside the nano-pores of the material (Zheng & Li 2004; Erzar & Forquin 2011b). The water content causes an internal viscosity and delays crack propagation which is so called Stefan effect. However the Stefan effect plays little role or even vanishes beyond a certain loading rate (1-10 /s). The influence of the 'Stefan effect' is excluded from the present study since only high strain rate well above 1/s is of interest here. Moreover modelling of the Stefan effect would require representation of free water content which is not within the remit of the present mesoscale model.

3. Under relatively higher strain rate above the order of 1 /s, the inertial effects at both micro- and macro- crack levels could be increasingly responsible for the increase of DIF. These inertial effects would be activated as a consequence of cracking of concrete.

4. The natural compositions of concretes i.e. the material property heterogeneity may also affect the dynamic behaviour of concrete (Song & Lu 2012).

It is therefore envisaged that a multiscale modelling simulation with consideration of both the cracks inception and the material property heterogeneity can provide comprehensive insight into the dynamic behaviour and tensile strength enhancement in concrete-like materials.

In this chapter a mesoscale model incorporating the cohesive element model, which extends from the model presented in Chapter 4, is developed to study the influences of the two key influencing factors described above on DIF in tension. In the model, the heterogeneity of the concrete material is considered by modelling the concrete specimen as a composite material consisting of three different components, namely coarse aggregates, mortar matrix and the interface between the aggregates and the mortar matrix (ITZ). The inception of cracks is implemented by inserting a zero-thickness cohesive element between all bulk elements in the mesoscale structure. The initiation and propagation of cracks can be modelled as a gradual loss of the cohesive strength with increasing separation along the mesh lines which are considered as potential crack lines. The cohesive law is set to be rate-independent following the conclusion in (Ruiz et al. 2001) where an intrinsic time scale is proved to be endowed in cohesive theories. This intrinsic time scale permits the material to discriminate between slow and fast loading rates and ultimately allows for the accurate prediction of dynamic fracture properties in materials like concrete.

The chapter is organised as follows. In Section 5.2, a robust 2D mesoscale cohesive elements model is developed in which cohesive elements are incorporated along all mesh grid lines to accommodate free development of fractures. A major focus is placed on developing an algorithm to insert cohesive elements between each pair of bulk elements in an original mesoscale structure and to identify their material attributes. For the numerical investigation, a direct dynamic tension loading method as proposed in (Miller et al. 1999) is adopted, which can effectively avoid stress wave propagation from the boundaries and early fracture near the boundaries. A parameter investigations is given in Section 5.3. In Section 5.4, the dynamic responses of concrete specimen and the mechanisms behind these responses are investigated and discussed based on the numerical results. In order to better understand the underlying contributors to the DIF from the perspective of the mesoscale with cohesive element model, three comparable models, namely homogeneous bulk element model, homogeneous cohesive element model and mesoscale bulk element model are also presented for a comparative analysis in Section 5.5. On this basis, the influences of the inertial effect from cracking and the material heterogeneity are discussed and identified individually. Finally some

concluding remarks and recommendations based on the numerical investigations are presented in Section 5.6.

5.2 Finite element model

5.2.1 Meso-structure generation

The generation of the random meso-structure in the concrete specimen both in 2D and 3D have already been presented in detail in the previous chapters. For the present study on the dynamic tension of concrete, previous evidences have pointed out that the dynamic inertial confinement, which is of a 3D nature, has little effect on the DIF in tension (Barpi 2004; Tu & Lu 2011). Therefore it is considered rational to opt to the use of 2D mesoscale model while maximizing the involvement of the cohesive descriptions.

The general steps in generating the basic 2D meso-structure with aggregates and the mortar matrix follow exactly the approach used in Chapter 4. For the cohesive cracking model, the evolved shape of a crack will be dependent upon the initial mesh grids. Although in a mesoscale model the overall shape of a crack may always be captured in a reasonable manner because of the fine mesh resolution needed for the mesoscale structure, triangular elements are preferred so that the detailed crack paths could be simulated more realistically. Figure 5.1 gives the meshed elements for aggregate and mortar components.

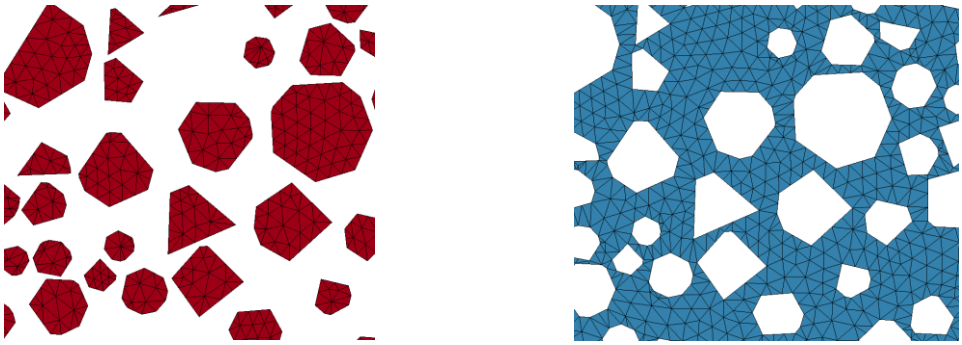

Aggregates Mortar matrix

Figure 5.1 Meso-structure of concrete model (Partial region)

5.2.2 Algorithm for insertion of Cohesive interface elements

The fracture mechanism of concrete under dynamic tension is more complex than in static loading. Previous experimental results reveal that cracking is no longer limited to developing in close connection with the ITZ but also run through mortar matrix and even the aggregate particles in high strain rate loading (Brara & Klepaczko 2006; Vegt et al. 2007; Zhang et al. 2015). Thus for a mesoscale model to fully capture all possible cracking routes, it is necessary to develop a model with possible discontinuity along all the mesh girds for all three parts, i.e. aggregates, mortar and ITZ.

In the present mesoscale model with cohesive interface elements, three different types of cohesive elements, namely the aggregate-aggregate (intra-aggregate) interface element, the mortar-mortar (intra-mortar) interface element and the aggregate-mortar interface element, can be identified according to the meso-structure of the concrete model. An algorithm is developed for the above-mentioned identification and cohesive element insertion. The procedure is performed with an in-house program coded with MATLAB. The proposed algorithm involves the following steps:

1. Obtaining the nodes and elements files; in the present study these are generated using ANSYS pre-processor;

2. Reading nodal coordinates, element connectivity arrays and then for each existing node i, identifying the number of solid elements, n_i, which share this node;

3. Duplicating nodes. For each original node i, (n_i-1) number of nodes are duplicated with the same coordinates of the node i. Creating an array *Nodes[i][j]* to store such duplicated nodes and corresponding original node at the same location, with *j=1* to *n*. And the original node *i* is stored in *Nodes[i][1]* while the duplicated nodes are stored in *Nodes[i][2]* to *Nodes[i][n]*.

4. Discretizing solid elements. For each original node *i,* loop over the number of solid elements, *n*, sharing this node. The first element using node *i* will keep its nodal connectivity unchanged. However for the second to the *n*-th solid element, the node *i* in the original connectivity will be replaced by the duplicated *Nodes[i][2]* to *Nodes[i][n]* respectively. This discretizing process will be implemented to all the original nodes.

5. Inserting cohesive elements. After updating all the nodal connectivity of the solid elements, all individual solid elements become discrete (dis-connected) units. A zero-thickness interface element is therefore used to connect two adjacent solid elements. This is done using an array *Edges[M][K],* which stores all the boundary edges of discrete elements where *M, K* is the element number and the index of edges of this element respectively. For each edge *K* in a discrete element *M,* there are two nodes *I* and *J* being connected by it. There should be one and only one edge K^* in other discrete elements *N* which connects two nodes I^* and J^* which have the same locations as nodes *I* and *J,* respectively. Inserting one interface element between two solid elements *M* and *N* with connectivity as $[I, J, I^*, J^*]$. Loop over all the edges of each discrete element, and then cohesive element can be inserted between each two adjacent discrete elements. Note if an edge is on the external boundary or it has already been treated, the process will continue to next edge. The sketch of a simple example on discretizing solid element and inserting cohesive element between two solid elements are shown in Figure 5.2.

6. Identifying material attributions for interface elements. After inserting interface element on each mesh line, it needs to identify the material type for each interface element according to the meso-structure of the concrete specimen. Firstly, subdividing the element file into three arrays AGG_ELE, MOR_ELE, and INT_ELE, which contain aggregate solid elements, mortar solid elements and the inserted cohesive elements respectively. Then loop over the number of interface elements, identifying the material type of the cohesive element one by one. If all nodes in an interface elements are shared by a solid element in AGG_ELE, the cohesive element is given the

aggregate-aggregate interface properties. Similarly, if all nodes in an interface element are contained by a solid element in MOR_ELE, then the interface element will be treated as a mortar-mortar interface element. The remaining interface elements which share part nodes with solid elements in AGG_ELE but also contain nodes in solid element in MOR_ELE will be aggregate-mortar interface elements and will be given the ITZ properties accordingly.

7. Creating input file for the analysis solver, herein LS-DYNA. Note that the above procedure is implemented based on a 2D plane condition in which, a line with duplicated nodes is used to model the interface element. However the cohesive constitutive material model used in LS-DYNA is restricted to 3D solid elements. To cater to this situation, the current 2D mesoscale model is analysed in a thin plate configuration, with a single layer of elements in the out-of-plane direction. Therefore nodes in this plane are further duplicated to form another plane. The nodes in the original plane and the nodes in the duplicated plane will form 3D solid elements. However it should be pointed out here that the nodal connectivity of a standard brick element and a cohesive element in LS-DYNA input file are totally different. The detail order of the nodal connectivity for each element can be referred to description in Chapter 5.

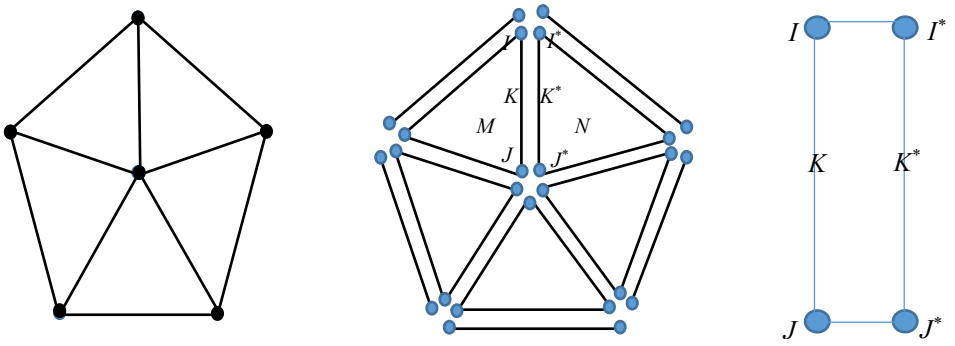

(a) Initial mesh (b) Discretizing solid element (c) Forming cohesive element

Figure 5.2 Sketch of inserting cohesive element in the initial mesh

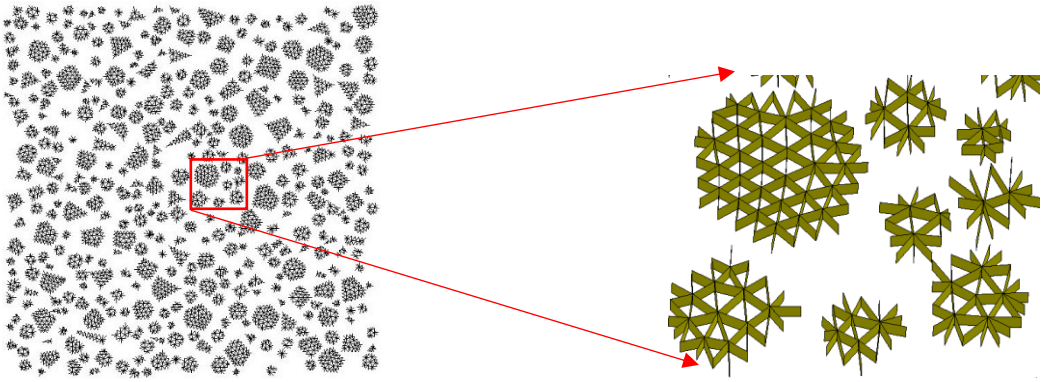

(a) Aggregate-aggregate interface elements

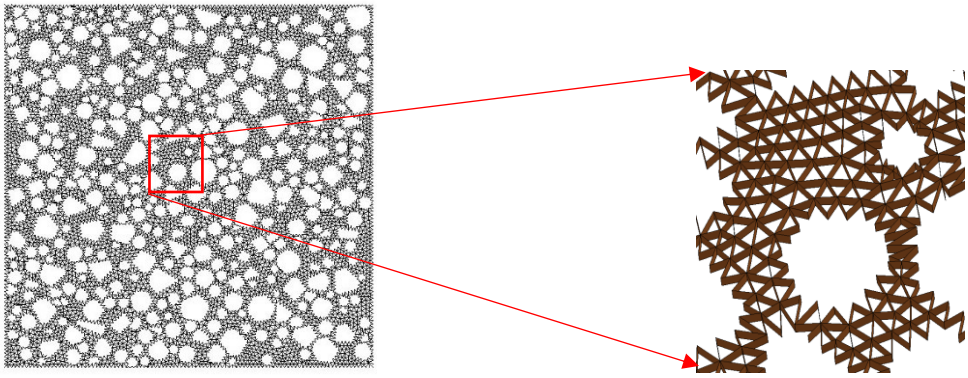

(b) Mortar-mortar interface elements

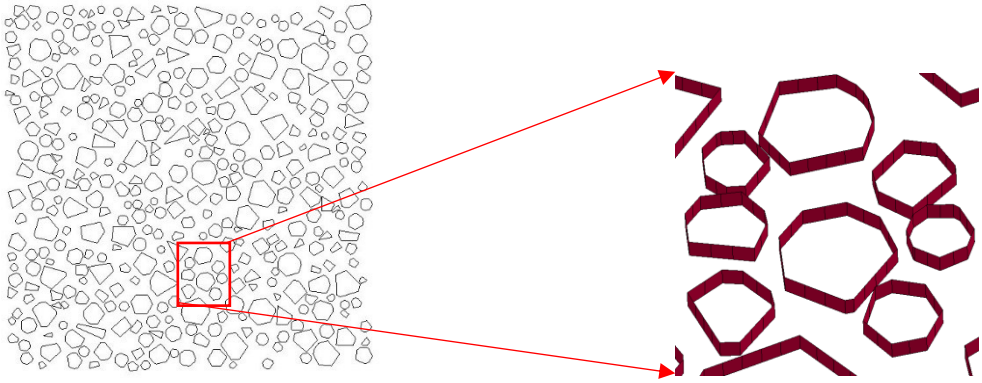

(c) Aggregate-mortar interface elements

Figure 5.3 Interface elements for three independent components

Figure 5.3 shows the insertion and identification process and the results for the three material types of cohesive element.

5.2.3 Material models

In the present study we postulate that the cracking procedure as well as the nonlinear behaviour of concrete develops only through fractures, and thus in the model they are governed by a constitutive relation between traction and opening displacement in the cohesive elements. The bulk material outside the cohesive zone remains undamaged and it continues to behave linear elastically. This is to say, a simple linear elastic material model is used for brick element while a nonlinear cohesive constitutive model is attributed to the zero-thickness interface elements. Therefore a suitable selection of the material constitutive model for the cohesive elements is a key to reproduce reliably the damage processes in current numerical model. The bilinear cohesive constitutive material model used in Chapter 4 is adopted again in present study due to its simple but efficient function. It considers the irreversible damage and allows for independent definitions of the constitutive relations for different fracture modes of tension and shear (see Figure 5.4).

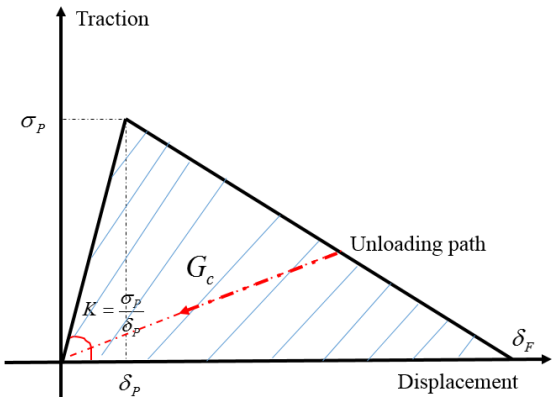

Figure 5.4 Cohesive constitutive model in pure mode

The linear stiffness of the bilinear cohesive model is defined as σ_P/δ_P , and this is followed by a linear softening during the damage (post peak). Thus a simple relationship exists between the energy release rate G_C, the peak traction σ_P, and the ultimate displacement (at zero traction) δ_F as:

$$G_C = \sigma_P \times \delta_F / 2 \tag{5.1}$$

The cohesive model can also simulate the complex fracture behaviour by combining normal and shear traction components together. As suggested by (Gerlach et al. 2005), the detailed coupling between two independent modes may be described as shown in Figure 5.5. $\sigma_I^P, \sigma_{II}^P$ and σ_M^P are the pure mode-I, the pure mode-II and the mixed-mode traction when fracture initiates and δ_I^P, δ_{II}^P, δ_M^P are their corresponding displacement respectively. The displacement in pure mode-I, pure mode-II and mixed-mode when cohesion is completely lost (interface is separated) are denoted by $\delta_I^F, \delta_{II}^F, \delta_M^F$ respectively. G_{IC} and G_{IIC} are the fracture energy release rate in mode-I and mode-II respectively. The detailed coupling law between independent mode-I and Mode-II fractures can be found in Chapter 4.

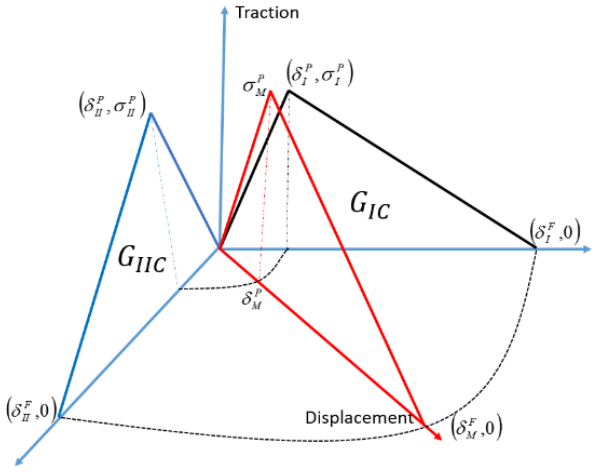

Figure 5.5 Cohesive constitutive model in mixed mode (Gerlach et al. 2005)

It should be noted that the damage of the cohesive element initiates when the traction reaches a criterion established in term of the tractions in pure mode-I and mode-II. But the fracture process is usually controlled by the fracture toughness which is a measurement of the energy required for a crack to grow in nonlinear materials like concrete. This means a crack can only propagate when the fracture energy release rate reaches a critical value G_C. Therefore the cohesive constitutive law incorporating with the critical energy release rate introduces a length scale, named cohesive zone length l_{cz} into the material description (Hillerborg et al. 1976; Ruiz et al. 2001). The

cohesive zone length is measured as the distance from the crack tip to the point where the maximum cohesive traction is attained. Many approaches have been proposed to predict the length of the cohesive zone, and a general form can be written as

$$l_{cz} = \kappa E \frac{G_C}{\sigma_P^2} \tag{5.2}$$

where E is the Young's modulus of the bulk material, G_C is the critical fracture energy, σ_{Peak} is the maximum interfacial strength, and κ is a parameter with a general value around 1 (Hillerborg et al. 1976). Camacho and Ortiz (1996) further noted that in the cohesive constitutive model an intrinsic time scale t_c can be introduced as a material description. This intrinsic time can be expressed as

$$t_c = \frac{\rho c \delta_F}{2\sigma_P} \tag{5.3}$$

where ρ is the mass density and c the longitudinal wave speed. Thus the cohesive material model endows the ability to discriminate the fast and slow loading rates by comparing the pulse duration τ and the characteristic time t_c. This means that if the pulse duration $\tau \gg t_c$, the material model would consider it as a quasi-static loading case and behaves a quasi-static loading response, and on the contrary, if the pulse duration $\tau \ll t_c$, the cohesive material model can also identify it as a very fast dynamic loading case and then shows up dynamic behaviour of the material. Therefore some special features of the dynamic behaviour of the brittle materials, such as micro-crack initiation time, crack propagation speeds, the failure patterns and ultimately the dynamic strength of brittle solids on loading rate may be well reproduced from the cohesive constitutive model (Ruiz et al. 2001).

5.3 Model setup

5.3.1 Specimen geometry and loading method

The concrete specimen used in the present study is a square (representing a cubic specimen) with a side length equal to 100 mm. The aggregate volume ratio in the specimen is around 45% with the maximum aggregate size around 8 mm. The

samples are loaded under displacement control with an imposed strain rate. A constant velocity boundaries v_0 are applied on both the top and bottom edges as illustrated in Figure 5.6.

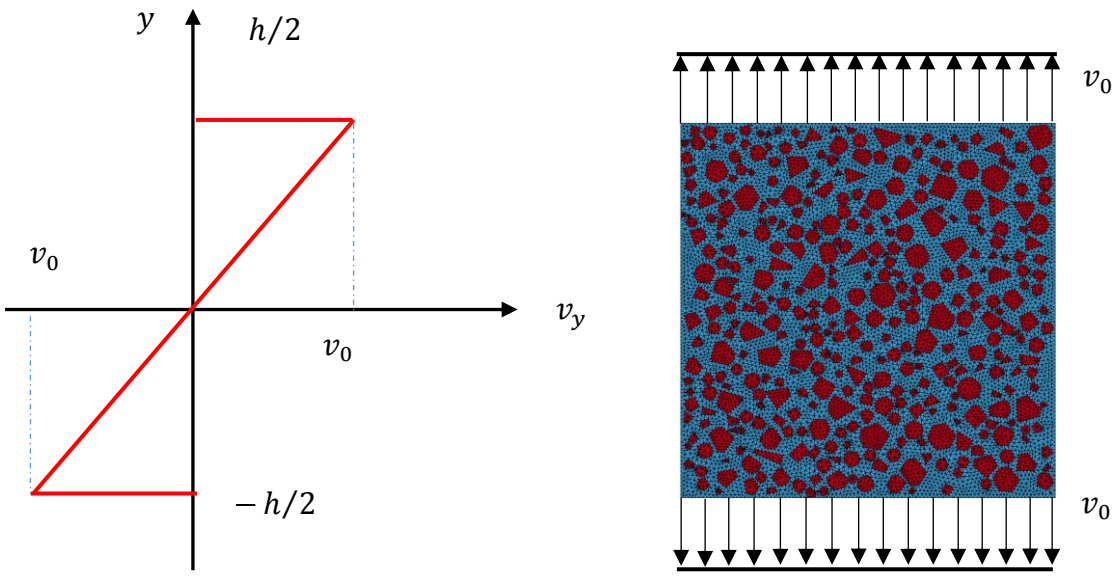

Figure 5.6 Boundary conditions for dynamic tension

However it should be noted that it is very difficult to test a concrete material under dynamic tensile loading directly owing to a very low tensile failure strain. Conventional testing apparatuses such as high speed hydraulic presses or Split Hopkinson Bar with the consideration of the stress wave propagation are mostly used. In the present study with a numerical simulation, we opt to directly applying the tensile loading on the boundary of the specimen to facilitate direct observations. A special treatment is used to avoid stress wave reverberation and an early failure near the boundary, such that all nodes in the FE model are prescribed an initial velocity according to a prescribed distribution along the specimen length, shown in Figure 5.6, as has been adopted in previous studies ((Miller et al. 1999). For a linear distribution of velocity we have:

$$v_y(y) = \frac{2v_0}{h} y \tag{5.4}$$

where v_0 is the loading velocity applied on the upper and lower boundary of the specimen and its value can be dependent on the imposed strain rate. h and y are the height (length) of the specimen, the vertical coordinate value of node in FE model respectively.

5.3.2 Material properties for mesoscale structure

The meso-mechanical approach requires defining the material properties for every constituent material component. As described earlier, the bulk elements in the concrete specimen should resemble the continuum properties before cracking while the cohesive elements accommodate the fracture process, or in other words damage. Therefore the bulk elements are modelled only with simple linear elastic material model while the zero-thickness cohesive element is assigned with a non-linear cohesive constitutive relation in terms of traction and opening displacement. The basic material properties for the aggregates and the mortar matrix are summarised in Table 5.1. These values are generic and suitable for a normal concrete with a static tensile strength of 3.5 MPa (López et al. 2008b).

Table 5.1 Material properties for the bulk element

Component	Density $\boldsymbol{\rho}$ (kg/mm^3)	Young's modulus $\boldsymbol{E}$ (MPa)	Poisson's ratio $\boldsymbol{\nu}$ (--)
Aggregate	2600	7000	0.2
Mortar	2300	3000	0.2

From Chapter 4, it has already been explained that the setting of the material parameters in the bilinear cohesive constitutive model can be very simple and straightforward. Only some key parameters such as the initial stiffness K_N, K_S, the peak traction σ_I^P, σ_{II}^P, and the fracture energy release rate G_{IC} and G_{IIC} in mode-I and mode-II respectively, need to be identified. While the peak traction and the fracture energy in Mode-I, σ_I^P, G_{IC} can be directly obtained from representative experiments for most engineering materials, the corresponding values in the shear direction may need extensive parameter studies for a specialised material due to a lack of the

relative experimental data. In the present study, the material properties in tension for the three independent interface components are directly determined on the basis of experimental data (for instance, Rosselló et al. 2006) taking into consideration of the suggested values from previous numerical work (for instance, López et al. 2008b). The shear properties for the three independent interfaces are set according to the studies in the last chapter where the shear strength and the shear fracture energy are reported to be 4 times of tensile strength and 10 times of the tensile fracture energy respectively. The detail material parameter values used for the three different interfaces are summarised in Table 5.2. One may also note that the properties of ITZ in present study are set at 50% of the mortar properties as generally accepted (see Chapter 4).

Table 5.2 Properties for the three interface components

Component	Tensile strength σ_I^P (MPa)	Fracture energy G_{IC} (N/mm)	Shear strength σ_{II}^P (MPa)	Fracture energy G_{IIC} (N/mm)
Aggregate-aggregate	16	0.08	64	0.8
Mortar-mortar	4.7	0.06	18.8	0.6
Aggregate-mortar	2.3	0.03	9.2	0.3

5.3.3 Parameters setting

5.3.3.1 Mesh size

As discussed in Chapter 4, the mesh size within the cohesive zone could have significant influence of the global response of the concrete specimen. General convergent value has been obtained in quasi-static loading cases (see Chapter 4). However the response of concrete in dynamic loading is more complex due to the involvement of the stress wave as well as the crack propagation speed. Because of the extremely short duration of the resulting waves the crack propagations is accomplished through the grid size in a numerical model, the numerical results may

be more sensitive to the element size. Previous numerical simulations (Gebre-Egzeabher 2010) show that a mesh size which fits to one dynamic impact might not be appropriate for another case, and this suggests that satisfying the convergence criterion in a quasi-static loading case may not be enough to guarantee a converging result in a dynamic loading case. For these reasons, in this section numerical tests with different mesh sizes under various loading rates will be presented to investigate the mesh size effect and to seek for an effective mesh size in the dynamic loading cases. Figure 5.7 shows the convergence results for tensile loadings under four different strain rates, namely, $\dot{\varepsilon} = 1$ s^{-1}, 100 s^{-1}, 400 s^{-1} and 1000 s^{-1}, in terms of nominal strength against mesh size. In order to eliminate any influence introduced by the initial stiffness of the cohesive element (see Eq. 4.5), while ensuring a minimum artificial compliance of intrinsic cohesive element (see Chapter 4), a constant but sufficiently large stiffness $K_N = K_S = 2\times10^7$ MPa / mm is used for all the cases.

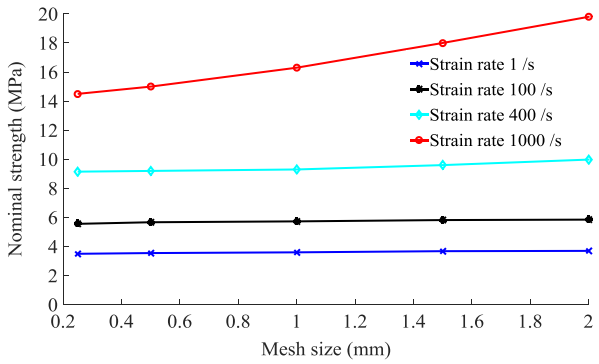

Figure 5.7 Mesh size effect under different loading rates

From Figure 5.7, it can be clearly observed that the present model is satisfactorily insensitive to the mesh size except for very high strain rates. Using a mesh grid size of 1 mm appears to be good enough even for a high strain rate of 400 /s. For ultra-high strain rates such as 1000 /s, smaller grid size would need to be considered. Based on this result, the mesh size chosen in the present study hereinafter is set to 1 mm taking into consideration of the computational time.

Considering the above mesh grid size and referring to Table 5.2 and Eq. (5.2), where the cohesive zone length for the aggregate-aggregate and mortar-mortar interface

components can be calculated as around 21.8 and 81.5 mm respectively, it may be postulated that the mesh size in dynamic tensile loading case should be at least twenty times smaller than the cohesive zone length of the interface. And this value is much smaller than the suggestion value $h_{mesh} \leq l_{cz}/3$ in most published work where only quasi-static loading condition is considered. It should be noted that the cohesive zone length calculated is at the direction along the crack propagation and the tension properties of the interface element in Table 5.2 are used for this calculation due to the dominant mode-I fracture model in present chapter.

5.3.3.2 Cohesive stiffness

As discussed in the last chapter, the initial stiffness for the intrinsic cohesive element can be a very important parameter which may influence the global response of the cohesive zone model. While small value of the initial stiffness may introduce artificial compliance, an extremely large stiffness may cause other numerical problems such as spurious oscillations of the traction and increasing of the computational time. A general guideline for this parameter may be expressed by the following equation (see detail in Chapter 4):

$$K = \frac{\alpha E}{h_{mesh}} \tag{5.5}$$

where E is the Young's modulus of the bulk material, h_{mesh} is the element mesh size in the cohesive zone, and α is the stiffness parameter which needs to be determined. Eq. (5.5) also implies that the stiffness of the cohesive element may be set appropriately only after the mesh size is determined.

In the last chapter, the suggested value of parameter α is around 50 which is deemed to be a sufficient value to reduce the compliance of the intrinsic cohesion in quasi-static loading cases. This conclusion is further checked herein for dynamic loading cases. For this purpose, the computed results in term of nominal stress and strain in three representative strain rates namely 1 s^{-1}, 100 s^{-1}, and 1000 s^{-1}, which represent a quasi-static loading, a relatively high strain rate loading and an ultra-high strain rate loading condition, respectively, with various values of α for the mesh size 1 mm

are presented in Figure 5.8. The nominal stress is calculated as the upper boundary loading force divided by the initial width while the nominal strain is determined from the displacement on the upper boundary divided by the half height of the specimen.

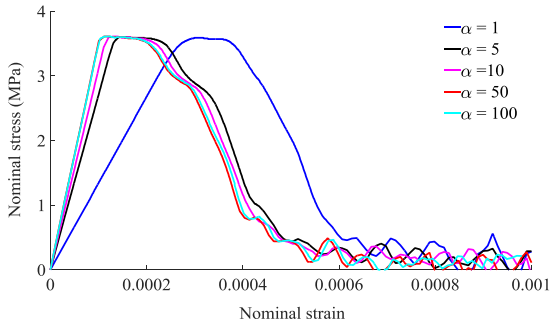

(a) Stiffness on strain rate 1 /s

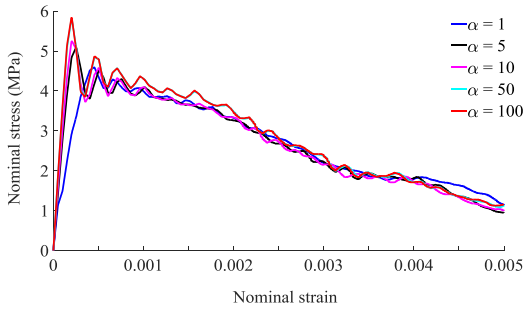

(b) Stiffness on strain rate 100 /s

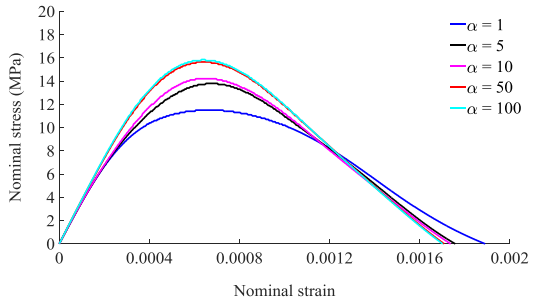

(c) Stiffness on strain rate 1000 /s

Figure 5.8 Stiffness influences under different loading rates

From Figure 5.8, it can be found that the initial cohesive stiffness only influences the global stiffness of the nominal stress-strain curve in the quasi-static loading case (strain rate 1 /s); but it can also affect the dynamic strength in the high loading rates (strain rate 100 /s and 1000 /s). In all cases, however, the use of a value $\alpha = 50$ for the stiffness parameter appears to guarantee a stable and converging result.

Therefore in the present study hereinafter $\alpha = 50$ is adopted. Thus according to Eq. (5.5) and the data in Table 5.2, the stiffness for the interface elements for aggregate-aggregate and mortar-mortar can be subsequently determined, as $K_N = K_S = 3.5 \times 10^6$ MPa / mm (aggregate-aggregate interface) and $K_N = K_S = 1.5 \times 10^6$ MPa / mm (mortar-mortar interface). For the interface element between aggregate and mortar matrix, it is difficult to explicitly calculate the stiffness because of the difficulty in assigning a proper Young's modulus for this region. Therefore a somewhat reduced value from the mortar-mortar interface, being $K_N = K_S = 1.0 \times 10^6$ MPa / mm, is chosen herein.

5.4 Dynamic response in concrete specimen

As stated earlier, concrete materials are very sensitive to the strain rate, especially in tension. However the mechanisms behind its global dynamic behaviour is not clear, and debates are still ongoing as whether it is a material effect or a structure effect, and if both how much may be attributed to each effect. Ožbolt et al. (2014) carried out a simple elastic-cohesive finite element model subjected to direct tension by numerical simulation. The results are evaluated in terms of apparent and true strength where the apparent strength is defined as the resistance strength measured in elastic element while the true strength is recorded as the reaction strength measured in the cohesive element. It is found that under static loads the true and apparent strength are always equal, while under dynamic loads they are different. Hence they concluded that the true strength is the real material response which is controlled by rate dependent constitutive law, but the apparent strength under higher strain rate is actually mixed up with structural inertial effect which is invoked by cracking of concrete. They argued that this inertial influence should be automatically accounted for through dynamic analysis, i.e. it should not be a part of the constitutive law. It is

not a purpose of this study to judge the correctness of this theory. However it should be noted at this juncture again that the structural inertial effect described above is purposely excluded from the present analysis by introducing a specified loading condition as described in Section 5.3.1.

Examination of the response is focused within the mesoscale parts of the model. To facilitate the evaluation of the stress distribution while the stress wave propagates and reflects between the two end face, the mesoscale region is fictitiously divided into seven equal strips along the loading (axial) direction, with a width around 14 mm for each strip, as depicted in Figure 5.9.

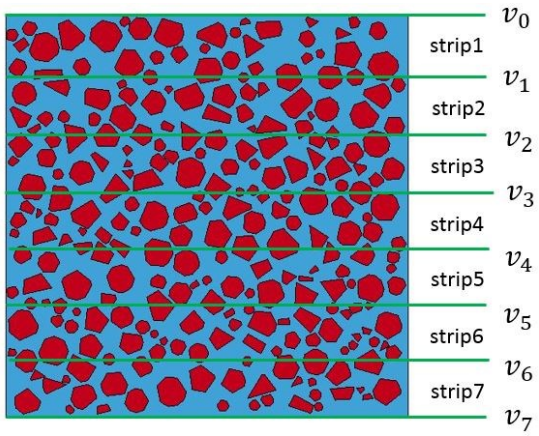

Figure 5.9 Strips to evaluate the stress distribution in the specimen

Figure 5.10 shows the development of (average) axial stress in the five strips for the above three strain rates, respectively along with the corresponding final cracking patterns. The stresses in all the strips show almost the same response under each strain rate. This tends to confirm that a relative uniform stress state could be achieved even for the extremely high strain rate 1000 /s under the artificial loading condition, thus precluding the structural inertial effect proposed in (Ožbolt et al. 2014) from the numerical analysis. Hence if there exhibits any strength enhancement with the increase of strain rate, the mechanism should come from the material effect rather than the structural effect. Actually from the results in Figure 5.10, the dynamic axial strength in individual strips apparently increases with the increase of the strain rate, and so does the number of cracks.

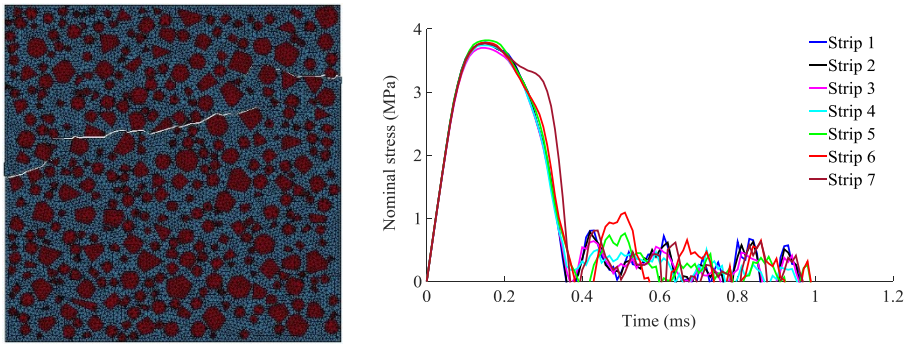

(a) Stresses in strips at strain rate 1/s

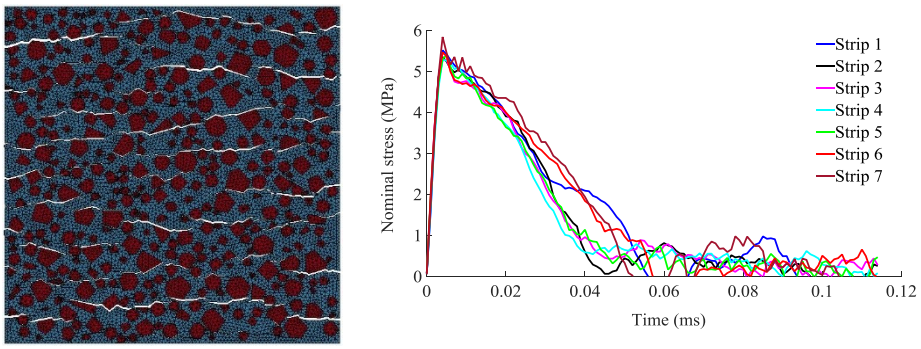

(b) Stresses in strips at strain rate 100/s

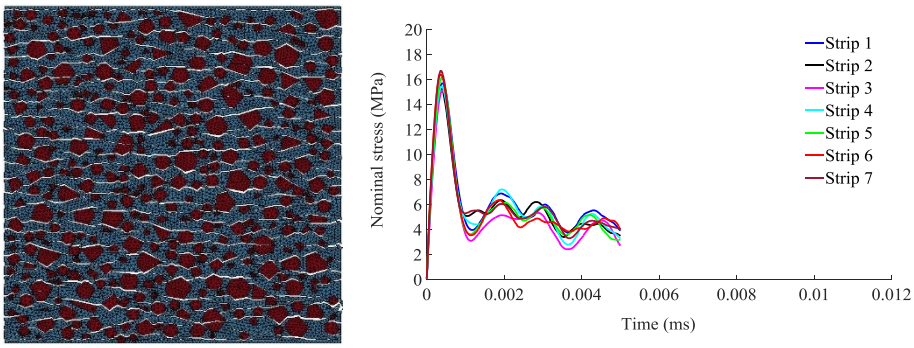

(c) Stresses in strips at strain rate 1000/s

Figure 5.10 Strip stresses and crack patterns under different loading rates

In the area of theoretical research on the dynamic response of concrete at the material level, there are also two kinds of clearly contradictory views. One is based on the visco-elastic-plastic theory (Gary & Bailly 1998), the other one is based on the

fracture and damage mechanics. For the first category, visco-elastic-plastic models are generally established by introducing parameters related to viscoplastic strain rate into the plastic model to describe the dynamic mechanical properties of concrete. For the second category, fracture and damage mechanics principles are used to interpret the dynamic response of concrete. In this approach, the dynamic strength enhancement is related to the inertial effects of the crack initiation and propagation in the specimen (Lu & Li 2011; Pyo & El-Tawil 2013). Moreover, the material heterogeneity is also found to be a factor which can contribute to the difference between the dynamic and static tensile strength, i.e. an increase of in the heterogeneity coefficient leads to an increase in the strain-rate dependency (Ma et al. 2010).

A rate-independent cohesive constitutive material model is used in the present study which means the viscosity behaviour of concrete is not considered. Hence the strength enhancement at higher strain rate from the present numerical simulation should be attributed to the cracking of concrete which can be interpreted with fracture mechanics principle and the material property heterogeneity. The specific mechanism behind the dynamic behaviour in concrete will be discussed in detail in the next section.

5.5 Results and discussion

5.5.1 Comparison models

As stated earlier, the dynamic strengths obtained from the present numerical simulations show significant increase when higher strain rates are imposed (see Figure 5.10). Since the structural inertial effect has been effectively excluded, the observed dynamic strength enhancement is attributable only to the intrinsic material response, herein through the cohesive mechanisms which incorporate inherent time and length scales.

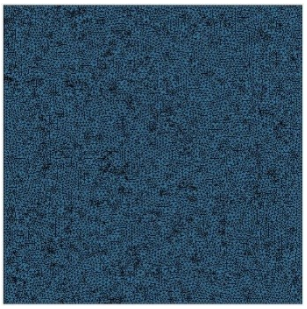

(a) Homogeneous solid element (HS) model

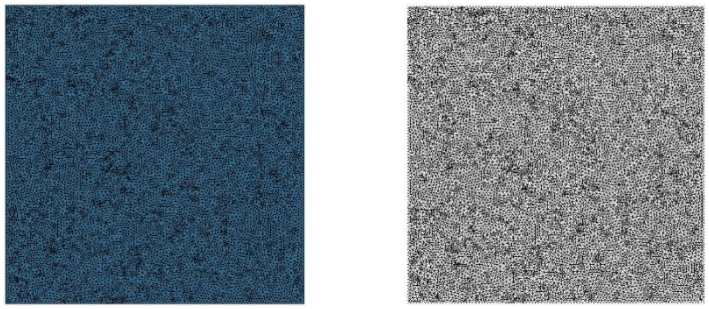

(b) Homogeneous cohesive element (HC) model (left: brick element; right: cohesive element)

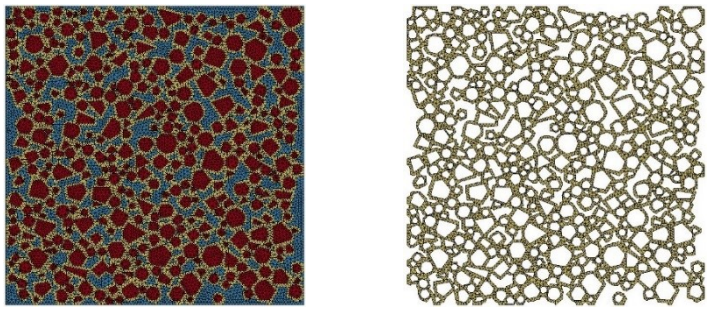

(c) Mesoscale solid element (MS) model (left: meso-structure; right: ITZ element)

Figure 5.11 Three comparison models

Two micro-mechanisms, namely crack propagation and material heterogeneity, are included in the current mesoscale cohesive numerical model. The observed dynamic tensile strength increase (i.e. the DIF) from the numerical results is a result of both contributors. To further demonstrate the individual contribution to the DIF from each mechanism, three comparative models are also presented here, namely a) a homogeneous solid element model (HS model), b) a homogenous cohesive element model (HC model), and c) a mesoscale solid element model (MS model). These

models will be compared with the current mesoscale cohesive element model (MC model).

In order to avoid introducing the mesh size problem among the models, the three comparative models use exactly the same mesh structure as the current mesoscale cohesive element model. For the homogeneous solid element (HS) model, all the elements are assigned the same material properties and the classical K&C concrete damage model in LS-DYNA is used. For the homogeneous cohesive element (HC) model, the bulk elements (mortar and aggregates) are homogenised with uniform material properties, whereas zero-thickness interface element is inserted everywhere between each two bulk elements. Similar to the original mesoscale cohesive element model (MC model), only a very simple linear elastic material model is employed for the bulk elements, and the nonlinear and cracking behaviour are represented by the cohesive constitutive material model. Finally for the mesoscale solid element (MS) model, the elements in aggregate and mortar components are exactly the same as their counterparts in the mesoscale cohesive element (MC) model but the interface component between aggregate and mortar (ITZ) is represent by a layer of solid elements surrounding the aggregate polygon. The detailed FE models are shown in Figure 5.11.

In the models with the cohesive elements (HC and the original MC models), the non-linear response is represented only by the cohesive constitutive model (MAT_138 in LS-DYNA) while the bulk elements are modelled by simple linear elastic properties. In the two solid element models (HS and MS models), the K&C concrete damage model (MAT_72R3 in LS-DYNA) is employed which simulates the macroscopic response of concrete. In order to facilitate a clear comparison, all three additional models described above are calibrated such that they predict the same quasi-static tension strength with the current mesoscale cohesive model. It is noteworthy that no DIF is pre-imposed at the material constitutive level for all models, and this means that any DIF (if indeed occurs) observed from the numerical results is attributable to mechanisms, structural or intrinsic, that develop during the dynamic response than from the rate dependent constitutive law.

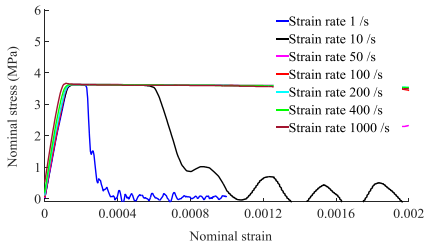

(a) Homogeneous solid element model

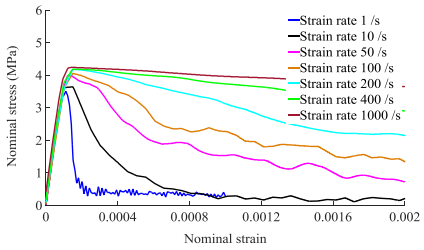

(b) Mesoscale solid element model

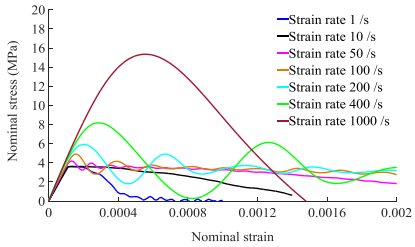

(c) Homogeneous cohesive element model

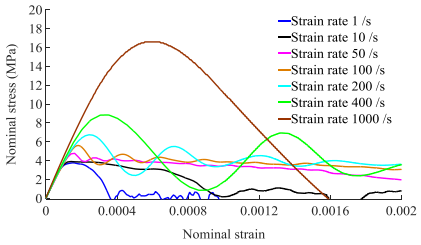

(d) Mesoscale cohesive element model

Figure 5.12 Dynamic tensile responses in four concrete models

Figure 5.12 shows the macroscopic responses in terms of nominal tensile strength and strain under different strain rate loading conditions for all the four models. The numerical results from the mesoscale cohesive element (MC) model, in which the micro mechanisms in term of micro crack inertial effect and the material heterogeneity are explicitly simulated, appears to predict the largest dynamic increase in strength as well as strain energy. The homogeneous cohesive element (HC) model tends to predict similar dynamic tensile response as the MC model but with a reduced dynamic increase effect, and this may be explained by a lack of representation of the heterogeneity in the composite material. On the contrary, there is nearly no strength enhancement under dynamic loading from the homogeneous solid element model in which no intrinsic time-dependent mechanisms are included. Small but noticeable dynamic strength enhancement is observed in the mesoscale solid element model.

The above comparisons suggest that the time-dependent cohesive behaviour and the micro-crack inertial effect, along with the material heterogeneity, are key

mechanisms responsible for the strain-rate sensitivity of the tensile behaviour of concrete-like material. In order to distinguish the specific contribution in the DIF from each of these mechanism, a further analysis of the simulation results is presented in the following sections.

5.5.2 Influence of the mesoscale structure

From Figure 5.13 and Figure 5.14 above, it is clearly observed that the mesoscale structure of the concrete can have a notable contribution on the DIF under dynamic loadings.

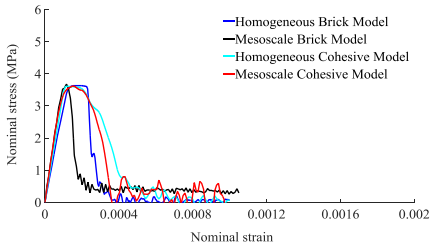

(a) Comparison at strain rate 1 /s

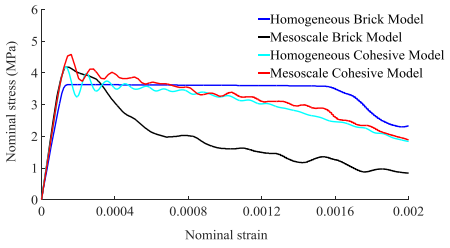

(b) Comparison at strain rate 50 /s

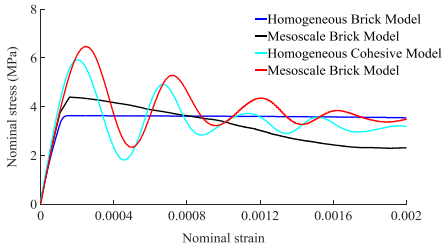

(c) Comparison at strain rate 200/s

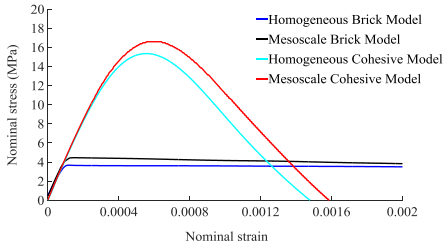

(d) Comparison at strain rate 1000 /s

Figure 5.13 Dynamic tensile response comparison of the four models under different loading rates

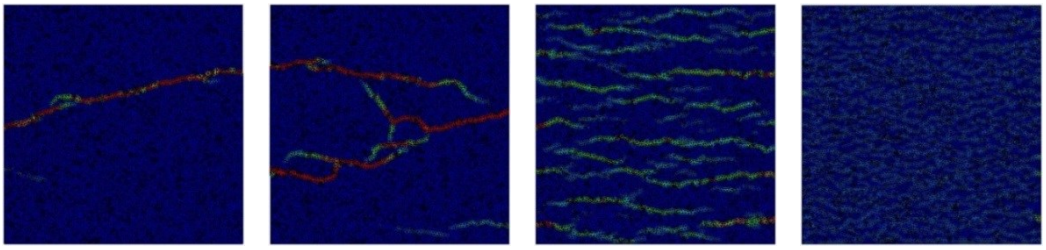

Strain rate 1 /s Strain rate 10 /s Strain rate 100 /s Strain rate 1000 /s

(a) Homogeneous model damage patterns

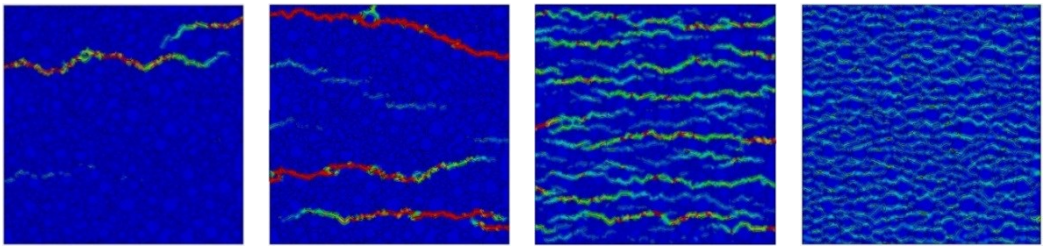

Strain rate 1 /s Strain rate 10 /s Strain rate 100 /s Strain rate 1000 /s

(b) Mesoscale model damage patterns

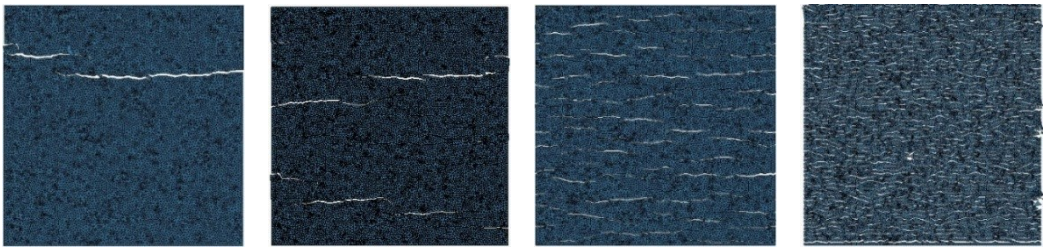

Strain rate 1 /s Strain rate 10 /s Strain rate 100 /s Strain rate 1000 /s

(c) Homogeneous cohesive crack patterns

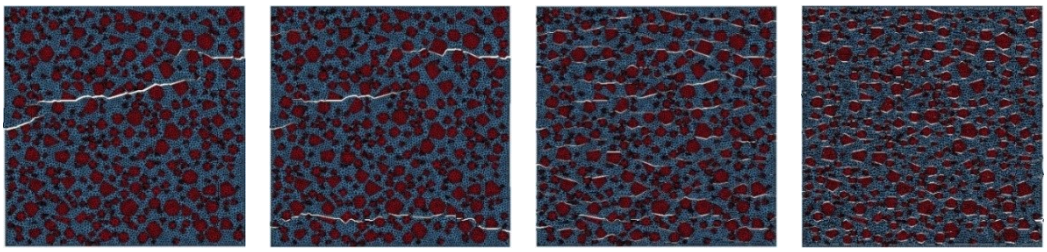

Strain rate 1 /s Strain rate 10 /s Strain rate 100 /s Strain rate 1000 /s

(d) Mesoscale cohesive crack patterns

Figure 5.14 Crack patterns comparison of four concrete models

Under a quasi-static loading, herein represented by a low strain rate case with strain rate of 1 /s, the four different models show almost the same nominal stress strain curves. When the loading rate increases to a moderate strain rate of 10 /s, there is nearly no increase of the nominal strength in the mesoscale solid element model, but a slight increase can be observed in the mesoscale cohesive element model. This tends to suggest that the cohesive element model is more sensitive to the material heterogeneity under dynamic loadings. When the loading rate further increases, for instances at strain rate 100 /s and 1000 /s, the nominal strengths in the two mesoscale models (MC and MS) both show slightly larger increases in the dynamic strength as compared with their respective counterparts in the homogeneous models. From the final failure patterns, the cracks in the mesoscale models exhibit more wavy paths compared with the corresponding homogeneous models. On average the difference in the predicted DIF between a mesoscale model and a homogenous model is on the order of 10%.

The above observations confirm that the material heterogeneity does have an influence on the dynamic response of the concrete. It is also worth noting that the increase magnitude due to the mesoscale structure of concrete appears to be independent of the loading rate in both cohesive element and solid element model. In any event, the degree of increase due to the material heterogeneity is generally limited, the more significant increase of DIF under high loading rates must come from other micro mechanisms, as discussed in what follows.

5.5.3 Influence of cracking in concrete

From Figure 5.13 and Figure 5.14 above, it can also be clearly observed that the nominal strengths in cohesive element models increase significantly while the nominal strengths in solid element models show limited increase when higher loading rates are imposed on the specimens. The underlying difference between the cohesive element model and the solid element models is that the cohesive element model can explicitly simulate the initiation and propagation of cracks through the time-dependent cohesive interfaces. Therefore it is reasonable to postulate that the dynamic resistance increase obtained from the cohesive element models is mainly

due to the micro crack inertial effect on initiation and propagation from micro-mechanic mechanism.

According to the work by (Camacho & Ortiz 1996), the cohesive theories, in addition to building a characteristic cohesive zone length into the material description, endow the cohesive constitutive behaviour with an intrinsic time scale in terms of the longitudinal wave speed and the cohesive material parameters. The cohesive model exhibits different mechanic response when subjected to fast and slow loading rates due to this intrinsic time scale. This sensitivity to the loading rates confers the cohesive models the ability to predict subtle features of the dynamic behaviour of brittle solids, such as crack-growth initiation time and propagation speed and the dependence of the cracking pattern on strain rate. Hence the dynamic strength enhancement under high strain rate are captured in the current cohesive element model.

It is worth mentioning here that a qualitative analysis conducted by (Weerheijm & Forquin 2013) suggested that the micro-crack inertial effect on dynamic strength enhancement can only occur beyond a loading rate $\dot{\sigma} = 5000\ \mathrm{GPa/s}$ ($\dot{\varepsilon} \approx 150\ /\mathrm{s}$) in a concrete material with the maximum aggregate size $d_{aggr} = 10\ \mathrm{mm}$ and tensile strength $f_t = 3\ \mathrm{MPa}$ when a longitudinal speed $C_r = 1800\ \mathrm{m/s}$ is considered. Lu and Li (2011) conducted a similar qualitative analysis based on micro-mechanism model and demonstrated that micro-crack inertia is one of the mechanisms responsible for the increase of the dynamic tensile strength with strain-rate observed in the dynamic tensile tests on concrete-like materials. From their results, the DIF curves as a function strain rate can be separated into two parts. For strain rate up to the order of $\dot{\varepsilon} = 100\ /\mathrm{s}$, the DIF grows slowly with the increase of the strain rate. But when the strain rate is beyond 100 /s, the DIF increases rapidly. This is consistent with the conclusion in (Weerheijm & Forquin 2013) that the micro-crack inertial effect can only dominate the apparent rate dependency of the tensile strength at a relatively high strain rate.

The numerical results in present study well reproduce this tendency with the cohesive element models. As shown in Figure 5.15, the strength enhancement is very

limited at the strain rate up to 100 /s. However when the loading rate further increases, the DIFs show very steep increase and the value reaches around 5 at strain rate 1000 /s.

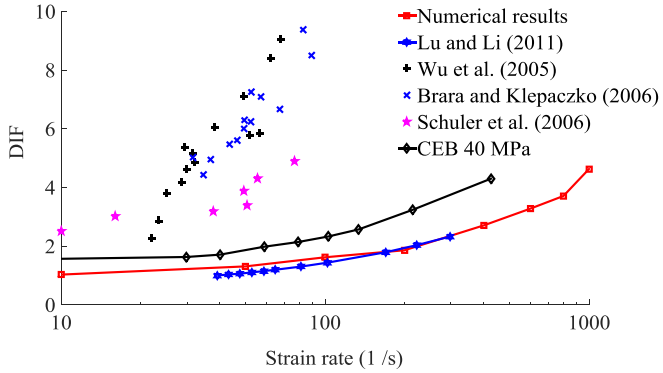

Figure 5.15 Strain rate influence on the tensile strength of concrete

The next micro mechanism behind the dynamic strength enhancement phenomenon could come from the multiple micro-cracks interaction and coalescence in the concrete specimen. It can be observed from the cracking patterns in Figure 5.14 that the number of cracks increases when the loading rate increases. A single major crack can be observed at a low strain rate such as 1 /s, whereas multiple cracks in a distributed manner occur in the specimen at a higher strain rate of order of 100 /s. The transition from a single crack to distributed cracks has a strong influence on the macroscopic behaviour of the concrete. The local stress state is modified around these micro-cracks by a stress-relief wave propagating on both sides of a crack (Weerheijm & Forquin 2013). The rapid release of microscopic tensile stress in the vicinity of the existing micro-cracks acts to delay the coalescence of the cracks in the interaction zone, resulting an increase the peak strength.

However if we further compare the computational results with some representative experimental data, herein collected from (Beton 1993; Wu et al. 2005; Brara & Klepaczko 2006; Schuler et al. 2006), the numerical models appear to still underestimate the total dynamic strength enhancement. Note that the experimental data cover a limited strain rate range up to about 100 s^{-1} (see Figure 5.15). This tends to suggest that the rate-independent (albeit time-dependent with an inherent time

scale) cohesive constitutive model alone does not fully capture the bulk dynamic tensile response in concrete specimens. The total dynamic strength enhancement of concrete may partly be attributable to the rate-dependency in the constituent materials. Nevertheless, the present mesoscale cohesive model has provided systematic insight into the effect of cohesive crack initiation and coalescence on the dynamic behaviour of concrete. Further incorporation of additional factors such as a partially rate dependence in the constitutive descriptions at the constituent material to fit experimental data is a matter of calibration, which will not be discussed in the present study.

5.6 Summary and Concluding Remarks

In this chapter a robust 2D mesoscale cohesive element model is firstly developed, in which cohesive elements are incorporated between all interfaces between the bulk elements. This approach enables an explicit simulation of the crack initiation and propagation in the concrete specimen along the ITZ as well through the bulk elements. Moreover, the model allows the use of simple constitutive description of the bulk materials while nonlinear behaviour is achieved by the cohesive and cracking behaviour through the cohesive elements. As such, the classical mesh-related problems in a continuum-based model for cracking are largely eliminated, making the model highly suitable for investigation of cracking behaviour for both quasi-static and dynamic applications.

Much effort has been devoted to developing an algorithm to insert cohesive element throughout the mesh grids in a concrete specimen, at all interfaces between the bulk elements, and furthermore to identifying the cohesive element properties based on the original mesoscale structure. Parameter studies about the mesh size and the cohesive element stiffness are conducted in order to ensure the generality and reliability of the numerical results.

The model is then employed to investigate the dynamic tensile behaviour under high strain rates. To better understand the micro-mechanism behind the dynamic strength enhancement under dynamic tension as observed from past experimental works, three comparative models, namely a homogenous solid element model, a

homogeneous cohesive element model, and a mesoscale solid element model, are also presented along with the mesoscale cohesive element model. By comparison of the results from all four models under a direct tension loading condition with various loading rates, the following conclusions can be drawn:

1. Cracking through the cohesive mechanism and the micro-inertia effect associated with cracking, as well as the material heterogeneity, are largely responsible for the sensitivity of the dynamic tension resistance, thus contributing to the dynamic increase factor (DIF) of the dynamic tensile strength.

2. Comparison of the results from the homogenous models, including both the homogenous solid element model and the homogenous cohesive element model, with their counterpart mesoscale model, indicates that the material heterogeneity does have an influence on the DIF under dynamic loading; however the degree of influence is generally limited.

3. The intrinsic time scale which is incorporated in the cohesive constitutive model enables the cohesive model to simulate the micro crack inertial effect on the crack initiation and propagation, which manifests as a rate enhancement of the dynamic strength on the strain rate. Such a rate-sensitive mechanism tends to be activated in the present mesoscale cohesive model at a relatively high strain rate in the order of 100 /s. This observation supports the general argument from past studies that there exists a transition of rate-sensitivity which divides the DIF curve into two distinctive segments.

4. The growing distribution of micro cracks with the increase of the loading rate contributes to the enhancement of the dynamic resistance as well as the strain energy.

Chapter 6 : Re-visit of the simulation on size effect using the mesoscale model with cohesive interface model

6.1 Introduction

In Chapter 3, a preliminary investigation into the size effect problem was conducted on notched concrete beams using a continuum-based mesoscale numerical approach. In order to obtain objective results, especially for the evolution of the local fracture process, the damage-plasticity material constitutive model was enhanced by incorporating a characteristic length of micro-structure by means of a non-local theory. However as mentioned in Section 3.4 the numerical results from the nonlocal treatment are highly dependent on the chosen value of the characteristic length and the weighting function, which can be case dependent and hence are not easy to determine.

A more comprehensive numerical framework which incorporates explicit interface descriptions in the mesoscale structure have been developed in Chapter 4 and 5 in this thesis. This model has shown its advantage on modelling the micro-crack initiation and macro-crack propagation during the fracture process in concrete-like materials under various complex loading conditions. In the present chapter, the above model is employed to check against the preliminary conclusions regarding the size effect as obtained previously from the continuum-based model, and to further enhance the understanding about the fracture process and its role in influencing the size effect.

6.2 Numerical model

6.2.1 Geometric properties

As mentioned earlier, the main aim of the study in this chapter is to verify the results obtained from the continuum based framework in Chapter 3 and extend the observations. Thus the experimental test conducted by Wu et al. (2011) are reproduced again with the mesoscale cohesive element model. The geometrical dimensions of the concrete beams and the loading method are set exactly the same as the ones used in the experimental test. The detailed information of the model setup can be found in Table 3.1 in Chapter 3.

The previous studies in Chapter 3 show that the damage zone only localize in a region close to the notch while the remaining part is intact with no damage during the whole loading process in a notched concrete beam under three-point bending. Therefore in the present study, a 'multi-scale' approach is adopted, such that the meso-structure and cohesive contact interface element model is only used in the critical middle regions while the remaining parts of the beam are modelled as homogeneous materials with elastic properties resembling the average response of the concrete. Following the exploration in Chapter 3, the size of the mesoscale region is selected to be $b_{ms} = D$ (see Figure 6.1).

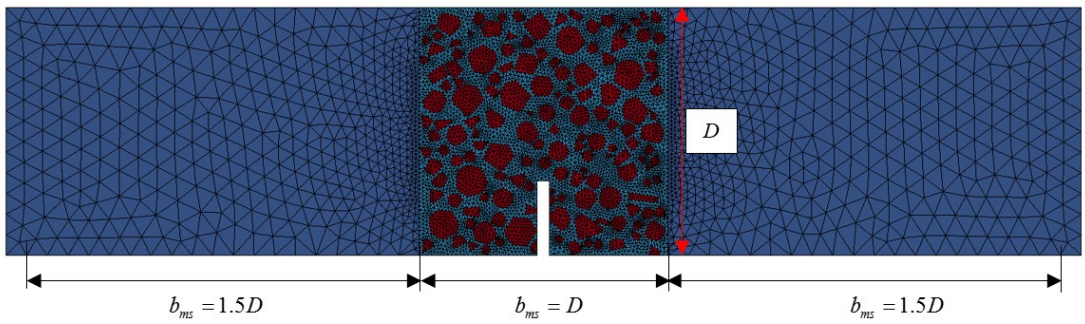

Figure 6.1 Numerical model set up

6.2.2 Meso-structure and interface element insertion

The meso-structure of concrete in terms of the aggregate shape and distribution is exactly the same as that used in Chapter 3. After generation of the mesoscopic geometric structure, ANSYS pre-processor is used to perform the FE-meshing. Triangular elements are used for better tracking the crack propagation path as mentioned in Chapter 5. At this stage, only two components, i.e. aggregate and mortar are modelled. The meshed elements for aggregate and mortar components are shown in Figure 6.2.

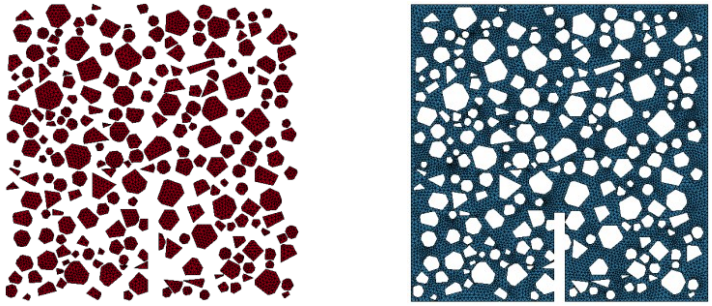

Aggregte elements Mortar elements

Figure 6.2 Meso-structure of concrete

When the meso-structure of the concrete has been meshed, the inserting procedure presented in Chapter 5 is atopted here to generate cohesive elements between along each mesh line. Since no damage (or cracking) occurs within the strong aggregates during a quasi-static loading, as observed from the simulations presented in the preceding chapters, it is deemed unnecessary to insert cohesive elements within the aggrgates. Therefore in the present model, only two types of cohesive elements are generated within the meso-structure, namely the mortar-mortar interface elements and the aggregate-mortar interface elements, which are shown in Figure 6.3.

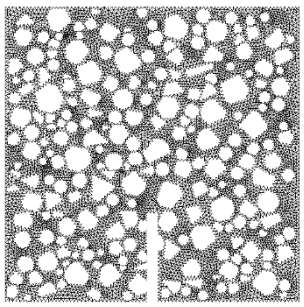

Mortar-mortar interface element

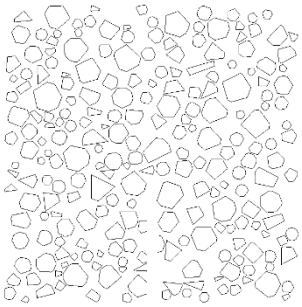

Aggregate-mortar interface element

Figure 6.3 Cohesive elements in the meso-structure

6.2.3 Material model and properties

Similar as the treatment in Chapter 5, the cracking procedure as well as the softening behaviour of concrete is represented only via a constitutive relation between traction and opening displacement in the cohesive elements. The bulk material outside the cohesive zone remains undamaged and it continues to behave linear elastically. This is to say, a simple linear elastic material model is used for the bulk (brick) elements while a nonlinear cohesive constitutive model is employed for the zero-thickness interface elements. Simple bilinear cohesive constitutive material model as used in Chapter 4 & 5 is adopted here. This model considers the irreversible damage and allows for independent definitions of the constitutive relations for different fracture modes of tension and shear. The detailed information about this material model can be found in Section 4.2.2 & 5.2.3.

The material properties of the homogeneous domain of the beam model are directly taken from the experimental data but only the linear elastic response is considered, with the Young's modulus being E = 35 GPa and the Poisson's ratio being v = 0.2.

For the 'multi-scale' region in the middle part, the material properties for the different components are obtained such that the macro response of concrete beam matches that in the experimental test, with consideration of the general guidelines on the assignment of the material properties for a mesoscale concrete model as described in previous chapters. The detailed properties for the bulk elements and the two interface components are given in Table 6.1 and Table 6.2 respectively. The

properties used in the cohesive and contact interface elements, such as the initial stiffness K_N and K_S, the kinetic frictional coefficient μ and the static friction stress limit *SFSL,* can be found in Chapter 4&5. The detailed values for these parameters are summarised in Table 6.3.

Table 6.1 Material properties for the bulk elements

Component	Density $\boldsymbol{\rho}$ (kg/mm^3)	Young's modulus $\boldsymbol{E}$ (MPa)	Poisson's ratio $\boldsymbol{\nu}$ (--)
Aggregate	2600	7000	0.2
Mortar	2300	4000	0.2

Table 6.2 Properties for the two interface components

Component	Tensile strength $\boldsymbol{\sigma_I^P}$ (MPa)	Fracture energy $\boldsymbol{G_{IC}}$ (N/mm)	Shear strength $\boldsymbol{\sigma_{II}^P}$ (MPa)	Fracture energy $\boldsymbol{G_{IIC}}$ (N/mm)
Mortar-mortar	4.7	0.06	18.8	0.6
Aggregate-mortar	2.3	0.03	9.2	0.3

Table 6.3 Properties for cohesive plus contact interface elements

Component	Normal stiffness $\boldsymbol{K_N}$ (MPa)	Shear stiffness $\boldsymbol{K_S}$ (MPa)	Frictional coefficient $\boldsymbol{\mu}$	Static friction stress limit ***SFSL*** (MPa)
Mortar-mortar	2.0e6	2.0e6	0.71	36
Aggregate-mortar	1.0e6	1.0e6	0.71	18

6.2.4 Mesh size studies

In Chapter 3, in order to ensure a mesh independent result for both global response and local fracture process, a non-local approach with a micro characteristic length R_c was introduced into the continuum-based mesoscale concrete model. However as it was pointed out in Chapter 3, the determination of the characteristic length for the mesoscale concrete model is not straightforward and can be case dependent.

Moreover there are still some inherent deficiencies of the nonlocal treatment at a mesoscale level, such as the boundary problem, the time-consuming calculation process and the 'blurred' damage process in terms of the initiation and propagation of the fracture process zone (see Chapter 3). All of these tend to render the non-local approach to be of a limited purpose.

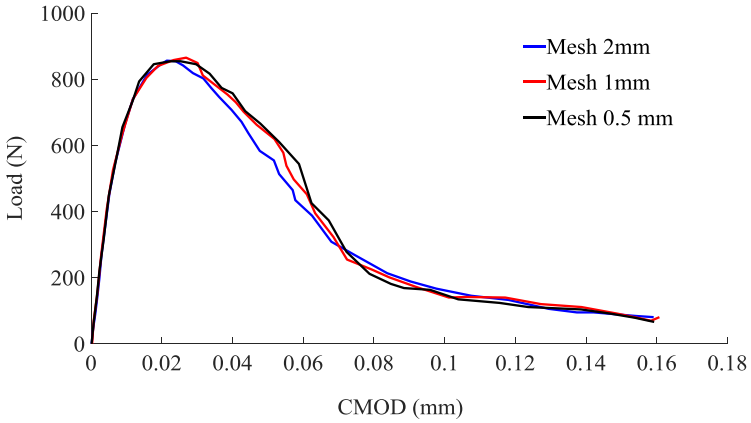

Figure 6.4 Mesh size studies on global response

In Chapter 4&5, the mesoscopic cohesive plus contact interface model has already shown its advantage in obtaining a mesh independent result both globally and locally. In view of these observations and the explicit representation of fracture in such a model, it is reasonable to postulate that the evolution of the local fracture process can be well simulated with such a model in a rather mesh-independent manner, even no nonlocal approach for the bulk material description is employed. To confirm this, a small sized beam (D = 40 mm) is meshed with three different grid sizes, namely 2 mm, 1 mm, and 0.5 mm, respectively, and the corresponding results for both global response and the local fracture process zone evolution are presented in Figure 6.4 and Figure 6.5. The global responses are represented by load vs. crack mouth opening displacement (CMOD) curves, in which the load is recorded as the force applied on the specimen while the CMOD is measured as the relative horizontal displacement of the points on the notch mouth shown in Figure 6.5.

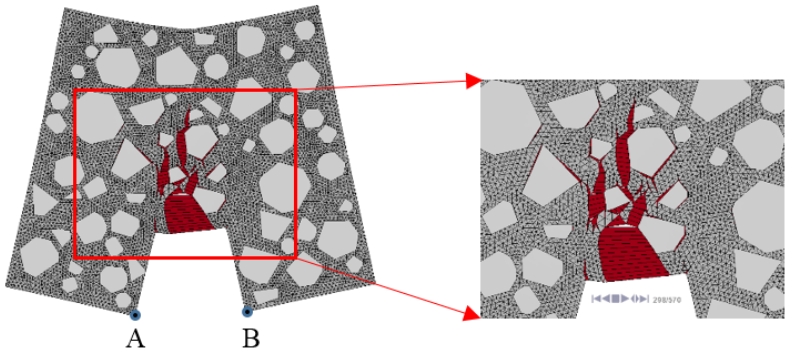

(a) Mesh 0.5 mm

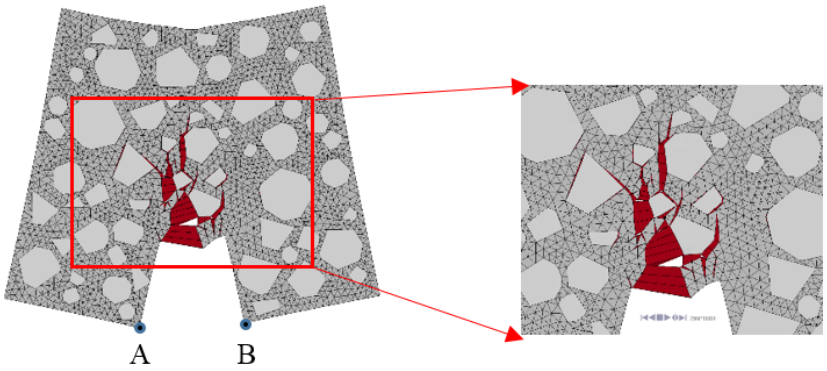

(b) Mesh 1 mm

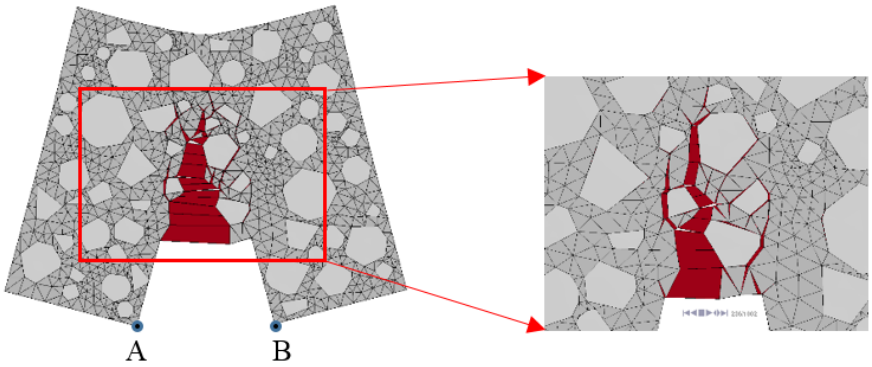

(c) Mesh 2 mm

Figure 6.5 Mesh size studies on the local fracture process zone

As it is shown in the Figure 6.4, the load vs. CMOD curve from the mesoscale cohesive plus contact model is indeed mesh insenstive as expected. From plots of the damage patterns at failure as shown in Figure 6.5, the fracture process zone widths

obtained from the models with differen meshes are almost identical. These observations clearly demonstarte the advantages of the current mesoscale model with a cohesive plus contact approach for the interfaces in obtaning a mesh independent result from both global and local responses. It should be noted that these mesh independent results are obtanined directly from the local fracture process without any other special treamtment such as the fracture energy convervation or nonlocal approach which are generally used in the continnum based numerical framework (see Chapter 3). Finally a mesh size of 1 mm is adopted in the simulations presented in the remainng parts of this chapter.

6.3 Model verification

6.3.1 Macroscopic load-CMOD response

Before checking the evolution of the local fracture process in the three concrete beams of different sizes, the macroscopic response in terms of the Load-CMOD relationship is compared and verified with the experimental results first.

As shown in Figure 6.6-6.8, a very good agreement between the numerical results and he experimental curves is achieved for all the three beams, and this confirms the capacity of the current model in capturing the global response of concrete beams in such a loading mode.

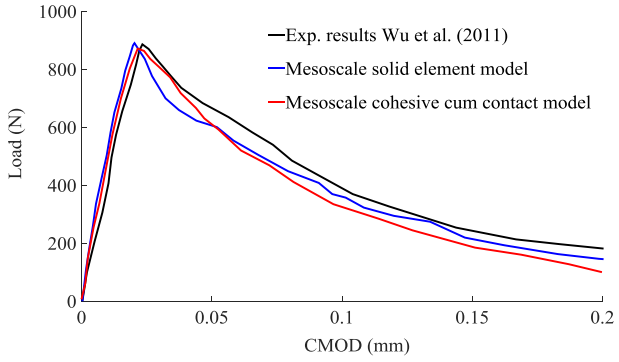

Figure 6.6 Load-CMOD curves for small specimen (D = 40 mm)

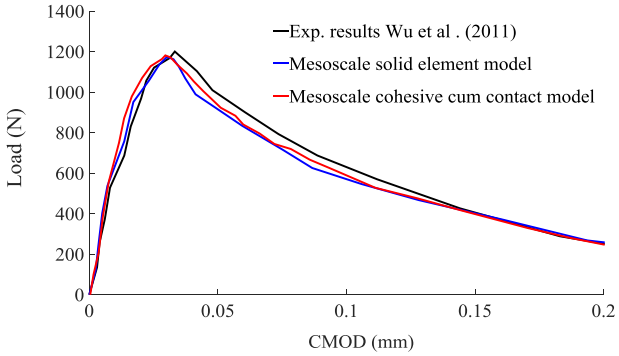

Figure 6.7 Load-CMOD curves for medium specimen (D = 60 mm)

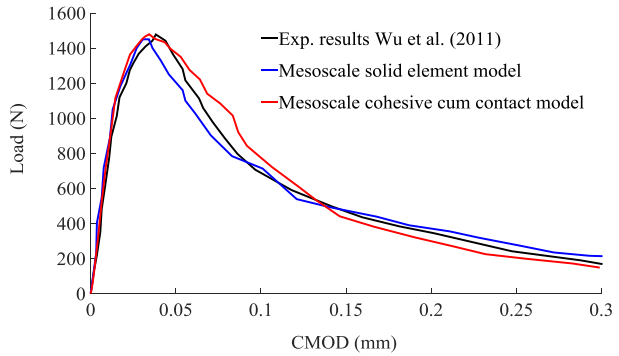

Figure 6.8 Load-CMOD curves for large specimen (D = 80 mm)

6.3.2 Evolution of Fracture process zone (FPZ)

The evolution of the local fracture process in the three concrete beams from the current mesoscale model with cohesive plus contact interfaces are dipicted in Figure 6.9 - 6.11. The fracture process is displayed directly from the deformation measurement. In order to clearly observe the formation and evolution of the fracture process zone based on the initiation and propagation of the microcracks, the deformation contours in all the models are scaled up by a factor of 200.

As can be observed from these figures, the fracture process zone is actually composed with a main crack and many secondary microcracks. The main crack initiates above the notch due to the stress concentration at the notch tip. It then propagates upwards due to bending. The secondary microcracks mainly initiate and then propagate through the weak ITZs along the boundary of the strong aggregate

particles. The main crack extends by bridging the interfacial micro-cracks which occur around adjacent aggregates. During the growth of the main crack, many new microcracks initiates while some microcracks formed earlier stop growing and even close. The evolution path of the fracture process zone is strongly curved due to the random spatial distribution of aggregate particles with weak ITZs.

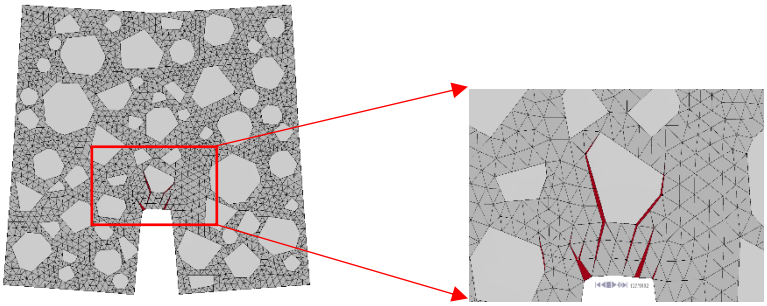

(a) Crack pattern at a pre-peak stage (71.4% of the peak load)

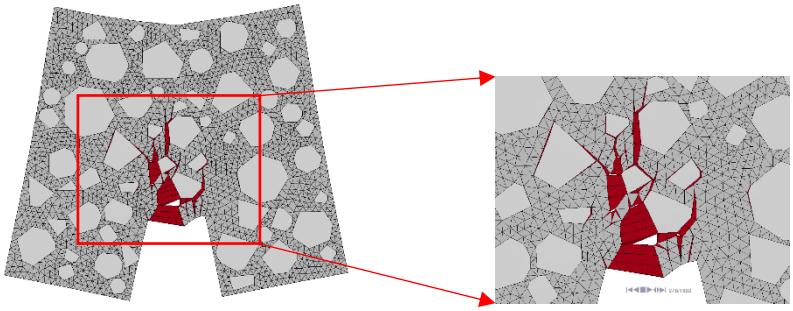

(b) Cracks pattern around the peak load

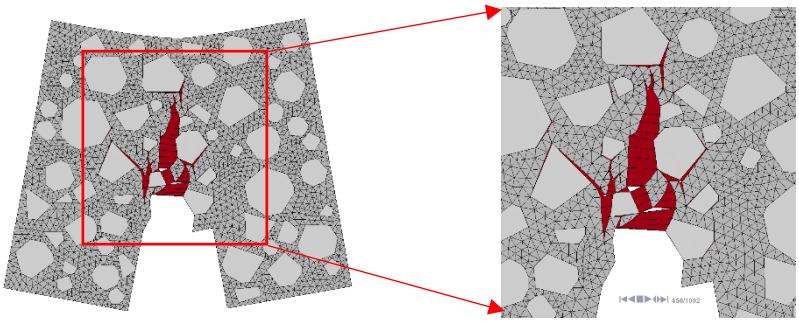

(c) Cracks pattern at a post-peak stage (60.6% of the peak load)

Figure 6.9 Evolution of the fracture process zone in small concrete beam (D = 40 mm)

The fracture process zone takes shape before the load reaches its maximum value and it can extend remarkably around the peak load. There is already a sizable fracture process zone at the peak load but the macro-crack has not formed yet. At the post-peak loading stage, the fracture process zone futher extends upward with the appearance of many new microcracks. In the meantime, the macrocrack forms and propagates along the trajectory of the main crack in the FPZ. Since the distance of the fracture process zone is generally measured from the stress free crack mouth ($\sigma_{traction} = 0$) to the crack tip ($\sigma_{traction} = \sigma_{peak}$) (see Chapter 3), the length of FPZ may gradually decrease during this stage.

In spite of the new insight into the local fracture process, some important observations from the contimuum-based mesoscale model enhanced by nonlocal treatment in Chapter 3, particularly in terms of the shape and size of the fracture process zone (See Figure 3.15-3.17 in Chapter 3), can still be confirmed. The width of the fracture process zone is almost identical with the new simulation while its length is similar.

The above simulated process regarding the development mechanism of cracks in concrete agree well with experimental observations based on DIC, X-ray and CT techniques (e.g. Alam et al. 2014; Ren et al. 2015; Saliba et al. 2016). Recall that the simulation of the development of the microcracks in the fracture process zone was not well captured or at least blurred in the continuum-based mesoscale model as shown in Chapter 3. This demonstrates a further advantage of the current mesoscale model with cohesive plus contact interfaces in capturing the very local fracture process in concrete materials.

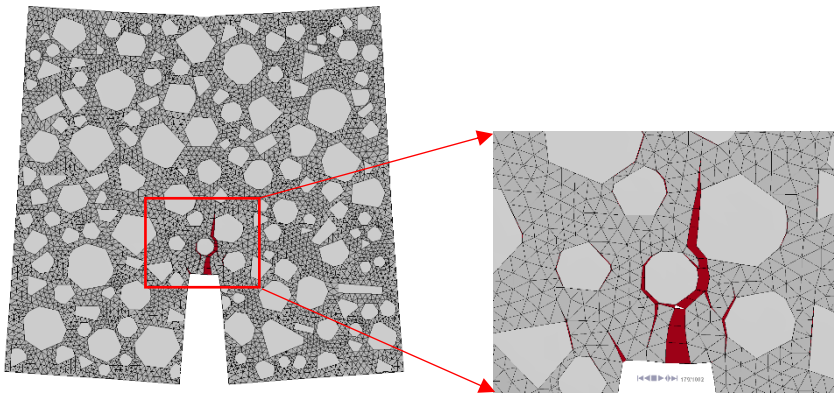

(a) Cracks pattern at the loading point corresponding to 85.1% of the peak load in the pre-peak region

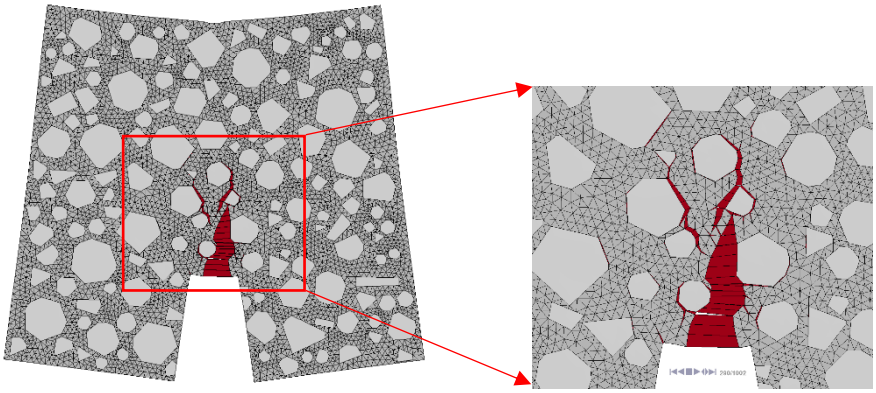

(b) Cracks pattern at the loading point corresponding to peak load

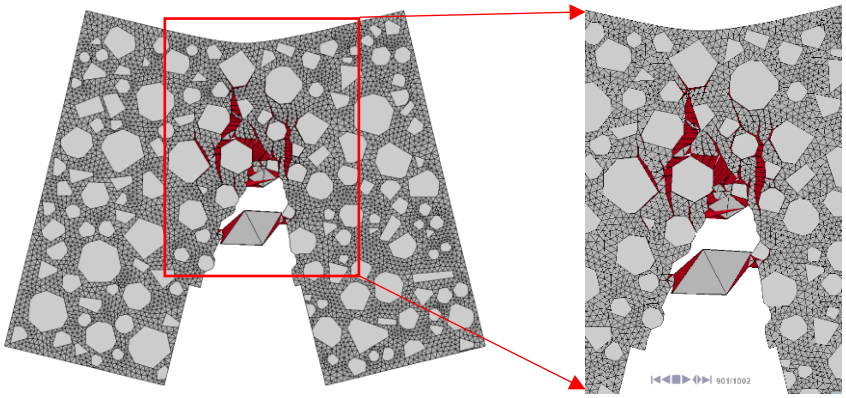

(c) Cracks pattern at the loading point corresponding to 40% of peak load in the post-peak region

Figure 6.10 Evolution of the fracture process zone in medium concrete beam (D = 60 mm)

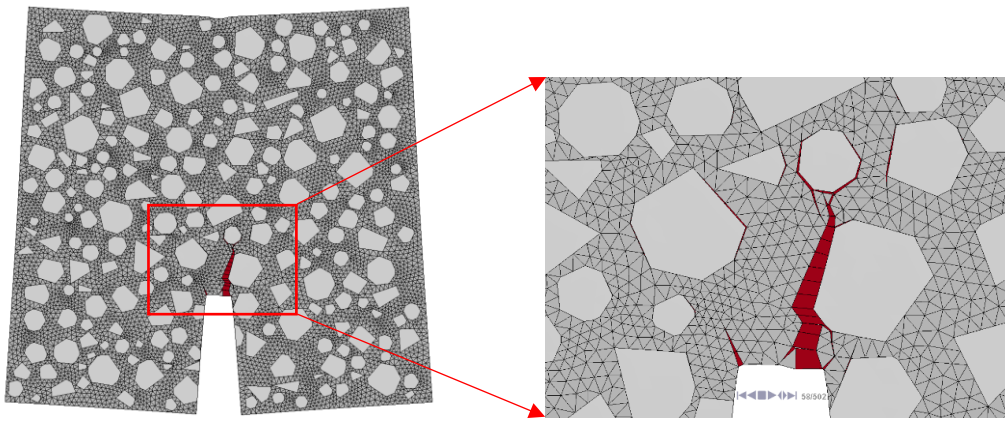

(a) Cracks pattern at a pre-peak stage (80.1% of the peak load)

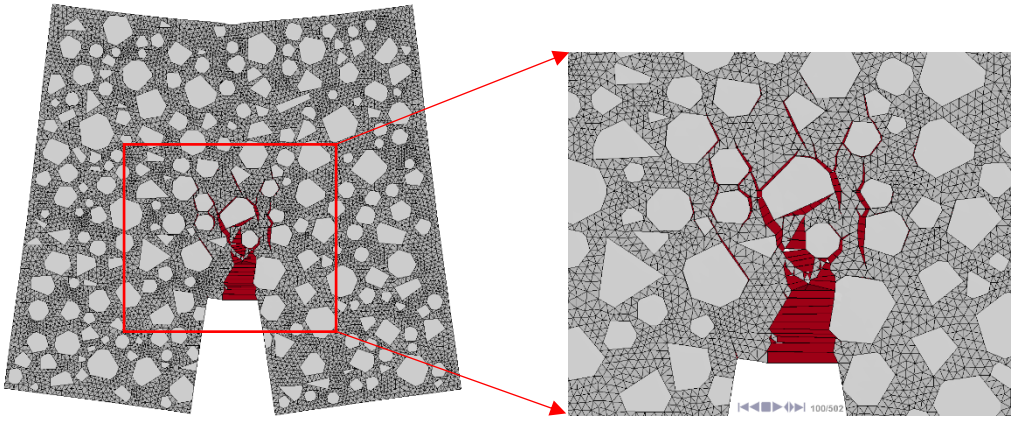

(b) Cracks pattern around the peak load

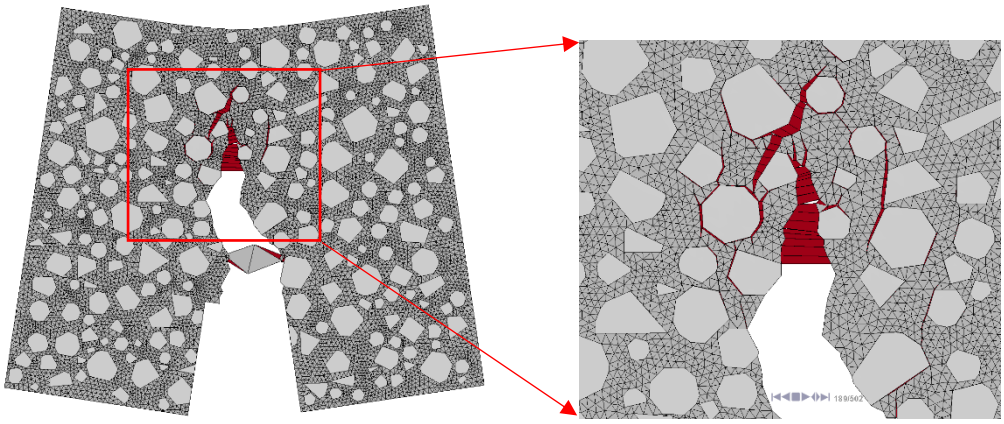

(c) Cracks pattern at a post-peak stage (31.4% of peak load)

Figure 6.11 Evolution of the fracture process zone in large concrete beam (D = 80 mm)

6.4 Size effect on the fracture process zone

In Chapter 3, the shape and size of the fracture process zone in different sized concrete beams were discussed in detail based on the simulation from a continuum mesoscale model. Generally the width of the fracture process zone is insenstive to the beam size while its length is strongly dependent on the beam size. Thus the width of the fracture process zone may be considered as a material constant and the size dependent length of the fracture process zone may be deemed as the intrinsic reason of the size effect. In this section, such an understanding is verified and checked by the new mesoscale model with cohesive and contact interfaces. Five different sized concrete beams (D = 40, 60, 80, 120, 160 mm) as adopted in Chapter 3 are simulated and the results are discussed below.

Figure 6.12 compares the shape and size of the fracture process zones for the five different concrete beams at peak loading point from the two different numerical models. As can be observed, the shapes of the FPZs from the two models are very similar in all the five concrete beams. The conclusion drawn in Chapter 3 that the width of FPZ is insensitive to the beam size but the length of FPZ is strongly dependent on beam size can be confirmed from the renewed simulation using the mesoscale combined with the cohesive plus contact model. However, the cohesive plus contact model generally predicts much longer length of the FPZs than the continuum-based model does. This may be related the difficulty in determining the the tip of the fracture process zone in the contimuum numerical model, similar to the same difficulty as experienced in experimental studies. Nevertheless, if we futher compare the relative fracture process zone length ($l_{FPZ}/(D-a_0)$) at the peak loading points for the five different beams, the trend of a decreasing fracture process zone length with increasing specimen is captured by both sets of the models, as it is shown in Figure 6.13. The relative fracture process zone length in the cohesive-contact model tends to show a more apparent size dependent tendency.

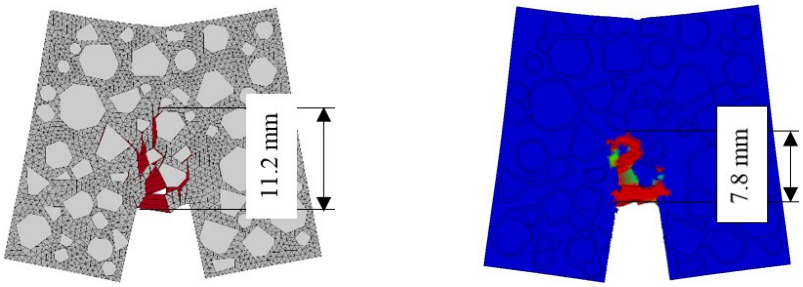

Cohesive plus contact model Continuum-based model

(a) D = 40 mm

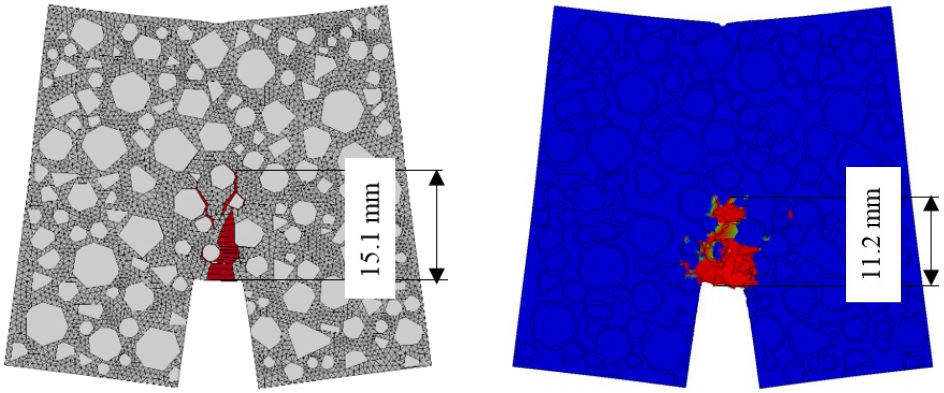

Cohesive plus contact model Continuum-based model

(b) D = 60 mm

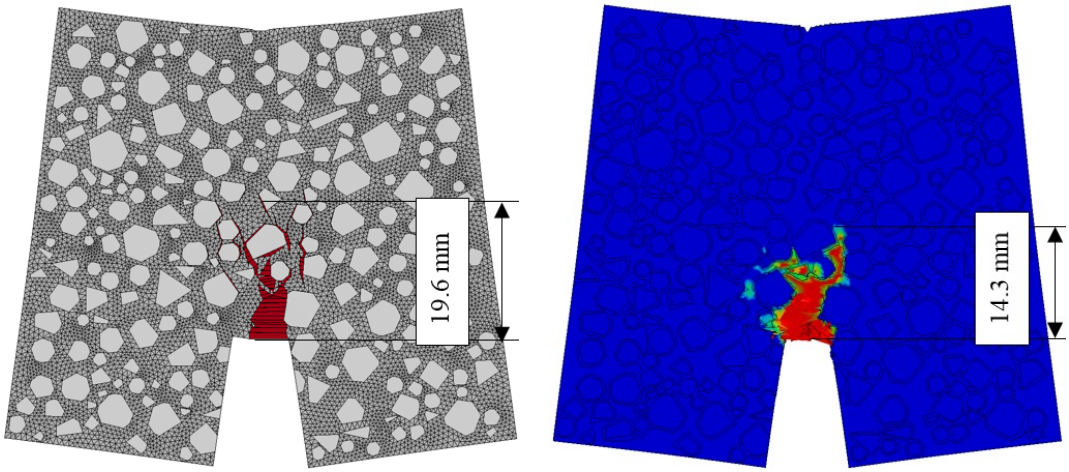

Cohesive plus contact model Continuum-based model

(c) D = 80 mm

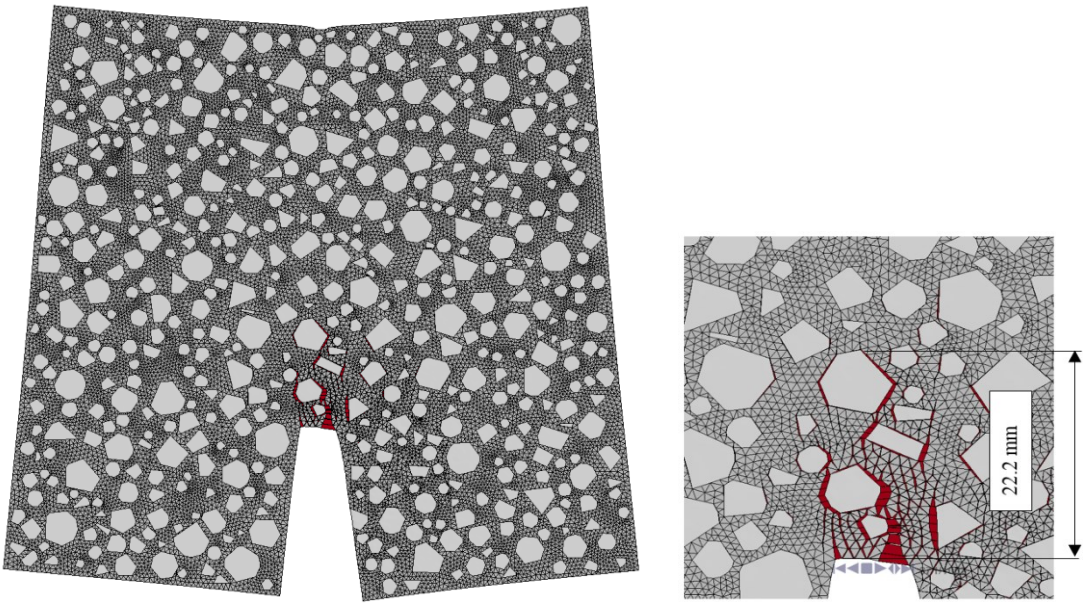

Cohesive plus contact model

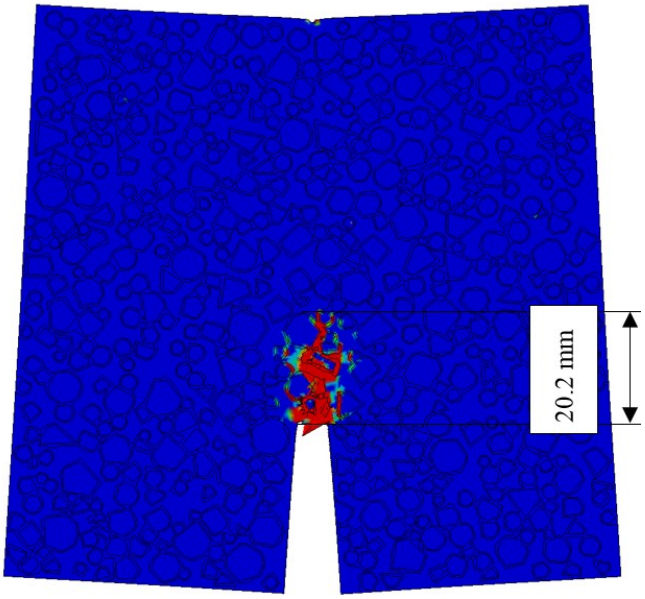

Continuum-based model

(d) D = 120 mm

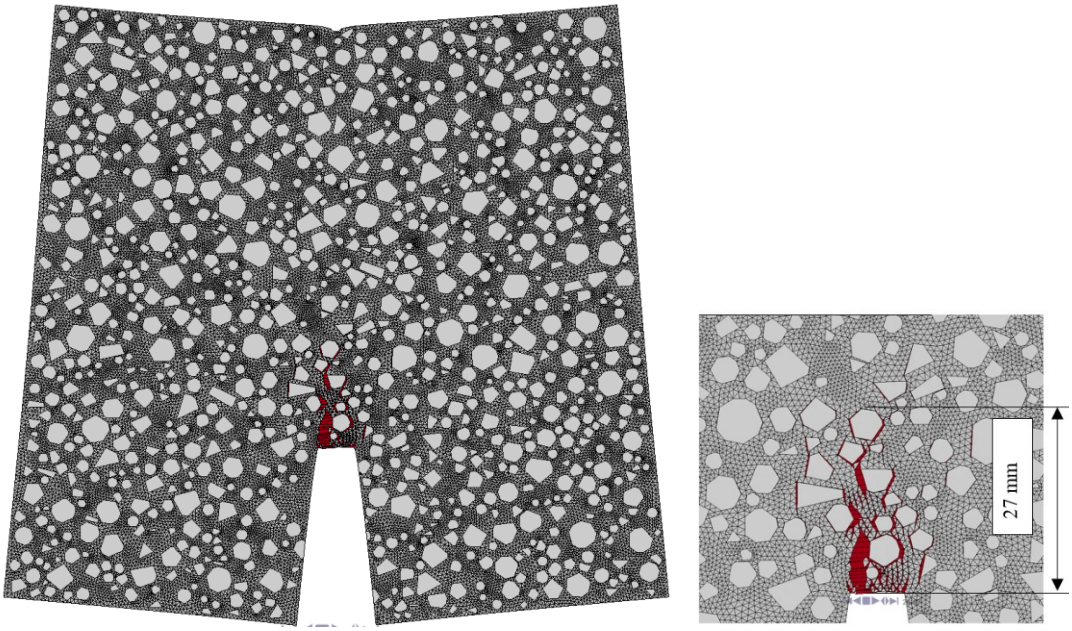

Cohesive plus contact model

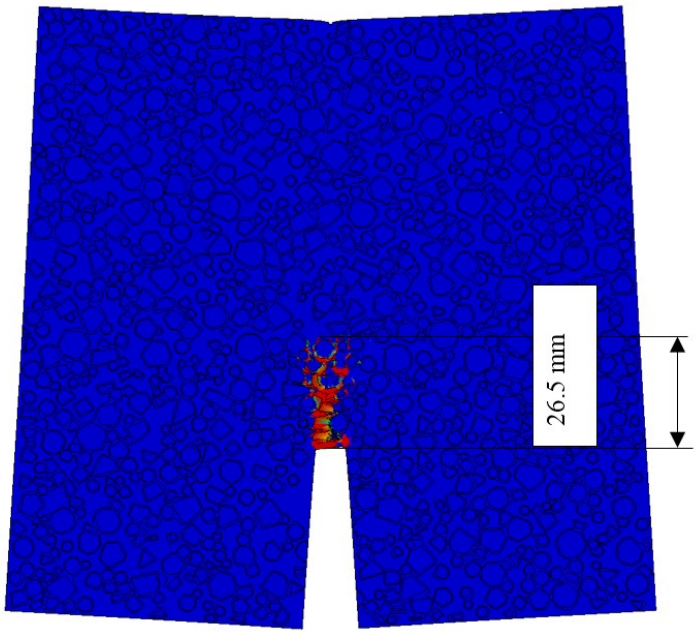

Continuum-based model

(e) D = 160 mm

Figure 6.12 The shape and size of the fracture process zone for different sized beams

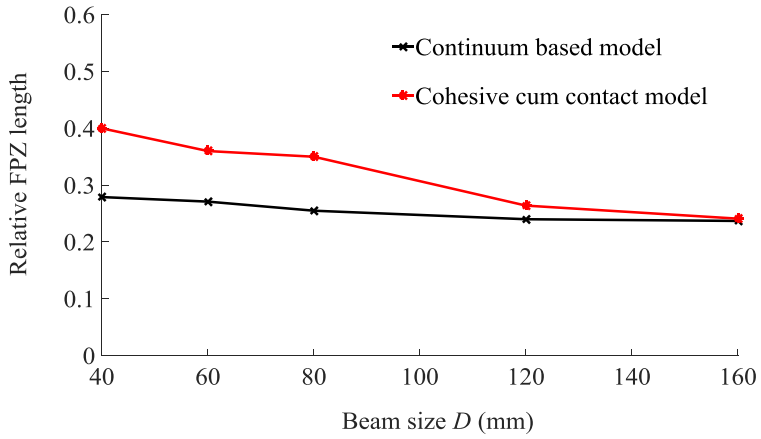

Figure 6.13 Relative fracture process zone length at peak load

In summary, the main observations regarding the size effect in Chapter 3 are confirmed with the more robust mesoscale model with cohesive-contact interfaces.

6.5 Conclusions

In this chapter, the size effect problem discussed in Chapter 3 is re-visited with the cohesive plus contact model which has been developed in Chapter 4 & 5 in this thesis. The new model shows its unique advantages in simulating the local fracture process from an explicit mesoscopic viewpoint. Mesh independent results for both global and local responses in the concrete specimen can be obtained directly without any special treatment.

The simulation results have brought new insight into the mechanisms of evolution of the fracture process zone from the perspective of micro-crack initiation and propagation. The results also confirm the general observations based on the continuum model in Chapter 3. The width of the fracture process zone keeps almost constant during the process of fracture it is insensitive to the size of the concrete specimen. This indicates that the fracture process zone width may indeed be considered as a material property. On the contrary, the length of the fracture process zone is subject to continuous increase with the loading, and it is strongly dependent on the specimen size - the larger the specimen size, the longer the length of the fracture process zone at the peak loading point. However, the relative fracture

process zone length, which is defined as the length of the fracture process zone divided by the ligament length above the notch, shows an opposite tendency. The size-dependent length of the fracture process zone appears to be an intrinsic reason for the size effect phenomenon.

The comparative results suggest that the method used in Chapter 3, namely a continuum-based mesoscale framework enhanced by a nonlocal treatment can be an effective alternative to the more detailed (and hence more computationally intensive) cohesive-based mesoscale model for the investigation of the size effect, although there is limitation with the continuum-based model in terms of the ability of capturing the mechanisms of the micro-crack initiation and propagation in the concrete.

Chapter 7 : 3D Mesoscale Finite Element Modelling of Concrete

7.1 Introduction

In previous chapters, a robust 2D mesoscale concrete framework has been developed and implemented in various loading conditions in discussing the failure mechanisms of concrete structures. However, as reviewed in Section 1.1, there are some inherent limitations of the 2D mesoscale concrete model in representing the realistic stress and strain conditions in concrete, particularly when pressure and confining stress becomes important such as in dynamic compression. Therefore, it is desirable to develop a robust 3D mesoscale framework in which the random material heterogeneous structure in 3D can be more realistically represented.

Previous research on the development of 3D mesoscale concrete model has largely been limited to simplified shape of aggregate particles like spheres, ellipsoids (Leite et al. 2004; Häfner et al. 2006; Mishnaevsky Jr 2006; Wriggers & Moftah 2006), whereas more realistic depiction of aggregates suffer from a relatively low aggregate packing density (Song & Lu 2011; Yin et al. 2015; Wang et al. 2016). The work reported in this chapter is concerned about a full 3D mesoscale model in which a realistic representation of the actual shapes and sizes of aggregate particles is achieved and at the same time high volumetric aggregate ratios of aggregate are also attained. In the proposed approach, 3D polyhedral-shaped aggregates are represented by convex hull in R^3, which is the minimum convex set containing a series of points generated randomly. Gravel and crushed shapes of polytopes are both considered to enable greater flexibility in the simulation of real shapes of aggregate particles. The standard take-and-place procedure is used for generating the main 3D meso-structure. Extending from a basic framework (Song & Lu 2011), the present study focuses on improving the efficiency in the generation of the 3D mesoscale geometry and the robustness of finite element meshing for the highly unstructured mesoscale model, as well as enabling the realisation of high density packing of aggregates. The

mesoscale model generated from the enhanced procedure is verified against standard experimental observations under quasi-static compression and tension. The model is then further applied to simulate the dynamic behaviour of concrete under high strain rate compression.

7.2 Overview of generation of 3D mesoscale geometry

Similar to the generation of the 2D mesoscale model, the classical 'Take-and-Place' procedure (Wang et al. 1999) is used to generate the 3D meso-structure in the first step (Song & Lu 2011). An overview of the basic procedure in 3D is given in this subsection.

The 'Take' process generates an individual aggregate (polytope) through a random sampling operation in terms of the size and the shape parameters. The 'place' process subsequently places the aggregate into the predefined 3D specimen space, satisfying geometric constraints including no-intersection with other aggregates and the specimen boundaries. The whole process is executed in a sequential manner controlled by the target aggregate volume ratio, starting with the largest aggregate size group, and carrying on until the smallest size group is completed. The generation of 3D meso-structure is implemented in MATLAB.

7.2.1 Aggregate size distribution

In normal concrete, the coarse aggregate is defined to consist of particles having a nominal size greater than 4.75 mm (Wriggers & Moftah 2006). For normal concrete the coarse aggregates take up around 40-50% of the mixture volume. The particle size distribution for aggregate is usually defined by a grading curve. Herein we adopt a standard Fuller grading curve, which can be expressed as:

$$P(d) = 100 \times \left(d / d_{\max}\right)^n \tag{7.1}$$

where P is the cumulative volume percentage of aggregates below size d, d_{max} is the maximum size of the aggregates. The exponent n is normally in the range of 0.45-0.70. Herein n is assumed to be 0.5. Thus the volume ratio of aggregate within each grading segment $[d_s, d_{s+1}]$ can be calculated as (Wriggers & Moftah 2006):

$$V_R[d_s, d_{s+1}] = \frac{V_{agg}[d_s, d_{s+1}]}{V_s} = \frac{P(d_{s+1}) - P(d_s)}{P(d_{\max}) - P(d_{\min})} \times v_p \tag{7.2}$$

where $V_{agg}[d_s, d_{s+1}]$ is the volume of aggregate within the discretized aggregate size range $[d_s, d_{s+1}]$. $P(d_i)$ can be calculated from Eq. (7.1) provided the aggregate size is given. v_p is the total amount volume percentage of aggregate in concrete and V_s is the volume of concrete specimen. d_{max} , d_{min} are the maximum and minimum coarse aggregate particle size.

The basic reference case of concrete that we will employ in the development of the mesoscale model will be the type of medium aggregates with the coarse aggregates varying in size between 4 to 12 mm. For simplicity the aggregates are divided into four size segments, namely, 4-6 mm, 6-8 mm, 8-10 mm, and 10-12 mm. For a coarse aggregate volume ratio of 45%, which is the target volume ratio to be achieved in the 3D mesoscale model, the percentages of the above four aggregate groups will be 14%, 12%, 10%, and 9% respectively.

7.2.2 Individual aggregate particle generation

In an actual concrete specimen, the aggregate shape and surface texture can be classified as rounded, angular or polyhedral. Highly irregular particles can also have flaky and elongated shape. In this study, polyhedron-shaped aggregates are considered. Other special shapes, such as round or ellipsoid, are relatively simple to generate, and they may also be approximated by polyhedrons with specially chosen shape parameters.

One classical approach to describe the shapes of gravel aggregates mathematically is based on the morphological analysis. In 2D, the shape of a gravel aggregate can be characterised by transforming the boundary contour of each particle into polar coordinates. Thus the trace of an aggregate can then be expressed with the polar radius r as a Fourier series (i.e. harmonic function) of the polar angle θ (Beddow & Meloy 1980):

$$r(\theta) = r_0 + \sum_{m=1}^{\infty} A_m (\cos\ m\theta + \varphi_m) \tag{7.3}$$

where r_0 is the average radius. The term $\sum_{m=1}^{\infty} A_m(cosm\theta + \varphi_m)$ characterises the particle contour where A_m are the amplitudes of the Fourier frequencies with whose corresponding phase angles φ_m and m are the harmonic numbers. According to the morphological law proposed by Beddow and Meloy (1980), there should be a linear relation between log(A_m) and log(m):

$$\log(A_m) = a \log(m) + b \tag{7.4}$$

where a and b are parameters characterizing the shape of the set of particles. Thus numerically the shape of a gravel particle may be approximated by a series of short straight line segments in 2D (Wang et al. 1999). An inscribed polygon of circle can then be used to represent the relatively regular aggregate while an elongation and shrinking procedure can be applied on it to produce elongated and flaky aggregate.

This idea can be extended to 3D case, where the spherical harmonic mathematical analysis is used to characterise the boundary of a real aggregate (Liu et al. 2011). Similarly regular aggregates can be represented by inscribed polyhedrons of spheres while un-regular aggregates can be produced by applying elongation and shrinking procedure as is done in 2D case.

7.2.1.1. Regular aggregates

As it is stated above, an inscribed polyhedrons of sphere is used to characterise the real shape of regular aggregate. Thus the generation process starts from picking a set of random points on the surfaces of the spheres. These random points can be expressed as the following equations using spherical coordinates by radius r_0, inclination angle θ, azimuth angle φ:

$$R_{ix} = r_0 \sin\theta \cos\phi \tag{7.5a}$$

$$R_{iy} = r_0 \sin\theta \sin\phi \tag{7.5b}$$

$$R_{iz} = r_0 \cos\theta \tag{7.5c}$$

It is worth noting that variables r_0, θ and φ are random numbers from a uniform distribution. Thus we can have:

$$r_0 = \frac{1}{2} \times [d_1 + \lambda \times (d_2 - d_1)] \tag{7.6a}$$

$$\theta = \gamma \times 2\pi \tag{7.6b}$$

$$\phi = \chi \times \pi \tag{7.6c}$$

where d_1 and d_2 are the minimum and maximum diameters for each segment in the size distribution, λ, γ, χ are three independent random numbers uniformly distributed between 0 and 1. The points used to generate the polytope also have random numbers n, which may significantly influence the shape of an aggregate. Generally a larger number of points make it possible to generate gravel shape aggregate while small number of point produce angular shape aggregate. This will be shown later.

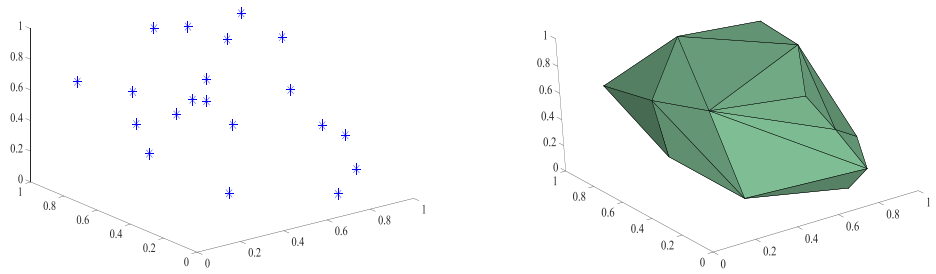

Figure 7.1 An example convex Hull. Left = random points; right = generated convex hull

After picking a series of random points as specified above, we create the aggregate particles by bounded polyhedrons. The convex hull for a set of points is the minimum convex polyhedron containing all the predefined points (De Berg et al. 2000). Thus it is possible to generate a random shaped aggregate particle from a set of 3D random points. The convexity of the polyhedron can be automatically fulfilled without separate checking at every step. Furthermore, the adopted take-and-place procedure guarantees that a prescribed aggregate size grading (Fuller curve herein) is followed. Figure 7.1 gives an example of a convex hull generated using Matlab with a computational geometry function named Qhull.

7.2.1.2. Crushed aggregates

The shapes of aggregate particles created above are inscribed polyhedrons of sphere which are relatively regular. Both flaky and elongated aggregates can be realised from the regular polytopes by shrinking or elongation. Here flaky shape refers to a polyhedron in which the thickness is small relative to the other two dimensions while elongated shape indicates that a polytope in which the length is considerably larger than the other two dimensions. To keep the volume at a constant value during the process, a flaky (elongated) shape is implemented by introducing a random shrinkage (elongation) ratio s on one dimension but expanding (shrinking) the other dimensions simultaneously, keeping the nominal volume of the aggregate unchanged, thus:

$$R'_{ix} = s \times R_{ix} \tag{7.7a}$$

$$R'_{iy} = R_{iy} / \sqrt{s} \tag{7.7b}$$

$$R'_{iz} = R_{iz} / \sqrt{s} \tag{7.7c}$$

where (R_{ix}, R_{iy}, R_{iz}) is the original coordinate for the i^{th} vertex on a regular polytope while $\left(R'_{ix}, R'_{iy}, R'_{iz}\right)$ is the transformed one.

In summary a series of random parameters (five in total) are required to produce an arbitrary shape of 3D aggregate particle. With different values of these parameters, the shape of polytopes can be quite different. As shown in the Figure 7.2, the polytope with only 10 random points has clear angular edges and corners, and with increase of the random points the shape of the polyhedron becomes smoother. Considering the actual aggregate shapes and a balanced computing time, the number of random points used to create the polytopes is controlled between 15 and 25 in the present study. Shrinking and elongation can then be performed to create elongated and flaky particles. As can be seen in Figure 7.3, for s>1, the algorithm would create an elongated polyhedron while for s<1, it would generate a flaky polytope. It should be noticed here that the ratio s is taken as random number from 0.5 to 1.5 in our implementation to avoid highly irregular shapes of the particles.

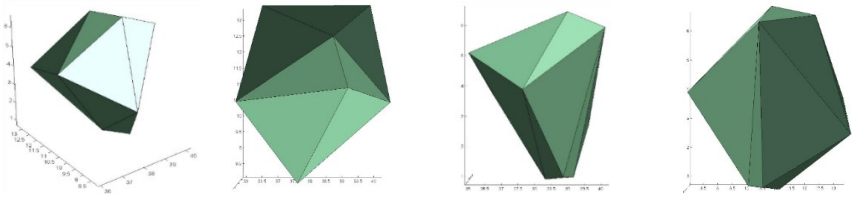

Global view X-Y view X-Z view Y-Z view

(a) Polytopes with 10 random points

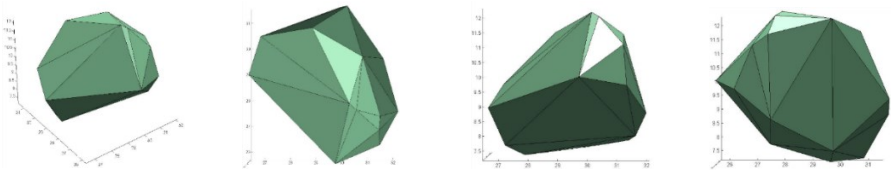

Global view X-Y view X-Z view Y-Z view

(b) Polytopes with 20 random points

Figure 7.2 Sample polytopes shape with different number of random points

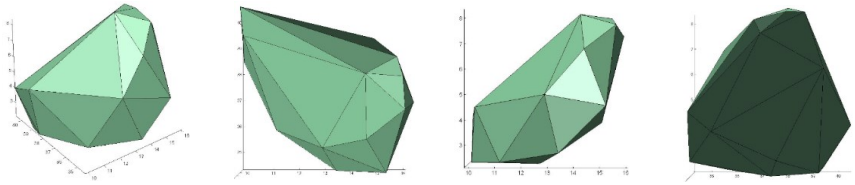

Global view X-Y view X-Z view Y-Z view

(a) $s = 0.5$

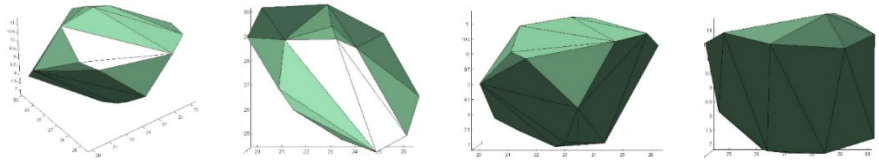

Global view X-Y view X-Z view Y-Z view

(b) $s = 1.5$

Figure 7.3 Examples of flaky and elongated particles generation with 20 random points

7.2.3 Placing particles

After generating an individual aggregate particle, the 'place' process is carried out to place the particle into the predefined sample space in a random manner, subjected to prescribed physical constraints.

The most important and time consuming step in the placing process is the intersection checking between two polytopes. Two obvious conditions should be satisfied for placing a valid particle. Firstly the whole polytope should be completely within the boundary of the concrete specimen, for instance a cube herein; this can be ensured relatively easily by making sure all of the random points which have been used to form the vertices of the polytope are within the boundary of the defined space. Secondly there should not be any intersection with any existing (already placed) aggregates. The check of this condition would require much more intensive computation in 3D modelling. To increase the check efficiency, only the neighbouring aggregates need be checked, and this is done in two steps. The first step is to identify the neighbouring aggregates which may have a chance to intersect with the new aggregate. At this step the new aggregate, as well as the existing ones, is represented by a bounding sphere which shares the same centre point as the convex hull and covers all vertices of the polytope, as illustrated in Figure 7.4. Any aggregate which has the distance of its centre to the centre of the new aggregate to be smaller than the sum of the radii of the two spheres is picked out as candidates of intersection. In the second step, a more detailed check is carried out on the limited number of candidate particles.

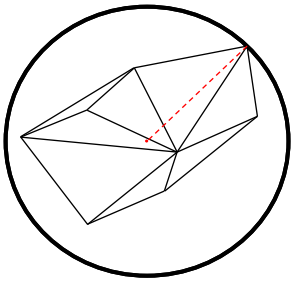

Figure 7.4 Local checking space

The clipping and capping algorithm (Ahn & Shashkov 2008) is then employed to detect the intersection between the aggregate being placed and the existing particles picked out above. The algorithm is based on the concept that any 3D convex polytope can be represented by a list of plane indicating a facet (i.e. any bounded polytope in 3D can be reconstructed by the boundary surfaces in half-spaces) (De Berg et al. 2000). Then the intersection checking between two convex polytopes can be converted to the intersection of the polygonal surfaces in one polytope with the cutting planes in the other polytope. Full details of the algorithm on clipping and capping can be found in (Ahn & Shashkov 2008).

7.2.4 Enhancement on the placing of aggregates

In the usual "place" procedure, once an aggregate being placed is found to intersect with any existing aggregates, this aggregate will be abandoned and a new polytope is regenerated and placed into a new position, and the checking process is carried out all over again. In the present study, in order to increase the success rate of placing the aggregate and hence improve the placing efficiency, a translate-and-rotate procedure is employed on the aggregate which is being placed. The detail of this procedure is described as follows.

Let point $P_i\ (X_i, Y_i, Z_i)$ be the coordinate of an individual vertex of the particle being placed in the concrete specimen. The translation is done by translating the particle by a small distance. For simplicity, each of these incremental components is treated as independent random variable but following a same uniform distribution within a range of a small fraction of the nominal aggregate size, both positive and negative. The translated coordinates in the Cartesian system for each vertex of the particle are thus:

$$\mathbf{P}_i' = (x_i + \Delta x, y_i + \Delta y, z_i + \Delta z) \tag{7.8}$$

where $\Delta x, \Delta y, \Delta z$ are increments in the three axis directions, respectively.

For a 50 mm sample cube with nominal aggregate size of 10 mm being studied in the numerical simulation which will be described later, the increment in each axis direction is taken in the range of (-1.5mm, +1.5mm).

The intersection check is immediately carried out after the translation. If intersection is found to still exist, a random rotating operation is performed. According to Euler's rotation theorem, any rotation of an object in 3-dimenisonal Euclidean space can be achieved by three elemental rotations, namely α, β, γ with respect to $x, y \; and \; z$ axis respectively. In the random rotating operation, these three angles are sampled independently within their variable range, i.e. -90 to +90 degrees. It should be noted that the final rotation matrix can be dependent on a sequence of three rotations, one about each principle axis. In the present procedure the rotation is done first about the x-axis, then the y-axis, and finally the z-axis. Such a sequence of rotations can be represented as the matrix product:

$$T = R_z(\gamma) R_y(\beta) R_x(\alpha) \tag{7.9}$$

where

$$R_x(\alpha) = \begin{bmatrix} 1 & 0 & 0 \\ 0 & \cos\alpha & -\sin\alpha \\ 0 & \sin\alpha & \cos\alpha \end{bmatrix}, \; R_y(\beta) = \begin{bmatrix} \cos\beta & 0 & \sin\beta \\ 0 & 1 & 0 \\ -\sin\beta & 0 & \cos\beta \end{bmatrix}, \; R_z(\gamma) = \begin{bmatrix} \cos\gamma & -\sin\gamma & 0 \\ \sin\gamma & \cos\gamma & 0 \\ 0 & 0 & 1 \end{bmatrix} \tag{7.10}$$

The intersection check is carried out again after the rotation. This completes one round of translation-rotation operation and the associated check. To avoid waste of effort for a bad position, a limit number of translate-and-rotate operations can be set. From the trial analysis in the present study, a limit of 50 times appears to be adequate.

When compared with the procedure without consideration of the translate-and-rotate method it is found that the translate-and-rotate procedure not only reduces the computing time (by about 60%) but also can result in an increase in the aggregate volume percentage (by about 4%). Despite the improvement, however, when a high volume ratio of aggregates such as 40-50% is desired the enhanced 'take-and-place'

procedure would still become very time-consuming and likely to fail to achieve such high packing density. Thus an alternative approach would be needed to further increase the aggregate percentage, and this will be discussed in the next section.

7.3 Finite element meshing and generation of supplementary aggregates

7.3.1 Meshing methodology

Due to the randomly shaped aggregate particles, the meso-structure is highly unstructured. For meshing unstructured domain, triangle and tetrahedral meshing are mostly used in the grid refinement. Specific smoothing algorithms for meshing unstructured domain include Octree, advancing front and Delaunay refinement (Owen 1998). A typical way to work around the difficulty arising from meshing directly the highly unstructured mesoscale geometry has been to firstly perform a background meshing and then bundle groups of the meshed elements into aggregates of desired shapes (Riedel et al. 2008; Du et al. 2011). The obvious drawback of such an approach is that the actual surfaces of the aggregates cannot be preserved and instead saw-tooth shaped boundaries will result.

In the present study, a direct approach to meshing the mesoscale structure of concrete is adopted. An advanced meshing code, called TetGen (Si 2015), is employed to do this task. This meshing code is one type of Delaunay triangulation, and it aims to maximize the minimum angle of all the angles of a triangle in the triangulation. By this kind of refinement, skinny or badly shaped triangles may largely be avoided. A typical way in this algorithm is to generate an initial node set by meshing the boundary of the geometry. The boundary nodes are then triangulated with Delaunay triangulation. However it should be noted that not all the boundaries of the structure, especially in 3D, can conform to the Delaunay triangulation. Hence a generalization of the Delaunay triangulation called constrained Delaunay triangulation (CDT), which forces certain required segments into the triangulation, has been proposed in computational geometry literature (Shewchuk 2008). The TetGen code which is based on the (CDT) treats the 3D unstructured geometry to a more general input called piecewise linear complex (PLC) (Si & Gärtner 2005). A PLC can be easily

decomposed into a constrained Delaunay tetrahedronlization provided it has a CDT. The code successfully resolves the problem of non-existence of a CDT by updating the input PLC into another PLC which is topologically and geometrically equivalent to the original one and does have a CDT. The advantage of using this type of meshing method is that it can retain realistic boundaries between aggregate and mortar. This provides an essential basis for the simulation of stress concentration, crack initiation and damage accumulation in concrete from a mesoscopic perspective.

Figure 7.5 and Figure 7.6 show an example of the 3D structure and meshing result of a cubic concrete specimen. Note that up to this point only aggregate and mortar elements have been generated; the polytope particles represent the aggregates and the remaining domain belongs to the mortar material.

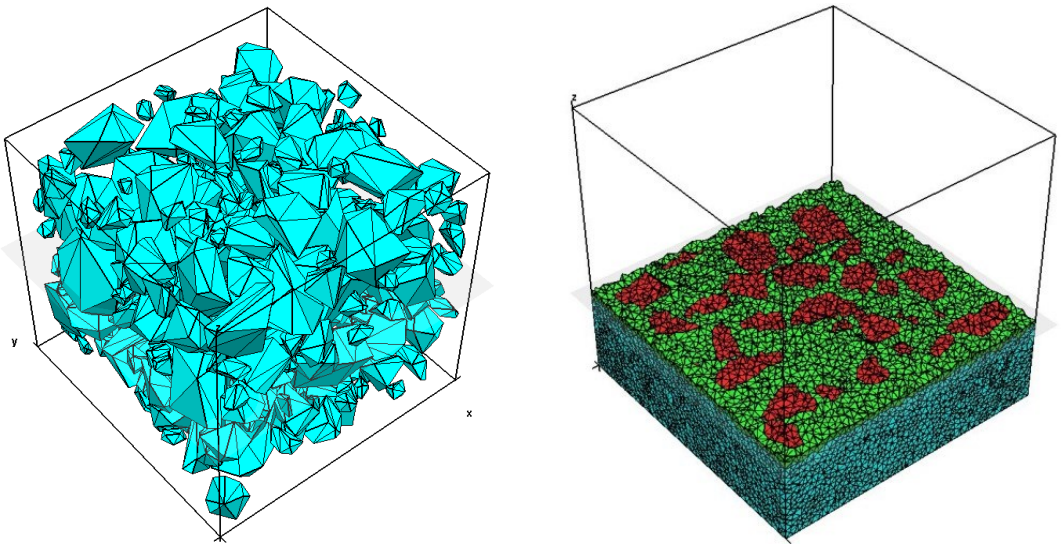

Figure 7.5 3D meso structure and mesh result

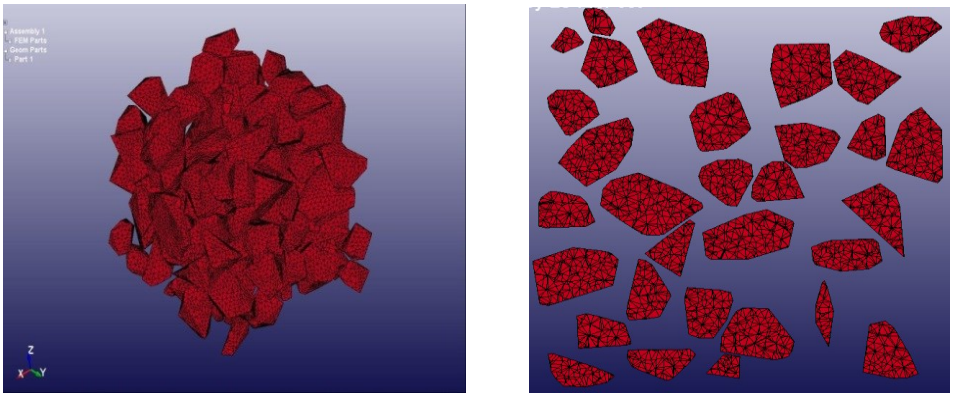

(a) Aggregates elements left = 3D view, right = a plane cut view

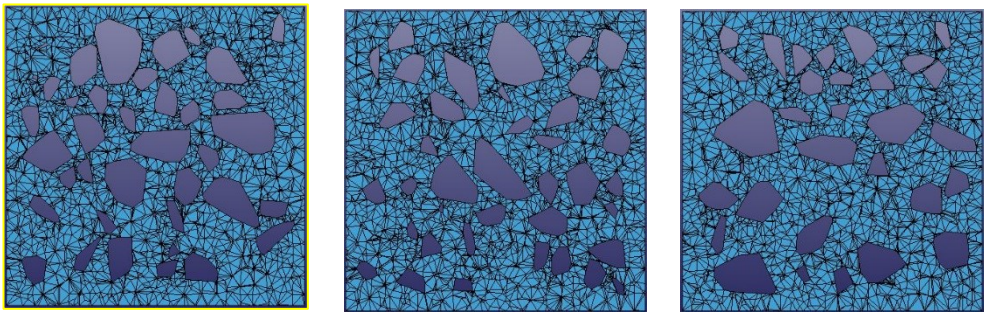

(b) Mortar elements x, y, z plane cut view respectively

Figure 7.6 Meshing results for aggregates and mortar

The generation of the third phase, i.e. the ITZ can be made by different methods depending upon the way the ITZ is to be modelled, for example by “shrinking” the already formed aggregates to leave an interface layer between the aggregates and the mortar matrix which is subsequently meshed as ITZ. Using cohesive elements is another option; however, due to complex stress conditions at the mortar-aggregate interface, typical cohesive element formulation is found to exhibit poor performance in a mesoscale model (Tu & Lu 2011). This problem has been discussed in length and a robust approach combining the cohesive element with a contact plus friction algorithm in a 2D mesoscale framework has been presented in the previous chapters. However, in the present 3D mesoscale model, with consideration of the computational cost, the equivalent solid layer approach is retained to represent the effect of ITZ.

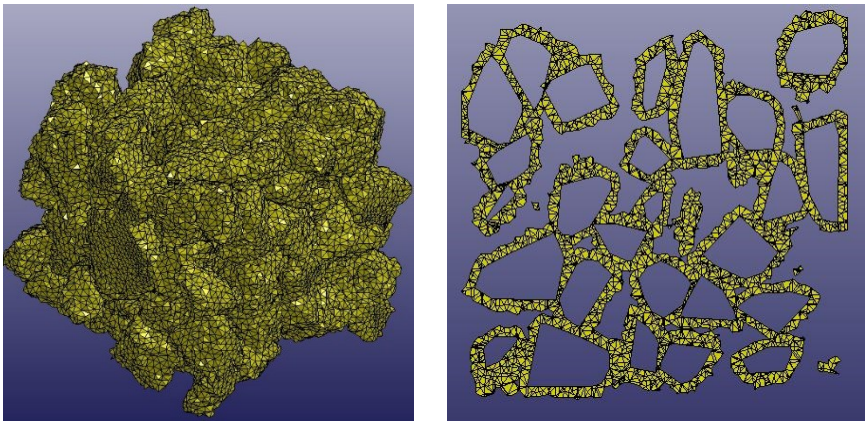

Figure 7.7 ITZ layer; left = 3D view, right = a plane cut view

As an alternative to shrinking aggregates, in the current scheme the equivalent ITZ layer is generated after the initial meshing of mortar domain, by choosing mortar elements that immediately come into contact with the aggregates. The procedure is straightforward and one just needs to pick up those elements in mortar domain which have shared nodes with the aggregates. This means if a mortar element shares at least one node with any aggregate, then the element will be defined as an interface element. Otherwise the element remains in the mortar domain. An in-house selection program has been developed using MATLAB to identify the layer of elements surrounding aggregate particles. Figure 7.7 shows the identification results and the ITZ elements thus defined.

7.3.2 Creation of supplementary aggregates

As has been discussed above, a practical limitation of the take-and-place method when applied in 3D meso-scale modelling is the packing density; even with the enhancement operations it is difficult to achieve an aggregate volume ratio as high as 40-50%, which is typical in normal concrete.

Based on the experiences from the present study, the maximum aggregate volume ratio that may be achieved from the standard take-and-place procedure is around 30% when the grading curve is closely followed, and with the enhanced operations described in Section 4.2.4 the ratio may be increased to about 34%.

To facilitate the discussion let us stay with the particular cubic concrete specimen, and we aim to generate an aggregate volume ratio of 45%. For simplicity we have subdivided the aggregates into four discretized ranges according to the Fuller curve, namely i) 4-6 mm, 14%; ii) 6-8 mm, 12%; iii) 8-10 mm, 10%; and iv) 10-12 mm, 9%. We firstly follow the standard take and place procedure and start from the largest aggregate size group (10-12 mm). We find that the volume percentage of the first two size groups, i.e. the 10-12 mm and 8-10 mm groups herein, can be perfectly completed. But for the third group 6-8 mm, the maximum aggregate ratio that can be achieved is around only 10%, and further attempt to fill in the remaining 2% can be extremely time consuming and may not succeed at all. It is still possible to pack some aggregates of the next group (4-6 mm), but only a small fraction of the target volume percentage for this group may be achieved. Clearly the missing amounts of aggregates in the two smallest size groups (6-8 mm and 4-6 mm herein) can only be generated using methods outside the take-and-place procedure.

To tackle the above difficulties we propose to proceed from the incomplete aggregate packing after the take-and-place procedure to finite element meshing, and create supplementary aggregates from the meshed FE domain by grouping selected mortar elements in qualified neighbourhood to form the remaining aggregates. The neighbourhood is identified by a virtual sphere whose diameter matches the nominal size of the aggregates to be created. The positioning of the sphere is random but a valid position should have the sphere meeting a similar set of criteria as an aggregate in the normal take-and-place procedure, namely no intersection or overlapping with any existing aggregates. In this sense the general effect of such a procedure to generate the supplementary aggregates is analogous to the take-and-place procedure.

The operation is controlled by the remaining aggregate volume ratio for each segment size group, which means the secondary aggregates are formed one by one until the target aggregate volume ratio is fulfilled.

For each size group requiring the generation of the supplementary aggregates, a virtual sphere of nominal diameter equal to the upper-end size in the size group, d_2, is employed to encircle a target space for a new aggregate. For example d_2 = 8 mm for the 6-8 mm group. The process can then be subdivided into two main steps:

Step 1: Placing the centre of such a virtual sphere into the mortar space in a random manner. Considering that by this stage all mortar elements have been meshed and a library can be created to contain all mortar elements with their respective nodal coordinates, placing the virtual sphere can be effectively done by putting its centre to the centroid of a mortar element at random. A checking process then proceeds to see if the location of the sphere is a valid one with no intersection with other aggregates and the boundary.

Step 2: After the base mortar element (centre of the sphere) is successfully selected from the above step, the new aggregate grouping process and the new ITZ identifying process can be carried out with respect to the virtual spherical space.

Figure 7.8 illustrates schematically the relative position of a virtual sphere in the mortar domain, where "i", "k" denotes a random mortar element, respectively, to which a trial sphere is placed. For illustration purpose, "i" indicates an invalid base element while "k" represents a valid base element. More detailed operations and the associated algorithms are given in what follows.

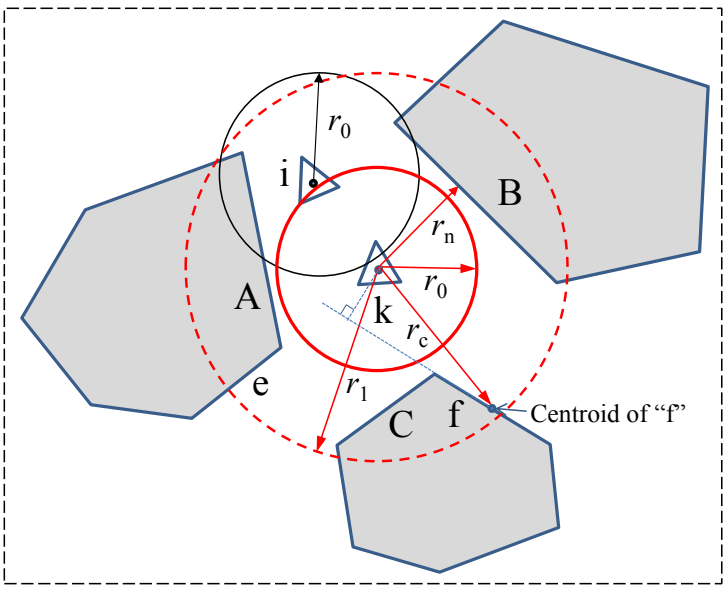

Figure 7.8 Schematic of placing the virtual sphere and intersection checking

The general procedure for creating secondary aggregates is programmed using MATLAB code. Understandingly a proper location of the base element and a suitable

grouping process are equally important in determining an adequately shaped secondary aggregate. Discussions on these two topics in detail will be given in Section 7.3.2.1 and Section 7.3.2.2 respectively.

7.3.2.1 Base element

As stated above it is important to choose a proper location for the base mortar element because it is essentially the centre of the virtual sphere for the formation of a supplementary aggregate and will therefore significantly influence the shape of the secondary aggregate. A valid base mortar element should satisfy the following three conditions:

1. It should not result in any overlapping or intersection between any two supplementary aggregates.

2. The base element should be kept at a certain distance away from the boundary surfaces of the specimen, such that the virtual sphere does not intersect the boundary surfaces.

3. The base element should have a minimum distance from the surfaces or edges of the surrounding aggregates (polytopes) created in the first batch with the 'take-and-place' procedure.

Condition 1 can be satisfied by checking the distance between the base element and any previously selected base elements (stored in a valid base elements array $VB_i(x_i, y_i, z_i)$, where i is the order number of the valid base element and (x_i, y_i, z_i) is its centroid coordinates), such that

$$\delta_k \geq 0.5(d_2 + d_p) \tag{7.11}$$

where d_2 is the diameter of the current virtual sphere, and d_p is the diameter of the virtual sphere for an already formed supplementary aggregate.

Condition 2 can be satisfied by checking the distance from the base element to any of the boundary surfaces. This distance by default should be greater than the radius of the virtual sphere. For a cubic or prismatic specimen, this condition may be

implemented more efficiently by creating a reduced specimen space by shrinking all sides by the same margin (equal to the radius of the virtual sphere), and checking that the base element falls within the shrunk space.

Condition 3 is checked after meeting the first two conditions. The procedure is not straightforward and involves several considerations, as detailed below.

a) The primary check is the normal distance from the base element to the surfaces of an existing aggregate polytope, i.e. the distance r_n shown in Figure 7.8. The centroid point for each candidate base element is available after the meshing (herein from the post-processor LS-PREPOST 4.2). Its normal distance to a surface of a polytope can be calculated using the following formula:

$$\left|r_n\right| = \frac{\left|ax_0 + by_0 + cz_0 + d\right|}{\sqrt{a^2 + b^2 + c^2}} \tag{7.12}$$

where point $P_0 = (x_0, y_0, z_0)$ represents the centroid of the base element, and the plane representing a surface of a polytope being checked is $ax + by + cz + d = 0$.

Geometric data generated in the Take-and-Place procedure are processed to establish the planes for all the surfaces of an aggregate polytope. These geometric data include the coordinates of all the vertex points, and the three co-planar vertex points for each surface of the polytope. These data are extracted from the output of the convex hull generation procedure in MATLAB described in Section 7.2.2.

Let the three vertex points on a surface of a polytope be $A(x_1, y_1, z_1)$,$B(x_2, y_2, z_2)$ and $C(x_3, y_3, z_3)$, the normal vector of the surface can be obtained as:

$$\vec{n} = \overrightarrow{AB} \times \overrightarrow{AC} = \begin{vmatrix} \vec{i} & \vec{j} & \vec{k} \\ x_2 - x_1 & y_2 - y_1 & z_2 - z_1 \\ x_3 - x_1 & y_3 - y_1 & z_3 - z_1 \end{vmatrix} = ai + bj + ck \tag{7.13}$$

The equation for the plane is therefore:

$$a(x - x_1) + b(y - y_1) + c(z - z_1) = 0 \tag{7.14}$$

This equation can be re-written in a general form as:

$$ax + by + cz + d = 0 \tag{7.15}$$

where $d = -ax_1 - by_1 - cz_1$.

By default, the normal distance should be equal or greater than the radius of the virtual sphere, i.e.

$$|r_n| \geq r_0 = 0.5d_2 \tag{7.16}$$

b) As can be seen from Figure 7.8, for a candidate base element "k", only the surfaces of adjacent polytopes that are likely to bound the virtual sphere should be checked. Checking against unrelated surfaces of polytopes not only waste the computing time, but may result in false rejection of a valid base element because of not meeting the normal distance criterion to these irrelevant surfaces.

To identify the surfaces of polytopes that need checking, we propose to define a proximity spherical region $S(i)$ surrounding the base element under consideration. The spherical region is drawn from the candidate base element with an enlarged radius equal to two times of that of the virtual sphere, i.e. $r_1 = 2r_0 = d_2$. A surface whose centroidal distance to the base element falls within the spherical domain $S(i)$ is considered as a relevant surface and will subsequently be checked, otherwise the surface is considered to be outside the region of interest and will not be checked. Surfaces identified as within the proximity region will be stored in an array called $SurDom(k,j)$, where k is the order number of the spherical domain and j is the serial number of the surfaces within the spherical domain.

All surfaces stored in $SurDom(k,j)$ are checked with respect to the normal distance criterion for the validation of the base element. The default criterion has been expressed in Eq. (7.16). If the distances from the base element to all these surfaces satisfy the criteria, the base element is valid. Otherwise additional checks will be warranted, as explained next.

c) If the above normal distance check fails for a particular surface, another layer of check is entered into operation to ensure that the surface is not one that is only marginally related to the base element, such as "e" and "f" in Figure 7.8. As

schematically shown in the figure, “e” and “f” have been identified to be within the proximity sphere, but they are not “facing” the base element and therefore checking for the normal distance criterion is not reasonable and could result in rejection of a valid base element such as element “k” shown in the figure.

For simplicity, the following additional checks are carried out in conjunction with the normal distance check, such that when a normal distance check to a surface fails, the base element will be rejected only if any of the following conditions is met:

i) the distance from the base element to any vertex point of the surface is smaller than the specific limit, which by default will be r_0. (Otherwise the virtual sphere will surely intersect with the surface)

ii) the distance from the base element to the centroid of the surface is smaller than r_0, and

iii) the distance to the middle point of any edge of the surface is smaller than the specific limit, which by default is also taken as r_0.

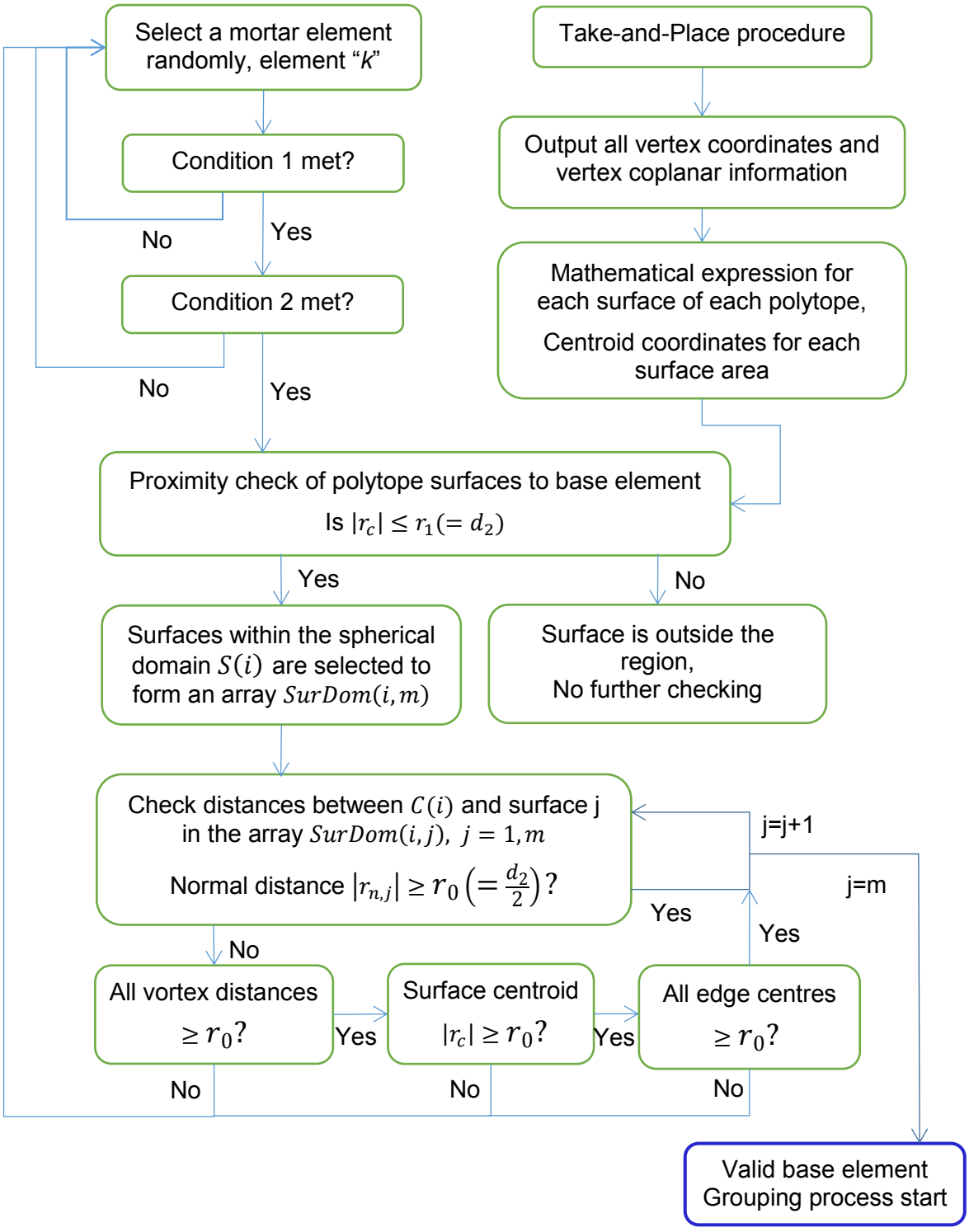

Figure 7.9 Flowchart for selection of a base element for a supplementary aggregate

Conditions ii) and iii) above are designed to cater for the extreme situation where the size of the current virtual sphere is considerably smaller than the size of the surface being checked against; in such a situation passing the vortex points check may not guarantee that there is sufficient space between the base element and the surface.

A special case worth noting is that there may be no element in the array $SurDom(i,j)$ for a candidate base element. This means the candidate base element is at least d_2 distance away from the centroid point of any surface in any existing polytope. Therefore this base element can be directly progressed as a valid base element without further checking.

The flowchart for the validation of a base element is shown in Figure 7.9.

7.3.2.2 Grouping process

After successfully selecting a valid base element, the next step is to create a new aggregate by grouping the mortar elements within the virtual sphere. The aggregate grouping process and the corresponding ITZ layer identifying process can be carried out simultaneously in this step. The procedure is as follows:

1. A mortar element is taken and checked. If all the four nodes of the mortar element are within the virtual sphere, the element is attributed the aggregate property and thus clustered into the new aggregate.

2. On the contrary, if none of the nodes of the mortar element is within the virtual sphere, the element remains as mortar and retains its mortar material property.

3. If some of nodes of a mortar element are within the virtual sphere while the remaining nodes are not, then the element is crossing the interface element and is given the equivalent ITZ property.

It should be pointed that because the space remaining for grouping is highly irregular and unstructured, some clusters formed in this way may not have the required volume to fall within the targeted size segment. To eliminate such clusters an equivalent volume check is included to judge the validity of the cluster to become an

aggregate. For simplicity the critical volume is defined as the volume of the smallest sphere within the size segment, i.e. $V_{cr} = 4\pi(d_1/2)^3/3$ in the aggregate size segment of $[d_1, d_2]$.

The volume of each newly generated aggregate through the above grouping procedure can be obtained by adding all elements included in the cluster. The volume of an individual element can be calculated from the coordinates of all nodes of the element which can be directly output after the FE meshing. In the present mesoscale model tetrahedron element is used to mesh the 3D mesoscale structure. Let the coordinates of the four nodes of a tetrahedron element be $N_1(x_1, y_1, z_1)$, $N_2(x_2, y_2, z_2)$, $N_3(x_3, y_3, z_3)$ and $N_4(x_4, y_4, z_4)$, respectively, the volume of the element can be calculated by the standard expression:

$$V = \begin{vmatrix} 1 & 1 & 1 & 1 \\ x_1 & x_2 & x_3 & x_4 \\ y_1 & y_2 & y_3 & y_4 \\ z_1 & z_2 & z_3 & z_4 \end{vmatrix} \tag{7.17}$$

The grouping cluster can be considered as a valid secondary aggregate only when its volume is no smaller than a nominal volume for the size range to which the new aggregate is supposed to belong. Otherwise the cluster would be discarded and the procedure will repeat from the very beginning where a new base element candidate is selected by random from the mortar domain. In this way the new aggregates generated here can be made to follow exactly the target size distribution.

Figure 7.10 shows the generation results of supplementary aggregates. It can be observed that all these aggregates are in reasonable gross shapes, although local irregularities exist as a result of grouping neighbouring mortar elements. Considering that the aggregates generated in this process are supplementary to the primary aggregates generated from the take-and-place procedure, the local irregularities are deemed to have only secondary effect, and hence are not further treated in the present study.

The final meso-structure can be determined subsequently after generating all the aggregates and identifying the corresponding ITZ layers, shown in Figure 7.11.

Comparing to Figure 7.5 and Figure 7.6 where only the primary aggregates from the take-and-place procedure are shown, the increased packing density due to the addition of the supplementary aggregates is remarkable.

Figure 7.10 Supplementary aggregates (3D isometric view)

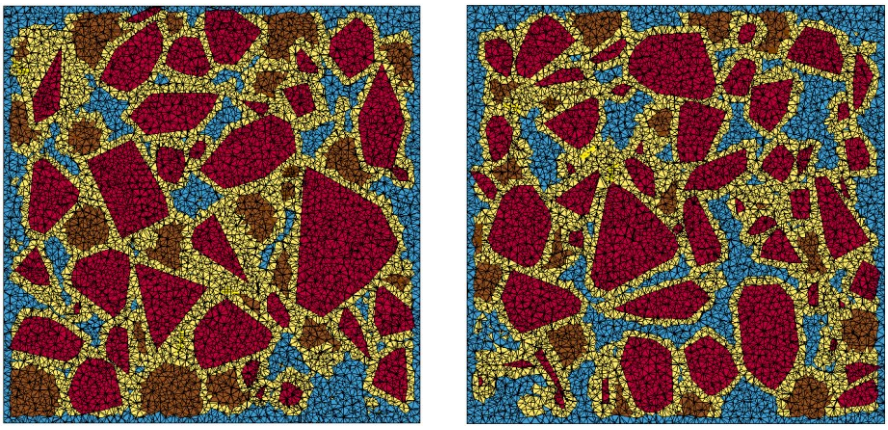

x = 20 cut plane view x = 40 cut plane view

Figure 7.11 Typical section views of final meso-structure of concrete

7.4 FE analysis of general behaviour of concrete using the mesoscale model

In this section, verification of the 3D mesoscale model is presented, and this is followed by the application of the model to simulate the behaviour of concrete under various loading conditions. The underlying meso-mechanical damage process will be examined and discussed.

7.4.1 Material model and material parameters

As stated in Chapter 3, from a mesoscopic perspective damage and fracture in concrete mainly occur in the mortar matrix and along ITZ. Therefore it is important to choose an appropriate nonlinear material model for these two components in order to properly describe the underlying damage process. For the present 3D mesoscale model, the K&C concrete damage model is also employed for these two parts considering its suitability under complex stress and loading conditions, including tension, shear, compression as well as the high strain rate dynamic loading.

The coarse aggregates in normal concrete are usually much stronger than the mortar matrix in strength and rigidity. Therefore for most quasi-static loading conditions, a simple linear-elastic material model can be considered for the aggregates similar to the treatment in Chapter 3. However for high dynamic loading such as shock and blast, the rapid propagation of stress wave could result in high stresses being developed in aggregates in a very different way as compared to low rate loading conditions, and this could subject the aggregates to potential failure (Song & Lu 2012). Under this circumstance, a nonlinear material model becomes necessary. Herein we also use the concrete damage model (K&C model) for aggregates with a failure strength matching that of the chosen aggregate type in this chapter.

Normal concrete of grade 30 MPa in cubic compressive strength (to be consistent with the mesoscale specimen configuration) is analysed using the mesoscale model. For this grade of concrete, the standard strength of mortar is around 35 MPa (Nagai et al. 2005; Lu & Tu 2011) The properties of the ITZ layer are difficult to determine precisely but it is generally known to be weaker and is about 50% of the strength of

the mortar matrix. For this reason, the ITZ layer is assumed to have a strength at 50% of the mortar strength. For the aggregates, a nominal strength of 150 MPa, representing natural crushed stones, is assumed. Table 7.1 summarises the material properties for mortar, ITZ and coarse aggregate for the 30 MPa concrete in the mesoscale model.

Table 7.1 Material parameters

Component	Compressive strength f_c (MPa)	Density ρ (kg/m^3)	Poisson's ratio ν (--)
Aggregate	150	2600	0.23
Mortar	35	2000	0.2
ITZ	17.5	2000	0.2

As it has already been commented in Chapter 3 (Section 3.3.3), in the concrete material model used (K&C model) a crack localisation band width L_c is employed to control the mesh sensitivity of the softening stage of the response, such that the total fracture energy over the L_c band would be constant and equal to the physical material fracture energy G_f. The default value for L_c is set at 25.4 mm, presuming a nominal aggregate size of 1/3 inch (8.5 mm) as is often used in protective structures, and that a coarse mesh with element size on or above the base value of 25.4 mm is employed. For models in which the element size (h_c) is smaller than this, L_c should normally be set equal to h_c if softening is certain to localise within one element band such as in simple tension, otherwise L_c will be multiples of h_c and the precise choice will be subject to empirical judgement. For the mesoscale model herein and under general loading (other than direction tension or shear) it has been found that $L_c = 12$ mm is adequate and this value is used in all compression analyses.

7.4.2 Model setup

3D mesoscale model of a cube specimen is developed. The size of the cube is 50 mm, which is commonly used in dynamic testing of concrete samples and is also a

suitable size for quasi-static testing with coarse aggregates in a size range of 4-12 mm. It is worth noting that without considering any defects the model may be regarded as representing a 150 mm cube if all dimensions are scaled up by a factor of 3.

Figure 7.12 shows the numerical model setup for uniaxial loading. The specimen is restrained at the bottom along the axial direction, i.e. all nodes on the bottom face are restrained in the z-axis but set free in the lateral (x- and y-axis) directions, while loading is applied from the top face in the z direction. Other boundary conditions can be simulated by imposing different lateral constraints on the top and bottom faces; for instance a complete restraint in the lateral directions would simulate an upper bound friction condition at the loading and support faces. Specific confinement can also be simulated by imposing a given level of confining stress on the side faces.

In order to be able to produce the full range of the concrete response including the softening stage, the loading is applied in a displacement-controlled manner through imposing a velocity boundary condition. The transient analysis code LS-DYNA is employed to perform the analysis using an explicit time integration scheme.

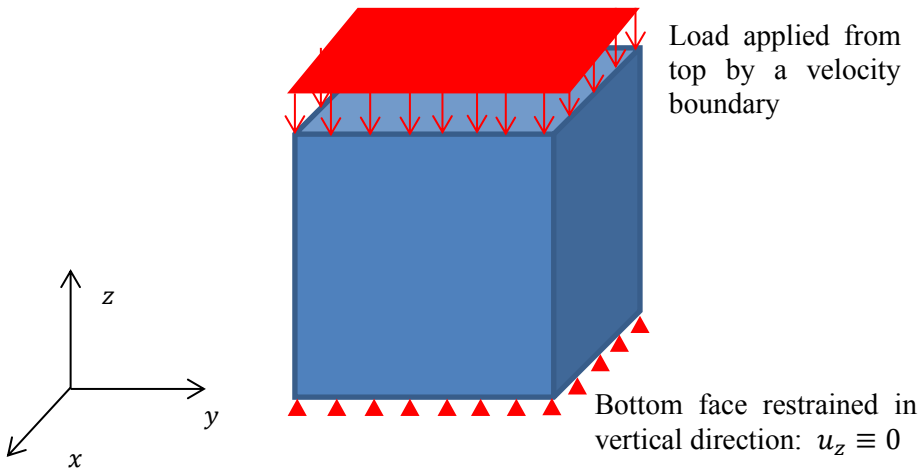

Figure 7.12 Model configuration

To minimise spurious oscillation in the simulation of quasi-static loading with an explicit transient analysis procedure, the loading through the velocity boundary condition is made to follow a smoothed transition pattern.

As stated before tetrahedral meshing is used in the present 3D mesoscale model to mesh the highly unstructured multi-layer domains. For tetrahedral mesh, several element formulations are available in general FE packages including LS-DYNA. Considering the fact that in the 3D mesoscale model the mesh is already considerably fine due to the need to mesh the mesoscale geometry, the 4-node tetrahedron element is employed after a mesh sensitivity study comparing the use of the 4-node and 10-node tetrahedron elements as well as the 8-node hexahedron element at the mesoscale mesh resolution for the 50-mm concrete cube specimen.

7.4.3 Verification under quasi-static compression

The 3D mesoscale cubic specimen is examined firstly under a quasi-static compression. It is generally known that the compressive behaviour of a concrete specimen can be strongly influenced by the frictional constraint between the specimen and loading platen (Van Vliet & Van Mier 1995). In the current 3D mesoscale model, it is possible to simulate the varying friction force applied on the loading face by incorporating the friction coefficient after defining the mutual contact between specimen and a loading platen. For simplicity, two borderline scenarios are simulated herein; the lower bound is represented by a friction-free condition while the upper bound is represented by a complete lateral constraint on the top and bottom faces. The friction effect in typical laboratory tests should fall in-between the two borderline conditions.

The computed axial stress - strain curves for the above mentioned lower and upper boundary conditions are shown in Figure 7.13(a). A pair of experimental curves with “low” friction and “high” friction are shown in Figure 7.13(b) for a comparison. Note that the grade of concrete in the experiment was not exactly 30 MPa so the absolute strengths would not be compared.

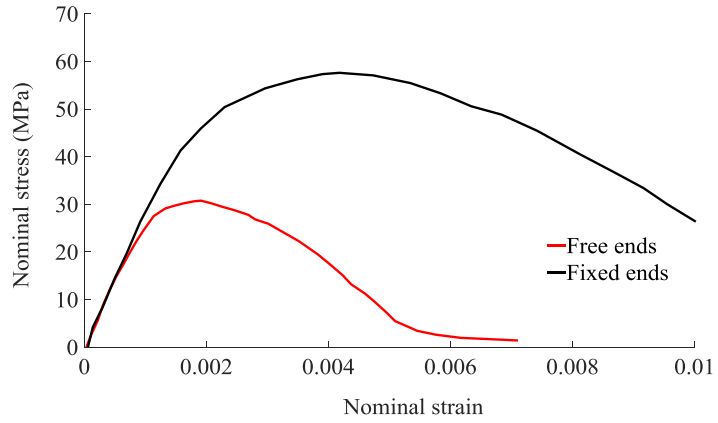

(a) Computed curves

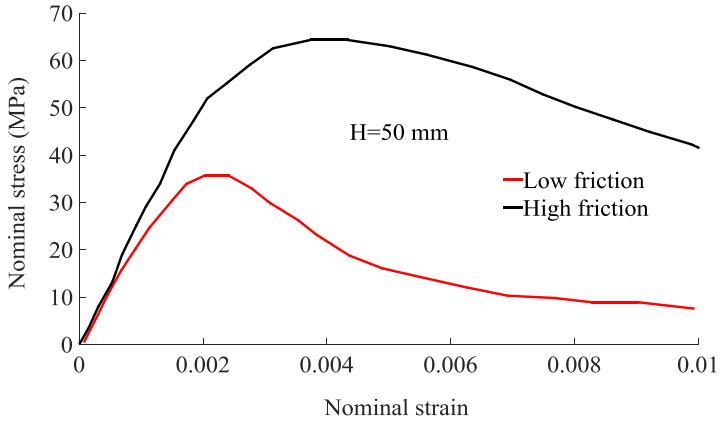

(b) Typical experimental curves (Van Vliet & Van Mier 1995)

Figure 7.13 Computed stress strain curves in comparison with typical experimental results

As can be seen, the results from the mesoscale model show very good overall agreement with the experimental data in terms of elastic response (modulus), peak strains, and softening phase of the response. Both the computed and experimental results exhibit strong effect of the loading boundary conditions.

Figure 7.14 and Figure 7.15 show the damage patterns for low and high surface frictions respectively. The damage is represented by the plastic strain and this will be employed in similar damage illustrations hereinafter. Both of the global damage patterns and internal macro crack patterns agree well the experimental observations.

Under the zero/low friction condition (Figure 7.14) it can be seen that the specimen was effectively separated into a series of small columns by the formation of the macro-cracks which were basically parallel to the applied load. From the internal crack section, the cracks appear to follow the weakest path throughout the whole specimen and concentrate in the ITZ zones. The coalescence of the damaged areas finally results in the failure of the specimen and this is clearly observed in the global damage pattern. Under a friction boundary, as seen from Figure 7.15, lateral confining stress develops as the specimen deforms, and the confinement is largest in the triangular (cone-shaped) regions zones near the end faces. Cracks grow more rapidly in the material outside the confined zones and eventually lead to the well-known "hour glass" failure mode.

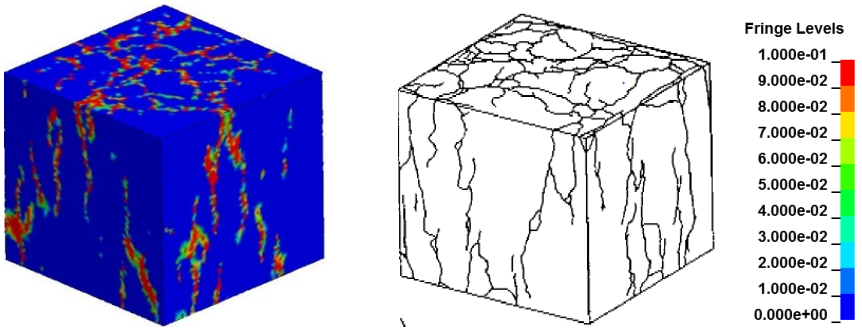

(a) Global damage patterns (colour scale represent plastic strain hereinafter)

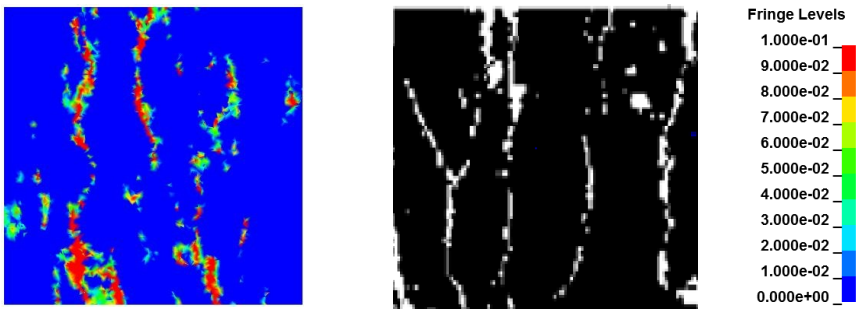

(b) Internal damage patterns

Figure 7.14 Damage patterns comparison under lower loading-face friction between numerical results (left) and experimental observations (right) (Vonk 1992)

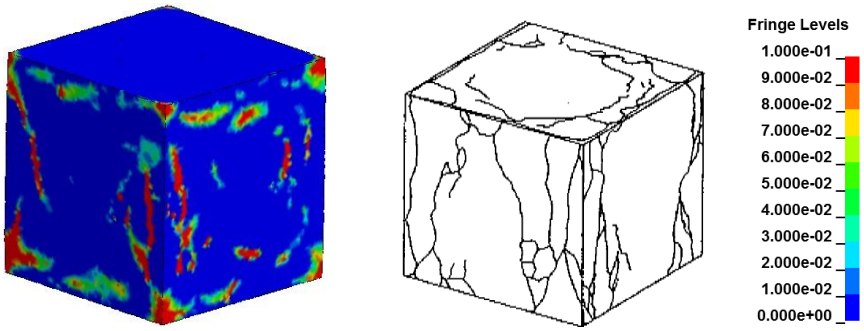

(a) Global damage patterns

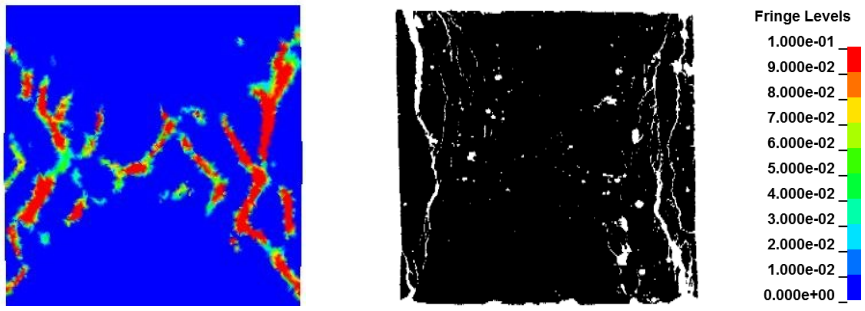

(b) Internal damage patterns

Figure 7.15 Comparison of damage patterns under high surface friction between numerical results (left) and experimental observations (right) (Vonk 1992)

7.4.4 Verification under quasi-static tension

In this section, the 3D mesoscale model is used to analyse the behaviour of concrete under uniaxial tension. The same material property parameters as in the compression analysis are used. Usually in modelling of concrete under tension, an artificially enhanced layer at each end of the specimen would be required to avoid premature damage occurring at loading faces due to stress concentration in the numerical model. However with a mesoscale model this treatment does not seem to be necessary, and trial simulations indicate that damage can hardly appear at the loading faces because the interface elements between aggregates and mortar tend to present weaker links within the loaded specimen. This feature in its own right shows already the advantage of the mesoscale model in better representing the damage mechanisms. For this reason, the velocity loading boundary condition is applied directly on the top

face in a same fashion as the compression loading. No lateral constraint (friction) is considered in the simulation of tension.

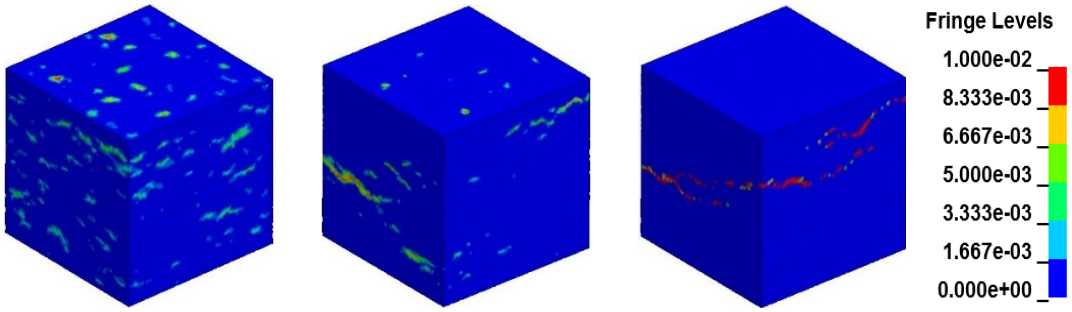

Pre-peak peak load post-peak

Figure 7.16 Development of crack patterns

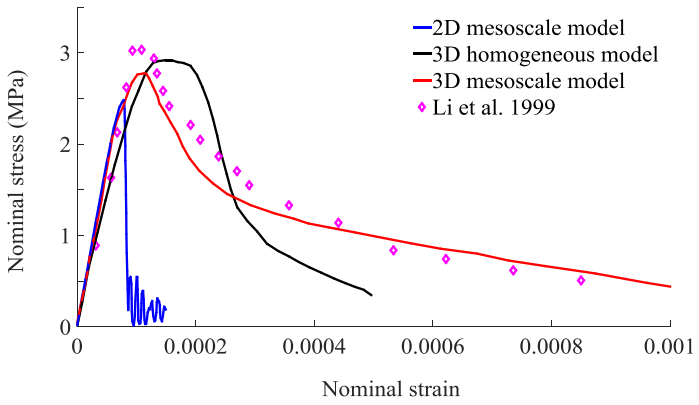

Figure 7.17 Computed nominal stress-strain curve under direct tension

Figure 7.16 depicts a typical simulated fracture process of concrete under uniaxial tension. The corresponding tensile stress-strain curve is given in Figure 7.17. It can be observed that upon the peak stress many micro-cracks developed and are spread mostly around the interface zone between mortar and aggregates. As the strain increases, macro cracks develop gradually while the other micro-cracks stop opening further. As the applied deformation further increases, localization which is a well-known phenomenon in tension can be observed clearly from the 3D mesoscale simulation.

The direct tensile strength obtained in 3D mesoscale model is around 2.7 MPa, which is reasonable for the 30-MPa concrete under consideration. The strain at peak strength is around 1.2×10^{-4} which agrees very well with many experimental observations (Li & Ansari 1999; Swaddiwudhipong et al. 2003). Here if we also compare the results with the ones computed from 2D mesoscale model in (Lu & Tu 2011) the 3D model again produces more reliable results than 2D model; in the 2D analysis the strain around peak load is much lower than the expected value. The relative lower strains at peak loads under both compression and tension indicate that 2D mesoscale model lacks the ability to produce realistic stress and strain states in concrete specimen. As for result from the 3D homogeneous model, it seems the softening part after peak load is too brittle. This may be because the homogeneous model fails to predict a curve path of crack propagation. Due to the existence of strong aggregate, the crack would propagate around the aggregate, which would consume more energy.

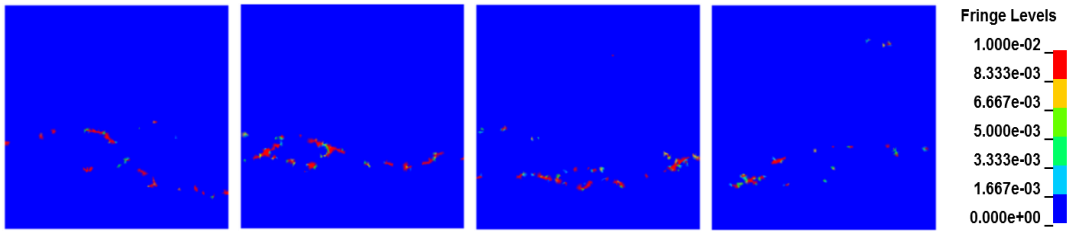

$x = 5$ $x = 15$ $x = 30$ $x = 45$

(a) x-cut sections

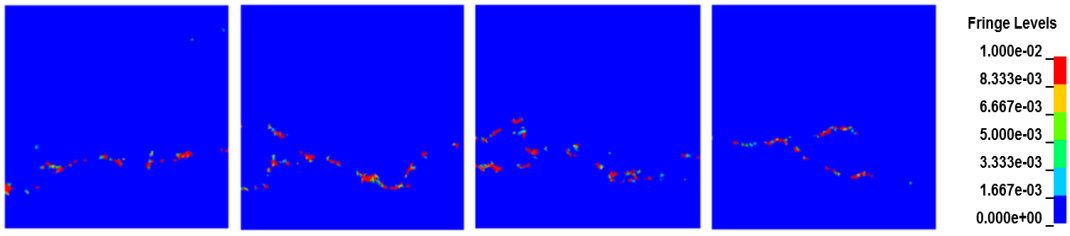

$y = 5$ $y = 15$ $y = 30$ $y = 45$

(b) y-cut sections

Figure 7.18 Internal crack patterns

The current 3D mesoscale model successfully predict this mechanism, which is evident from the internal crack pattern in Figure 7.18 from a few cut-sections in the x and y directions. It can be seen that the crack propagation path is not smooth, as would be in the case with a homogenous FE model, and follows clearly the track of the interface between mortar matrix and the aggregate particles. Some well-known fracture mechanisms such as crack deflection, crack branching and bridging can be well observed from the crack patterns on the cut sections.

7.4.5 Analysis of confined compression

The compressive behaviour of concrete is known to be sensitive to the lateral confinements. Generally speaking, with the increase of lateral confinement pressure, both the compressive strength and the ductility tend to show significant enhancement (Imran & Pantazopoulou 1996; Sfer et al. 2002; Papanikolaou & Kappos 2007).

The 3D mesoscale model is tested under confined compression. Several levels of confining stress are considered in the simulation, namely 1.5, 4.5, 9 and 30 MPa. For these simulations, the loading method for the confined compression is similar to that described in Chapter 4, except that the confining pressures are applied on all the side faces of the specimen in the 3D model here.

The axial stress - strain responses of the specimen at different levels of the confining pressure are presented in Figure 7.19. As expected the compressive strength of the concrete increases markedly with the increase of the confining pressure. Under relatively low confining pressure, the axial stress-strain curves exhibit well-defined peaks and clear softening branches. Both the peak strength and the ductility increase persistently with the increase in the confining pressure. Under further increased confinement, the post-peak branch turns to be flat and with an eventually exhibit a hardening stage. The transition from post-peak softening to hardening, i.e. the compressive behaviour of concrete specimen changes from quasi-brittle to apparently ductile, happens with a confining pressure of the order of 9 MPa. This phenomenon echoes very well the observations from other studies (Sfer et al. 2002; Papanikolaou & Kappos 2007). A comparison with the experimental data from (Sfer et al. 2002) is also given in Figure 7.19. A good agreement can be observed in general. It is noted

that at a high level of confinement with a pressure of 30 MPa, the numerical result appears to overestimate the confined strength, especially in the early nonlinear stage. This may be related to the fact that the experimental specimens were cylinders (150 mm in diameter and 300 mm in length) whereas the 3D mesoscale model is a cube of 50 mm. Nevertheless a good agreement in the overall comparison is evident.

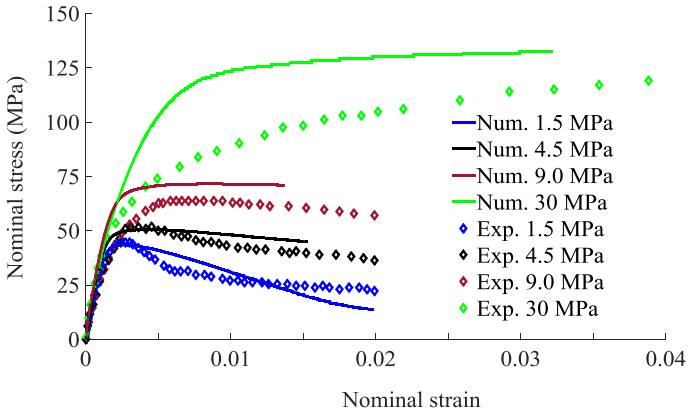

Figure 7.19 Axial stress strain response under different levels of confining pressures.

Figure 7.20 shows damage patterns from the 3D mesoscale model. As can be seen, the failure crack patterns for different levels of confining pressures are different. In the lower confining pressure end, the macro-cracks at failure are nearly vertical (parallel to the axial compression), showing a splitting mode of failure. As the confining pressure increases, the damage (crack) zone becomes increasingly less oriented, and eventually turns into a crushing failure with well distributed fracture throughout the whole specimen. Experimental evidences (e.g. Rutland & Wang 1997) tend to show a similar trend.

From all of these comparisons, it is reasonable to say that the 3D mesoscale model has the capability to estimate the real stress strain state and the damage behaviour under various loading conditions with acceptable accuracy. Therefore a true 3D mesoscale model becomes a desirable solution to predict and better understand the failure mechanisms of concrete from micromechanical analysis. The model is further applied in the analysis of dynamic compression of concrete, which will be discussed in the next section.

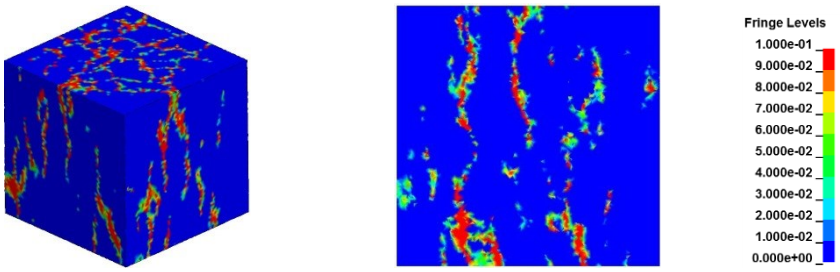

(a) 0 MPa

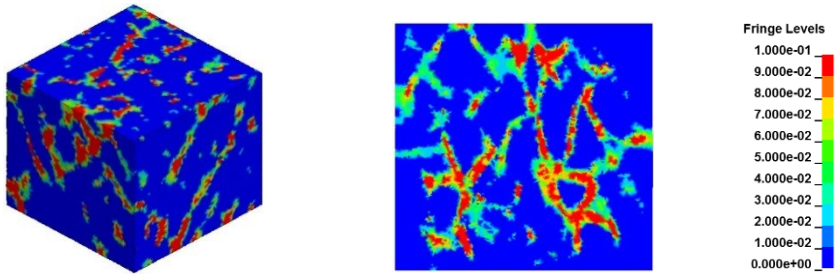

(b) 4.5 MPa

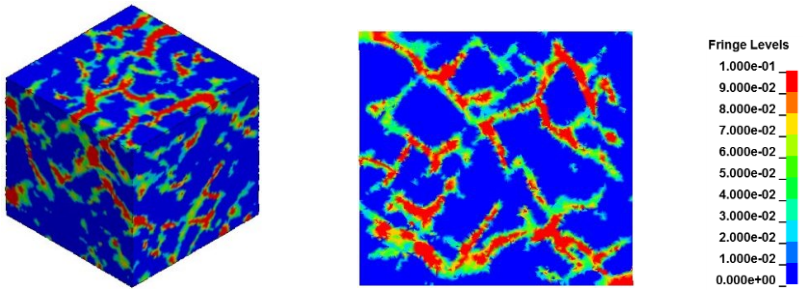

(c) 30 MPa

Figure 7.20 Global and internal damage patterns for different confining pressures

7.5 Application to dynamic compression

In this section the 3D mesoscale model is employed for a dynamic analysis of concrete under high strain rate compression. Experimental data on the dynamic compression of concrete generally suggest an apparent increase of the dynamic compressive strength with the increase of the strain rate, and a dynamic increase factor (DIF) is customary used in the engineering community to account for the strength enhancement due to high strain rates. However, the true mechanism

underlying the occurrence of the DIF is still a subject of continued debate. As far as dynamic compression is concerned, a prevailing theory suggests that the DIF is largely attributed to the lateral inertial confinement (e.g. Donze et al. 1999; Li & Meng 2003). More recent numerical studies using 2D-type mesoscale models provide further support to this argument (e.g. Zhou & Hao 2008a; Lu et al. 2010) and further point out possible contribution of the mesoscale heterogeneity towards the dynamic strength enhancement. However, a full representation of the mesoscale heterogeneity effect could only be achieved with a true 3D mesoscale.

The application of the present 3D mesoscale model to simulate the dynamic compression is straightforward. The dynamic loading is simulated by applying a velocity boundary condition in a similar way as in the quasi-static analysis, but with a high velocity in order to achieve a desirable strain rate and stress distribution. Note that in the dynamic simulation herein, no friction is considered at the loading face. To facilitate a direct observation of the contribution of the structural inertial effect, the constituent materials are considered to be rate insensitive, i.e., no embedded strain rate enhancement factor is adopted in the material properties in all the models. Thus any increase in the apparent compressive strength of the simulated test specimen is attributable only to the sample-wide dynamic effect, as well as the material heterogeneity. The apparent dynamic compressive strength is evaluated from the average peak stress on both the loading and supporting faces. For a comparison, a 2D homogeneous model, a 2D mesoscale model and a 3D homogeneous model are also analysed for the same variation range of the strain rates.

Figure 7.21 shows the variation of the predicted DIF with the strain rate from the simulations using the models mentioned above. Four empirical equations on DIF of concrete from the literature (MC90 1993; Tedesco et al. 1994; Grote et al. 2001a; Lu & Xu 2004) are also included for a comparison.

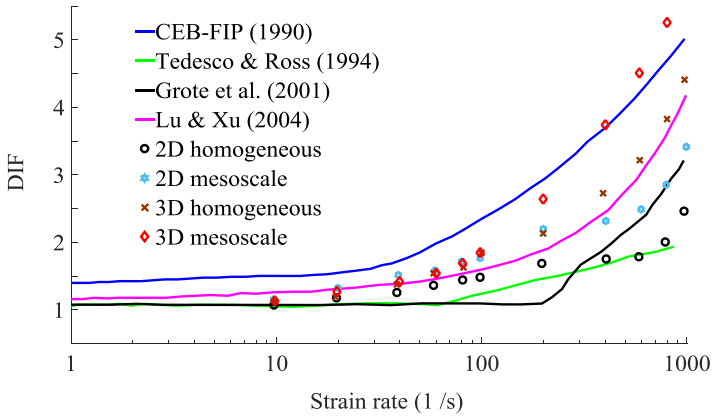

Figure 7.21 Predicted DIF with the strain rate

It is worth mentioning here that for dynamic compression test there is an upper limit of the strain rate concerning the stress and strain uniformity requirement upon the specimen reaching failure, and this strain limit is directly related to the length of the specimen. For 30-MPa concrete specimen of 50 mm in length a strain rate up to about 100 s^{-1} is considered as acceptable (Song & Lu 2012). Beyond this strain rate limit the peak stress at the loading and reaction ends may not be reached at the same time. A detailed discussion on such a phenomenon is beyond the scope of the present analysis. Herein for simplicity the apparent dynamic strength is evaluated as the average of the peak stresses at the loading and reaction ends, regardless whether they have been reached at the same time.

As can be observed from Figure 7.21, all models exhibit an apparent increase in the compressive strength as the strain rate increases, despite that no strain rate enhancement has been incorporated in the material constitutive model. The general trend of the DIF curves in numerical models resemble well with the curves given by the empirical formulas. The 3D mesoscale model tends to predict the upper bound DIF among all numerical results, and this is deemed to be attributable to the enhanced contribution from the aggregates, as well as a fuller representation of the inertial confinement effect. Further comparison of the DIFs between 2D and 3D numerical models shows that the 2D numerical models markedly underestimate the DIF in the specimen, due apparently to an insufficient representation of the lateral inertial-induced confining effect in the third direction.

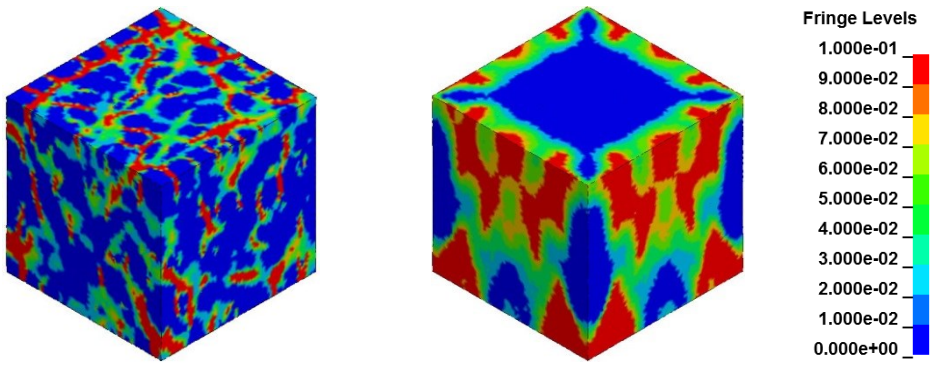

Figure 7.22 Damege distribution at strain rate 200 /s (left: 3D mesoscale model; right: 3D homogeneous model)

The mesoscale heterogeneity is believed to contribute to the dynamic compression strength increase in two aspects, namely a) by promoting the distribution of damage (fracture) and thus better mobilise the strength of the specimen as a whole; this is evident from the damage distributions in Figure 7.22, and b) by having the stronger aggregates participate directly in the resistance, thus boost the overall stress level which then manifests as an increase of the apparent strength. This can be examined easily from the stress level achieved in the aggregates in the 3D mesoscale model. Figure 7.23 shows the damage distributions in aggregates at the peak load stage for different strain rates. Note that damage only occurs in aggregates if the stress attained the "yield" strength level of 150 MPa. It can be seen that damage in aggregates appears under a strain rate of 50 s^{-1} and it becomes increasingly more significant as the strain rate further increases.

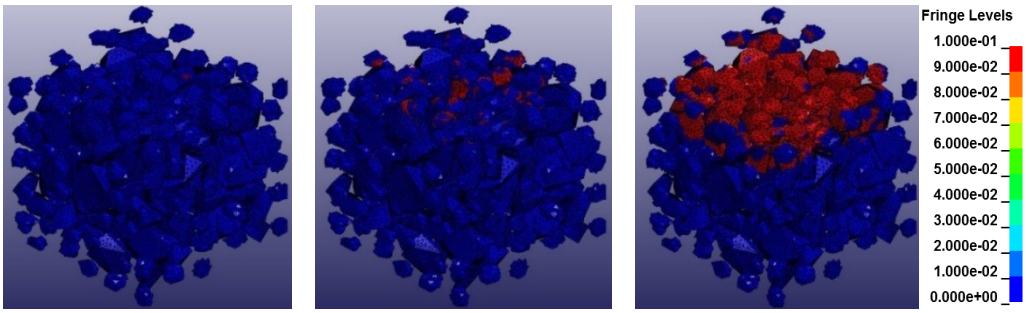

Strain rate 50 (1/s) Strain rate 200 (1/s) Strain rate 400 (1/s)

Figure 7.23 Damage conditions of aggregates at peak load

7.6 Conclusions

A comprehensive procedure has been developed to generate 3D mesoscale finite element model for concrete-like materials that can accommodate realistic (high) packing density of aggregates.

The mesoscopic geometric structure of a concrete specimen is generated in two steps. A take-and -place procedure is employed first to produce and pack convex polytopes as aggregates into a specimen space, which is a cube or prism in the present study. A fast detection of particle inclusion intersection procedure and a translate-and-rotate procedure are incorporated to enhance efficiency and effectiveness of the packing process. Finite element meshing is subsequently made using an efficient meshing code suitable for meshing the highly unstructured domains due to the existence of randomly shaped aggregate particles. The interface elements are formed by selecting an equivalent layer of elements surrounding the aggregate particles.

To tackle the shortcoming of the take-and-place procedure in terms of a limited packing density (in the range of 30-34%), an algorithm to identify and group suitable mortar elements into supplementary aggregates has been developed. The algorithm enables the supplementary aggregates to largely retain the randomness in the size and location of the aggregates, and at the same time fit to a desired grading curve.

The 3D mesoscale is verified in the simulation of the quasi static response of concrete under uniaxial compression, uniaxial tension, as well as confined compression. The simulated results resemble favourably the corresponding experimental observations.

The 3D mesoscale is also applied for simulation of the dynamic behaviour of concrete under high strain rate compression. Comparisons between the 3D mesoscale model and other modelling approaches demonstrate clearly the advantages of the 3D mesoscale model in terms of realistic representation of the stress field and the effect of the inertial confinement, as well as the participation of the aggregates in the dynamic resistance under high strain rates.

The procedure presented in this chapter for the 3D mesoscale model is readily applicable for material investigation of concrete, with no restriction on aggregate shapes and volumetric ratios, or loading and boundary conditions. The model can also be implemented in the analysis of a structural component where the stress conditions may be highly complicated. To control the computational cost in a structural component analysis it is possible to incorporate a two-scale approach such that the critical regions are modelled by the mesoscale model while the remaining regions by a homogenous model. As the 3D mesoscale model is developed in a continuum framework, interface between different scale regimes within the model domain is straightforward.

Chapter 8: Conclusions and recommendations for future work

The principal objective of this research has been to advance the development of mesoscale modelling for concrete-like materials and to analyse the intrinsic failure mechanisms of concrete-like material from a mesoscale point of view. To this end, new developments have been carried out to the mesoscale modelling framework to cater for the needs of simulating the fracture process in concrete under complex loading conditions, with a particular focus on two key aspects: a) realistic representation of the 3D meso-structure of concrete by achieving random aggregate particles and at the same time enabling the realisation of high density packing of aggregates; b) realistic modelling of the fracture process of concrete by developing a cohesive plus contact interface approach which allows modelling the micro-crack initiation and propagation.

The mesoscale models are subsequently applied to investigate into the micromechanical failure mechanisms of concrete, including fracture propagation in tension and compression, the well-known size effect, and the strain rate effect under high rate loading.

8.1 Summary of main conclusions

8.1.1 Mesoscopic analysis of size effect in concrete materials

The following specific conclusions have been drawn on the size effect phenomenon:

1. The mesoscale heterogeneity has a sensible influence on the shape and size of the fracture process zone (FPZ), which in turn influences the size effect.

2. The width of the fracture process zone is insensitive of the beam size, which may therefore be considered as a material constant. This is consistent with existing theory about the size effect

3. The length of FPZ at maximum load is strongly dependent on the beam depth. The greater the beam depth, the longer is the fracture process zone. But the relative (normalised) length of fracture process zone at peak loading point, measured by the ratio of length of FPZ to the beam depth, tends to show an opposite trend, that it actually decreases with the increase of the beam size.

4. The stress interaction theory proposed has led to the establishment of a quantitative relationship between the nominal strength and the FPZ property parameters. Verification on the numerical simulation data shows the relationship predicts the size effect on the nominal strength rather accurately.

8.1.2 3D mesoscale finite element modelling of concrete

A comprehensive 3D mesoscale model framework for modelling of concrete allowing the realisation of practically any shapes and packing density of aggregates is developed.

1. The current 3D mesoscale model can produce more reliable results than 2D mesoscale model or other homogenous models regarding to the stress and strain states within concrete. Specifically, homogenous models or 2D mesoscale model are highly dependent upon material constitutive behaviour while the current 3D mesoscale model is not. The 3D model captures more accurately the inherent regularization effect of the heterogeneity created by the presence of random aggregates.

2. The numerical simulation results without material DIF in the constitutive model support the augmentation that the compressive dynamic strength enhancement is largely contributed by the lateral inertial confinement within the sample structure.

3. Numerical simulation results using the real 3D mesoscale concrete model clearly demonstrate the advantage of 3D mesoscale model on representing the real stress environment and the effect of the inertial confinement under high strain rate compression.

4. The mesoscopic heterogeneity can also make a significant contribution to the overall dynamic increase factor (DIF), especially on very high strain rate case like 200 /s above.

8.1.3 Modelling of the fracture process at mesoscale

To more realistically model the meso-mechanical fracture process in concrete, a cohesive and contact-friction interface approach is proposed to simulate ITZ in the mesoscale model. By enabling an explicit simulation of the crack initiation and propagation in concrete specimen, the model shows several advantages as follows:

1. The contact-friction mechanism is successfully introduced into the mesoscale concrete model, which effectively overcomes the problems with the classical cohesive model under complex loading conditions including compression.

2. The model allows the use of simple constitutive description of the bulk materials while nonlinear behaviour is achieved by the cohesive fracture and the friction behaviour through the interface elements.

3. The classical mesh-related problems in a continuum damage-based model for cracking are largely eliminated, making the model highly suitable for investigation of cracking behaviour for both quasi-static and dynamic application.

4. The model can explicitly simulate the micro-cracks initiation and propagation, which has brought new insight into the evolution of the fracture process at the mesoscale viewpoint.

8.1.4 Mesoscopic analysis of failure mechanisms in concrete

The intrinsic mechanisms governing the fundamental behaviour of concrete in terms of the local cohesive fracture process and friction process are further explored by applying the mesoscale cohesive plus contact model in various loading conditions, including quasi-static uniaxial tension, quasi-static uniaxial compression,

compression with lateral confinement, three-point bending and the dynamic strain rate loadings both in tension and compression.

1. The tensile strength of concrete material is dominated by the cohesion strength of ITZ, while the compressive strength of concrete materials is a result of the combined effects from actions of cohesion and friction along the micro-crack surfaces.

2. The well-known confining effect of concrete materials may be explained by the physical frictional theory from a mesoscale view point. As the lateral confinement increases, the normal pressures on crack surfaces will also rise, leading to an increase in the friction stress between two crack surfaces. Thus the global strength increases.

3. The material heterogeneity does have an influence on the DIF under dynamic loadings both for compression and tension, however the degree of influence is generally limited.

4. The mesoscale cohesive plus contact ITZ concrete model predicts rather accurate results of the strength enhancement under dynamic compression, which indicates that the friction resistance induced by lateral confinement during the dynamic compressive loading also contributes to the dynamic compressive strength enhancement (compressive DIFs).

5. The micro-inertial effect associated with cracking is largely responsible for the sensitivity of the dynamic tension resistance, thus contributing to the dynamic increase factor (DIF) of the dynamic tensile strength.

6. The micro crack inertial effect on the crack initiation and propagation can be well captured in the cohesive plus contact model by incorporating the intrinsic time scale into the cohesive constitutive model.

7. The numerical results from the cohesive plus contact model show that the micro-crack inertial effect can only be activated at a relatively high strain rate in the order of 100 /s, which supports the general argument from past studies

that there exists a transition of rate-sensitivity which divides the DIFs in tension into two distinctive regimes.

8. The growing distribution of the micro cracks with the increase of the loading rate also causes enhancement of the dynamic resistance as well as the strain energy.

8.2 Recommendations for further research

With the availability of the 3D mesoscale model, comprehensive numerical studies can be carried out to more systematically evaluate the effect of the meso-mechanical processes in influencing the failure mechanisms of concrete.

The 3D mesoscale concrete model can also be easily implemented in the analysis of a structural component where the stress conditions may be highly complicated. To control the computational cost in a structural component analysis it is possible to incorporate a two-scale approach so that the critical regions are modelled by the mesoscale model while the remaining regions may be modelled by homogeneous model. As the 3D mesoscale model is developed in a continuum framework, interface between different scale regimes within the model domain is straightforward.

At present the cohesive plus contact model has been realised in 2D mesoscale model. In principle the algorithm can be easily extended to 3D, and by doing so both realistic 3D stress environment and explicit representation of the fracture processes can be accommodated in a unified framework, allowing for numerical investigation in a further broadened spectrum of problems with concrete structures. Of course such a complete 3D mesoscale with cohesive and contact-friction capabilities will pose much increased demand on the computational cost, and in this respect enhancement in the computational efficiency will require dedicated research.

Finally, investigations into the potential coupling action between the size effect and the strain rate effect on the behaviour of concrete in dynamic loading conditions may provide additional explanations on the experimental observations of the rate and size dependence of the dynamic properties of the concrete materials.

References

ACI. (2008). Building code requirements for structural concrete (ACI 318-08) and commentary: *American Concrete Institute*.

Achintha, M., & Burgoyne, C. (2013). Fracture energy of the concrete–FRP interface in strengthened beams. *Engineering Fracture Mechanics, 110*, 38-51.

Ahn, H. T., & Shashkov, M. (2008). Geometric algorithms for 3D interface reconstruction. Paper presented at the *Proceedings of the 16th International Meshing Roundtable.*

Al-Rousan, T., Masad, E., Tutumluer, E., & Pan, T. (2007). Evaluation of image analysis techniques for quantifying aggregate shape characteristics. *Construction and Building Materials, 21*(5), 978-990.

Alam, S. Y., Kotronis, P., & Loukili, A. (2013). Crack propagation and size effect in concrete using a non-local damage model. *Engineering Fracture Mechanics, 109*, 246-261.

Alam, S. Y., Saliba, J., & Loukili, A. (2014). Fracture examination in concrete through combined digital image correlation and acoustic emission techniques. *Construction and Building Materials, 69*, 232-242.

Alfano, G., & Sacco, E. (2006). Combining interface damage and friction in a cohesive - zone model. *International Journal for Numerical Methods in Engineering, 68*(5), 542-582.

Barenblatt, G. I. (1962). The mathematical theory of equilibrium cracks in brittle fracture. *Advances in applied mechanics, 7*, 55-129.

Barpi, F. (2004). Impact behaviour of concrete: a computational approach. *Engineering Fracture Mechanics, 71*(15), 2197-2213.

Bazant, Z., Le, J.-L., & Hoover, C. G. (2010). Nonlocal boundary layer (NBL) model: overcoming boundary condition problems in strength statistics and fracture analysis of quasibrittle materials. *Fracture Mechanics of Concrete and Concrete Structures—Recent Advances in Fracture Mechanics of Concrete, B.-H. Oh, Ed., Korea Concrete Institute, Seoul*, 135-143.

Bažant, Z., & Pfeiffer, P. (1986). Shear fracture tests of concrete. *Materials and structures, 19*(2), 111-121.

Bazant, Z., & Planas, J. (1998). Fracture and size effect. *Concrete and Other Quasibrittle Materials, 16*.

Bazant, Z. P. (1984). Size effect in blunt fracture: concrete, rock, metal. *Journal of Engineering Mechanics, 110*(4), 518-535.

Bazant, Z. P. (1994). Nonlocal damage theory based on micromechanics of crack interactions. *Journal of engineering mechanics, 120*(3), 593-617.

Bažant, Z. P. (1999). Size effect on structural strength: a review. *Archive of applied mechanics, 69*(9-10), 703-725.

Bažant, Z. P. (2000). Size effect. *International Journal of Solids and Structures, 37*(1), 69-80.

Bažant, Z. P. (2004). Scaling theory for quasibrittle structural failure. *Proceedings of the National Academy of Sciences of the United States of America, 101*(37), 13400-13407.

Bazant, Z. P., & Jirásek, M. (2002). Nonlocal integral formulations of plasticity and damage: survey of progress. *Journal of engineering mechanics, 128*(11), 1119-1149.

Bažant, Z. P., & Oh, B. H. (1983). Crack band theory for fracture of concrete. *Matériaux et construction, 16*(3), 155-177.

Beddow, J. K., & Meloy, T. (1980). Testing and characterization of powders and fine particles. *Heyden and Son Ltd.,* 1980.

Benkemoun, N., Hautefeuille, M., Colliat, J. B., & Ibrahimbegovic, A. (2010). Failure of heterogeneous materials: 3D meso-scale FE models with embedded discontinuities. *International Journal for Numerical Methods in Engineering, 82*(13), 1671-1688.

Beton, C. E.-I. (1993). CEB-FIP model code 1990: design code. *No. 213, 214*.

Beyer, K., Abo-El-Ezz, A., & Dazio, A. (2010). Quasi-static cyclic tests on different types of masonry spandrels: *vdf Hochschulverlag AG an der ETH Zürich*.

Bobiński, J., Tejchman, J., & Górski, J. (2009). Notched concrete beams under bending--calculations of size effects within stochastic elasto-plasticity with non-local softening. *Archives of Mechanics, 61*(3-4), 283-307.

Borino, G., Failla, B., & Parrinello, F. (2003). A symmetric nonlocal damage theory. *International Journal of Solids and Structures, 40*(13), 3621-3645.

Brara, A., & Klepaczko, J. (2006). Experimental characterization of concrete in dynamic tension. *Mechanics of materials, 38*(3), 253-267.

Bresler, B., & Bertero, V. (1975). Influence of high strain rate and cyclic loading of unconfined and confined concrete in compression. Paper presented at the *the 2nd Canadian Conference on Earthquake Engineering.*

Buste, A., Lalbin, X., Worswick, M., Clarke, J., Finn, M., Altshuller, B., & Jain, M. (1999). Prediction of strain distribution in aluminum tailor welded blanks. Paper presneted at *the Numisheet.*

Caballero, A., López, C., & Carol, I. (2006). 3D meso-structural analysis of concrete specimens under uniaxial tension. *Computer Methods in Applied Mechanics and Engineering, 195*(52), 7182-7195.

Camacho, G. T., & Ortiz, M. (1996). Computational modelling of impact damage in brittle materials. *International Journal of solids and structures, 33*(20), 2899-2938.

Carol, I., Idiart, A., López, C., & Caballero, A. (2011). Cracking and fracture of concrete at meso-level using zero-thickness interface elements *Numerical Modeling of Concrete Cracking* (pp. 51-97): Springer.

Cedolin, L., Bisi, G., & Nardello, P. (1999). Mode II fracture resistance of concrete. *Concrete Science and Engineering, 1*(1), 37-44.

Chaboche, J., Girard, R., & Schaff, A. (1997). Numerical analysis of composite systems by using interphase/interface models. *Computational Mechanics, 20*(1-2), 3-11.

Code, C.-F. M. (1990). Evaluation of the time dependent behavior of concrete: September.

Cotsovos, D., & Pavlović, M. (2008). Numerical investigation of concrete subjected to high rates of uniaxial tensile loading. *International journal of impact engineering, 35*(5), 319-335.

De Berg, M., Van Kreveld, M., Overmars, M., & Schwarzkopf, O. C. (2000). *Computational geometry*: Springer.

Donze, F., Magnier, S.-A., Daudeville, L., Mariotti, C., & Davenne, L. (1999). Numerical study of compressive behavior of concrete at high strain rates. *Journal of engineering mechanics, 125*(10), 1154-1163.

Du, C., Sun, L., Jiang, S., & Ying, Z. (2011). Numerical simulation of aggregate shapes of three-dimensional concrete and its applications. *Journal of Aerospace Engineering, 26*(3), 515-527.

Duan, K., & Hu, X. (2004). Specimen boundary induced size effect on quasi-brittle fracture. *Strength, Fracture and complexity, 2*(2), 47-68.

Dugdale, D. (1960). Yielding of steel sheets containing slits. *Journal of the Mechanics and Physics of Solids, 8*(2), 100-104.

Erzar, B., & Forquin, P. (2010). An experimental method to determine the tensile strength of concrete at high rates of strain. *Experimental Mechanics, 50*(7), 941-955.

Erzar, B., & Forquin, P. (2011a). Experiments and mesoscopic modelling of dynamic testing of concrete. *Mechanics of Materials, 43*(9), 505-527.

Erzar, B., & Forquin, P. (2011b). Free water influence on the dynamic tensile behaviour of concrete. Paper presented at *the Applied Mechanics and Materials*.

Espinosa, H. D., & Zavattieri, P. D. (2003). A grain level model for the study of failure initiation and evolution in polycrystalline brittle materials. Part I: Theory and numerical implementation. *Mechanics of Materials, 35*(3), 333-364.

Falk, M. L., Needleman, A., & Rice, J. R. (2001). A critical evaluation of cohesive zone models of dynamic fractur. *Le Journal de Physique IV, 11*(PR5), Pr5-43-Pr45-50.

Fatima, E., Jhamb, A., & Kumar, R. (2013). Ceramic dust as construction material in rigid pavement. *American Journal of Civil Engineering and Architecture, 1*(5), 112-116.

Figueira, D., Sousa, C., Calçada, R., & Serra Neves, A. (2016). Design recommendations for reinforced concrete interfaces based on statistical and probabilistic methods. *Structural Concrete*.

Forquin, P., Riedel, W., & Weerheijm, J. (2013). Dynamic test devices for analyzing the tensile properties of concrete.

Galindo-Torres, S., Pedroso, D., Williams, D., & Li, L. (2012). Breaking processes in three-dimensional bonded granular materials with general shapes. *Computer Physics Communications, 183*(2), 266-277.

Gary, G., & Bailly, P. (1998). Behaviour of quasi-brittle material at high strain rate. Experiment and modelling. *European Journal of Mechanics-A/Solids, 17*(3), 403-420.

Gebre-Egzeabher, K. (2010). Mesh size effect on the dynamic response of engineering structures using numerical methods. Paper presented at *the EGU General Assembly Conference Abstracts.*

Georgin, J., & Reynouard, J. (2003). Modeling of structures subjected to impact: concrete behaviour under high strain rate. *Cement and Concrete Composites, 25*(1), 131-143.

Gerlach, S., Fiolka, M., & Matzenmiller, A. (2005). Modelling and analysis of adhesively bonded joints with interface elements for crash analysis. Paper presented at *the Proceedings of the LS-DYNA conference*, Bamberg.

Grassl, P., Grégoire, D., Solano, L. R., & Pijaudier-Cabot, G. (2012). Meso-scale modelling of the size effect on the fracture process zone of concrete. *International Journal of solids and structures, 49*(13), 1818-1827.

Grassl, P., & Jirásek, M. (2010). Meso-scale approach to modelling the fracture process zone of concrete subjected to uniaxial tension. *International Journal of Solids and Structures, 47*(7), 957-968.

Grégoire, D., Rojas-Solano, L., & Pijaudier-Cabot, G. (2013). Failure and size effect for notched and unnotched concrete beams. *International Journal for Numerical and Analytical Methods in Geomechanics, 37*(10), 1434-1452.

Grote, D., Park, S., & Zhou, M. (2001a). Dynamic behavior of concrete at high strain rates and pressures: I. experimental characterization. *International Journal of Impact Engineering, 25*(9), 869-886.

Grote, D., Park, S., & Zhou, M. (2001b). Experimental characterization of the dynamic failure behavior of mortar under impact loading. *Journal of Applied Physics, 89*(4), 2115-2123.

Häfner, S., Eckardt, S., Luther, T., & Könke, C. (2006). Mesoscale modeling of concrete: Geometry and numerics. *Computers & Structures, 84*(7), 450-461.

Hentz, S., Donzé, F. V., & Daudeville, L. (2004a). Discrete element modelling of concrete submitted to dynamic loading at high strain rates. *Computers & structures, 82*(29), 2509-2524.

Hentz, S., Daudeville, L., & Donzé, F. V. (2004b). Identification and validation of a discrete element model for concrete. *Journal of Engineering Mechanics, 130*(6), 709-719.

Hillerborg, A., Modéer, M., & Petersson, P.-E. (1976). Analysis of crack formation and crack growth in concrete by means of fracture mechanics and finite elements. *Cement and concrete research, 6*(6), 773-781.

Hu, X., & Duan, K. (2008). Size effect and quasi-brittle fracture: the role of FPZ. *International journal of fracture, 154*(1-2), 3-14.

Huang, Y., Yang, Z., Ren, W., Liu, G., & Zhang, C. (2015). 3D meso-scale fracture modelling and validation of concrete based on in-situ X-ray Computed Tomography images using damage plasticity model. *International Journal of solids and structures, 67*, 340-352.

Hughes, B., & Gregory, R. (1972). Concrete subjected to high rates of loading in compression. *Magazine of Concrete Research, 24*(78), 25-36.

Hughes, B., & Watson, A. (1978). Compressive strength and ultimate strain of concrete under impact loading. *Magazine of concrete research, 30*(105), 189-199.

Imran, I., & Pantazopoulou, S. (1996). Experimental study of plain concrete under triaxial stress. *ACI Materials Journal-American Concrete Institute, 93*(6), 589-601.

Jensen, R. P., Edil, T. B., Bosscher, P. J., Plesha, M. E., & Kahla, N. B. (2001). Effect of particle shape on interface behavior of DEM-simulated granular materials. *International Journal of Geomechanics, 1*(1), 1-19.

Jia, Z., Castro-Montero, A., & Shah, S. (1996). Observation of mixed mode fracture with center notched disk specimens. *Cement and Concrete research, 26*(1), 125-137.

Kim, K., & Lim, Y. M. (2011). Simulation of rate dependent fracture in concrete using an irregular lattice model. *Cement and Concrete Composites, 33*(9), 949-955.

Klepaczko, J., & Brara, A. (2001). An experimental method for dynamic tensile testing of concrete by spalling. *International journal of impact engineering, 25*(4), 387-409.

Koutromanos, I., & Shing, P. (2012). Cohesive crack model to simulate cyclic response of concrete and masonry structures. *ACI Structural Journal, 109*(3), 349-358.

Krayani, A., Pijaudier-Cabot, G., & Dufour, F. (2009). Boundary effect on weight function in nonlocal damage model. *Engineering Fracture Mechanics, 76*(14), 2217-2231.

Latham, J.-P., Munjiza, A., Garcia, X., Xiang, J., & Guises, R. (2008). Three-dimensional particle shape acquisition and use of shape library for DEM and FEM/DEM simulation. *Minerals Engineering, 21*(11), 797-805.

Leite, J., Slowik, V., & Apel, J. (2007). Computational model of mesoscopic structure of concrete for simulation of fracture processes. *Computers & structures, 85*(17), 1293-1303.

Leite, J., Slowik, V., & Mihashi, H. (2004). Computer simulation of fracture processes of concrete using mesolevel models of lattice structures. *Cement and concrete research, 34*(6), 1025-1033.

Li, Q., & Ansari, F. (1999). Mechanics of damage and constitutive relationships for high-strength concrete in triaxial compression. *Journal of engineering mechanics, 125*(1), 1-10.

Li, Q., Lu, Y., & Meng, H. (2009). Further investigation on the dynamic compressive strength enhancement of concrete-like materials based on split Hopkinson pressure bar tests. Part II: numerical simulations. *International Journal of Impact Engineering, 36*(12), 1335-1345.

Li, Q., & Meng, H. (2003). About the dynamic strength enhancement of concrete-like materials in a split Hopkinson pressure bar test. *International Journal of Solids and Structures, 40*(2), 343-360.

Lilliu, G., & van Mier, J. G. (2003). 3D lattice type fracture model for concrete. *Engineering Fracture Mechanics, 70*(7), 927-941.

Lin, W.-T., Cheng, A., Huang, R., & Cheng, T.-C. (2013). A method for testing the strength of concrete using uniaxial direct tension. *Journal of the Chinese Institute of Engineers, 36*(3), 295-303.

Liu, L., Shen, D., Chen, H., & Xu, W. (2014). Aggregate shape effect on the diffusivity of mortar: A 3D numerical investigation by random packing models of ellipsoidal particles and of convex polyhedral particles. *Computers & Structures, 144*, 40-51.

Liu, X., Garboczi, E., Grigoriu, M., Lu, Y., & Erdoğan, S. T. (2011). Spherical harmonic-based random fields based on real particle 3D data: improved numerical algorithm and quantitative comparison to real particles. *Powder Technology, 207*(1), 78-86.

López, C. M., Carol, I., & Aguado, A. (2008a). Meso-structural study of concrete fracture using interface elements. II: compression, biaxial and Brazilian test. *Materials and structures, 41*(3), 601-620.

López, C. M., Carol, I., & Aguado, A. (2008b). Meso-structural study of concrete fracture using interface elements. I: numerical model and tensile behavior. *Materials and structures, 41*(3), 583-599.

Lu, Y., & Li, Q. (2011). About the dynamic uniaxial tensile strength of concrete-like materials. *International journal of impact engineering, 38(4),* 171-180

Lu, Y., Song, Z., & Tu, Z. (2010). Analysis of dynamic response of concrete using a mesoscale model incorporating 3D effects. *International Journal of Protective Structures, 1*(2), 197-217.

Lu, Y., & Tu, Z. (2011). Mesoscale modelling of concrete for static and dynamic response analysis-Part 2: numerical investigations. *Structural Engineering and Mechanics, 37*(2), 215-231.

Lu, Y., & Xu, K. (2004). Modelling of dynamic behaviour of concrete materials under blast loading. *International Journal of solids and structures, 41*(1), 131-143.

Ma, G., Wang, X., & Li, Q. (2010). Modeling strain rate effect of heterogeneous materials using SPH method. *Rock mechanics and rock engineering, 43*(6), 763-776.

Malvar, L. J., Crawford, J. E., Wesevich, J. W., & Simons, D. (1997). A plasticity concrete material model for DYNA3D. *International Journal of Impact Engineering, 19*(9), 847-873.

Man, H.-K., & Van Mier, J. (2011). Damage distribution and size effect in numerical concrete from lattice analyses. *Cement and concrete composites, 33*(9), 867-880.

Man, H.-K., & van Mier, J. G. (2008). Size effect on strength and fracture energy for numerical concrete with realistic aggregate shapes. *International journal of fracture, 154*(1-2), 61-72.

Mattock, A. H. (2001). Shear friction and high-strength concrete. *Structural Journal, 98*(1), 50-59.

MC90, C. (1993). Design of Concrete Structures. *CEB-FIP Model Code 1990: Thomas Telford*.

Mihashi, H. (1983). A stochastic theory for fracture of concrete. *Fracture mechanics of concrete*, 301-339.

Miller, O., Freund, L., & Needleman, A. (1999). Modeling and simulation of dynamic fragmentation in brittle materials. *International Journal of Fracture, 96*(2), 101-125.

Mishnaevsky Jr, L. (2006). Microstructural effects on damage in composites–computational analysis. *Journal of Theoretical and Applied Mechanics, 44*(3), 533-552.

Moës, N., & Belytschko, T. (2002). Extended finite element method for cohesive crack growth. *Engineering Fracture Mechanics, 69*(7), 813-833.

Mohamad, M., Ibrahim, I., Abdullah, R., Rahman, A. A., Kueh, A., & Usman, J. (2015). Friction and cohesion coefficients of composite concrete-to-concrete bond. *Cement and Concrete Composites, 56*, 1-14.

Morel, S., & Dourado, N. (2011). Size effect in quasibrittle failure: Analytical model and numerical simulations using cohesive zone model. *International Journal of Solids and Structures, 48*(10), 1403-1412.

Muralidhara, S., Prasad, B. R., Eskandari, H., & Karihaloo, B. L. (2010). Fracture process zone size and true fracture energy of concrete using acoustic emission. *Construction and Building Materials, 24*(4), 479-486.

Nagai, K., Sato, Y., & Ueda, T. (2004). Mesoscopic simulation of failure of mortar and concrete by 2D RBSM. *Journal of Advanced Concrete Technology, 2*(3), 359-374.

Nagai, K., Sato, Y., & Ueda, T. (2005). Mesoscopic simulation of failure of mortar and concrete by 3D RBSM. *Journal of Advanced Concrete Technology, 3*(3), 385-402.

Nakamura, H., Tran, K., Kawamura, K., & Kunieda, M. (2010). Crack propagation analysis due to rebar corrosion. Paper presented at *the Proceedings of the 7th International Conference on Fracture Mechanics of Concrete and Concrete Structures (FramCoS-7),* Korea.

Otsuka, K., & Date, H. (2000). Fracture process zone in concrete tension specimen. *Engineering Fracture Mechanics, 65*(2), 111-131.

Owen, S. J. (1998). A Survey of Unstructured Mesh Generation Technology. Paper presented at *the IMR.*

Ožbolt, J., Bede, N., Sharma, A., & Mayer, U. (2015). Dynamic fracture of concrete L-specimen: Experimental and numerical study. *Engineering Fracture Mechanics, 148*, 27-41.

Ožbolt, J., Bošnjak, J., & Sola, E. (2013). Dynamic fracture of concrete compact tension specimen: Experimental and numerical study. *International Journal of solids and structures, 50*(25), 4270-4278.

Ožbolt, J., Sharma, A., İrhan, B., & Sola, E. (2014). Tensile behavior of concrete under high loading rates. *International journal of impact engineering, 69*, 55-68.

Papanikolaou, V. K., & Kappos, A. J. (2007). Confinement-sensitive plasticity constitutive model for concrete in triaxial compression. *International Journal of solids and structures, 44*(21), 7021-7048.

Park, K., & Paulino, G. H. (2011). Cohesive zone models: a critical review of traction-separation relationships across fracture surfaces. *Applied Mechanics Reviews, 64*(6), 060802.

Park, S., Xia, Q., & Zhou, M. (2001). Dynamic behavior of concrete at high strain rates and pressures: II. Numerical simulation. *International Journal of Impact Engineering, 25*(9), 887-910.

Pedersen, R., Simone, A., & Sluys, L. (2008). An analysis of dynamic fracture in concrete with a continuum visco-elastic visco-plastic damage model. *Engineering Fracture Mechanics, 75*(13), 3782-3805.

Pedersen, R., Simone, A., & Sluys, L. (2013). Mesoscopic modeling and simulation of the dynamic tensile behavior of concrete. *Cement and concrete research, 50*, 74-87.

Pina-Henriques, J., & Lourenço, P. B. (2006). Masonry compression: a numerical investigation at the meso-level. *Engineering computations, 23*(4), 382-407.

Prado, E., & Van Mier, J. (2003). Effect of particle structure on mode I fracture process in concrete. *Engineering Fracture Mechanics, 70*(14), 1793-1807.

Puri, U., & Uomoto, T. (2002). Characterization of distinct element modeling parameters for fresh concrete and its application in shotcrete simulations. *Journal of materials in civil engineering, 14*(2), 137-144.

Pyo, S., & El-Tawil, S. (2013). Crack velocity-dependent dynamic tensile behavior of concrete. *International journal of impact engineering, 55*, 63-70.

Ren, W., Yang, Z., Sharma, R., Zhang, C., & Withers, P. J. (2015). Two-dimensional X-ray CT image based meso-scale fracture modelling of concrete. *Engineering Fracture Mechanics, 133*, 24-39.

Rice, J. R., & Beltz, G. E. (1994). The activation energy for dislocation nucleation at a crack. *Journal of the Mechanics and Physics of Solids, 42*(2), 333-360.

Riedel, W., Wicklein, M., & Thoma, K. (2008). Shock properties of conventional and high strength concrete: Experimental and mesomechanical analysis. *International Journal of Impact Engineering, 35*(3), 155-171.

Ross, C. A., Jerome, D. M., Tedesco, J. W., & Hughes, M. L. (1996). Moisture and strain rate effects on concrete strength. *Materials Journal, 93*(3), 293-300.

Ross, C. A., Tedesco, J. W., & Kuennen, S. T. (1995). Effects of strain rate on concrete strength. *Materials Journal, 92*(1), 37-47.

Rosselló, C., Elices, M., & Guinea, G. (2006). Fracture of model concrete: 2. Fracture energy and characteristic length. *Cement and Concrete Research, 36*(7), 1345-1353.

Roubin, E., Vallade, A., Benkemoun, N., & Colliat, J.-B. (2015). Multi-scale failure of heterogeneous materials: A double kinematics enhancement for Embedded Finite Element Method. *International Journal of solids and structures, 52*, 180-196.

Ruiz, G., Ortiz, M., & Pandolfi, A. (2000). Three-dimensional finite-element simulation of the dynamic Brazilian tests on concrete cylinders. *International Journal for Numerical Methods in Engineering, 48*(7), 963-994.

Ruiz, G., Pandolfi, A., & Ortiz, M. (2001). Three-dimensional cohesive modeling of dynamic mixed-mode fracture. *International Journal for Numerical Methods in Engineering, 52*(1-2), 97-120.

Rutland, C. A., & Wang, M. L. (1997). The effects of confinement on the failure orientation in cementitious materials experimental observations. *Cement and concrete composites, 19*(2), 149-160.

Sacco, E., & Toti, J. (2010). Interface elements for the analysis of masonry structures. *International Journal for Computational Methods in Engineering Science and Mechanics, 11*(6), 354-373.

Saliba, J., Matallah, M., Loukili, A., Regoin, J.-P., Grégoire, D., Verdon, L., & Pijaudier-Cabot, G. (2016). Experimental and numerical analysis of crack evolution in concrete through acoustic emission technique and mesoscale modelling. *Engineering Fracture Mechanics*.

Schlangen, E., & Van Mier, J. (1992). Simple lattice model for numerical simulation of fracture of concrete materials and structures. *Materials and Structures, 25*(9), 534-542.

Schuler, H., Mayrhofer, C., & Thoma, K. (2006). Spall experiments for the measurement of the tensile strength and fracture energy of concrete at high strain rates. *International journal of impact engineering, 32*(10), 1635-1650.

Scrivener, K. L., Crumbie, A. K., & Laugesen, P. (2004). The interfacial transition zone (ITZ) between cement paste and aggregate in concrete. *Interface Science, 12*(4), 411-421.

Sfer, D., Carol, I., Gettu, R., & Etse, G. (2002). Study of the behavior of concrete under triaxial compression. *Journal of Engineering Mechanics, 128*(2), 156-163.

Shewchuk, J. R. (2008). General-dimensional constrained Delaunay and constrained regular triangulations, I: Combinatorial properties. *Discrete & Computational Geometry, 39*(1-3), 580-637.

Si, H. (2015). TetGen, a Delaunay-based quality tetrahedral mesh generator. *ACM Transactions on Mathematical Software (TOMS), 41*(2), 11.

Si, H., & Gärtner, K. (2005). Meshing piecewise linear complexes by constrained Delaunay tetrahedralizations. Paper presented at *the Proceedings of the 14th international meshing roundtable.*

Skarżyński, Ł., Syroka, E., & Tejchman, J. (2011). Measurements and calculations of the width of the fracture process zones on the surface of notched concrete beams. *Strain, 47*(s1).

Skarżyński, Ł., & Tejchman, J. (2016). Experimental Investigations of Fracture Process in Concrete by Means of X-ray Micro-computed Tomography. *Strain, 52*(1), 26-45.

Snozzi, L., Caballero, A., & Molinari, J.-F. (2011). Influence of the meso-structure in dynamic fracture simulation of concrete under tensile loading. *Cement and Concrete Research, 41*(11), 1130-1142.

Song, Z., & Lu, Y. (2011). An algorithm for generation of 3D mesostructure of concrete for finite element analysis. Paper presented at *the 19th UK-ACME Conference.*

Song, Z., & Lu, Y. (2012). Mesoscopic analysis of concrete under excessively high strain rate compression and implications on interpretation of test data. *International Journal of Impact Engineering, 46*, 41-55.

Swaddiwudhipong, S., Lu, H.-R., & Wee, T.-H. (2003). Direct tension test and tensile strain capacity of concrete at early age. *Cement and concrete research, 33*(12), 2077-2084.

Swartz, S., Lu, L., Tang, L., & Refai, T. (1988). Mode II fracture-parameter estimates for concrete from beam specimens. *Experimental Mechanics, 28*(2), 146-153.

Swartz, S., & Taha, N. (1991). Crack propagation and fracture of plain concrete beams subjected to shear and compression. *Structural Journal, 88*(2), 169-177.

Tada, H., Paris, P. C., & Irwin, G. R. (2000). The stress analysis of cracks handbook ASME International. *New York*.

Tedesco, J., Hughes, M., & Ross, C. (1994). Numerical simulation of high strain rate concrete compression tests. *Computers & Structures, 51*(1), 65-77.

Tejchman, J. (2010). Calculations of fracture process zones on meso-scale in notched concrete beams subjected to three-point bending. *European Journal of Mechanics-A/Solids, 29*(4), 746-760.

Tu, Z., & Lu, Y. (2009). Evaluation of typical concrete material models used in hydrocodes for high dynamic response simulations. *International Journal of Impact Engineering, 36*(1), 132-146.

Tu, Z., & Lu, Y. (2011). Mesoscale modelling of concrete for static and dynamic response analysis-Part 1: model development and implementation. *Structural Engineering and Mechanics, 37*(2), 197-213.

Turon, A., Camanho, P. P., Costa, J., & Dávila, C. (2006). A damage model for the simulation of delamination in advanced composites under variable-mode loading. *Mechanics of Materials, 38*(11), 1072-1089.

Turon, A., Davila, C. G., Camanho, P. P., & Costa, J. (2007). An engineering solution for mesh size effects in the simulation of delamination using cohesive zone models. *Engineering Fracture Mechanics, 74*(10), 1665-1682.

Tvergaard, V. (1990). Effect of fibre debonding in a whisker-reinforced metal. *Materials Science and Engineering: A, 125*(2), 203-213.

Van Vliet, M., & Van Mier, J. (1995). Softening behaviour of concrete under uniaxial compression. *Fracture mechanics of concrete structures, 1*, 383.

Vandewalle, L. (2000). RILEM TC 162-TDF: Test and design methods for steel fibre reinforced concrete. *Materials and structures, 33*(225), 3-6.

Vegt, I., Breugel, V., & Weerheijm, J. (2007). Failure mechanisms of concrete under impact loading. *Fracture Mechanics of Concrete and Concrete Structures, FraMCoS-6, 1*, 579-587.

Veselý, V., & Frantík, P. (2010). Reconstruction of a fracture process zone during tensile failure of quasi-brittle materials. *Applied and Computational Mechanics, 4 (122)* , 237-250

Vonk, R. A. (1992). Softening of concrete loaded in compression. *Technische Universiteit Eindhoven.*

Vulovic, S., Zivkovic, M., & Grujovic, N. (2008). Contact Problems Based on the Penalty Method. *Scientific Technical Review, 63*(3-4), 2126-2132.

Wang, L., Park, J.-Y., & Fu, Y. (2007). Representation of real particles for DEM simulation using X-ray tomography. *Construction and Building Materials, 21*(2), 338-346.

Wang, X., Zhang, M., & Jivkov, A. P. (2016). Computational technology for analysis of 3D meso-structure effects on damage and failure of concrete. *International Journal of solids and structures, 80*, 310-333.

Wang, Z., Kwan, A., & Chan, H. (1999). Mesoscopic study of concrete I: generation of random aggregate structure and finite element mesh. *Computers & Structures, 70*(5), 533-544.

Weerheijm, J., & Forquin, P. (2013). Response mechanisms of concrete under impulsive tensile loading.

Weerheijm, J., & Van Doormaal, J. (2007). Tensile failure of concrete at high loading rates: new test data on strength and fracture energy from instrumented spalling tests. *International journal of impact engineering, 34*(3), 609-626.

Weibull, W. (1951). A statistical distribution function of wide applicability, presented to the American society of mechanical engineers. Atlantic City, *NJ, 23*, 981-997.

Wriggers, P., & Moftah, S. (2006). Mesoscale models for concrete: Homogenisation and damage behaviour. *Finite elements in analysis and design, 42*(7), 623-636.

Wu, H., Zhang, Q., Huang, F., & Jin, Q. (2005). Experimental and numerical investigation on the dynamic tensile strength of concrete. *International journal of impact engineering, 32*(1), 605-617.

Wu, Z., Rong, H., Zheng, J., Xu, F., & Dong, W. (2011). An experimental investigation on the FPZ properties in concrete using digital image correlation technique. *Engineering Fracture Mechanics, 78*(17), 2978-2990.

Yin, A., Yang, X., Zhang, C., Zeng, G., & Yang, Z. (2015). Three-dimensional heterogeneous fracture simulation of asphalt mixture under uniaxial tension with cohesive crack model. *Construction and Building Materials, 76*, 103-117.

Zhang, D., & Wu, K. (1999). Fracture process zone of notched three-point-bending concrete beams. *Cement and Concrete Research, 29*(12), 1887-1892.

Zhang, S., Lu, Y., Chen, X., Teng, X., & Yu, S. (2015). Further investigation on the real rate effect of dynamic tensile strength for concrete-like materials. *Latin American Journal of Solids and Structures, an ABCM Journal, 12*(2).

Zheng, D., & Li, Q. (2004). An explanation for rate effect of concrete strength based on fracture toughness including free water viscosity. *Engineering Fracture Mechanics, 71*(16), 2319-2327.

Zhou, X., & Hao, H. (2008a). Modelling of compressive behaviour of concrete-like materials at high strain rate. *International Journal of solids and structures, 45*(17), 4648-4661.

Zhou, X., & Hao, H. (2008b). Mesoscale modelling of concrete tensile failure mechanism at high strain rates. *Computers & structures, 86*(21), 2013-2026

Appendix: List of publications

Zhou, R., Song, Z. & Lu, Y. (2016) 3D mesoscale finite element modelling of concrete. *Computers & Structures*. (Under revision)

Zhou, R. & Lu, Y. (2016) Modelling of mesoscopic fracture in concrete using a cohesive plus contact interface approach. (In final preparation to be submitted to *Journal of Engineering Mechanics-ASCE*)

Zhou, R. & Lu, Y. (2016) Mesoscopic analysis of dynamic fracture in concrete with zero-thickness interface elements. (In final preparation to be submitted to *International Journal of Impact Engineering*)

Zhou, R. & Lu, Y. (2016) Mesoscopic analysis of size effect in concrete materials. (In final preparation to be submitted to *Engineering Fracture Mechanics*)

Zhou, R., & Lu, Y. (2014) Numerical simulation of size effect in concrete beams. *Infrastructure and Environment Scotland 2nd Postgraduate Conference*, 2nd September Edinburgh, UK

Zhou, R. & Lu, Y. (2015) 3D Mesoscale analysis of strain rate effects in concrete under compression. *The First International Conference on Structural Safety under Fire & Blast*, 2-4 September, Glasgow, UK

Lu, Y. & **Zhou, R**. (2015) A 3-D perspective of dynamic behaviour of heterogeneous solids. *11th International DYMAT Conference*, 7-11 September, Lugano, Switzerland.